SALT DAMAGE CRITERION
PROOF-OF-CONCEPT RESEARCH

FINAL REPORT
30 September 2000 – 29 September 2002

by

Kerry L. DeVries
Kirby D. Mellegard
Gary D. Callahan

November 2002

Contract DE-FC26-00NT41026

RESPEC
P.O. Box 725
Rapid City, South Dakota 57709

SALT DAMAGE CRITERION
PROOF-OF-CONCEPT RESEARCH

Topical Report RSI-1675
DE-FC26-00NT41026

by

Kerry L. DeVries
Kirby D. Mellegard
Gary D. Callahan

RESPEC
P.O. Box 725
Rapid City, South Dakota 57709

prepared for

United States Department of Energy
National Energy Technology Laboratory
626 Cochrans Mill Road
Pittsburgh, Pennsylvania 16236

November 2002

ABSTRACT

The purpose of this study was to conduct a field-scale application demonstrating the use of continuum damage mechanics to determine the minimum allowable operating pressure of compressed natural gas storage caverns in salt formations. A geomechanical study was performed of two natural gas storage caverns (one existing and one planned) utilizing state-of-the-art salt mechanics to assess the potential for cavern instability and collapse. The geomechanical study consisted primarily of laboratory testing, theoretical development, and analytical/numerical tasks. A total of 50 laboratory tests was performed on salt specimens to aid in the development and definition of the material model used to predict the behavior of rock salt. Material model refinement was performed that improved the predictive capability of modeling salt during damage healing, recovery of work-hardened salt, and the behavior of salt at stress states other than triaxial compression. Results of this study showed that the working gas capacity of the existing cavern could be increased by 18 percent and the planned cavern could be increased by 8 percent using the proposed method compared to a conventional stress-based method. Further refinement of the continuum damage model is recommended to account for known behavior of salt at stress conditions other than triaxial compression that is not characterized accurately by the existing model.

EXECUTIVE SUMMARY

Product movement to and from compressed natural gas (CNG) storage caverns in salt is accomplished simply by compression and expansion of the stored gas. The storage cavern economics can be improved by lowering the minimum gas pressure and decreasing the quantity of cushion gas required for the storage facility. The constraint that typically limits the minimum gas pressure for a CNG storage cavern is the potential for salt dilation that can lead to spalling in the cavern roof and/or walls and subsequent damage to the cavern or hanging string(s). When the deviatoric stress state (caused by the difference between the gas pressure inside a cavern and the in situ stress of the surrounding salt) becomes too large, dilation (microfracturing resulting in increased porosity) occurs in the salt. Spalling of the salt along the roof or wall of a cavern can occur when damage in the salt becomes severe enough to initiate macrofracturing.

Criteria currently available for predicting the onset of dilation include stress-based and damage-based methods. Stress-based criteria have been used extensively in the last several years to estimate the potential for dilation around salt storage caverns. The stress-based approach simply indicates whether or not the salt has experienced a stress state that could cause dilation. Use of salt damage criteria requires sophisticated material models that not only indicate if and when dilation occurs but also quantifies the degree of dilation. Some salt damage models are capable of tracking the history of damage accumulation and subsequent healing of microfractures that is expected to occur for the salt when the cavern is at or near maximum pressure.

This research report describes the first-time application of a salt damage criterion to determine the minimum allowable gas pressure of actual CNG storage caverns. An objective of this project was to assess differences for minimum gas pressure determined using both stress-based and damage-based criteria, with lower minimum gas pressures expected for the damage-based criterion. The idea that the minimum gas pressure in CNG salt caverns may be reduced using a salt damage criterion is based on the concept that an accurate prediction of the behavior of salt can be obtained by an advanced model that tracks the history of damage and healing of the salt.

For this proof-of-concept project, a damage-based design criterion was applied to two Bay Gas Storage CNG caverns (one existing cavern and one newly constructed cavern) in the McIntosh salt dome located northwest of Mobile, Alabama. The existing cavern is referred to as Bay Gas Well No. 1, and the cavern under development is referred to as Bay Gas Well No. 2. This project demonstrates that a limited laboratory test matrix comprised of approximately 37 tests can be used to define the material model for salt that is capable of predicting the formation and evolution of salt damage. Assessment of the minimum allowable gas pressures may then be performed using this material model for salt and evaluating the accumulation of damage.

The Multimechanism Deformation Coupled Fracture model (MDCF model) was used in this study to characterize the behavior of salt. The MDCF model was originally developed to aid in the prediction of radioactive waste disposal at the Waste Isolation Pilot Plant near Carlsbad, New Mexico. Because this National Energy Technology Laboratory project represents the first application of the salt damage criterion using the MDCF model to predict CNG cavern response, discrepancy resolution and model refinement activities were considered necessary to correct known deficiencies and to address other potential unforeseen problems. Major material model modifications were made during this study to improve application of the MDCF model to CNG storage, including:

1. Modification of the healing term to include damage (microfracture) orientation. As a result of this modification, when conditions for damage healing occur, recovery (crack closure and sintering) occurs normal to the microfractures, as dictated by the orientation of the damage. This update alleviated known deficiencies that impacted the healing rate and stresses within the salt surrounding the storage caverns during damage recovery.

2. Update of the transient creep recovery term to predict more accurately the creep rate of salt when the deviatoric stress has decreased (i.e., the gas pressure in the cavern is significantly greater than the minimum gas pressure). Although much of the closure that occurs for a CNG storage cavern occurs when the cavern is at or near minimum pressure, the creep response of hardened salt when the gas pressure is greater than the minimum pressure was found to have a significant impact on the annual closure rate of the caverns.

3. Reformulation of the dilation boundary term to reflect a material that is weaker under triaxial extension than triaxial compression states of stress. The original formulation of the MDCF model did not capture this known behavior of salt and resulted in predictions of minimum gas pressure that may not be conservative.

The first two modifications were determined to be necessary before this project was initiated; however, the need to make the third modification was realized during the course of this study. The need for all of these modifications was evident from laboratory tests, which subsequently guided their development. A total of 50 mechanical and mineralogic tests was performed on salt core recovered from the Bay Gas Well No. 2 wellbore: 6 Brazilian tests, 12 constant strain rate tests, 8 constant mean stress tests, 14 creep tests, and 10 mineralogic tests. The laboratory tests were used to evaluate the 19 free parameters of the MDCF model and to aid in model refinement efforts.

Numerical calculations show that the stress state of the salt near the caverns is much closer to triaxial extension than triaxial compression when the caverns are at or near minimum gas pressure. After reviewing the MDCF model, it was observed that the model predicts salt is stronger in triaxial extension than in triaxial compression. Most rocks behave differently in triaxial compression and extension with the material being weaker in extension. As a first attempt to alleviate this deficiency, theoretical development of a new MDCF model effective

stress measure based on a Mohr-Coulomb-type criterion was completed. Because of time and economic constraints, laboratory testing at stress states other than triaxial compression was limited to the completion of one successful creep test in triaxial extension. As a result, complete development of the model was not fully realized during this project. However, development of the model was sufficient for use in numerical calculations of the storage caverns.

To perform the numerical calculations with the modified stress measures based on the Mohr Coulomb criterion, parameter values were determined that provide reasonable, yet conservative, agreement with laboratory tests at triaxial compression states of stress. The parameter values determined are also expected to provide a conservative estimate for the onset of dilation at triaxial extension states of stress; however, experimental data are not available to confirm this assumption. The numerical calculations using the proposed stress measures based on the Mohr-Coulomb criterion predict that a minimum gas pressure of 5.5 MPa (800 psi) is allowable for the Bay Gas caverns; whereas, the minimum gas pressure determined using the original model formulation predicted that a pressure of 2.8 MPa (400 psi) was sufficient to maintain stability. The more conservative results predicted using the modified effective stress measures are recommended (i.e., 5.5 MPa (800 psi)) for the Bay Gas caverns. The recommended minimum pressure is the value necessary to satisfy the cavern stability design constraint based on the potential for salt dilation. Other design factors (e.g., cavern closure and subsidence) also have to be considered when determining the actual minimum allowable gas pressure to be used for a CNG storage cavern.

For comparative purposes, the minimum allowable gas pressures for the Bay Gas caverns were determined using a conventional stress-based criterion commonly used to evaluate CNG storage caverns. Minimum allowable gas pressures of 8.3 and 6.9 MPa (1,200 and 1,000 psi) were predicted using the stress-based criterion for Well No. 1 and Well No. 2, respectively. Differences determined for minimum gas pressures of Well No. 1 and Well No. 2 are attributable to the different cavern geometries. Thus the damage-based approach predicts lower allowable minimum gas pressures than predicted by the conventional stress-based criterion. The lower minimum gas pressures predicted using the damage-based criterion increases the initial working gas capacities of Bay Gas Well No. 1 and Well No. 2 by about 18 and 8 percent, respectively.

Based on the results of this study, the damage-based mechanics approach using the MDCF model is a viable option for determining the minimum gas pressure for CNG storage caverns. However, it is recommended that further refinement and development of the MDCF model be performed before it is routinely applied to cavern analyses. Laboratory testing at stress states other than triaxial compression is required to characterize the behavior of salt at conditions similar to those experienced during CNG storage operation.

TABLE OF CONTENTS

TABLE OF CONTENTS
(Continued)

TABLE OF CONTENTS
(Continued)

LIST OF TABLES

LIST OF FIGURES

LIST OF FIGURES
(Continued)

1.0 INTRODUCTION

1.1 BACKGROUND

The working gas capacity of many storage caverns can be increased if the minimum level of internal pressure in storage caverns can be reduced without jeopardizing cavern stability. Geomechanical evaluations are typically used to assess cavern stability during operation. The approach generally used in the geomechanics evaluation of a salt cavern scheduled for compressed natural gas (CNG) storage is to determine an acceptable operating pressure range that meets various design constraints, including the potential for salt dilation [Ratigan et al., 1993]. When the deviatoric stress state (caused by the difference between the gas pressure inside a cavern and the in situ stress of the surrounding salt) becomes too large, dilation (microfracturing resulting in increased porosity) occurs in the salt. Spalling of the salt along the roof or wall of a cavern can occur when the dilation in the salt becomes severe enough to initiate macrofracturing, which may result in loss of containment.

RESPEC recently completed a project for the Department of Energy (DOE) which demonstrated that the minimum gas pressure in many CNG storage caverns could potentially be lowered while meeting the design constraints using a continuum damage mechanics approach [DeVries et al., 1998]. Additionally, the continuum damage approach was deemed economically feasible for use by the CNG industry in the previous project [Nieland et al., 1999]. In the previous project, a relatively sophisticated constitutive model for salt developed for the Waste Isolation Pilot Plant (WIPP) to predict the response of a nuclear waste repository was applied to CNG storage caverns. The constitutive model, referred to as the Multimechanism Deformation Coupled Fracture (MDCF) model, has the capability to predict the onset of dilation and can quantify the severity of microfracturing or damage within the salt as a function of time. A limiting value for the severity of damage was established to provide a conservative design criterion for maintaining cavern stability. The MDCF model is given in Appendix A in its original form without modifications suggested by the present study.

The objective of the current project is to prove the technology developed for determining the minimum gas pressures of CNG caverns based on the salt damage criterion described by DeVries et al. [1998] and Nieland et al. [1999]. In the earlier work, two major conclusions were reached: (1) the minimum gas pressure in storage caverns could be lowered using a continuum damage mechanics approach and the salt damage criterion and (2) an efficient test matrix could be applied to provide site-specific data for the material properties required in the salt constitutive model used for the advanced design criterion. However, these conclusions were based largely on hypothetical information unrelated to a specific application. For example, cavern analyses related to the first conclusion used damage properties for WIPP with the creep characteristics of another salt. This was necessary because WIPP salt was the only salt for which damage parameters had been determined. Through sensitivity studies of simulated test

responses, an efficient test matrix was devised that could be used to determine the parameter values for the MDCF constitutive model used for the advanced design criterion analyses supporting the second conclusion. However, this test matrix had never been applied to a particular salt formation.

1.2 SCOPE

The scope of work considered in this project represents a proof-of-concept research effort to demonstrate the viability of an advanced design criterion to improve the working gas capacity in natural gas storage caverns. RESPEC, an engineering consulting and services firm, and Bay Gas Storage Company, Ltd. (Bay Gas), a subsidiary of EnergySouth, Inc. and a natural gas storage and pipeline company, planned to use the advanced design criterion to permit and operate two Bay Gas storage caverns (one existing cavern and one newly constructed cavern) in the McIntosh salt dome located northwest of Mobile, Alabama. RESPEC and Bay Gas proposed to refine and to demonstrate the use of a new design criterion based on salt damage (microcracking) for determining the minimum gas pressure for storing natural gas in salt caverns.

In this research, laboratory tests were performed to derive accurately and effectively the site-specific creep, damage, and healing parameters of a constitutive model that can be used to assess the stability of compressed natural gas storage caverns. Numerical simulations were performed using the material properties for salt determined from laboratory testing and the geometrical, operational, and geological model of an existing and a planned storage cavern in the McIntosh Dome. The simulations were used to establish an operating pressure range for gas storage based on the new design criterion that resulted in structurally stable and gas-tight conditions. To meet the objectives of this project, the scope of work was subdivided into five main tasks:

1. Site Characterization

2. Laboratory Testing

3. Model Refinement

4. Parameter Value Determination

5. Cavern Analysis.

The work performed under each of these tasks is discussed in a separate chapter. Because this project represents the first application of the new design criterion, a model refinement task was included in the scope of work. Model refinement was necessary to correct known deficiencies of the MDCF model for its application to the natural gas storage industry. The MDCF model was initially developed for aiding in the prediction of the WIPP nuclear waste repository. Model refinement was performed to improve the predictive capability of the model

under operating conditions typical of those experienced by natural gas storage caverns in salt formations.

1.3 REPORT ORGANIZATION

This report contains nine chapters, including this introduction. Chapter 2.0 describes the McIntosh site-specific information collected for this study. The laboratory testing program is described in Chapter 3.0. The work efforts that have been performed under the model refinement task are given in Chapter 4.0. Chapter 5.0 presents results of the parameter value determination task. Chapter 6.0 describes the numerical analyses used to assess cavern stability. Chapter 7.0 provides conclusions and a brief summary of the project. Recommendations regarding use of the continuum damage mechanics approach for analyzing CNG storage caverns are provided in Chapter 8.0. A list of cited references is given in Chapter 9.0, followed by appendices containing supporting documentation.

2.0 SITE CHARACTERIZATION

Bay Gas operates a single natural gas storage cavern, referred to as Bay Gas Well No. 1, in the McIntosh salt dome located approximately 40 miles northwest of Mobile, Alabama. In addition to the existing cavern, Bay Gas is in the process of solution mining a 4.22-million-barrel (MMbbls) cavern (Bay Gas Well No. 2) for natural gas storage within the McIntosh Dome. The McIntosh Dome is approximately 1,800 meters (6,000 feet) in diameter with the existing and planned caverns located approximately half-way between the center of the dome and the dome flanks, as shown in Figure 2-1. This chapter describes the site information that was gathered and evaluated to determine site-specific conditions required to perform geo-mechanical analyses of the existing and planned Bay Gas storage caverns such as: in situ stress, cavern geometry, operating pressure history, and stratigraphy of the surrounding and overlying geologic units. Site characterization activities were divided into two categories: (1) compilation of existing material and (2) acquisition of new geologic data from the Bay Gas Well No. 2 wellbore.

2.1 COMPILATION OF EXISTING DATA

Existing data available regarding the operation and local setting at the McIntosh Dome include papers and journal articles in the public domain and records that Bay Gas recorded during the development and operation of Bay Gas Well No. 1. Site-specific information from both of these areas is discussed separately below.

2.1.1 Literature Search for Public Domain Records

In addition to the Bay Gas Well No. 1 natural gas storage cavern, nine brine wells and one compressed air energy storage (CAES) cavern have been developed in the McIntosh Dome. The nine brine wells are operated by Olin Chemical, of which six have been plugged. A litera-ture search was performed to identify relevant public domain publications; most publications available are related to the CAES project. A partial list of publications discovered during the literature search is given below. Additional publications on the CAES project can be purchased from the Electrical Power Research Institute (EPRI) but are not given in the following list. While this list is not exhaustive, it provided sufficient information to proceed with the geomechanical analysis without further investigation.

- **Dahlstrom, D. J., 1988.** *McIntosh Dome Salt Core Testing,* Technical Letter Memorandum RSI/TLM-150, prepared by RE/SPEC Inc., Rapid City, SD, for CAES Technology, Palo Alto, CA.
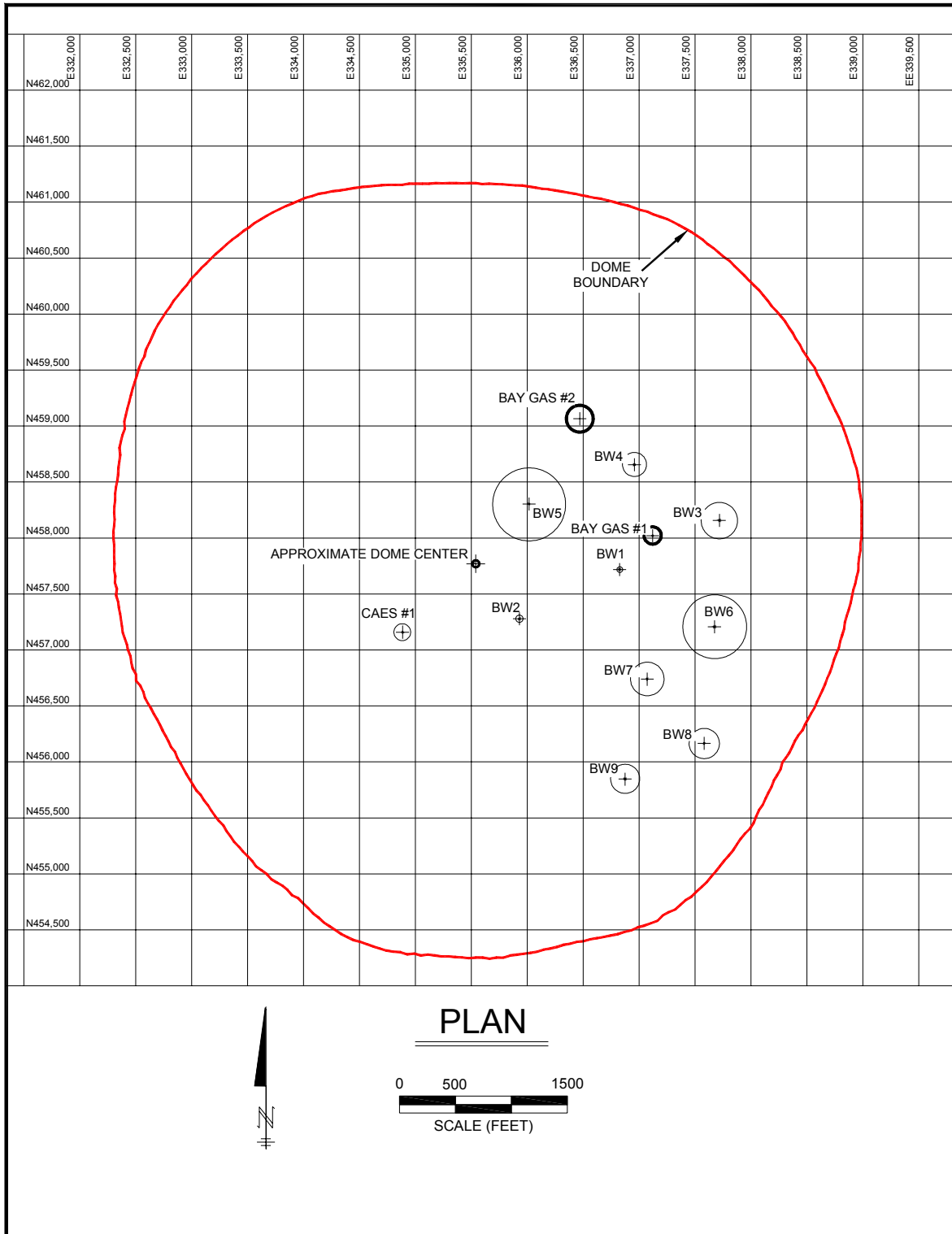
Figure 2-1. Plan View Illustrating the Location of the Bay Gas Caverns at the McIntosh Dome.

- **Medley, A. H., 1987.** "Status of Compressed Air Energy Storage Project, McIntosh, AL – Part II," *Solution Mining Research Institute Fall Meeting*, Denver, CO, October 19–20.

- **Medley, A. H., 1988.** "Status of Compressed Air Energy Storage Project, McIntosh, AL – Part II," *Solution Mining Research Institute Spring Meeting*, Mobile, AL, April 25.

- **Medley, A. H., 1988.** "Part III – Status of McIntosh, Alabama 100 MW Compressed Air Energy Storage (CAES) Project," *Solution Mining Research Institute Fall Meeting*, Dallas, TX, October 17–19.

- **Medley, A. H., 1989.** "Status of McIntosh, Alabama 110 MW CAES Project," *Solution Mining Research Institute Spring Meeting*, New Orleans, LA, May 1.

- **Mehta, B. R., 1987.** "Compressed Air Energy Storage (CAES) in Salt Caverns," *Solution Mining Research Institute Spring Meeting*, Tulsa, OK, April 27.

- **Mehta, B. R., 1987.** "Status of Compressed Air Energy Storage Project, McIntosh, AL – Part I," *Solution Mining Research Institute Fall Meeting*, Denver, CO, October 19–20.

- **Mehta, B. R., 1988.** "Status of Compressed Air Energy Storage Project, McIntosh, AL – Part I," *Solution Mining Research Institute Spring Meeting*, Mobile, AL, April 25.

- **Pfeifle, T. W. and J. L. Ratigan, 1993.** *Mechanical Properties Testing and Chemical and Mineralogic Analyses of Salt From the Bay Gas Storage Well #1, McIntosh Dome, Alabama*, RSI-0454, prepared by RE/SPEC Inc., Rapid City, SD, for PB-KBB, Inc., Houston, TX.

- **Serata, S. and B. Mehta, 1992.** "Design and Stability of Salt Caverns for Compressed Air Energy Storage (CAES)," *Solution Mining Research Institute Spring Meeting*, Kyoto, Japan, April 6–9.

- **Serata, S., B. Mehta, and M. Hiremath, 1989.** "Geomechanical Stability Analysis for CAES Cavern Operation," *Storage of Gases in Rock Caverns*, Nilsen and Olsen (eds.), A. A. Balkema, Rotterdam, pp. 129–135.

- **Thoms, R. L. and R. M. Gehle, 1985.** "Hydrofracture Gradients in Salt Domes – Progress Report," *Solution Mining Research Institute Fall Meeting*, Houston, TX, October 14–15.

Many of the reports on the CAES project addressed the topic of economics; however, a few of the papers provided a limited discussion on numerical modeling studies and underground construction. Helpful information determined from the literature search included: (1) stratigraphy surrounding the dome, (2) approximate dome geometry, (3) approximate location and dimensions of brine caverns within the dome, and (4) elevation of the brine and CAES caverns. Based on this information, it was assumed that the Bay Gas caverns are sufficiently remote from other caverns and the flanks of the salt dome that they will not influence the numerical

analysis results. Therefore, structural models of the Bay Gas storage caverns can assume single isolated caverns developed in an all-salt formation.

2.1.2 Bay Gas Well No. 1 Existing Data

Existing data associated with Bay Gas Well No. 1 and the local setting at the McIntosh salt dome were obtained from Bay Gas and reviewed. Data obtained include:

1. Temperature surveys taken between 1994 and 1998 of Bay Gas Well No. 1

2. Litho density and gamma ray logs of the Bay Gas Well No. 1 wellbore

3. Maps illustrating well locations, cavern spacings, and the salt dome boundary at the McIntosh salt dome

4. Bay Gas Well No. 1 cavern pressure history

5. Sonar data of Bay Gas Well No. 1 taken in 1994 and 2001

6. Casing shoe depth of Bay Gas Well No. 1

7. Sediment and caprock thickness and elevation.

Figure 2-2 illustrates the geometry of Bay Gas Well No. 1 based on the 1994 sonar. Drilling of this cavern began in August 1992 with the cavern put into service about 2 years later (September 1994). The casing shoe of the cavern is located at a depth of 1,223 meters (4,012 feet) below ground with the top of salt located at a depth of approximately 121.9 meters (400 feet). Approximately a 6-meter- (20-foot-) thick caprock lies on top of the salt with sediments extending above the caprock to ground surface.

The initial solution-mined cavern volume was approximately 2.7 MMbbls. As shown in Figure 2-2, the cavern has a flat roof and a nearly cylindrical shape between depths of 1,265 and 1,494 meters (4,150 and 4,900 feet) with an average diameter of approximately 50 meters (164 feet). Between depths of 1,494 and 1,524 meters (4,900 and 5,000 feet), the cavern diameter tapers to 22 meters (72 feet). The cavern diameter remains essentially unchanged until the bottom of the cavern at a depth of 1,615 meters (5,300 feet). A total of over 1.1 million barrels of less than fully saturated brine has been pumped into the cavern since the cavern went into service. The brine was injected on four separate occasions, typically during the winter and withdrawn during the fall, to help maintain the storage capacity of the cavern. Although the salinity of the brine injected is not known, the 2001 sonar data from the lower portion of the cavern indicates that any enlargement of the cavern has been negated by creep closure.

Since the cavern was put into service in 1994, it has been used to supply natural gas to various customers, including Alabama Electric Cooperative, an electrical power generator. Seasonal variations in cavern pressure are the predominant trend with peak pressure in the
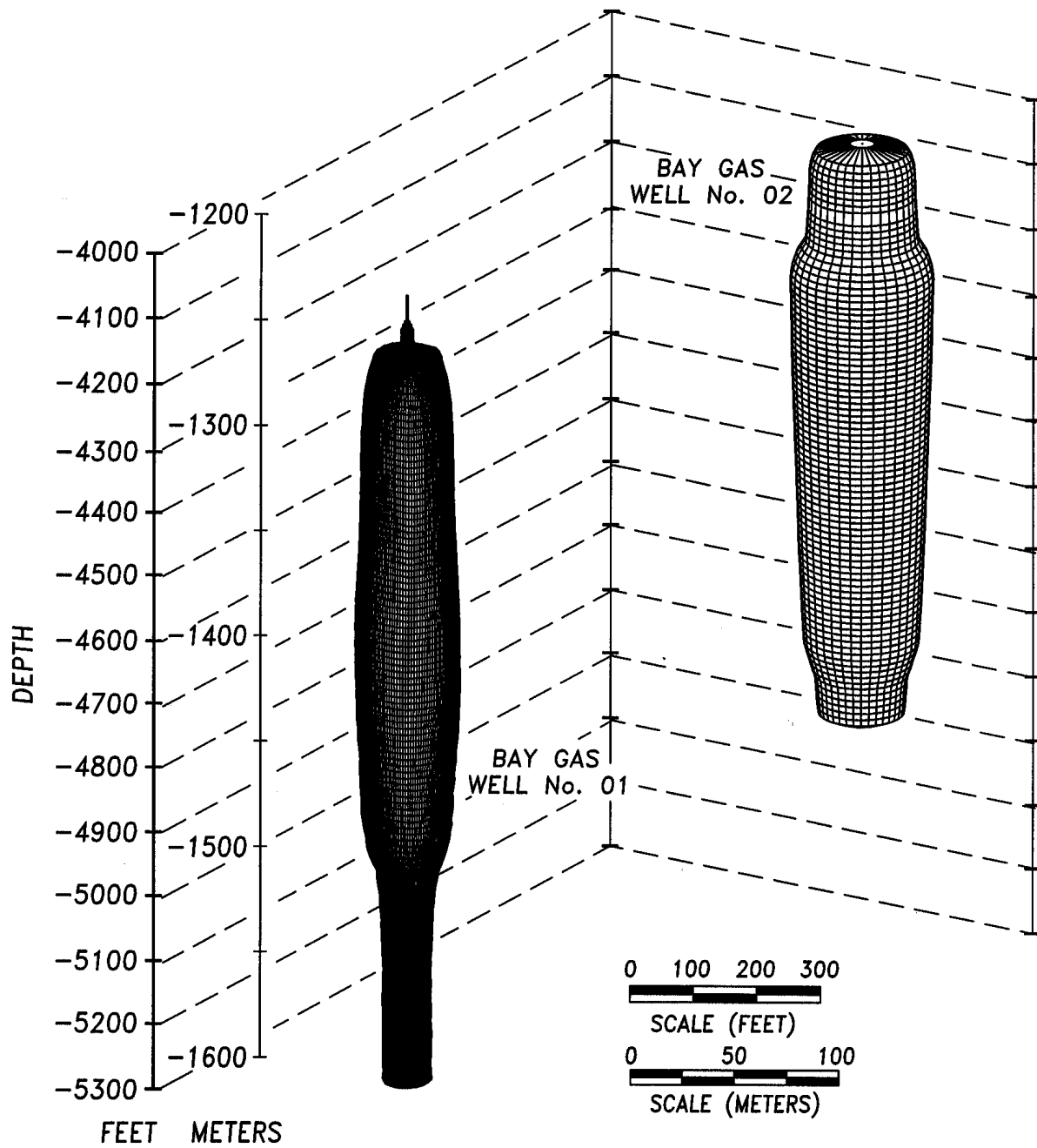
Figure 2-2. Isometric View of the Existing and Planned Bay Gas Caverns.

cavern occurring during the summer months and minimum pressure in the cavern occurring during the winter months, as shown in Figure 2-3. During the last 6 years of service, cavern pressure typically ranged between 21.0 MPa (3,050 psi) and 9.0 MPa (1,300 psi), but has been as low as 8.4 MPa (1,217 psi) at the wellhead.

The annual temperature logs taken between 1994 and 1998 from Bay Gas Well No. 1 were examined. Temperature as a function of depth obtained from each of these logs is provided in Figure 2-4. As shown in Figure 2-4, the temperature gradient is essentially linear with depth between elevations of 152 and 1,219 meters (500 and 4,000 feet). Based on this data, a surface temperature of 26.9ºC (80.4ºF) and geothermal gradient of 0.018675ºC/meter (0.01025ºF/foot) can be used to define the in situ temperature at the McIntosh Dome.

2.2 ACQUIRED DATA FROM THE BAY GAS WELL NO. 2 WELLBORE

Drilling of the wellbore for the Bay Gas Well No. 2 natural gas storage cavern was initiated on February 7, 2001. Since that time, the wellbore was drilled to a total depth of 1,603 meters (5,260 feet) below ground surface and cased. Wellbore logging was performed following drilling of the wellbore to final depth. The final geometry of the cavern, based on a solution-mining simulation, was provided to RESPEC by Sofregaz US (Sofregaz US (now PB Energy Storage Services) was contracted to design and develop the cavern) and is provided in Figure 2-2. The casing shoe of the cavern is located at a depth of 1,223 meters (4,012 feet) below ground with the top of the cavern located at a depth of approximately 1,331 meters (4,100 feet).

The cavern is expected to be put into operation in April 2003; however, solutioning of the lower portion of the cavern will continue under gas until the final cavern volume is obtained. Following solution mining, the maximum diameter of the cavern is expected to be 73.2 meters (240 feet).

2.2.1 Bay Gas Well No. 2 Core Retrieval

A total of approximately 36 meters (120 feet) of rock-salt core was recovered from the Bay Gas Well No. 2 wellbore at locations near the (1) top of the cavern, (2) cavern midheight, and (3) bottom of the cavern. A 9-meter- (30-foot-) long core-barrel was used to cut 100-millimeter- (4-inch-) diameter salt core. Approximately 18 meters (60 feet) of core were taken from near the top of the cavern between depths of 1,250.0 and 1,267.6 meters (4,101 and 4,158 feet). Nine meters (30 feet) of core were taken from near the cavern midheight between depths of 1,411 and 1,420 meters (4,630 and 4,660 feet). Similarly, 9 meters of core were taken from the bottom of the wellbore at depths between 1,594 and 1,603 meters (5,230 and 5,260 feet). The core samples were wrapped in Saran Wrap to prevent moisture loss and packed in protective tubing to prevent damage before being shipped to the RESPEC Materials Testing Laboratory in Rapid City, South Dakota.
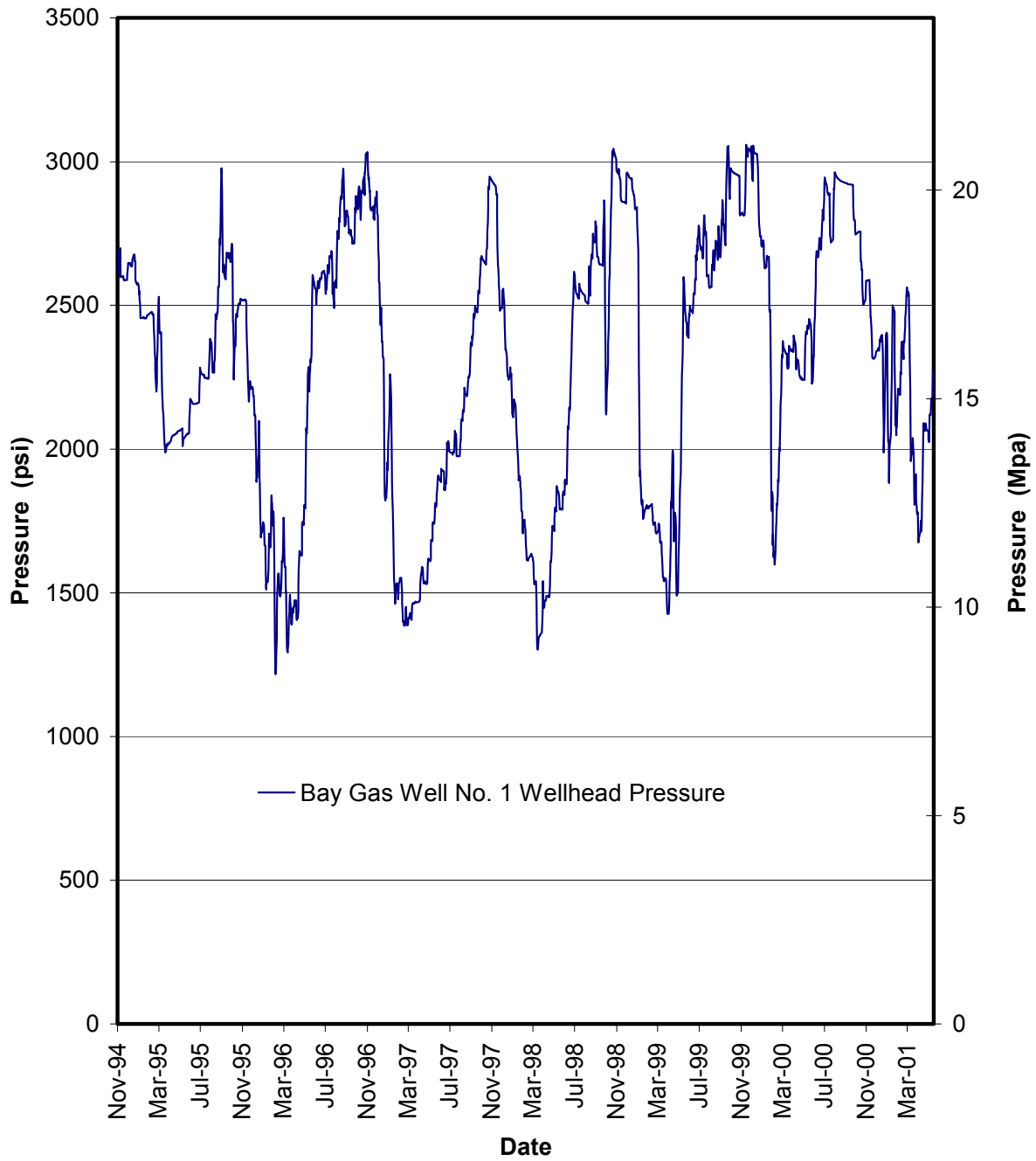
Figure 2-3. Wellhead Pressure of Bay Gas Well No. 1.
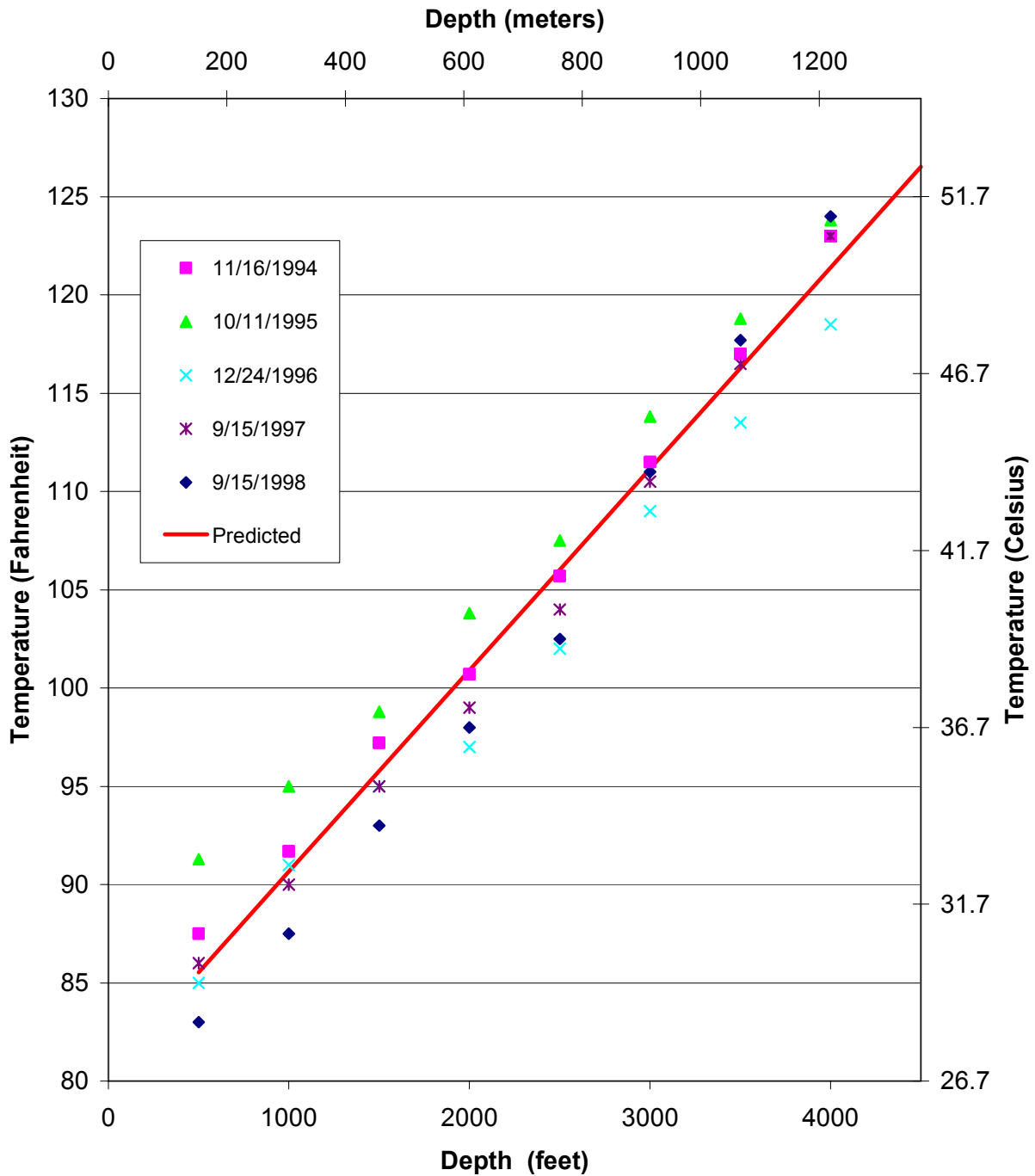
Figure 2-4. Temperature Profiles From Logs of Bay Gas Well No. 1 From 1994 Through 1998.

Not all recovered core was suitable for testing using the RESPEC rock testing machines. The outer surface of approximately 8 meters (25 feet) of core obtained near the top of the cavern between 1,250 and 1,257 meters (4,101 and 4,126 feet) below ground surface was severely eroded when less than fully salt-saturated drilling mud was used during coring. However, the next 10 meters (33 feet) of core were deemed suitable for testing and provided enough finished test specimens to complete the proposed test matrix described in Chapter 3.0. Salt core recovered from near the midheight and bottom of the cavern was also shipped to RESPEC. This core was used to determine if the mineralogic and mechanical properties of the salt vary with depth and to provide additional salt specimens for testing as needed.

2.2.2 Bay Gas Well No. 2 Wellbore Logging

Borehole logging was performed by Schlumberger on April 10, 2001, following completion of the wellbore drilling operation of Bay Gas Well No. 2 cavern. The well logs were reviewed and used to help define the site-specific material properties that are required to perform the geomechanical analyses discussed in Chapter 6.0 of this report. The downhole measurements taken by Schlumberger include the following logs:

1. Litho Density – used to determine density of material and material interfaces

2. Compensated Neutron – used to determine porosity

3. Gamma Ray – used to detect formation lithology

4. Dual Laterlog – used to determine porosity and composition of pore fluid

5. Long Spaced Sonic – used to determine dynamic properties of the formation.

No major features were discernable from the wellbore logs in the vicinity of the cavern, indicating that the cavern is located in a homogeneous salt formation. As a result, discrete features are not likely to play a role in cavern performance or stability. Based on the aforementioned logs, a lithostatic in situ stress state is assumed that varies with depth based on the density of the overlying strata determined from the litho density log.

The density of the salt was assumed to be 2.16 grams/cubic meter (135 pcf), which results in a vertical stress gradient of 0.0226 MPa/meter (0.94 psi/foot) below the top of salt. The top of salt is variable and is about 122 meters (400 feet) below ground level in the vicinity of the Bay Gas caverns. The caprock and sediment overlying the salt were assumed to have average densities of 2.53 grams/cubic meter (158 pcf), which results in an overburden stress of 3.03 MPa (440 psi) at the top of salt. Consequently, the in situ stress distribution before excavation of the caverns was assumed to be:

$$\sigma_r = \sigma_\theta = \sigma_z = 0.0226(z-122)+3.03 \qquad (2\text{-}1)$$

where σ_r, σ_θ, and σ_z are the radial, tangential, and vertical stress components in MPa and z is the depth below ground level in meters.

2.3 DEVELOPMENT OF NUMERICAL MODELS

Based on the information gathered during the site characterization activities, finite element models of the Bay Gas caverns were constructed. The finite element models were used to make calculations (see Chapter 6.0) of the Bay Gas caverns to evaluate the stress and displacements in the salt.

2.3.1 <u>Finite Element Model of Bay Gas Well No. 1</u>

A two-dimensional axisymmetric representation of Bay Gas Well No. 1 was developed based on sonar data of the cavern taken in July 1994, immediately before the cavern was dewatered and put into service. At that time, the total cavern volume was approximately 432,000 cubic meters (2.71 MMbbls). The finite element model was generated such that the volume of the cavern model replicated the actual volume of the cavern as determined by the sonar. This was accomplished by varying the cavern radius of the model with depth to match the volume-versus-depth computations obtained from the sonar data. Figure 2-2 provides an isometric view of the Bay Gas Well No. 1 cavern based on the July 1994 sonar. No apparent direction of preferential solutioning is observed for this cavern, which makes it ideally suited for representation by an axisymmetric model.

Although not illustrated, the finite element mesh used for the simulations of Bay Gas Well No. 1 contains 17,461 nodes and 17,031 quadrilateral and triangular elements. The area immediately outside the caverns is finely subdivided with the first and second layer of elements having a thickness of only 0.61 meter (2 feet). This extremely fine subdivision was used to accurately represent the high-stress gradients that are anticipated near the cavern. The model extends vertically from the top of the salt at a depth of 121.9 meters (400 feet) to a depth of 3,048 meters (10,000 feet). The outer radius of the model extends 1,828 meters (6,000 feet) from the axis of symmetry.

A traction of 3.03 MPa (440 psi) was applied to the top of the model to represent the overburden. A lithostatic initial stress state was assumed that varies linearly with depth based on an average material density of 2.16 Mg/m^3 (135 lb/ft^3) for salt. Normal movement was constrained along the centerline, outer radius, and bottom surface of the model. The upper surface of the model was free to move in both the radial and vertical directions. After excavation of the salt was simulated, normal tractions were specified along the surface of the cavern to simulate the fluid pressure inside the cavern. The magnitudes of these tractions were equal to the hydrostatic pressure based on the densities of the fluids in the cavern plus the pressure specified at the casing shoe.

2.3.2 Finite Element Model of Bay Gas Well No. 2

A two-dimensional axisymmetric representation of Bay Gas Well No. 2 was developed based on the final cavern dimensions following SMUG (solution mining under gas) operations predicted by solution-mining software. The cavern, as modeled, has a total volume of approximately 671,000 cubic meters (4.22 MMbbls) with a maximum radius of 73 meters (240 feet) and a height of about 305 meters (1,000 feet).

Although not illustrated, the finite element mesh used for the simulations of Bay Gas Well No. 2 contains 13,605 nodes and 13,221 quadrilateral and triangular elements. Mesh refinement, boundary locations, boundary conditions, and initial in situ stress distribution are the same as those applied to the Bay Gas Well No. 1 finite element model described above.

3.0 LABORATORY TESTING

3.1 BACKGROUND

The objectives of the proposed laboratory testing effort were to complete the laboratory tests recommended by Nieland et al. [1999] on salt core from the McIntosh Dome and to provide site-specific material properties for the McIntosh salt dome. Specifically, material parameter values needed to be determined for the advanced MDCF constitutive model for salt such that analyses could be performed specific to the new cavern development at the McIntosh Dome.

Following guidance given by Nieland et al. [1999], an efficient test matrix for this project was proposed that comprised load paths and boundary conditions attainable with the computerized, servocontrolled test systems in the RESPEC rock mechanics laboratory. All tests were performed at a single temperature because of the nearly isothermal nature of the anticipated cavern analyses. In addition, the right-circular, cylindrical specimens being tested were prepared from core samples having a nominal diameter of 100 millimeters (4 inches). A typical length-to-diameter ratio for specimens used in compression tests is between 2.0 and 2.5.

Five types of tests were used for estimating the parameters. The types of tests performed were:

- Brazilian indirect tensile strength (BIT) tests

- Unconfined quasi-static compressive (UCC) strength tests

- Confined constant strain rate (CSR) tests

- Confined constant mean stress (CMS) dilation tests

- Confined creep tests.

All testing was performed on salt core recovered from Bay Gas Well No. 2 drilled into the McIntosh Dome to a depth from ground surface of 1,603 meters (5,260 feet). RESPEC conducted the tests at its facility in Rapid City, South Dakota. The test matrices were designed so that all mechanical property tests would be performed on specimens recovered from the appropriate depths to assess the variability in the salt along the height of the proposed cavern. In addition to the mechanical property tests, X-ray diffraction and wet chemistry analyses were performed on a few samples to determine the mineralogical composition of McIntosh salt.

The Brazilian indirect tensile strength tests were performed to determine apparent tensile strength. Tensile strength can be a useful measure for comparisons between rock types, for comparing variations in rock strength from one location to another, and for estimating the dilation limit at zero mean stress. The unconfined compression tests provided data for determining: (1) compressive strength, (2) Young's modulus of elasticity, and (3) Poisson's

ratio. These strength and deformation properties are used directly in modeling of underground structures, in comparisons between rock types, and in examining variations in rock properties from one location to another. The constant mean stress dilation tests provide data used exclusively for determining the stress conditions that produce dilation (volume expansion as a result of microfracturing) in the salt. The creep tests were performed to assess the time-dependent deformation properties of the salt.

3.2 TEST SPECIMEN PREPARATION

Bay Gas provided the core used for the laboratory study. The salt cores were recovered from the Bay Gas Well No. 2 in the McIntosh Dome. The cores were sealed in plastic, wrapped in bubble wrap, and placed in plastic core tubes for shipping to RESPEC.

All specimen preparation activities were performed under RESPEC Test Procedure 02 (TP-02), RSI Standard Procedure for *Rock Specimen Preparation, Rev 4.* All of the specimens were given a unique identification number for tracking within the RESPEC laboratory. A typical specimen identification number is:

MD/BG2/4145.8

where:

MD = McIntosh Dome

BG2 = Bay Gas Well No. 2

4145.8 = core recovery depth (feet).

Salt specimens for testing were prepared by initially sawing a specimen from the 100-millimeter- (4-inch-) diameter field core and then finishing the ends with a milling machine. The diameter of the salt specimens was not reduced from that obtained in the field. Final specimen dimensions for the triaxial compression tests were approximately 100 millimeters (4 inches) in diameter and 200 millimeters (8 inches) in length. Final specimen dimensions for the indirect tensile (Brazilian) tests were diameters of 100 millimeters (4 inches) and lengths of 50 millimeters (2 inches).

3.3 MECHANICAL PROPERTIES TEST PROCEDURES

RESPEC personnel performed all the mechanical properties testing of the McIntosh salt specimens using the laboratory facility located in Rapid City, South Dakota. The strength tests and the dilation tests were performed on a servohydraulic test system, shown in Figure 3-1 where the prominent test system components are labeled. One notable feature of the test system shown in Figure 3-1 is the capability to mount the strain-measuring instrumentation directly on the specimen. The creep tests were performed on computerized static loading test

LOAD FRAME   PRESSURE VESSEL
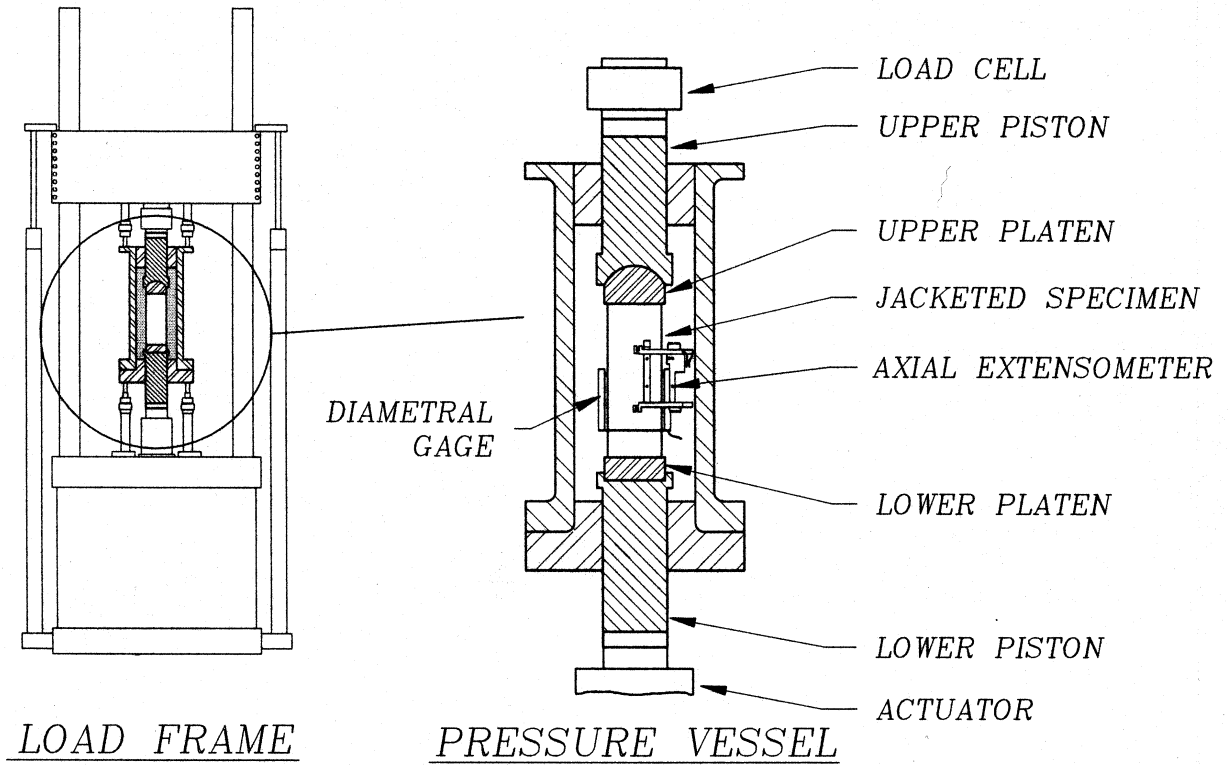
Figure 3-1. Schematic of UTS2 Load Frame and Pressure Vessel.

systems designed for maintaining stable loads over long periods of time. A typical static load frame is shown in Figure 3-2. A brief description of each type of mechanical properties test is given in separate sections that follow.

3.3.1 <u>Brazilian Indirect Tensile Strength Tests</u>

Apparent tensile strength of the salt was determined by means of the Brazilian indirect tensile (BIT) test. This method is termed an indirect method because a compressive, diametral line load is applied over the length of a cylindrical specimen having a L:D = 0.5:1. The compressive load induces a tensile stress at the center of the specimen perpendicular to the diametral line load. As the compressive line load increases, so does the tensile stress. The tensile strength is computed according to:

$$T_0 = \frac{2P}{\pi DL} \tag{3-1}$$

where:

T_0 = apparent tensile strength, MPa (psi)

P = line load at failure, MN (lbs.)

D = specimen diameter, m (in.)

L = specimen length, m (in.).

3.3.2 <u>Unconfined Compressive Strength Tests</u>

Unconfined compressive strength tests were performed to determine: (1) unconfined compressive (UCC) strength and (2) elastic moduli. The unconfined compressive strength tests were conducted at a temperature of 20°C (68°F) in axial strain control at an axial strain rate of 1×10^{-4} s^{-1}. Unload/reload cycles were conducted on some of the specimens. The data collected during the unload/reload cycles were used to estimate the elastic constants; i.e., Young's modulus, E, and Poisson's ratio, ν.

A typical stress-strain curve for an unconfined compression test would show that the stress-strain response during loading is quite nonlinear, particularly at higher stress levels. Initially, the stress increases rapidly with strain; however, the stress eventually reaches a peak and then decreases as the specimen continues to strain. This peak stress is defined as the unconfined compressive strength.

The load path may include an unload/reload cycle characterized by a decrease in stress followed by a comparable increase in stress at an axial strain level of approximately 0.25 to 0.50 percent. The data acquired during the cycle are used to calculate two elastic constants, Young's modulus, E, and Poisson's ratio, ν, using two mathematical equations as follows:
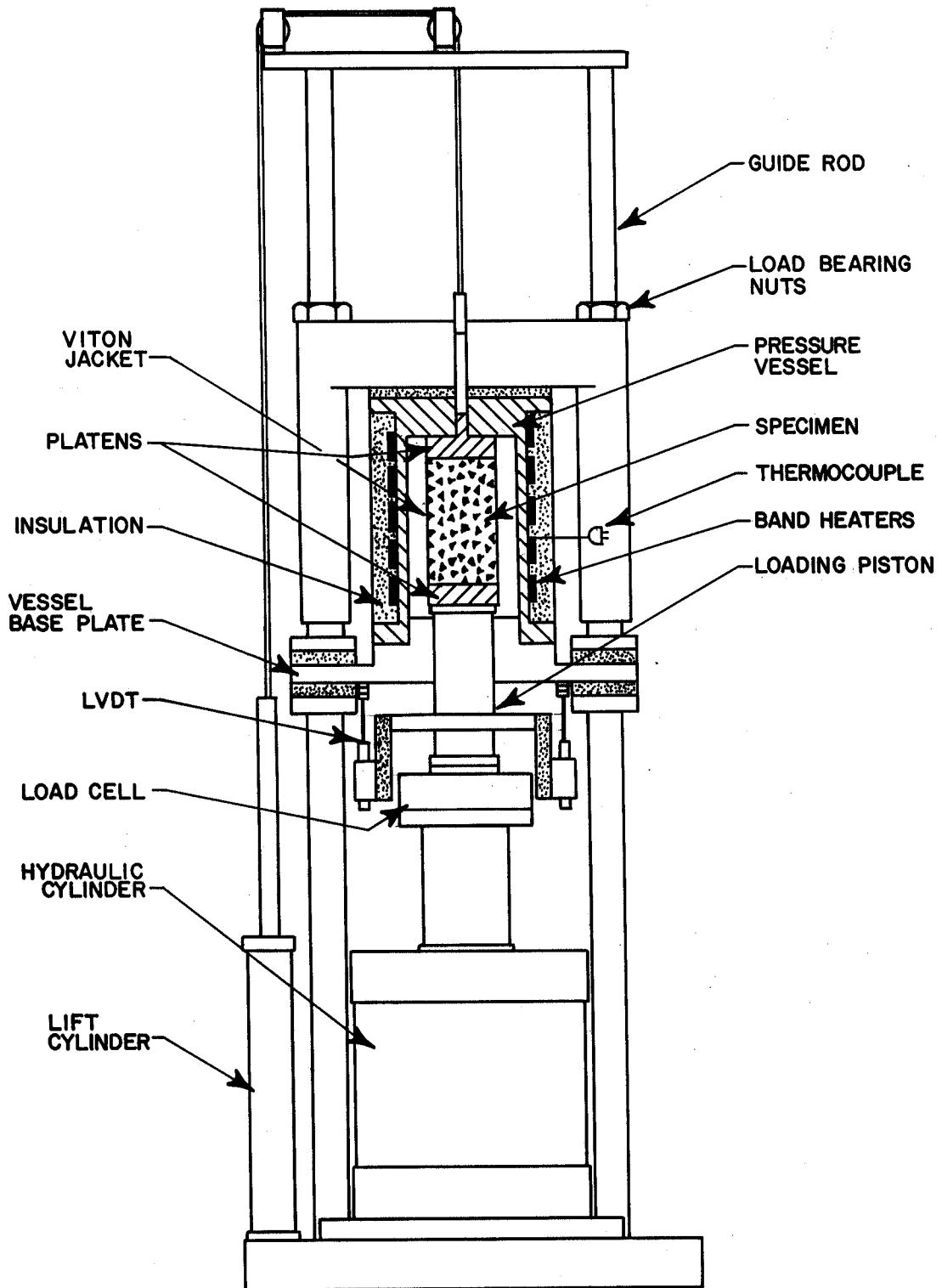
Figure 3-2. Schematic of Static Creep Test System.

$$E = \frac{\Delta\sigma}{\Delta\varepsilon_1} \tag{3-2}$$

$$\nu = -\frac{E}{\dfrac{\Delta\sigma}{\Delta\varepsilon_3}} \tag{3-3}$$

where $\Delta\sigma$ is the change in stress and $\Delta\varepsilon_1$ and $\Delta\varepsilon_3$ are the changes in axial and radial strain, respectively. Equation 3-2 and the denominator of Equation 3-3 represent the slopes of the stress versus axial strain and stress versus radial strain curves, respectively, generated during the unload/reload portion of the load path.

3.3.3 Confined Constant Strain Rate

In the confined constant strain rate (CSR) tests, the axial stress, σ_1, is increased and the confining pressure, σ_3, is held constant. The primary objective of these tests was to determine the elastic and strength characteristics of the salt.

In the CSR test, the test specimen is first loaded hydrostatically by applying radial stress (or confining pressure), σ_3, and axial stress, σ_1, in equal increments until the mean stress specified for the test has been reached. Then a stress difference (difference between the axial stress and the radial stress) is applied by increasing the axial stress while holding the radial stress constant. The application of the stress difference is controlled to maintain a constant axial strain rate. Tests are terminated when the specimen fails.

The stress difference versus strain curves for a typical CSR test are similar to those described for the UCC tests because the UCC test is simply a special case of the CSR test; i.e., a UCC test is a CSR test at a confining pressure of zero. Unload/reload cycles are used in the CSR tests to estimate elastic constants in the same fashion previously described for UCC tests.

3.3.4 Confined Constant Mean Stress Dilation Tests

In the confined constant mean stress (CMS) tests, the axial stress, σ_1, is increased and the confining pressure, σ_3, is simultaneously decreased at rates which produce no change in the mean stress $\left(\sigma_m = (\sigma_1 + 2\sigma_3)/3\right)$ imposed on the specimen. The primary objective of these tests was to determine the dilatational characteristics (volume expansion caused by microfracturing) of the salt.

In the CMS test described by Mellegard and Pfeifle [1998], the test specimen is first loaded hydrostatically by applying radial stress (or confining pressure), σ_3, and axial stress, σ_1, in equal increments until the mean stress specified for the test has been reached. Then a stress difference (difference between the axial stress and the radial stress) is applied by increasing the axial stress and simultaneously decreasing the radial stress. During this application of stress

difference, the axial stress rate is twice the radial stress rate (with opposite algebraic sign) to maintain a state of constant mean stress. Tests are terminated either when the specimen fails or when the confining pressure has been completely removed (i.e., tensile radial stresses cannot be induced in the test specimen with this test configuration).

Because the mean stress is not changing during the CMS tests, the volumetric strain remains virtually unchanged or indicates a small level of compaction at low to moderate stress differences. This behavior is consistent with a material that is not dilating. However, at some elevated stress difference, the volumetric strain rate accelerates and the volumetric strain becomes negative,[1] which implies that the specimen is being damaged through microfracturing (creation of voids). The specimen can sustain even larger stress differences beyond the point where dilation begins; however, it also experiences higher levels of damage (dilatant volumetric strain) at these stress conditions.

The data obtained from the CMS tests can be used to develop a relationship between mean stress and the stress difference that produces salt dilation. A common method used to develop such a relationship is to: (1) redefine the mean stress and stress difference levels which induce dilation in terms of stress invariants, and then (2) develop a mathematical model which relates the stress invariants in a manner consistent with the experimental data. Two stress invariants typically used to develop these models are the first invariant of the Cauchy stress tensor, I_1, and the second invariant of the deviatoric stress tensor, J_2. When CMS triaxial compression data are available, the two stress invariants can be defined as follows:

$$I_1 = 3\sigma_m = \sigma_1 + 2\sigma_3 \tag{3-4}$$

$$\sqrt{J_2} = \frac{\Delta\sigma}{\sqrt{3}} = \frac{\sigma_1 - \sigma_3}{\sqrt{3}} \tag{3-5}$$

The data can be plotted in the $\sqrt{J_2}$-versus-I_1 stress space where the data generally indicate a trend where $\sqrt{J_2}$ increases as I_1 increases. The trend is often modeled as a linear relationship, although nonlinear functions have also been fit to such data. A linear line fitted to the data will divide the stress space into two distinct regions, as shown in Figure 3-3. The region above and to the left of the line represents stress states where dilation will occur, while the region below and to the right of the line represents stress states where dilation will not occur. This dilation limit can be used directly in geomechanical analysis of underground caverns to determine regions in the salt that may be susceptible to dilation.

---

[1] Compressive stresses and strains are signed positive so negative volumetric strains imply a volume expansion.
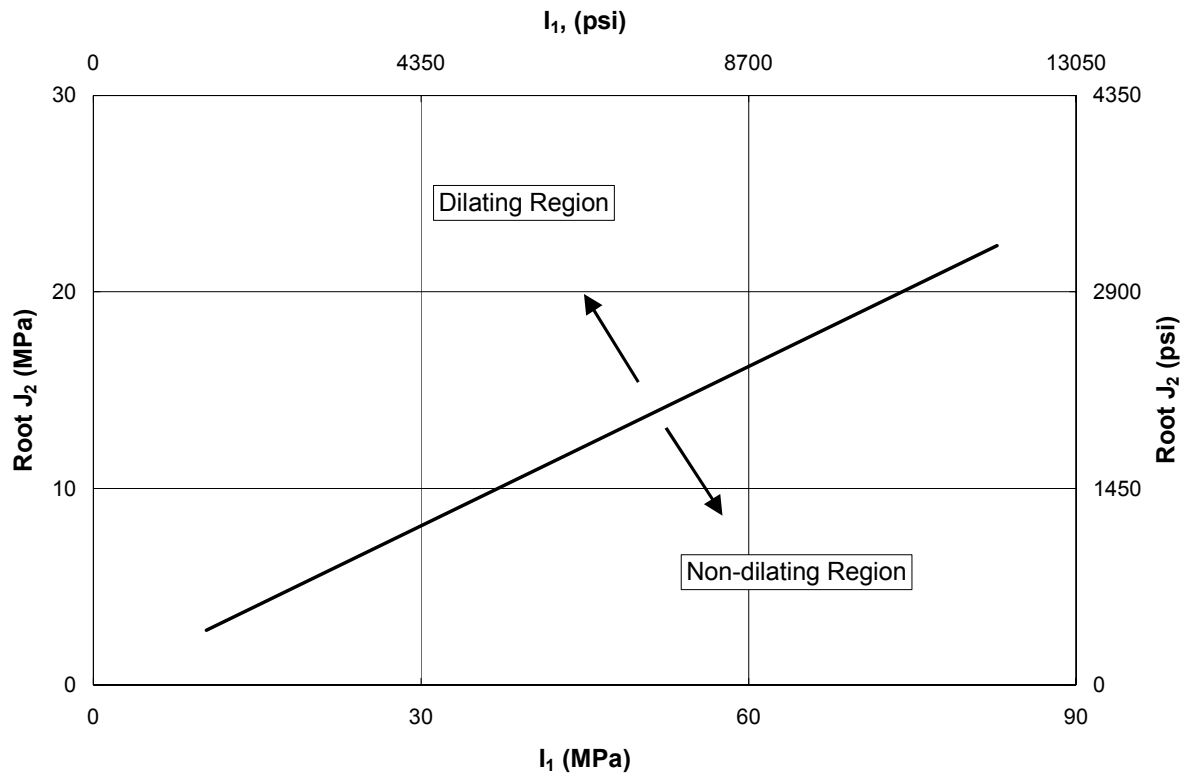
Figure 3-3. $\sqrt{J_2}$ -Versus- I_1 Dilation Criterion.

3.3.5 <u>Confined Creep Tests</u>

Confined creep tests are performed to evaluate the time-dependent behavior of materials (e.g., salt). A creep test is initiated by applying confining pressure to all exterior surfaces of a specimen that has been jacketed in a flexible membrane to protect it from the pressurizing medium and then heating the jacketed specimen to the prescribed test temperature. Once the confining pressure and temperature are stable, axial stress is quickly applied to the ends of the specimen until the target stress difference is reached, at which time, the confining pressure and stress difference are maintained at their specified levels for the duration of the test or until a subsequent stage is initiated by changing the level of applied axial stress.

During the test, axial force, confining pressure, axial displacement, radial displacement, and temperature are recorded. Axial stress is calculated from the axial force and the current cross-sectional area of the specimen. Axial and radial true (logarithmic) strains are calculated from the axial and radial displacements and the specimen dimensions. A typical strain-versus-time response from a creep test shows that at early times, the strain rates are high immediately after the increase in axial stress but then decrease with time as they approach nearly constant values.

3.4 TEST SYSTEM CALIBRATION PROCEDURES

The testing requires use of sophisticated, computer-controlled test systems equipped with electronic transducers used to measure force, pressure, displacement, and temperature. The transducers are calibrated at regular intervals using certified in-house standards that are traceable to the National Institute of Standards and Technology (NIST).

Verification procedures indicate that the transducer readings are accurate within 1 percent for load and pressure measurements and 2 percent for deformation and volume measurements. Also, temperature measurements are accurate within 1°C (2°F). The testing systems, including the electronics, are housed in an environmentally controlled facility in which the temperature is maintained at 20 ± 1°C (68 ± 2°F).

3.5 TEST RESULTS

The summary results of both the mechanical tests and the mineralogical studies are presented in the sections that follow. Individual test results are given in Appendix B.

3.5.1 <u>Brazilian Indirect Tensile Tests</u>

Six indirect tensile tests were performed. Two tests were performed on salt recovered from each of three nominal depths: 1,263 meters (4,145 feet), 1,416 meters (4,646 feet), and

1,595 meters (5,232 feet). All tests were performed at a temperature of 20°C (68°F). The test results are summarized in Table 3-1. The tensile strengths ranged from a low of 1.11 MPa (161 psi) to a high of 1.54 MPa (223 psi) and averaged 1.38 MPa (200 psi).

Table 3-1. Summary of Indirect Tensile Tests

Specimen I.D.	Depth		Strength	
	(m)	(ft)	(MPa)	(psi)
MD/BG2/4145.2	1,263	4,145.2	1.527	221.4
MD/BG2/4145.4	1,264	4,145.4	1.392	201.9
MD/BG2/4646.5	1,416	4,646.5	1.108	160.7
MD/BG2/4646.7	1,416	4,646.7	1.539	223.2
MD/BG2/5232.2	1,595	5,232.2	1.303	189.0
MD/BG2/5232.4	1,595	5,232.4	1.410	204.5

The tensile strengths given in Table 3-1 are plotted as a function of depth in Figure 3-4. The figure indicates that the tensile strength does not vary greatly among the three depths investigated, although the salt near the roof of the proposed cavern has the highest average strength. The tensile strengths in Table 3-1 are also compared with tensile strengths observed for several other salt types [Pfeifle et al., 1995] in Figure 3-5. The figure shows the average strength of each salt type along with error bars that indicate the range of values that were reported. The figure shows the tensile strength is similar to the tensile strengths determined for other salts.

3.5.2 Unconfined Quasi-Static Compressive Tests

Six unconfined quasi-static compressive tests were performed. Two tests were performed on salt recovered from each of three nominal depths of 1,265 meters (4,150 feet), 1,414 meters (4,637 feet), and 1,595 meters (5,233 feet). The compressive strength tests were conducted at a temperature of 20°C (68°F) in axial strain control at an axial strain rate of 1×10^{-4} s^{-1}.

Table 3-2 provides a summary of the unconfined compressive strengths determined from the six tests. The unconfined compressive strengths ranged from a low of 15.3 MPa (2,219 psi) to a high of 18.3 MPa (2,659 psi) and averaged 17.1 MPa (2,477 psi).

The unconfined compressive strengths given in Table 3-2 are plotted as a function of depth in Figure 3-6. The figure indicates that the unconfined compressive strength is lowest at the depth corresponding to the roof of the proposed cavern and increases with depth. The strengths
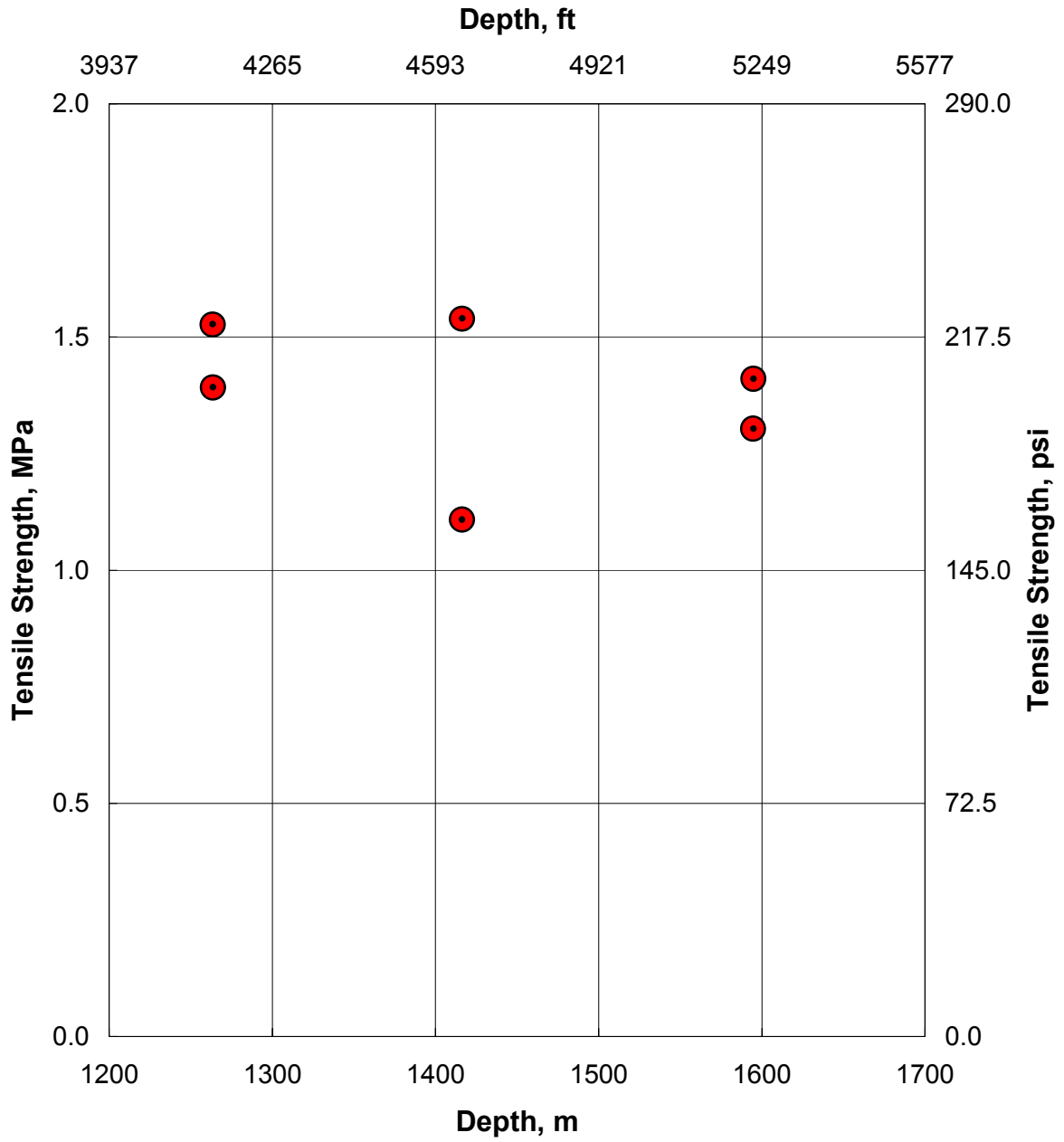
Figure 3-**4.** Indirect Tensile Strength as a Function of Depth.
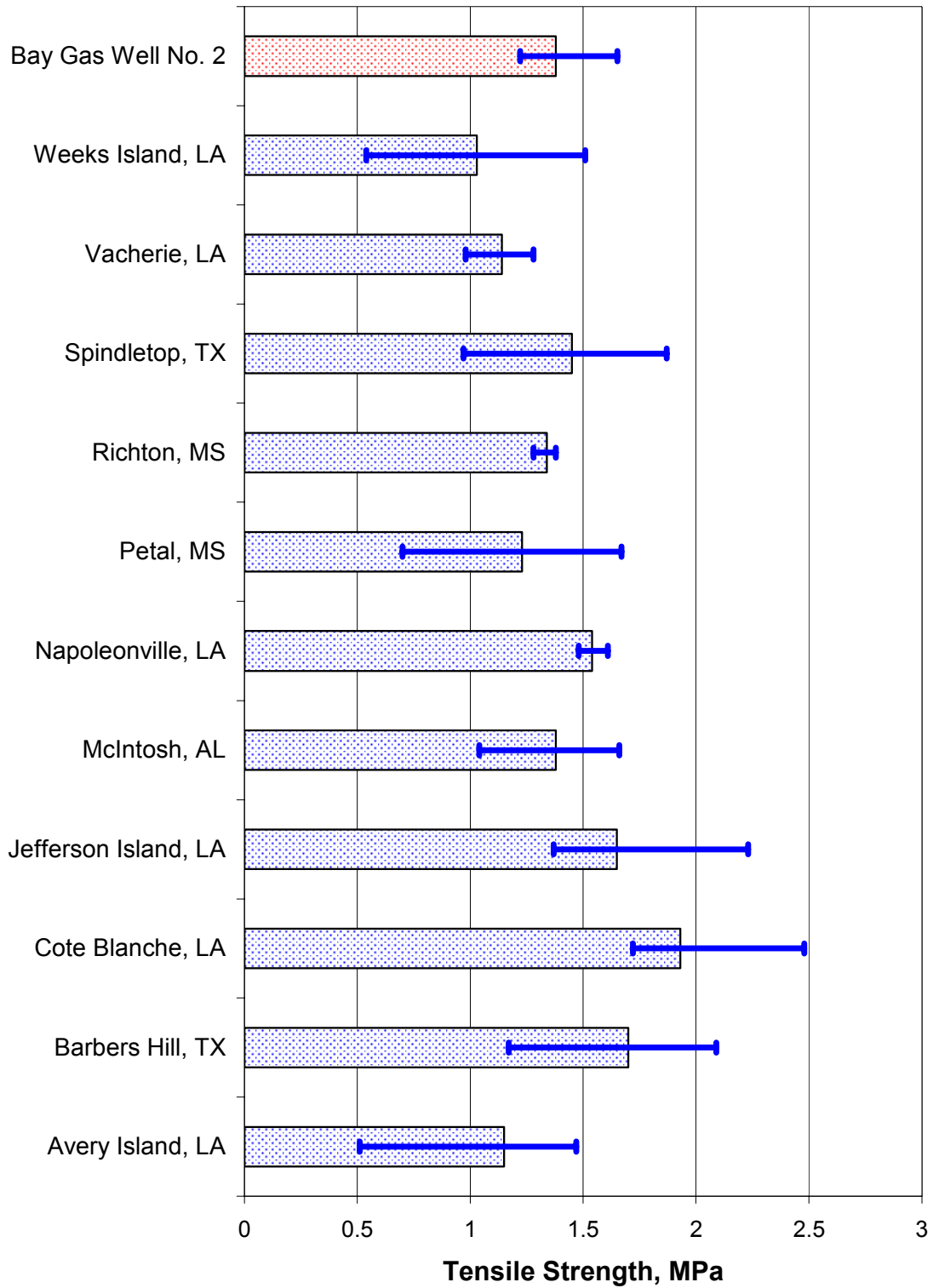
Figure 3-5. Comparison of Tensile Strength of Various Salts.

in Table 3-2 are also compared with unconfined compressive strengths observed for several other salt types [Pfeifle et al., 1995] in Figure 3-7. The figure shows the unconfined compressive strength is similar to the strengths determined for other salts.

Table 3-2. Summary of Unconfined Compressive Strength Tests

Specimen I.D.	Depth		Strength	
	(m)	(ft)	(MPa)	(psi)
MD/BG2/4149.8	1,265	4,149.8	16.1	2,333
MD/BG2/4153.0	1,266	4,153.0	15.3	2,219
MD/BG2/4637.1	1,413	4,637.1	17.8	2,575
MD/BG2/4637.7	1,414	4,637.7	17.3	2,503
MD/BG2/5232.9	1,595	5,232.9	17.7	2,572
MD/BG2/5233.6	1,595	5,233.6	18.3	2,659

All of the specimens in Table 3-2 incorporated unload/reload cycles in their load paths to generate data for estimating values of Young's modulus and Poisson's ratio. The elastic constants obtained from the tests are given in Table 3-3. The average value of Young's modulus was 19.6 GPa (2,835,504 psi) with no apparent trend between Young's modulus and depth. The values for Poisson's ratio given in Table 3-3 are generally larger than the value of about 0.35 that would be expected for salt. In fact, three of the specimens displayed values greater than 0.5, which is a value expected for an incompressible material. The explanation for this variance lies in the large crystal sizes seen in the salt. A general rule in testing cylindrical specimens of salt is that the specimen diameter should contain at least ten individual crystals. In many cases, these salt specimens had less than ten crystals through a diameter and the action of a few large crystals yielded unrepresentative radial deformations.

3.5.3 Confined Constant Strain Rate Tests

Six confined constant strain rate tests were performed. Two tests were performed on salt recovered from a nominal depth of 1,260 meters (4,134 feet) at each of three constant confining pressures: 1.0 MPa (150 psi), 5.2 MPa (750 psi), and 10.3 MPa (1,500 psi). These confined compressive strength tests were conducted at a temperature of 20°C (68°F) in axial strain control at an axial strain rate of $1 \times 10^{-4}\,\text{s}^{-1}$.

27
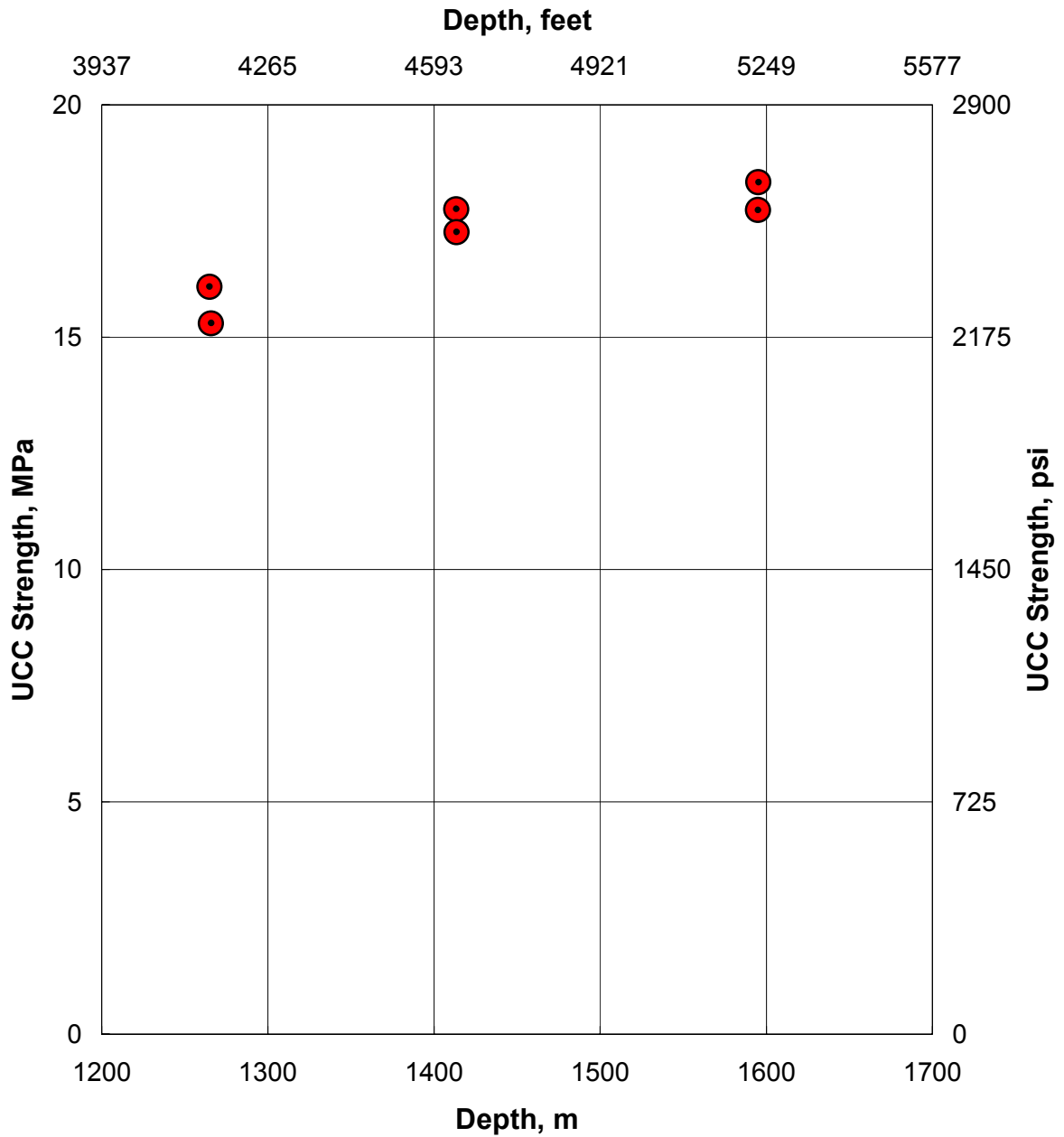
Figure 3-6. Unconfined Compressive Strength as a Function of Depth.

28
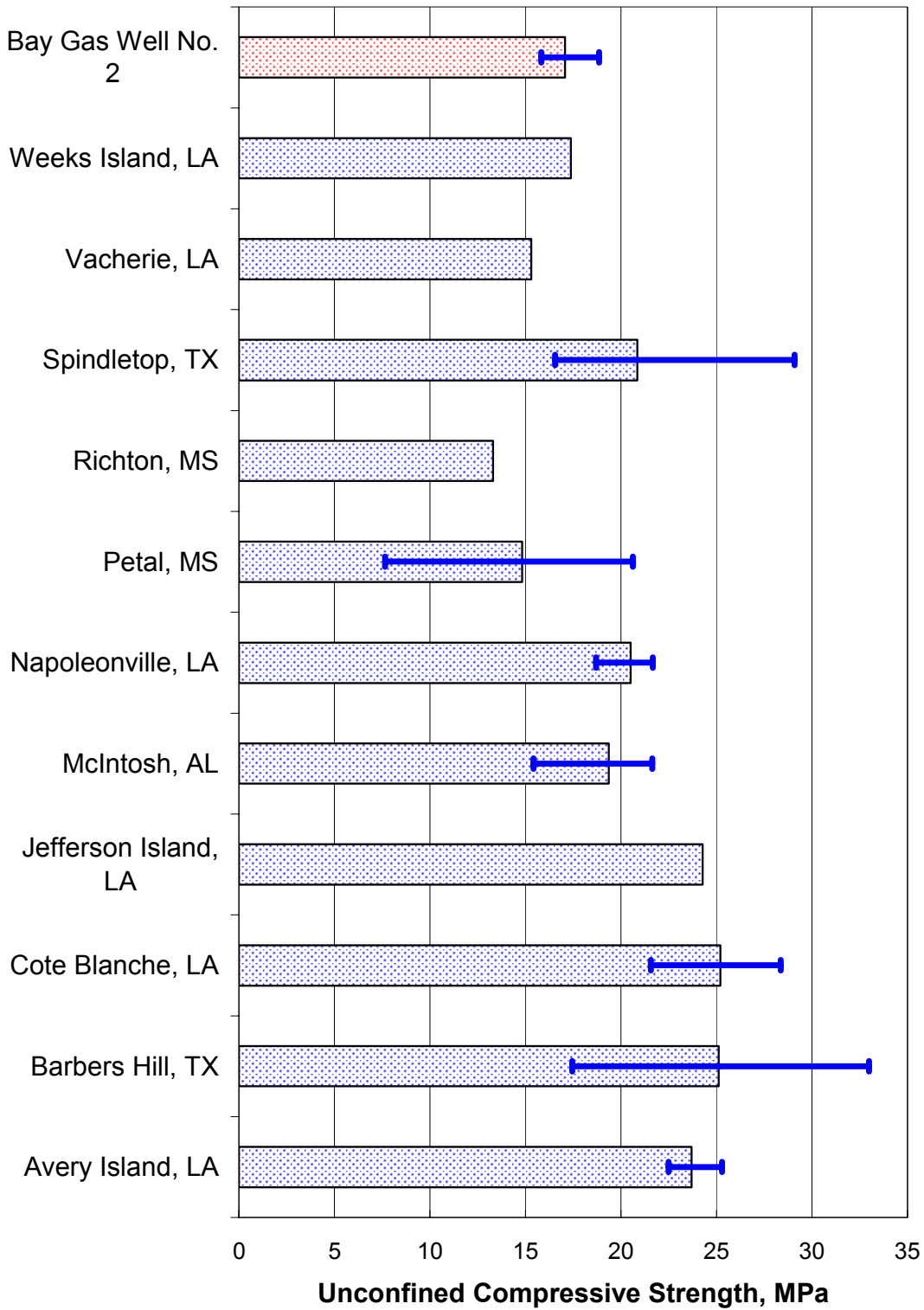
Figure 3-7. Comparison of Unconfined Compressive Strength of Various Salts.

29

Table 3-3. Unconfined Quasi-Static Compressive Elastic Constants

Specimen I.D.	Depth		Young's Modulus, E		Poisson's Ratio, v
	(m)	(ft)	(GPa)	(psi)	
MD/BG2/4149.8	1,265	4,149.8	22.0	3,188,550	>0.5
MD/BG2/4153.0	1,266	4,153.0	19.6	2,844,939	0.387
MD/BG2/4637.1	1,413	4,637.1	14.6	2,120,000	0.387
MD/BG2/4637.7	1,414	4,637.7	19.3	2,793,668	>0.5
MD/BG2/5232.9	1,595	5,232.9	20.8	3,019,017	0.422
MD/BG2/5233.6	1,595	5,233.6	21.0	3,046,851	>0.5
Averages			**19.6**	**2,835,504**	**0.398**

Table 3-4 provides a summary of the confined compressive strengths determined from the six tests. As expected, the confined compressive strengths increased with increasing confining pressure, ranging from an average strength of about 28 MPa (4,060 psi) at the lowest confining pressure of 1.0 MPa (150 psi) to an average strength of about 43 MPa (6,240 psi) at the highest confining pressure of 10.3 MPa (1,500 psi).

Table 3-4. Summary of Confined Constant Strain Rate Strength Tests

Specimen I.D.	Depth		Confining Pressure		Strength	
	(m)	(ft)	(MPa)	(psi)	(MPa)	(psi)
MD/BG2/4128.4	1,258	4,128.4	5.2	750	43.6	6,323
MD/BG2/4130.7	1,259	4,130.7	10.3	1,500	46.3	6,715
MD/BG2/4134.3	1,260	4,134.3	1.0	150	26.2	3,804
MD/BG2/4134.6	1,260	4,134.6	5.2	750	35.2	5,105
MD/BG2/4136.9	1,261	4,136.9	1.0	150	29.3	4,252
MD/BG2/4158.0	1,267	4,158.0	10.3	1,500	41.0	5,940

All of the specimens in Table 3-5 incorporated unload/reload cycles in their load paths to generate data for estimating values of Young's modulus and Poisson's ratio. The elastic constants obtained from the tests are given in Table 3-5. The average value of Young's modulus was 27.1 GPa (3,935,188 psi) and the average value for Poisson's ratio was 0.321. The elastic constants values determined from the CSR tests are significantly different than the values determined from the UCC tests. Moreover, the values determined using the CSR tests are

more representative of typical values expected for salt. The large crystal size effect that was cited as the cause of spurious results in the UCC tests is apparently reduced when elevated confining pressures are applied.

Table 3-5. Constant Strain Rate Elastic Constants

Specimen I.D.	Depth		Young's Modulus, E		Poisson's Ratio, v
	(m)	(ft)	(GPa)	(psi)	
MD/BG2/4128.4	1,258	4,128.4	28.4	4,112,756	0.288
MD/BG2/4130.7	1,259	4,130.7	29.5	4,272,635	0.309
MD/BG2/4134.3	1,260	4,134.3	23.6	3,425,700	0.369
MD/BG2/4134.6	1,260	4,134.6	28.2	4,092,686	0.304
MD/BG2/4136.9	1,261	4,136.9	23.7	3,434,460	0.344
MD/BG2/4158.0	1,267	4,158.0	29.5	4,272,953	0.309
Averages			**27.1**	**3,935,198**	**0.321**

3.5.4 <u>Confined Constant Mean Stress Tests</u>

Six confined constant mean stress dilation tests were performed on specimens obtained from a nominal depth of 1,265 meters (4,150 feet). Tests were terminated when the confining pressure had been completely removed (i.e., tensile radial stresses cannot be induced in the test specimen with this test configuration).

The data from the CMS tests were analyzed to identify the combinations of mean stress and stress difference that would initiate salt dilation. These data pairs were then cast in terms of the stress invariants J_2 and I_1, and the results are summarized in Tables 3-6 and 3-7 (Table 3-6 presents results in SI units and Table 3-7 uses English units).

The dilation trend exhibited by the CMS tests was compared to the dilation characteristics of the salt with a typical linear criterion developed by Van Sambeek et al. [1993] for Avery Island Dome salt and southeastern New Mexico bedded salt as:

$$\frac{\sqrt{J_2}}{I_1} = 0.27 \qquad\qquad (3\text{-}6)$$

This comparison is shown in Figure 3-8 where the dilation data from the CMS tests have been overlain on the typical linear criterion. The comparison is not good and indicates that a nonlinear function might better represent the McIntosh salt data.

31

Table 3-6. Summary of CMS Test Results (SI Units)

Specimen I.D.	Depth (m)	Mean Stress (MPa)	Dilation Stress (MPa)	I_1 (MPa)	$\sqrt{J_2}$ (MPa)
MD/BG2/4127.7	1,258	6.9	9.7	20.7	5.58
MD/BG2/4191.0	1,277	13.8	17.9	41.4	10.3
MD/BG2/4139.8	1,262	20.7	20.7	62.1	12.0
MD/BG2/4136.0	1,261	6.9	15.2	20.7	8.78
MD/BG2/4191.7	1,278	13.8	20.7	41.4	12.0
MD/BG2/4135.3	1,260	20.7	23.4	62.1	13.5

Table 3-7. Summary of CMS Test Results (English Units)

Specimen I.D.	Depth (m)	Mean Stress (MPa)	Dilation Stress (MPa)	I_1 (MPa)	$\sqrt{J_2}$ (MPa)
MD/BG2/4127.7	4,127.7	1,000	1,400	3,000	808
MD/BG2/4191.0	4,191.0	2,000	2,600	6,000	1,501
MD/BG2/4139.8	4,139.8	3,000	3,000	9,000	1,732
MD/BG2/4136.0	4,136.0	1,000	2,200	3,000	1,270
MD/BG2/4191.7	4,191.7	2,000	3,000	6,000	1,732
MD/BG2/4135.3	4,135.3	3,000	3,400	9,000	1,963

Two specialty CMS tests were performed to investigate the healing characteristics of McIntosh salt. Specimens MD/BG2/4644.3 and MD/BG2/4639.7 were loaded in the usual CMS fashion at a mean stress of 21 MPa (3,000 psi) to produce dilatant volumetric strains of approximately 1 percent and 2 percent, respectively. At that point, the loading was reversed and the stress difference was reduced back to a hydrostatic stress state of 21 MPa (3,000 psi) where the volumetric strain was monitored during what was termed a healing phase. Based on healing investigations completed using creep tests, a reduction of volumetric strain was expected during the healing stage in the CMS tests. However, the CMS healing stages showed no change in volumetric strain at all, indicating that the void-producing damage induced at a high rate of loading (the CMS test) has a different nature than the damage induced during constant stress loading (a creep test). Thus while an increase in dilatant volumetric strain is the manifestation of an increase in damage, the mechanism(s) that are operating to produce
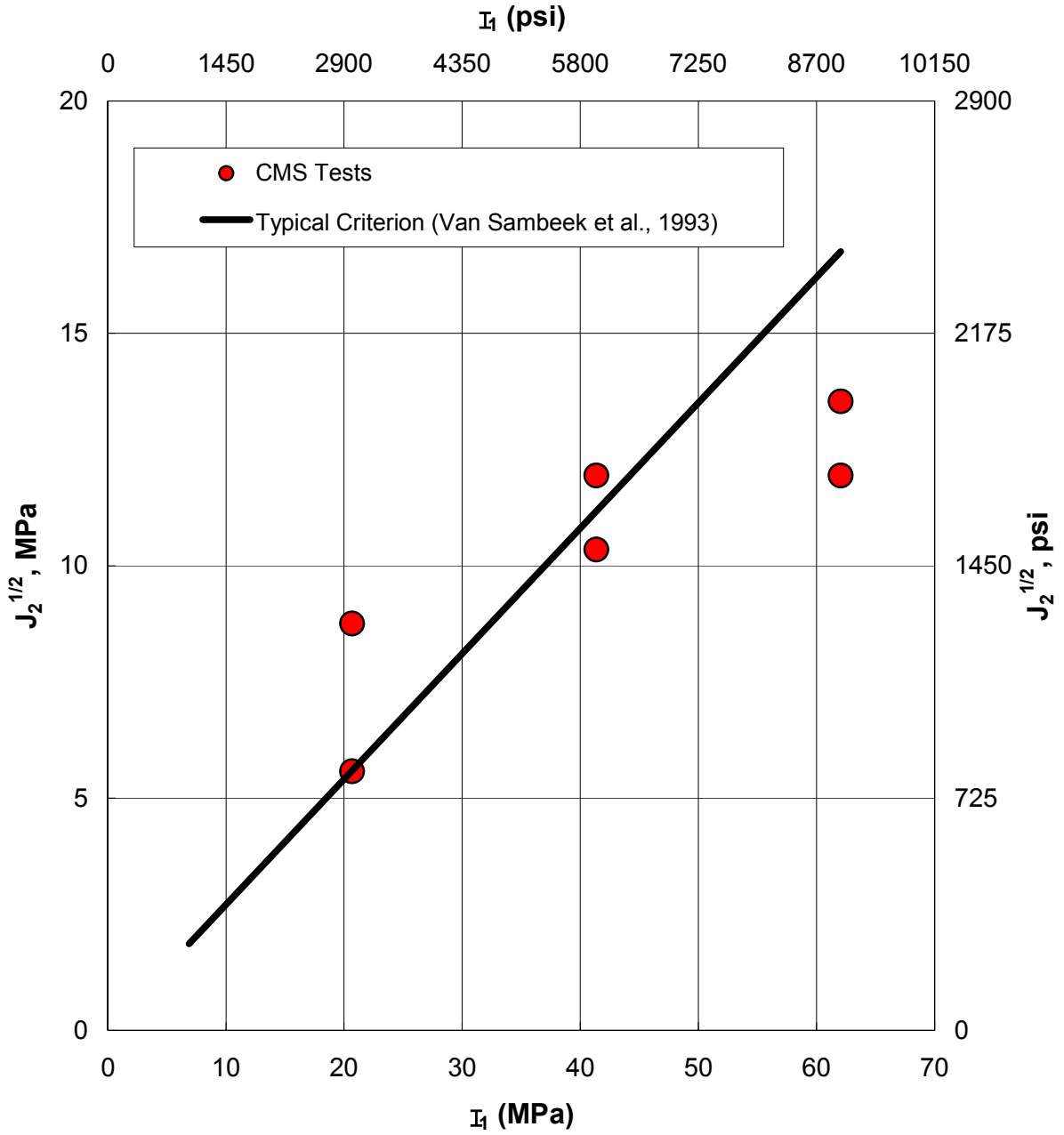
Figure 3-8. Dilation Criterion Comparison.

that damage may be different and so the reversal of damage (healing) may proceed differently. There is insufficient data available to warrant a change in the current approach to damage/healing analysis, but additional study of this phenomenon should be completed.

3.5.5 Creep Tests

Fourteen specimens were used to perform confined creep tests at a temperature of 52°C (125°F), which was considered to be a reasonable approximation of the anticipated average temperature at the proposed midheight of the Bay Gas caverns. Some of the specimens were subjected to multiple stages where one or both of the applied principal stresses were changed after some period of time. The suite of tests that were completed is presented in Table 3-8. These tests comprise a comprehensive test matrix that consumed 647 machine-days of creep time. Some of the stages in the column adjacent to the specimen identification column are shaded. The shading indicates that dilation was observed during that stage. The presence (or absence) of dilation plays a role in how the data are analyzed in the next chapter.

The test records for each of the specimens listed in Table 3-8 are contained in Appendix B where plots of strain-versus-time are presented for each specimen. The loading conditions are also contained in the plots. The strain measure used in the plots is total strain. Total strain includes not only the creep strain accumulated while stress is held constant, but also the elastic and inelastic strains induced during changes in stress. A summary of the strain responses observed during the various test stages is given in Table 3-9. The strain values given for each stage are the incremental strains; that is, they represent only the strains observed during that particular stage. The overall total strain experienced by any particular specimen can be calculated by summing the incremental strains recorded for each of its stages. In some cases, a stage continued until a reasonable estimate of the axial steady-state strain rate could be made. Steady-state strain rates estimates were made only for those specimens that were undamaged during a particular stage because a specimen undergoing damage (or healing) may not give a representative value of the steady-state strain rate of intact salt.

A special estimate of axial strain rates was made in the two stages applied to specimen MD/BG2/4647.5 to compare the difference between the two stages. Both stages were subjected to the same stress difference, but the first stage was in triaxial extension while the second stage was in triaxial compression. This test was not part of the original test matrix proposed by Nieland et al. [1999] but was performed as part of the model refinement task to provide data to illustrate the behavior of salt at stress states other than triaxial compression.

Additional discussion of the test results presented in Table 3-9 is provided in Chapter 5.0, but a cursory examination of some of the data indicates how strongly the steady-state strain rate depends on changes in the applied axial stress difference. A simple model relating the steady-state creep strain rate, $\dot{\varepsilon}_3$, to the imposed stress difference is a power law that is expressed by:

Table 3-8. Creep Test Matrix

Specimen I.D.	Test[a] Stage	Duration (days)	Axial Stress (MPa)	Axial Stress (psi)	Confining Pressure (MPa)	Confining Pressure (psi)
MD/BG2/4133.4	1	0.3	21.37	3,100	0.69	100
	2	0.7	0.69	100	0.69	100
	3	25	31.03	4,500	20.68	3,000
	4	2	20.68	3,000	20.68	3,000
	5	13	41.37	6,000	41.37	6,000
MD/BG2/4143.2	1	13	24.13	3,500	3.45	500
MD/BG2/4145.8	1	12	48.26	7,000	27.58	4,000
	2	21	41.37	6,000	27.58	4,000
	3	23	37.92	5,500	27.58	4,000
MD/BG2/4146.5	1	90	41.37	6,000	27.58	4,000
	2	70	37.92	5,500	27.58	4,000
MD/BG2/4147.4	1	41	20.46	2,967	3.22	467
MD/BG2/4148.2	1	12	15.86	2,300	2.07	300
	2	26	19.31	2,800	2.07	300
MD/BG2/4150.7	1	25	44.82	6,500	27.58	4,000
	2	59	41.37	6,000	27.58	4,000
	3	12	44.82	6,500	27.58	4,000
MD/BG2/4151.4	1	38	14.48	2,100	0.69	100
	2	25	27.58	4,000	13.79	2,000
MD/BG2/4153.5	1	56	37.92	5,500	27.58	4,000
MD/BG2/4155.0	1	8	12.41	1,800	2.07	300
MD/BG2/4156.3	1	2.3	22.75	3,300	2.07	300
	2	43	20.68	3,000	20.68	3,000
MD/BG2/4641.5	1	1	21.37	3,100	0.69	100
MD/BG2/4642.2	1	2.5	17.93	2,600	0.69	100
MD/BG2/4647.5	1	12.1	5.74	833	22.98	3,333
	2	14	40.22	5,833	22.98	3,333

(a) Shaded stages are those where dilation was observed.

Table 3-9. Summary of Creep Test Results

Specimen I.D.	Test[a] Stage	Duration (days)	Axial Strain	Radial Strain	Volumetric Strain	Axial Strain Rate (s^{-1})
MD/BG2/4133.4	1	0.3	0.04563	−0.03040	−0.01517	—
	2	0.7	−0.00038	0.00015	−0.00008	—
	3	25	0.00441	0.00099	0.00639	—
	4	2	−0.00055	0.00013	−0.00030	—
	5	13	0.00007	0.00101	0.00209	—
MD/BG2/4143.2	1	13	0.12110	−0.06283	−0.00456	—
MD/BG2/4145.8	1	12	0.10330	−0.05150	0.00030	5.83×10^{-8}
	2	21	0.00838	−0.00380	0.00077	—
	3	23	0.00328	−0.00156	0.00017	—
MD/BG2/4146.5	1	90	0.05007	−0.02275	0.00456	4.70×10^{-9}
	2	70	0.00284	0.00012	0.00308	—
MD/BG2/4147.4	1	41	0.11156	−0.05666	−0.00176	—
MD/BG2/4148.2	1	12	0.02101	−0.00959	0.00183	—
	2	26	0.06119	−0.03166	−0.00213	—
MD/BG2/4150.7	1	25	0.06108	−0.02957	0.00195	1.49×10^{-8}
	2	59	0.01391	−0.00542	0.00307	4.74×10^{-9}
	3	12	0.02814	−0.01401	0.00013	—
MD/BG2/4151.4	1	38	0.05076	−0.02759	−0.00442	—
	2	25	0.01194	−0.00391	0.00412	—
MD/BG2/4153.5	1	56	0.00527	−0.00162	0.00202	6.05×10^{-10}
MD/BG2/4155.0	1	8	0.00646	−0.00195	0.00257	1.77×10^{-9}
MD/BG2/4156.3	1	2.3	0.09131	−0.05153	−0.01175	—
	2	43	−0.00057	0.00491	0.00924	—
MD/BG2/4641.5	1	1	0.09039	−0.06980	−0.04920	—
MD/BG2/4642.2	1	2.5	0.10857	−0.08962	−0.07066	—
MD/BG2/4647.5	1	12.1	−0.03059	0.01547	0.00036	-1.19×10^{-8}
	2	14	0.02173	−0.00958	0.00258	6.21×10^{-9}

(a) Shaded stages are those where dilation was observed.

$$\dot{\varepsilon}_s = A(\Delta\sigma)^n \tag{3-7}$$

where $\Delta\sigma$ is the imposed stress difference, n is the stress exponent, and A is a fitting parameter. If the power law equation is transformed using logarithms, the following expression is obtained:

$$\log\dot{\varepsilon}_s = \log A + n\log(\Delta\sigma) \tag{3-8}$$

The logarithmic equation is a linear equation in the transformed steady-state strain rate versus stress difference space and the stress exponent, n, represents the slope of the line in logarithmic space. The value of n is an indication of how strongly the steady-state strain rate depends on changes in stress.

Six steady-state strain rate values in Table 3-9 (the extension/compression test was excluded) and their corresponding stress differences from Table 3-8 were substituted into Equation 3-8 and plotted in Figure 3-9. The line fitted through the data is also shown in Figure 3-9 and the slope of that line is 5.6. Other test programs on several other salt types have indicated that the range of values for the stress exponent range from 3 to 6 [Pfeifle et al., 1995]. Thus the creep of McIntosh salt apparently has a strong dependence on changes in stress but is still within the range observed for other types of salt. The constitutive model used to simulate the creep of the McIntosh salt is much more complex than the simple power law model used here for this cursory analysis, and a more refined approach to determining the stress dependence is presented in Chapter 5.0 where a slightly different value for the stress exponent is found.

3.5.6 <u>Mineralogic Tests</u>

The chemical and mineralogical composition of McIntosh salt was determined from tests performed by the Engineering Mining Experiment Station (EMES) at the South Dakota School of Mines & Technology (SDSM&T) located in Rapid City, South Dakota. Wet chemistry was used to determine the chemical composition of the salt and X-ray diffraction (XRD) was used to determine the mineralogical composition.

Three specimens were used for chemical and mineralogical testing with seven additional specimens tested for water insolubles. The specimens were ground and homogenized to ensure an average measurement of the bulk mineralogy represented by each specimen. The results indicate that McIntosh Dome salt is very pure with a halite content greater than 95 percent by weight. The individual results from each of the specimens are presented in Tables 3-10 and 3-11 that list the chemical and mineralogical composition, respectively.
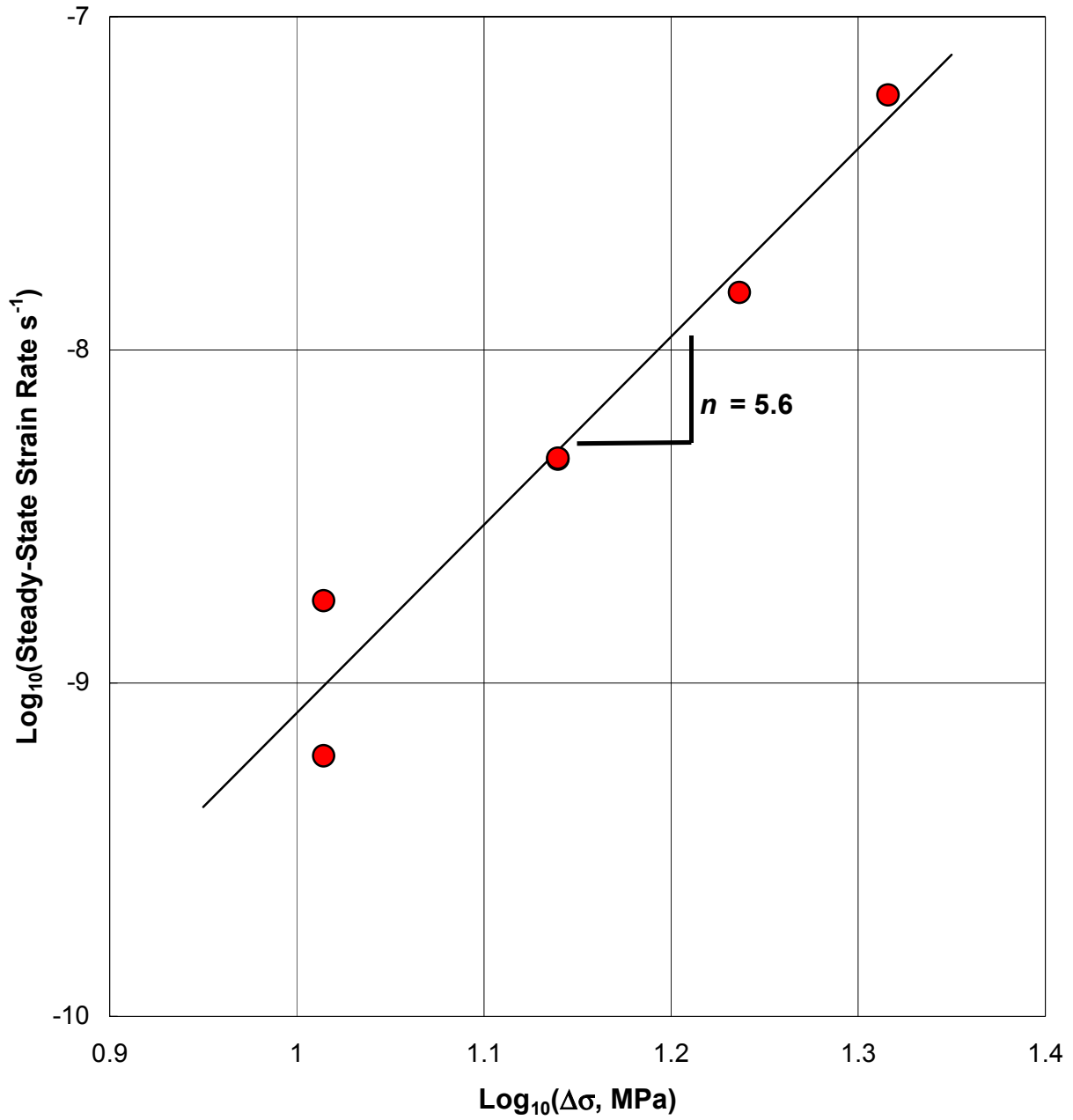
Figure 3-9. Stress Dependence of Steady-State Strain Rate for McIntosh Salt.

38

Table 3-10. Chemical Composition of McIntosh Salt

Specimen I.D.	Constituents in Weight by Percent						
	Na	Cl	Ca	K	Mg	SO$_4$	Water Insoluble
MD/BG2/4128.9	38.9	60.1	0.07	0.09	<0.01	0.22	0.64
MD/BG2/4140.6	36.9	56.8	1.32	0.09	0.08	4.30	0.43
MD/BG2/4151.9	39.1	60.3	0.04	0.12	<0.01	0.12	0.17
MD/BG2/4630.2							0.36
MD/BG2/4640.6							1.90
MD/BG2/4650.2							2.49
MD/BG2/5230.2							0.85
MD/BG2/5239.5							1.06
MD/BG2/4127.3							3.35
MD/BG2/5235.2							1.00

Table 3-11. Mineralogical Composition of McIntosh Salt

Specimen I.D.	Constituents in Weight Percent	
	Halite	Anhydrite
MD/BG2/4128.9	99.6 ± 0.5	0.3 ± 0.1
MD/BG2/4140.6	94.4 ± 0.7	5.6 ± 0.7
MD/BG2/4151.9	99.8 ± 0.2	0.2 ± 0.2

4.0 DISCREPANCY RESOLUTION AND MODEL REFINEMENT

The continuous change in the state of stress for the salt surrounding natural gas storage caverns when gas is injected and withdrawn was not a consideration during the development of the MDCF model for the WIPP. Additionally, development of the model ceased before the healing term in the model was complete. As a result, discrepancy resolution and model refinement activities were considered necessary in this first-time application of the salt damage criterion to correct known deficiencies associated with damage healing, the transient strain function during recovery, and address other potential unforeseen problems. It was envisioned that discrepancy resolution and model refinement would involve two components: (1) a laboratory testing component to refine the description of the healing mechanisms and the transient recovery function and (2) a theoretical component to develop mathematical descriptions for the transient recovery function and for the healing mechanisms, to correct known deficiencies in the healing model, and to implement the changes into our numerical analysis software so that cavern calculations could be performed.

A technically sound and feasible approach for implementing directional flow during damage healing using the finite element method was developed. During the course of this work, the possibility of changing the power-conjugate effective stress measures for shear-induced damage was contemplated. The transient recovery function has been known to be deficient during stress drops or decreases in the deviatoric stress. Recovery occurs when a storage cavern is at or near peak pressure during a storage cycle. As originally conceived, the recovery function has no influence when the reduction in deviatoric stress is significant. This behavior is in conflict with the laboratory evidence presented in Chapter 3.0. These refinements have been implemented into the finite element program SPECTROM-32 [Callahan et al., 1989]; however, additional theoretical considerations are recommended to update the power-conjugate effective stress measures for shear-induced damage. These issues are discussed separately in the next three sections.

4.1 MDCF MODEL HEALING TERM REFINEMENTS

The MDCF damage accumulation model includes stress-induced anisotropy by virtue of the effective stress measure used to describe the flow potential. Thus the volumetric bulking or dilation occurs normal to the minor principal stress (with compression assumed to be negative) representative of microfracturing occurring in the material. As presently written [Chan, 1996], the damage recovery or healing portion of the model also relies on a stress-induced anisotropy formulation without any knowledge of prior damage accumulation. Thus under certain conditions, damage recovery could be occurring in directions inconsistent with the original damage accumulation. This could occur if the principal stress directions change between the time when damage accumulates and damage recovery occurs. In addition, the damage recovery

is indeterminate under hydrostatic states of stress, predicts axial shortening under triaxial extension conditions, and predicts axial lengthening under triaxial compression conditions. To alleviate these difficulties, an isotropic flow potential was initially adopted. However, the isotropic flow condition also suffers deficiencies since the flow is the same in every direction. In fact, with fixed boundaries or under plane-strain conditions, large tensions may be produced with the isotropic flow potential when damage recovery occurs.

To alleviate these flow potential problems during damage recovery or healing, the stress normal to the initial damage accumulation was adopted for this proof-of-concept project as the effective stress governing the flow potential. The assumption used is that microfractures will be generated parallel to the minor principal stress and that further damage accumulation will not alter the orientation of the microfractures. Subsequently, when and if conditions for damage healing occur, the recovery (crack closure and sintering) occurs normal to the micro-fractures as dictated by the orientation of the damage. Thus the flow potential for damage healing is written as a function of the normal stress occurring on the oriented microfractures. The mathematical formulation for the healing portion of the MDCF model is presented in Appendix C, along with the development of the flow potential based on the stress normal to the microfractures.

4.2 ALTERNATIVE FORMULATION OF THE POWER-CONJUGATE EQUIVALENT STRESS MEASURES FOR SHEAR-INDUCED DAMAGE

The MDCF constitutive model evolved as additional laboratory test data became available. Initially, the model was described by Chan et al. [1992]. Since that time, the damage model has been updated as proposed by Chan [1993], Chan et al. [1995; 1996a; 1996b], and Chan [1996]. Unfortunately, the prior development and refinement of the MDCF model has relied primarily on triaxial compression states of stress. Analyses of underground caverns typically result in states of stress other than triaxial compression. Figure 4-1 shows contours of the Lode angle surrounding Bay Gas Well No. 1 at a relatively low internal gas pressure. The Lode angle is $+30°$ for triaxial compression stress conditions and $-30°$ for triaxial extension stress conditions. Figure 4-1 shows that a major portion of salt surrounding the cavern is near ($-30° < \psi < -20°$) triaxial extension conditions, which are poorly represented by the MDCF model. Because it is possible that salt may be weaker or behave differently at stress states other than triaxial compression, alternative formulations of the power-conjugate equivalent stress measures for shear-induced damage and flow were developed as a possible update to the MDCF model. The impetus of this work is motivated by the possibility that the minimum allowable gas pressure determined using the MDCF model may not be conservative because it was developed using tests performed solely under triaxial compression states of stress.

To partially examine this hypothesis, a creep test was conducted whereby the deviatoric stress was maintained constant and the stress state was changed from triaxial extension to
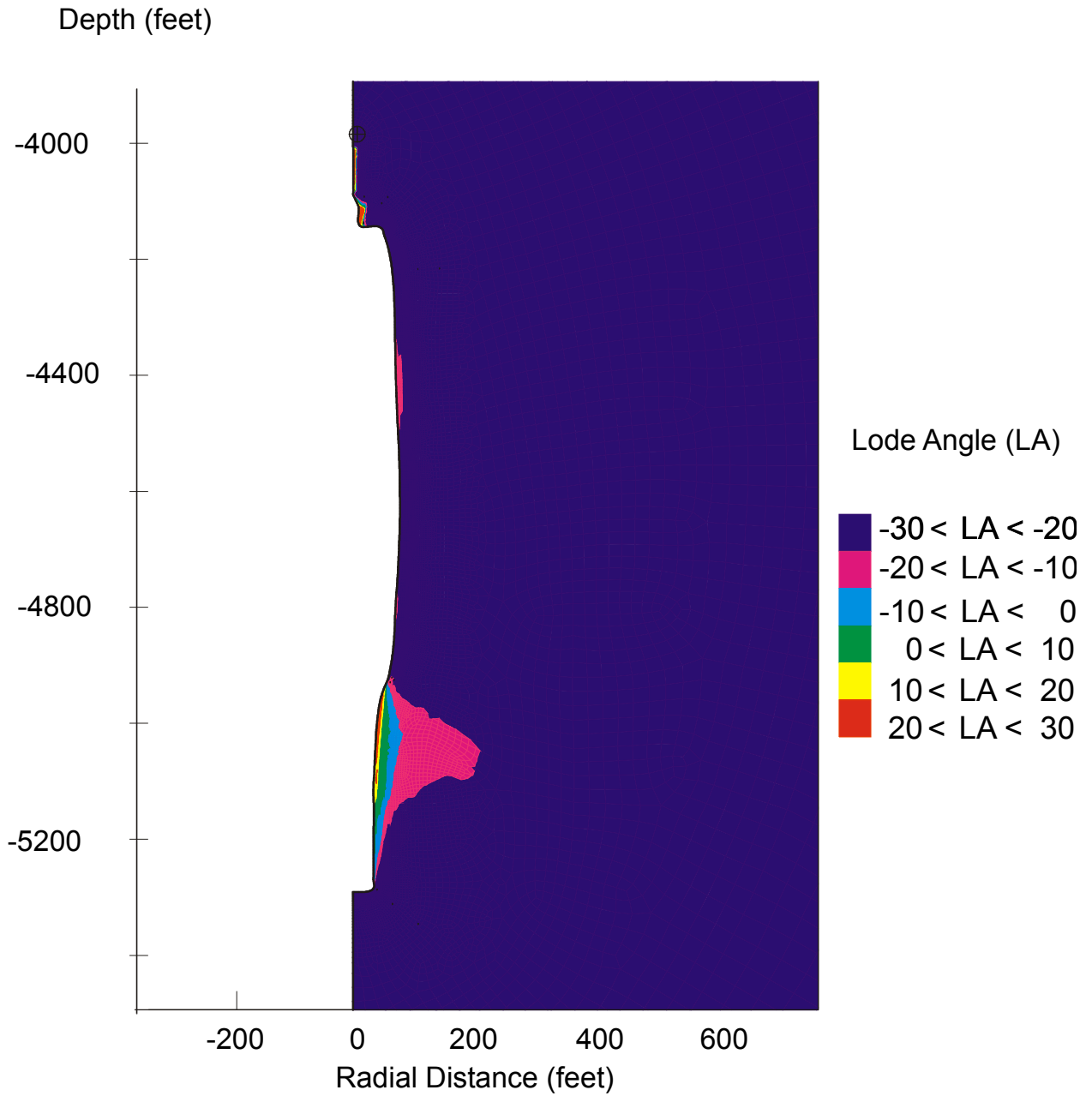
Figure 4-1. Lode Angle Contours Surrounding Bay Gas Well No. 1 at Minimum Gas Pressure.

42

triaxial compression. This test is shown in Figure B-37 of Appendix B. The present mathematical formulation of the MDCF model predicts that the strain rates are identical before and after the change from triaxial compression to triaxial extension or from triaxial extension to triaxial compression. As the test results show, differences in the strain rates of about a factor of two are observed.

Unfortunately, insufficient data are provided by this single creep test alone to derive, fit, formulate, and use a new mathematical description for the model that captures the behavior observed in the tests. However, Appendix D provides a review of rock behavior under states of stress common in underground caverns other than triaxial compression and introduces a potential modification to the power-conjugate equivalent stress measures for shear-induced damage. The new equivalent stress measure has been incorporated into the MDCF model and SPECTROM-32 as an option for the conduction of numerical experiments. However, confidence in the model's ability to predict the behavior of salt under conditions other than triaxial compression states of stress is compromised because of the limited amount of experimental data presently available.

4.3 RECOVERY FUNCTION REFORMULATION

Chapter 3.0 includes the results of three laboratory recovery experiments (see Figures B-24, B-25, and B-28 of Appendix B). These three tests were subjected to various stages of increases and decreases in the constant deviatoric stress maintained for any particular stage of the test. The objectives of these tests were to examine the specimen response following a deviatoric stress drop (recovery) and to examine the specimen response following a deviatoric stress increase (subsequent transient). The MDCF model includes the same transient function as was originally formulated for the multimechanism steady-state work-hardening/recovery (M-D) model [Munson et al., 1989]. The transient function (F) is composed of three branches, a work-hardening branch, an equilibrium or steady-state branch, and a recovery branch, which is written in that order (Appendix A, Equation A-6) as:

$$F = \begin{cases} \exp\left[\Delta\left(1 - \dfrac{\varsigma}{\varepsilon_t^*}\right)^2\right] & \text{for } \varsigma < \varepsilon_t^* \\[3mm] 1 & \text{for } \varsigma = \varepsilon_t^* \\[3mm] \exp\left[-\delta\left(1 - \dfrac{\varsigma}{\varepsilon_t^*}\right)^2\right] & \text{for } \varsigma > \varepsilon_t^* \end{cases} \tag{4-1}$$

where Δ and δ are work-hardening and recovery material parameters, and ζ is an internal variable governed by the evolutionary equation:

$$\dot{\zeta} = (F-1)\dot{\varepsilon}_s \tag{4-2}$$

where $\dot{\varepsilon}_s$ is the steady-state strain rate, and the transient strain limit $\left(\varepsilon_t^*\right)$ is described as:

$$\varepsilon_t^* = K_0 \exp(cT)\left(\frac{\sigma_{eq}}{\mu}\right)^m \tag{4-3}$$

where K_0, c, and m are material parameters; T is the absolute temperature; μ is the shear modulus used as a normalizing parameter; and σ_{eq} is the power-conjugate effective stress measure defined as the maximum shear stress. Equations 4-1 through 4-3 are the basic equations that govern transient response following changes in deviatoric stress. However, these functional forms were found to provide inadequate representation of the experimental data obtained in the testing program, particularly for the recovery branch. Thus alternate functional forms were derived to capture the behavior exhibited in the laboratory tests. A new transient function $\left(F_r\right)$ was developed for use in the definition of the internal variable ζ as:

$$F_r = \begin{cases} \exp\left[\Delta\left(1-\dfrac{\varsigma}{\varepsilon_t^*}\right)^2\right] & \text{for } \varsigma < \varepsilon_t^* \\[2ex] 1 & \text{for } \varsigma = \varepsilon_t^* \\[2ex] \exp\left[\Delta\left(1-\dfrac{\varepsilon_t^*}{\varsigma}\right)\right] & \text{for } \varsigma > \varepsilon_t^* \end{cases} \tag{4-4}$$

with Equation 4-2 rewritten as:

$$\dot{\zeta} = \text{sign}\left(\varepsilon_t^* - \zeta\right)\left(F_r - 1\right)\dot{\varepsilon}_s \tag{4-5}$$

To illustrate the effect of the change in the recovery function, simulations of the laboratory test labeled MD/BG2/4150.7 (Appendix B, Figure B-28) using the two different formulations are shown in Figure 4-2. Figure 4-2 plots the axial strain measured in the test along with the predicted results from the two recovery formulations given in Equation 4-1 for the previous or old formulation and Equation 4-4 for newly proposed recovery formulation. Test MD/BG2/4150.7 consisted of three stages with deviatoric stress levels of 17.2, 13.8, and 17.2 MPa (2,500, 2,000, and 2,500 psi), respectively. Figure 4-2 only shows Stages II and III of the test because the simulated results are identical for Stage I. Evaluation of the recovery parameters is discussed in the next chapter; however, Figure 4-2 shows that the new formulation is capable of predicting the behavior of this test quite well. Figure 4-2 also shows that the new formulation represents the Stage III results much better than the old recovery formulation. The Stage III improvement occurs because of the evolution of the internal variable provided in Stage II with the new formulation.
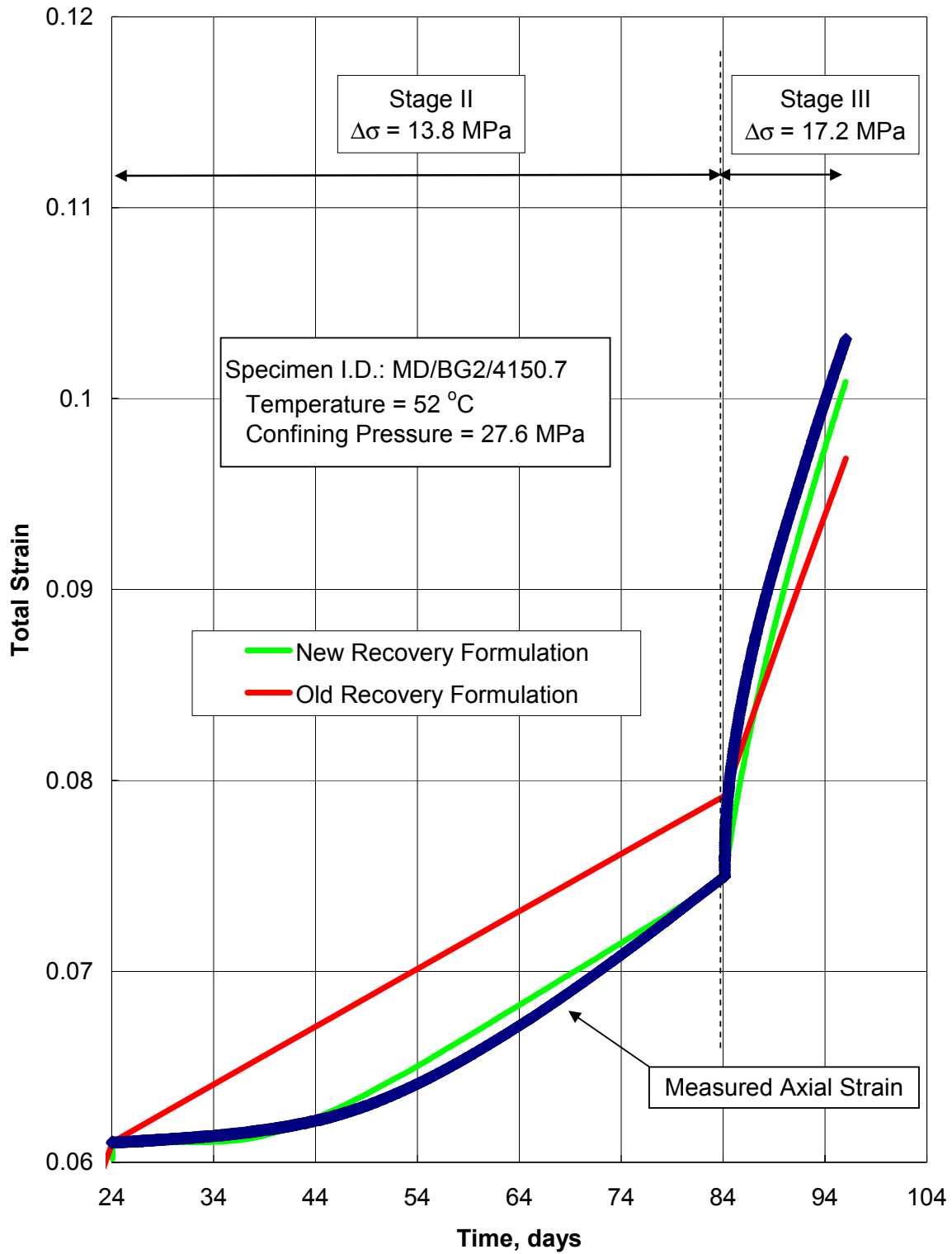
Figure 4-2. Comparison of Recovery Function Formulations for Test MD/BG2/4150.7.

4.4 MDCF MODEL MODIFIED FORMULATION

The final equations representing the modified MDCF model are given in Appendix E.

5.0 PARAMETER EVALUATION

The MDCF model contains 42 model parameters that must be determined before a geomechanical modeling study can be performed of the gas storage caverns at the McIntosh Dome. The goal of the parameter evaluation task is to determine values for the parameters of the MDCF model that accurately describe the creep and plastic behavior of the salt at the McIntosh Dome. The technical approach for determining the parameter values of the MDCF model and the model fitting results, including graphical comparisons of the model predictions to the measured data, are provided in this chapter.

5.1 TECHNICAL APPROACH

Because the MDCF model contains numerous parameters, it is not practical to determine all the parameters simultaneously using the entire database of laboratory test results. The technical approach used separated the problem into several smaller and more manageable least-squares analyses; wherein, only a few parameters had to be determined from any single analysis. Parameter values are determined based on the result that produces the lowest sum-of-squares error between the measured and predicted responses (either stress or strain). The steps to determine parameter values of the MDCF model include:

1. Identify those parameters that are deterministic.

2. Group parameters into sets that can be determined independently from other parameters in the model.

3. Identify prerequisites, if any, to determine parameters from each set (functional group of parameters).

4. Identify laboratory tests that can be used to determine the parameters in each functional group.

5. Develop software that includes the MDCF response models for the different laboratory load paths and responses (i.e., axial strain, volumetric strain, dilation stress).

6. Compile and organize the laboratory data into databases that are compatible with the nonlinear curve fitting software.

7. Assign weighting to each data point to reduce bias in the database. The goal is to reduce the bias of the fitting procedure with respect to strain magnitude such that the model will fit the low strain data equally as well as the larger strain data.

8. Select appropriate order for evaluating each functional group of parameters based on prerequisites.

9. Perform least-squares analyses to determine values for free parameters.

5.2 NUMERICAL ROUTINES

Nonlinear curve fitting techniques were used to determine site-specific parameter values for the MDCF model. The curve fitting techniques utilized the least-squares solution methodology to minimize the difference between the measured and predicted response. Two different least-squares solution programs were developed to determine parameter estimates for the MDCF model. The first uses Microsoft's spreadsheet program Excel employing the built-in *Solver* function in user-designed worksheets. The second program was developed using the FORTRAN programming language and is considerably more robust. Selection of which program to use for a particular analysis depended on the size and complexity of the problem. Relatively small and simple problems could be solved more efficiently using Excel; whereas, the FORTRAN software program is better suited for computations involving time-dependent behavior and numerical integration.

5.3 MODEL FITTING

The highly nonlinear functions comprising the MDCF model make parameter value determination an arduous process. The technical approach given above was followed to determine the parameter values of the MDCF model. The approach is based on the concept of fitting the model to the measured responses of laboratory tests that isolate material behavior that is characterized by a limited number of parameter values. For example, parameters that define steady-state creep can be determined from data measured at the end of long-term, high-confining pressure creep tests when no other deformation mechanisms (e.g., elastic or brittle) are operative. Also, it was determined by Nieland et al. [1999] that a number of the parameters can be treated as deterministic while others do not contribute significantly to the deformation under the loading conditions experienced in the salt surrounding natural gas storage caverns during operation.

The equations defining the MDCF model are provided in Appendix E. Table 5-1 lists both the free and deterministic parameters according to their role in the MDCF model. Free parameters were determined from the dependent variable response in laboratory tests performed on salt core recovered from the Bay Gas Well No. 2 wellbore. The remaining parameters were treated as deterministic and assigned the same values as those determined for salt at the WIPP [Munson et al., 1989].

Some of the parameters were classified as deterministic because they have little influence on the predicted response of the salt surrounding a natural gas storage cavern. This is because the MDCF model was initially developed to predict the extreme conditions at a nuclear waste repository in salt. For example, the stress and temperature conditions experienced in the salt during cavern storage are not within the regime where dislocation climb and glide dominate. As a result, parameters describing these mechanisms were classified as deterministic (B_1, B_2,

q, A_1, and n_1). Because of the relatively small change in temperature over the height of the storage caverns, parameters controlling the temperature dependency have little influence and are considered to be deterministic (Q_1/R, Q_2/R, and c).

Table 5-1. Functional Groups of MDCF Parameters

Function	Free Parameters	Deterministic Parameters
Transient Creep	α, β, K_0, α_r, β_r,	m, c
Steady-State Creep	A_2, n_2	B_1, B_2, q, A_1, n_1, Q_1/R, Q_2/R, μ, σ_0,
Shear Damage Strain Rate	c_0, c_2, n_3,	x_{3s}, c_3, ω_0
Damage Variable Rate[a]	ξ_s^1, ξ_s^2	t_0, x_4, ρ
Tension Damage[a]		x_1, x_{3t}, ξ_t, x_4
Healing	k_1, τ_0, τ_1	
Dilation Stress Boundary[a]	x_2, x_6	x_7, p_1, ρ
Damage Flow Potential	x_2, x_8	
Transient Damage	c_4	c_5

(a) Note: the parameters x_2, x_4, and ρ belong to more than one functional group.

Others parameters have a theoretical basis (m and σ_0) or are determined by mineralogy (ρ). Because no major distinction was observed by the geophysical logs, mineralogic analyses, or the laboratory tests performed on the salt from three different depths, the sensitivity of the salt to impurity content did not need to be addressed. Thus the parameter p_1 was also considered deterministic and was assigned a value of zero. Assigning a value of zero to the parameter p_1 negates the influence of impurity parameter (ρ). However, the influence of impurity is taken into account through adjustment of the parameter x_2, with the assumption that the salt impurity is homogeneous over the depth interval of the cavern.

Parameters associated with the shear damage strain rate (x_{3s} and c_3) and the damage variable rate (x_4) were treated as deterministic because they were determined to have very little or no influence on the laboratory load paths used [Nieland et al., 1999]. The functional form of the transient damage term (Appendix E, Equation E-15) contains two parameters (c_4 and c_5); however, these parameters can be lumped into a single constant by rearranging Equation E-15. Rather than rewrite the damage term, the original form of the MDCF model was retained and the parameter c_5 was considered to be deterministic.

Parameters associated with the development of cleavage fractures (x_1, x_3, ξ_t, and x_4) under tensile stress states were not evaluated in this project because design constraints do not permit tension within the salt formation surrounding a cavern.

The parameters x_7, t_0, and μ are normalizing constants used to provide the correct dimensional units of time and stress, respectively. Selection of values for these three parameters is arbitrary since other parameters in the model are fully correlated and will adjust proportionally to produce the same least-squares solution. To remain consistent with the original developers of the MDCF, x_7 is set equal to 1 MPa, t_0 is set equal to 1 second, and μ is given the value for the shear modulus of salt at the WIPP. Similarly, ω_0 is assigned a negligible value of 0.0001 since the damage rate equation requires a nonzero initial value.

Of the 42 parameters identified in Table 5-1, only 19 site-specific parameters are required to predict the behavior of salt caverns during natural gas storage at the McIntosh Dome. The 19 parameters were organized into functional groups, as shown in Table 5-1.

5.4 DATA REDUCTION

Data collection during laboratory testing resulted in thousands of measurements for most tests. Before fitting the response model to the strain-versus-time data, the raw data collected in all the laboratory creep tests were reduced and limited to 100 points per test. The procedure used to select the 100 data points from each test was based on an incremental time interval. The procedure was developed to ensure that the first and last data points in each test were included with data points at nearly equal time intervals in between. In certain cases, only a single stage of a multistage test was used in the fitting effort. In these cases, 100 data points were selected from the stage of interest.

5.5 MDCF RESPONSE MODEL FITS

The parameters for each functional group were determined from independent least-squares fits to the laboratory test measurements of McIntosh Dome salt. Separate discussions are provided for the evaluation of the creep, dilation boundary, damage, and healing terms. Graphical comparisons between the predicted and measured responses are provided in this section. Values for the MDCF model parameters determined from the fits are provided in Appendix F.

5.5.1 <u>Creep Parameter Evaluation</u>

Steady-state and transient creep parameters (A_2, n_2, α, β, and K_0) were determined from the first stage of the three creep tests subjected to a confining pressure of 27.6 MPa (4,000 psi) and stress differences of 10.3, 13.8, and 20.7 MPa (1,500, 2,000, and 3,000 psi). Figure 5-1
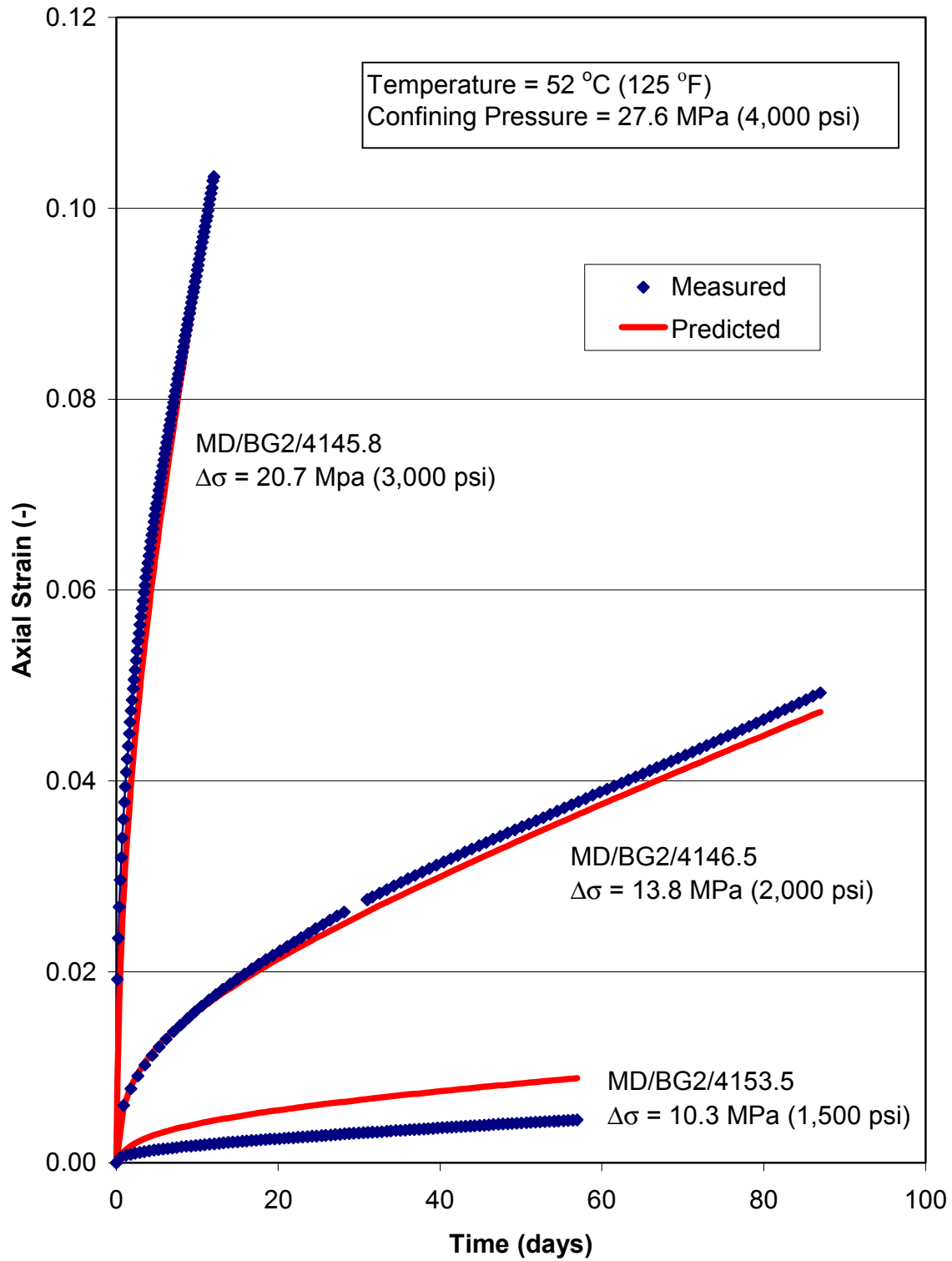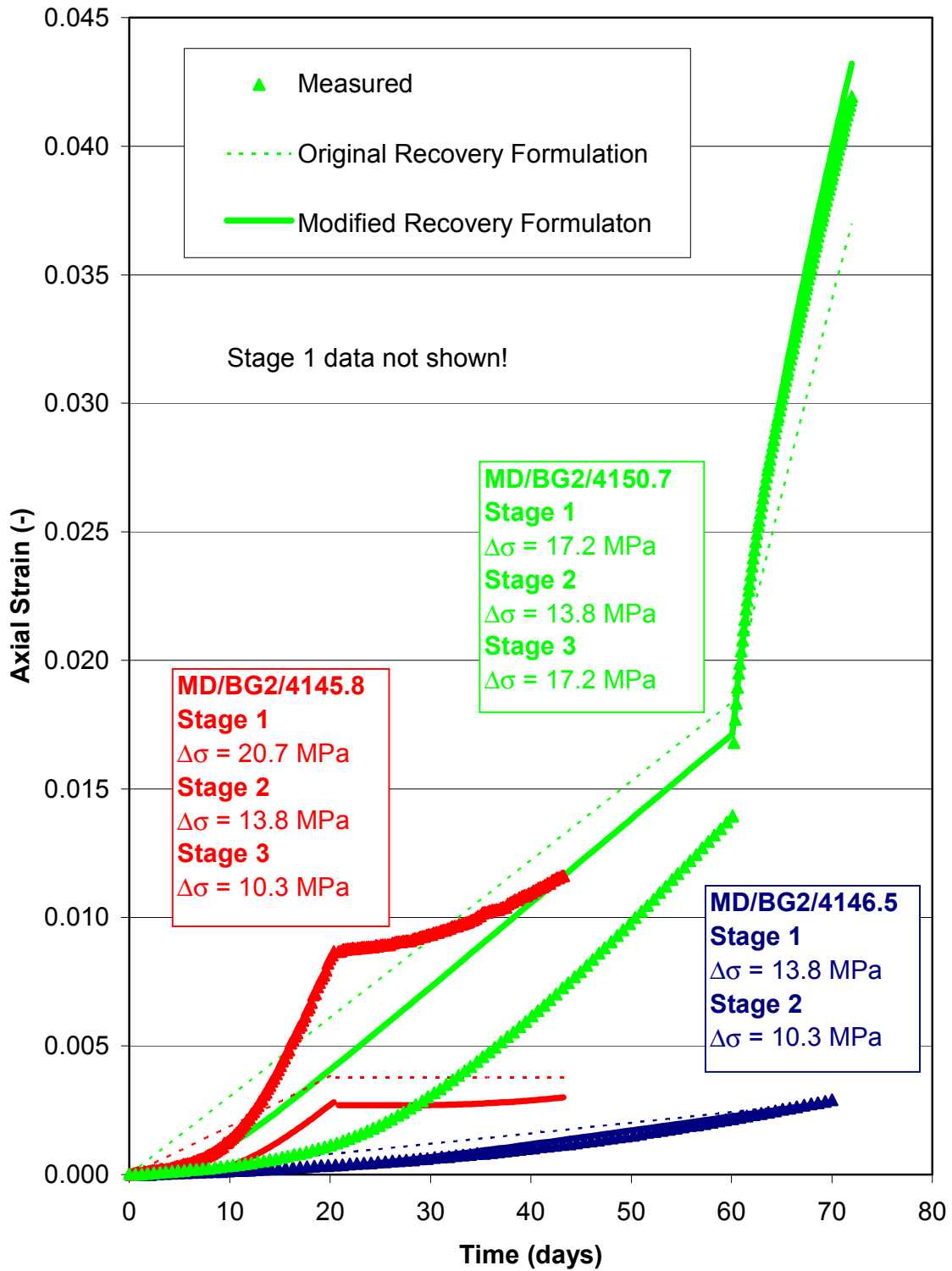
Figure 5-1. Comparison of Measured and Predicted Creep Tests Performed on Salt From Bay Gas Well No. 2 at 52°C (125°F) and 27.6 MPa (4,000 psi) Confining Pressure.

compares the MDCF model prediction for axial strain to the first stage of the laboratory creep tests. The model does an excellent job of predicting the steady-state strain rates over the range of stress differences tested. Because the relatively high confining pressure used suppresses dilation of the salt, the measured and predicted responses do not exhibit an accumulation of volumetric strain. The predicted transient strain response is considered good for these three tests; however, significantly more strain was predicted for the test performed at a stress difference of 10.3 MPa (1,500 psi) than was measured in the laboratory. The difference between the measured and predicted response is believed to be attributable to the transient strain response of the salt at low stress differences. Without duplicating the test, it is difficult to judge if the discrepancy is a result of salt variability or a deficiency of the model and/or parameter evaluation.

The transient creep recovery parameters $(\alpha_r$ and $\beta_r)$ were determined from the second stages of three stress drop tests. Figure 5-2 compares the measured and predicted axial strain as a function of time for the three stress drop tests. For illustrative purposes, time and strain were reset to zero at the time of the stress drop; thus, the data plotted in Figure 5-2 is the accumulated axial strain since the time of the stress drop. MDCF model predictions are provided in Figure 5-2 using the original model formulation of the recovery branch and the modified formulation that was developed as a part of this study (see Chapter 4.0). The original formulation of the MDCF model did not accurately capture the changing strain rates of salt following a reduction in shear stress similar to that experienced by the salt surrounding a natural gas storage cavern following injection of natural gas from a low pressure to a high pressure. As shown in Figure 5-2, the new formulation describes the recovery process of these creep tests more accurately as determined by separate fits using both the old and new formulations.

Some of the discrepancy between the measured and predicted responses shown in Figure 5-2 is believed to be attributable to variability in the salt recorded by the laboratory measurements. In two of the tests, the final stress difference was reduced to 13.8 MPa (2,000 psi); however, it is apparent in Figure 5-2 that these two tests are not approaching the same steady-state strain rate. This variability, combined with the limited number of tests available, made determination of the recovery branch parameter that describes stress dependency (β_r) speculative. Least-squares regression analyses using the stress drop tests performed for this study indicated extremely high correlation between the recovery parameters α_r and β_r. During the fitting effort, it was observed that for a given value of β_r, α_r would adjust accordingly to produce a nearly identical fit without reducing the sum-of-squares error. Based on this finding, it was necessary to reduce the recovery model parameter evaluation to determination of a single parameter (α_r). The stress dependency β_r was arbitrarily set equal to zero, as was done for WIPP salt [Munson et al., 1989]. Because the results are insensitive to the value of β_r, it is recommended that this parameter be treated as deterministic in all future studies until additional testing can be completed.

Figure 5-2. Comparison of Measured and Predicted Axial Strain Data of Stress Drop Tests Performed on McIntosh Salt.

### 5.5.2 Dilation Boundary Parameter Evaluation

MDCF model parameters that define the damage effective stress measure $\left(x_2 \text{ and } x_6 \right)$ were determined using the results of six CMS tests described in Chapter 3.0. Figure 5-3 shows the dilation boundary predicted by the model under conditions of a triaxial compression test (i.e., $\sigma_z > \sigma_x = \sigma_y$). The results shown in Figure 5-3 are presented in terms of the first invariant of the Cauchy stress tensor, I_1, and the square root of the second invariant of the deviatoric stress tensor, $\sqrt{J_2}$.

The MDCF dilation boundary indicates that the dilation stress increases with mean stress (or I_1) and divides the $\sqrt{J_2}$ -versus- I_1 stress space into two regions. The region below and to the right of the line represents a *nondilating* region. Conversely, the region above and to the left of the line represents a *dilating* region. Also shown in Figure 5-3 are the dilational stresses determined from the six CMS tests described in Chapter 3.0 and the dilation limit proposed for other Gulf Coast salts [Van Sambeek et al., 1993] given by a linear relationship referred to as the Damage Potential.

As shown in Figure 5-3, the dilation boundary predicted by the MDCF model is different than the linear dilation boundary given by the Damage Potential relationship. The MDCF model dilation limit is greater than the Damage Potential relationship for values of $\sqrt{J_2}$ less than 10.3 MPa (1,500 psi) but becomes significantly lower than the Damage Potential relationship for $\sqrt{J_2}$ greater than 10.3 MPa (1,500 psi). The results presented in Figure 5-3 for the MDCF model are for triaxial compression stress states and will most likely be different at other stress conditions, such as triaxial extension (i.e., $\sigma_z < \sigma_x = \sigma_y$).

5.5.3 Shear Damage Parameter Evaluation

The MDCF model free parameters that define the shear damage strain rate (c_0, c_2, n_3, x_8, ξ_s^1, ξ_s^2, and c_4) were determined from eight creep tests performed at low and moderate confining pressures (0.7 to 3.5 MPa (100 to 500 psi)). The original test matrix proposed by Nieland et al. [1999] called for six creep tests to be performed at low and moderate confining pressures. Two additional tests were added when it was discovered during the model fitting effort that these tests need to be performed beyond the onset of tertiary creep. These two tests would not have been performed if the six creep tests in the original test matrix had extended into the tertiary creep stage. The creep tests were terminated before the tertiary stage because the design criterion for salt damage is conservatively limited to low levels of damage, well below the onset of tertiary creep. Therefore, information about tertiary creep was not believed to be relevant for determination of the MDCF model parameters for cavern storage analyses. During the parameter evaluation effort, it became obvious that the only way to determine parameter values that define the evolutionary equation for damage (Appendix E, Equation E-22) was to simulate the accelerated strain rate during tertiary creep. This is true because the parameters
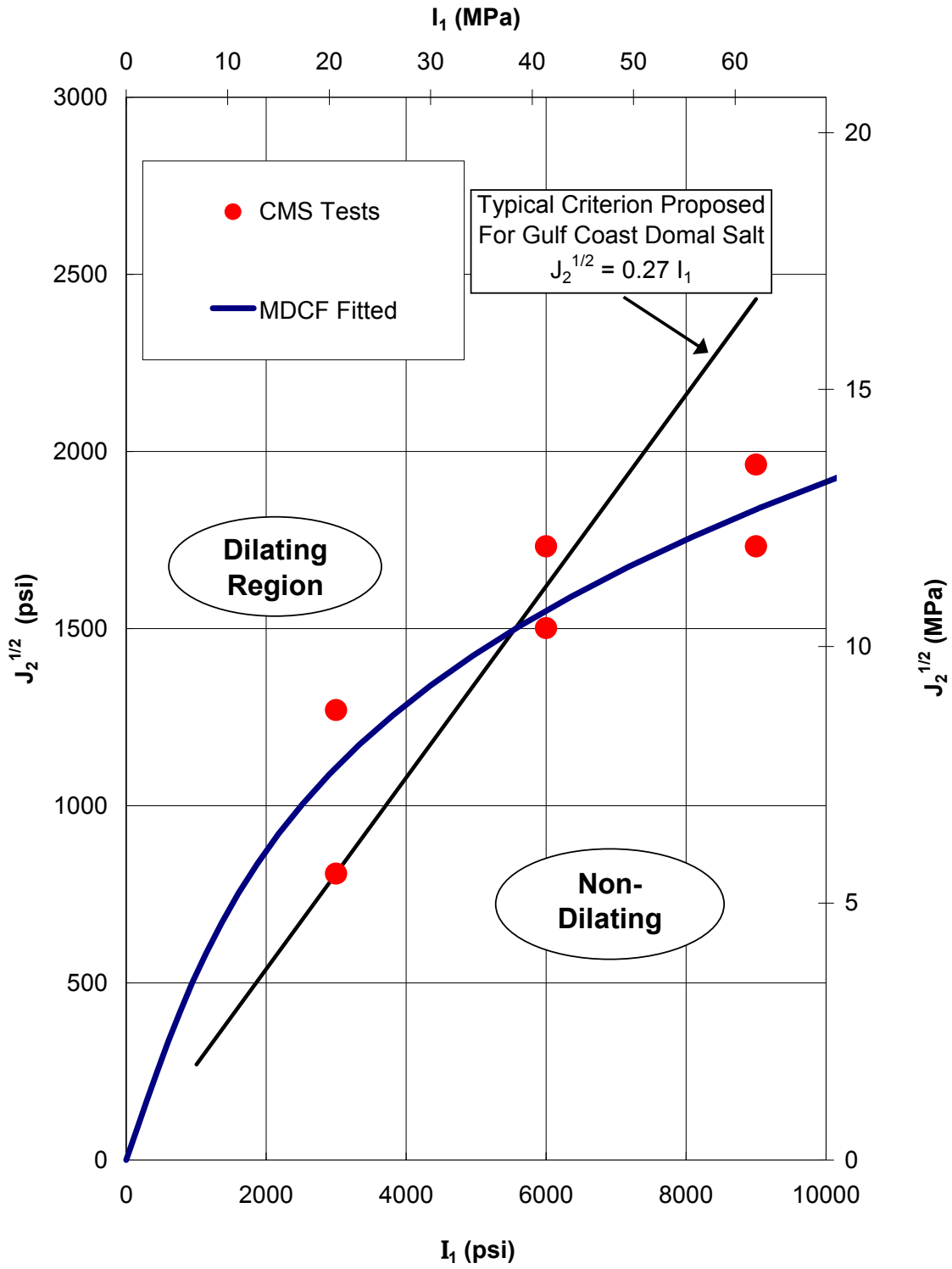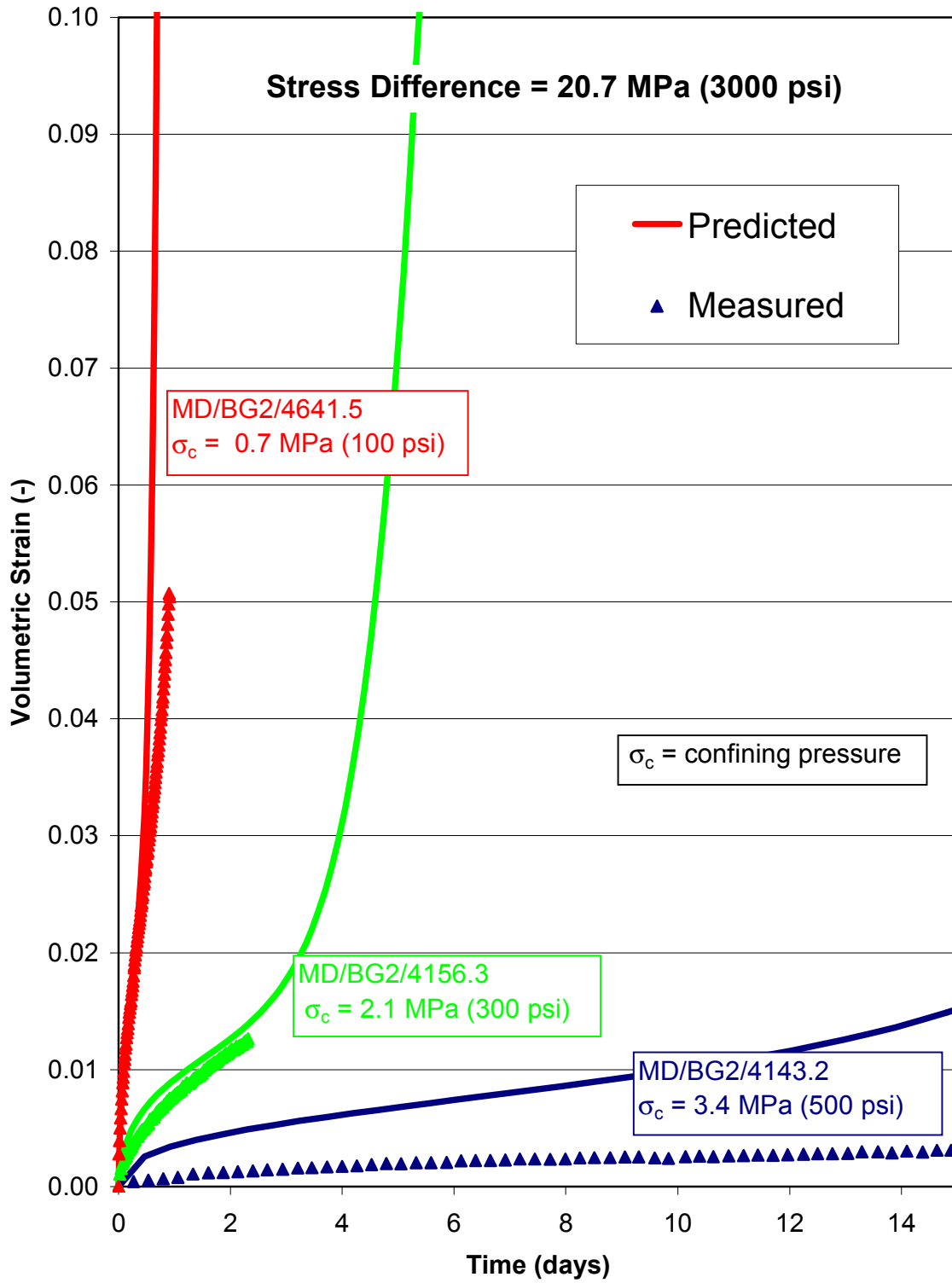
Figure 5-3. Comparison of Measured and Predicted Stress States for the Onset of Dilation.

55

that define the evolutionary equation were found to be insensitive to strain-versus-time data collected from tests terminated at low levels of damage. ξ_s^1 was set equal to ξ_s^2 because the data did not support the need for two separate damage rate expressions.

During the fitting effort, attempts were made to determine both the free and deterministic parameters that describe the damage process of salt. These attempts proved futile for a combination of reasons, including: (1) insensitivity of model parameters to the constant stress tests, (2) lack of reproducibility of the laboratory measurements, (3) determination of a unique set of parameters is prevented by high correlation amongst parameters, and (4) separation of the creep and damage strains from the total strain is not possible. *Efforts to determine only the free parameters that define damage were also unsuccessful using the eight laboratory creep tests performed at low and moderate confining pressures. To rectify the problem, the free parameters that define the damage stress dependency (n_3 and c_2) of the damage strain rate equation (Appendix E, Equation E-17) were set to values determined for WIPP salt.* Although determination of the parameters n_3 and c_2 is possible, the laboratory test matrix would have to be increased.

Because of the similarities observed between WIPP and McIntosh salt, use of the stress-dependency terms of the original developers of the MDCF model was a logical choice. Otherwise, it is expected that at least three multistage creep tests would have to be performed wherein the stress difference (shear stress) is held constant and the damage stress measure is incrementally increased for each successive stage in the multistage tests. The first stage of these tests is required to be of sufficient length to be considered very near the steady-state condition, thus reducing the contribution of the transient response during the later stages of the test. Performance of these tests for this project was prohibited by time and economic constraints. However, use of the WIPP parameters for n_3 and c_2, combined with fitted values for the parameters c_0 and c_4, produced results that compare favorably with the laboratory measurements.

The flow potential damage parameter x_8 was determined from least-squares regression analyses using the *volumetric strain* data obtained from the eight creep tests performed at moderate and low confining pressures; whereas, the remaining damage parameters were determined from the *axial strain* data. Figure 5-4 compares the measured and predicted inelastic volumetric strain response for the three creep tests performed at a stress difference of 20.7 MPa (3,000 psi) and confining pressures of 0.7, 2.1, and 3.5 MPa (100, 300, and 500 psi). Dilation or damage of the salt is reflected in the magnitude of the inelastic volumetric strain. If no dilation occurs, then the inelastic volumetric strain will be zero. Figure 5-4 illustrates that the volumetric strain accumulates faster at lower confining pressures and decreases rapidly for relatively small increases in the confining pressure. This response is also characterized quite well by the MDCF model. The MDCF model predicts that the test performed at a confining pressure of 2.1 MPa (300 psi) would have reached the tertiary creep stage within 4 days; thus, this test would have likely failed within 24 hours had it not been terminated. Failure (as

Figure 5-4. Comparison of Measured and Predicted Volumetric Strain Data of Creep Tests Performed at a Stress Difference of 20.7 MPa (3,000 psi).

57

indicated by the near-vertical strain-time response) of the creep test performed at 0.7 MPa (100 psi) confining pressure was predicted to occur within 1 day; whereas, failure of the creep test performed at 3.5 MPa (500 psi) confining pressure was not predicted during the 2 weeks that the test was performed.

Figure 5-5 is similar to Figure 5-4 except that the results are presented for the three creep tests performed at a stress difference of 17.2 MPa (2,500 psi) and confining pressures of 0.7, 2.1, and 3.2 MPa (100, 300, and 467 psi). As shown in Figure 5-5, the measured volumetric strain for the test performed at a confining pressure of 2.1 MPa (300 psi) (colored green) is less than that of the test performed at a confining pressure of 3.2 MPa (467 psi). The specimen subjected to 2.1 MPa (300 psi) confining pressure is believed to have produced anomalous results because previous testing programs have consistently demonstrated that volumetric strain (damage accumulation) is suppressed by higher confining pressures. Therefore, an accurate prediction of this test is not possible. In general, the relative response of the salt to various confining pressures is captured reasonably well, as illustrated in the comparison of the measured and predicted volumetric strain data provided in Figures 5-4 and 5-5.

5.5.4 <u>Healing Mechanism Parameter Evaluation</u>

The MDCF model parameters that describe damage healing (k_1, τ_0, and τ_1) were determined from fits to volumetric strain of three staged creep tests. During the first stage of the creep tests, specimens were subjected to a high shear stress and low confining pressure to induce damage. Then, the load on the specimen was changed to one that promotes healing. Figure 5-6 compares the measured and predicted volumetric strains during the healing stages of three constant stress tests. The healing test identified using red symbols in Figure 5-6 was performed in two stages. During the first healing stage, the specimen was subjected to a stress difference of 13.8 MPa (2,000 psi) and confining pressure of 20.7 MPa (3,000 psi). During the second stage of the healing test, a hydrostatic stress state of 41.4 MPa (6,000 psi) was applied. The test conditions were held constant during the other two healing tests, as identified in Figure 5-6. A hydrostatic stress state of 20.7 MPa (3,000 psi) was specified for the test identified using the green symbols; whereas, healing of the test identified using blue symbols in Figure 5-6 was subjected to a stress difference of 13.8 MPa (2,000 psi) and confining pressure of 13.8 MPa (2,000 psi).

The volumetric strains at the beginning of the healing stages of the tests were approximately 0.93 percent for the test performed at a stress difference of 13.8 MPa (2,000 psi) and confining pressure of 13.8 MPa (2,000 psi), 0.041 percent for the test performed under a hydrostatic stress of 20.7 MPa (3,000 psi), and 0.064 percent for the two-stage test identified above. Some volumetric strain was recovered before the onset of the healing portion of the test. This is because the specimens deform volumetrically during application of the healing stress state when lateral dimensions cannot be recorded. An estimate of the volumetric strain that occurred during application of the healing stress was determined assuming that the specimens were completely healed when the tests were terminated.
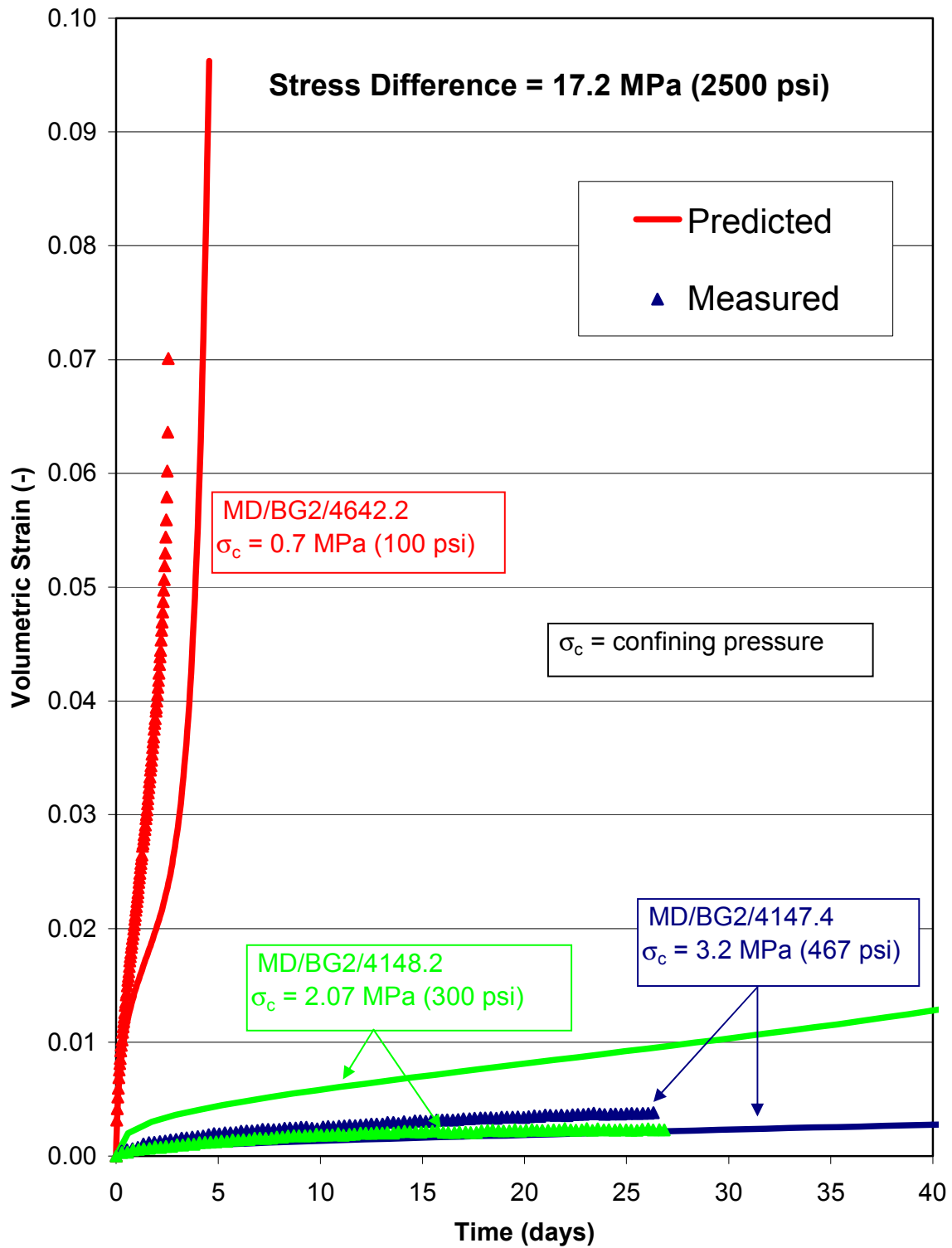
Figure 5-5. Comparison of Measured and Predicted Volumetric Strain Data of Creep Tests Performed at a Stress Difference of 17.2 MPa (2,500 psi).
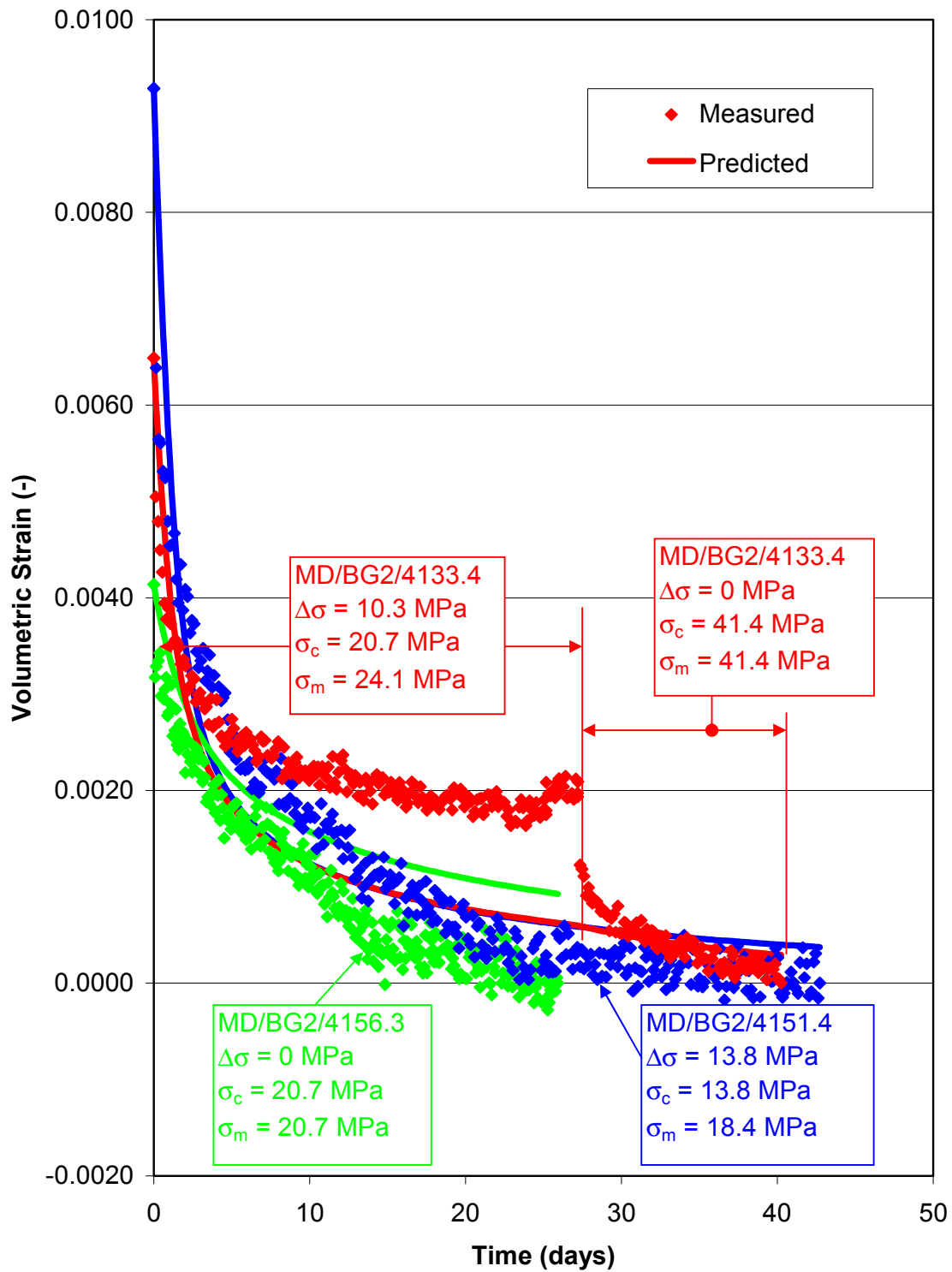
Figure 5-6. Comparison of Measured and Predicted Volumetric Strain Data of Damage Healing Tests Performed on McIntosh Dome Salt.

The results suggest that healing of damaged salt (where healing is defined here as a reduction in volumetric strain) is initially very rapid but then slows considerably. Based on times required to heal these damaged specimens at high mean stress, it is likely that months would be required to completely heal damaged salt around a salt cavern if the cavern were maintained at high gas pressures. Additionally, a reduction in volumetric strain does not necessarily constitute molecular bonding (the process thought necessary to regain the material characteristics of undamaged salt). As previously mentioned, laboratory efforts to quantify healing, other than volumetric strain measurements, were unsuccessful. *Because of the uncertainty in the ability to quantify healing of salt, it is recommended that cavern analyses do not take into account the benefit associated with healing, as predicted by the MDCF model.*

5.6 PARAMETER ESTIMATES FOR THE MODIFIED STRESS MEASURES FOR SHEAR-INDUCED DAMAGE

The original MDCF model formulation predicts that salt is stronger in triaxial extension than in triaxial compression. As a first attempt to alleviate this deficiency, theoretical development of a potential modification to the MDCF model power-conjugate effective stress measure for shear-induced damage and flow based on the Mohr-Coulomb criterion was performed as a part of this project. Determination of the parameters that define this stress measure is best accomplished with experimental data performed on tests ranging from triaxial extension to triaxial compression states of stress. Because this data is not available, parameters had to be determined based solely on the results of triaxial compression tests.

Parameters values required to define the proposed stress measures include η, C, and κ (see Equation D-14 in Appendix D). Values of 0.2, 2.0 MPa, and 0.25 were determined for η, C, and κ, respectively, that provide a conservative estimate for the dilation boundary of McIntosh salt at triaxial compression states of stress. It is assumed that the model will also provide a conservative estimate at stress states other than triaxial compression; however, this assumption was not fully validated. Figure 5-7 compares the dilation boundaries in $\sqrt{J_2}$ -versus- I_1 stress space using the alternative formulation for the power-conjugate stress measure for shear-induced damage. Figure 5-7 also shows the dilation boundaries of McIntosh salt based on the original formulation of the MDCF model. The dilation boundaries using the alternative formulation are linear in the $\sqrt{J_2}$ -versus- I_1 stress space with the material considerably weaker in extension than in compression. The MDCF model dilation boundaries are nonlinear with the material considerably stronger in extension than in compression. Calculations using the original and modified MDCF model formulations for shear-induced damage stress measures are provided in Chapter 6.0 that further illustrate the significance of this term.

5.7 PROPOSED TEST MATRIX

The original laboratory test matrix proposed by Nieland et al. [1999] included a total of 37 tests. The types of tests proposed were chosen based on two criteria: (1) they had to be
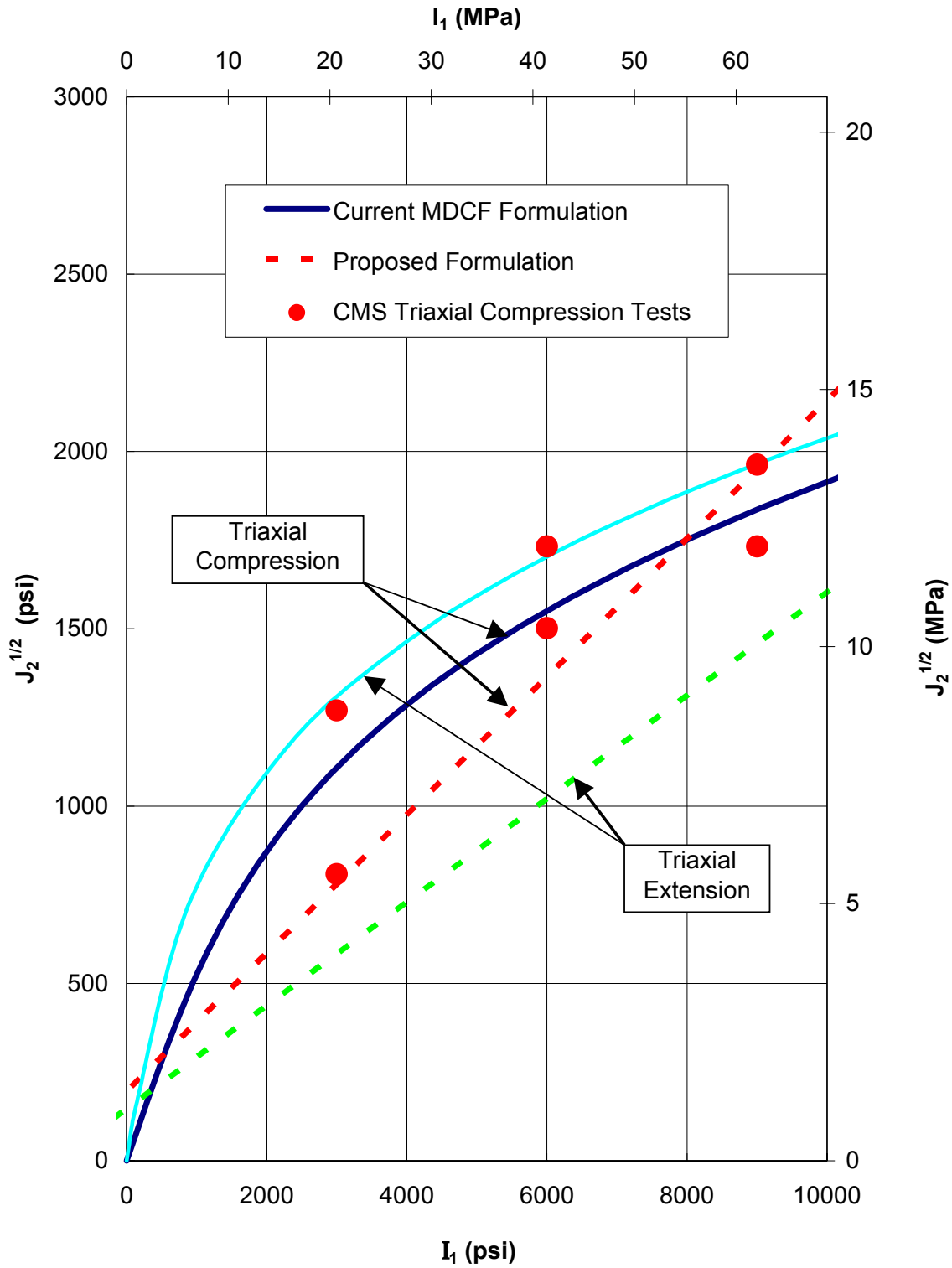
Figure 5-7. Illustration of Dilation Boundaries at Triaxial Extension and Triaxial Compression Stress States Using an Alternative Formulation for the Power-Conjugate Effective Stress Measure for Shear-Induced Damage.

conventional tests that most laboratories could perform and (2) they had to incorporate load paths where at least some of the constitutive model parameters displayed high sensitivity coefficients. Five types of tests were proposed: (1) nine constant stress creep tests, (2) six constant mean stress tests, (3) six constant strain rate tests, (4) six hydrostatic compression tests and (5) ten mineralogic analyses tests. A goal of this project was to determine if the proposed test matrix was adequate for determining the free parameters of the MDCF model. Experience gained in performing this project has provided a better understanding of the type of tests that proved to be the most beneficial. Based on the results of this project, it is recommended that the original test matrix be modified as discussed below.

The ability to quantify healing using conventional laboratory testing machines was found to be a formidable task. It is believed that an extensive research project, possibly utilizing specialized equipment, is required to obtain the understanding necessary to include the benefit of healing as part of the geomechanical studies of CNG storage caverns. An alternative and conservative approach used in this study is to assume that healing will not occur during storage operation. If this approach is taken, the six hydrostatic compression tests proposed by Nieland et al. [1999] do not have to be performed.

Two free parameters that define the damage stress dependency (n_3 and c_2) of the damage strain rate equation could not be determined from the data collected during the laboratory testing task. To determine these parameters, it is recommended that two of the creep tests performed at moderate confining pressures be extended to include additional stages wherein the shear stress remains constant but the damage stress measure is increased. It is recommended that a similar test be added to the test matrix to provide additional data for evaluating these parameters.

Because this project represents a first-time application of the approach to determine parameter estimates for the MDCF model, more tests were performed than identified in the original test matrix proposed by Nieland et al. [1999]. Many of these tests were performed for the model refinement task to provide information regarding the behavior of salt during healing, recovery, and at stress states other than triaxial compression. The minimum number of tests recommended to determine parameter values for the MDCF model and material properties for analyzing CNG storage caverns is provided in Table 5-2. Additional testing may be warranted to increase confidence in characterizing the salt behavior if large variations are observed for the redundant tests. The proposed test matrix consists of 35 mechanical properties tests. Differences between the original test matrix proposed by Nieland et al. [1999] and that given in Table 5-2 include: (1) addition of one constant stress creep tests, (2) identification of multiple-stage creep tests, and (3) removal of the hydrostatic healing tests. Ten mineralogic analysis tests are also recommended to determine the chemical and mineralogical composition of the salt.

Table 5-2. Proposed Constant Temperature Test Matrix

Test Type	Quantity	Stress Conditions		
		$\Delta\sigma$	σ_3	σ_m
Quasi-Static Triaxial Compression	6		Unconfined	
	2		Low	
	2		Medium	
	2		High	
Constant Mean Stress Triaxial Compression	2			Low
	2			Medium
	2			High
Constant Stress Triaxial Compression Creep	1	Low	Very Low	
	1	Medium	Very Low	
	1	Medium	Low	
	1 (Multiple Stage)	Medium	Medium Low Very Low	
	1	High	Very Low	
	1	High	Low	
	2 (Multiple Stage)	High	Medium Low Very Low	
	1	Low	High	
	1 (Multiple Stage)	Medium Low	High	
	1 (Multiple Stage)	High Medium	High	
Brazilian	6			

(1) The shaded tests are run to determine parameters that describe damage.

(2) Examples of high, medium, low, and very low confining pressures (σ_3) for McIntosh salt are 27.6, 3.4, 2.07, and 0.7 MPa, respectively.

6.0 CAVERN ANALYSES

Geomechanical modeling was used to predict cavern stability and performance during development and under various operating scenarios during natural gas storage for two Bay Gas Storage caverns. The information obtained from the site investigation was incorporated into finite element models that are representative of the caverns and their surroundings. The allowable minimum operating pressure was established from the numerical simulations based on the salt damage criterion using the MDCF model [DeVries et al., 1998] and the stress-based criterion commonly used for design of natural gas storage caverns [Ratigan et al., 1993]. This chapter provides a brief description of the technical approach used to analyze the response of the caverns and present selected results. Results include the minimum allowable gas pressures determined using the salt damage criterion, minimum gas pressures determined using a stress-based criterion, associated cavern closure histories for typical natural gas service cycles, and working gas capacity of the caverns. Gas pressures reported in this chapter are pressures at the casing shoe, unless stated otherwise.

The formulation of the MDCF model used for all the calculations includes the new recovery and healing formulations; however, the healing term was made inoperative for the calculations. To assess the significance of the power-conjugate equivalent stress measures for shear-induced damage, calculations were performed using the *original* and *modified* formulations (see Chapter 4.0, Section 4.2). Calculations using the original formulation used the complete set of parameter estimates determined from the parameter evaluation task described in Chapter 5.0. Calculations using the modified formulation used the same parameter estimates as the original formulation with the exception of those parameters necessary to define the stress measures as discussed in Chapter 5.0, Section 5.6.

6.1 PROBLEM DESCRIPTION

The gas pressure in a solution-mined cavern helps support the geological loads acting on the salt surrounding the cavern. As the gas pressure decreases, the loads that must be supported by the surrounding salt increase. If the loads in the salt exceed the strength of the salt, the salt will microfracture (damage or dilate) and lose strength. Numerical simulations were performed using the geometrical, geological, and material properties discussed in Chapters 2.0 and 5.0 of this report. For the simulations of the storage caverns, SPECTROM-32 was used to model the following stages of cavern development and operation:

- Cavern excavation by solutioning

- Cavern dewatering

- Natural gas service cycles determined in concert with Bay Gas.

6.1.1 Gas Service Cycles

The gas service cycle used for this study is a cycle similar to that experienced by Bay Gas Well No. 1 during the first 6 years of service (see Figure 6-1). This annual service cycle was approximated by assuming a linear pressure decrease from maximum pressure to minimum pressure during a 150-day withdrawal period. Injection of the cavern back to maximum pressure was simulated to occur at a constant rate for 215 days. The maximum gas pressure specified for the caverns was 22.7 MPa (3,290 psi) or about 0.82 psi/foot at the casing shoe. Simulations were performed using minimum gas pressures of 10.2, 5.5, 2.8, and 0 MPa (1,470, 800, 400, and 0 psi) to provide four different annual gas cycles for evaluating cavern performance. The simulation using a minimum gas pressure of 10.2 MPa (1,470 psi) was used to represent the gas service cycle currently used by Bay Gas. The other minimum gas pressures (5.5, 2.8, and 0 MPa) were arbitrarily selected to provide a range in pressures for evaluating cavern response. The annual gas service cycles were repeated ten times during each cavern analysis to provide estimates for: (1) damage accumulation and (2) closure rates of the caverns for each gas service cycle over a 10-year period.

6.1.2 Criteria Used to Evaluate Minimum Gas Pressure

The MDCF model was formulated such that damage produces a softening effect as proposed by Kachanov [1958]. The Kachanov damage variable reduces the load-bearing capacity through a reduction in the effective area using a continuum damage mechanics approach. For the MDCF model, the Kachanov damage variable (ω) is determined from an evolutionary equation (Appendix E, Equation E-22) and provides a scalar measure for the level of damage. In addition to the damage state variable, damage is quantified through the model's prediction of dilatant volumetric strain. Either one or both of these variables can be used as a design constraint for assessing cavern stability; however, DeVries et al. [1998] have proposed a critical damage value of 0.0025 as a conservative estimate for material damage that does not greatly influence the structural integrity of salt for evaluating CNG storage caverns. This critical damage value was maintained in this study as the design criterion for assessing cavern stability. Values of the damage less than 0.0025 indicate that the salt will remain stable; whereas, a value of damage at any location exceeding 0.0025 indicates that the stability of the cavern may be jeopardized.

The objective of this project was to determine the operating pressure range for a given gas service cycle that satisfies the damage-based criterion. The original thinking was that any damage accumulated while the cavern was at minimum pressure would heal during the time that the cavern was at pressures sufficient to reverse the damage process. Thus minor excursions of the salt into the dilation regime could be allowed without comprising cavern stability. The extent of these excursions would be subject to the constraint that the damage could not exceed a value of 0.0025 at any time during the simulation of the gas service cycle.
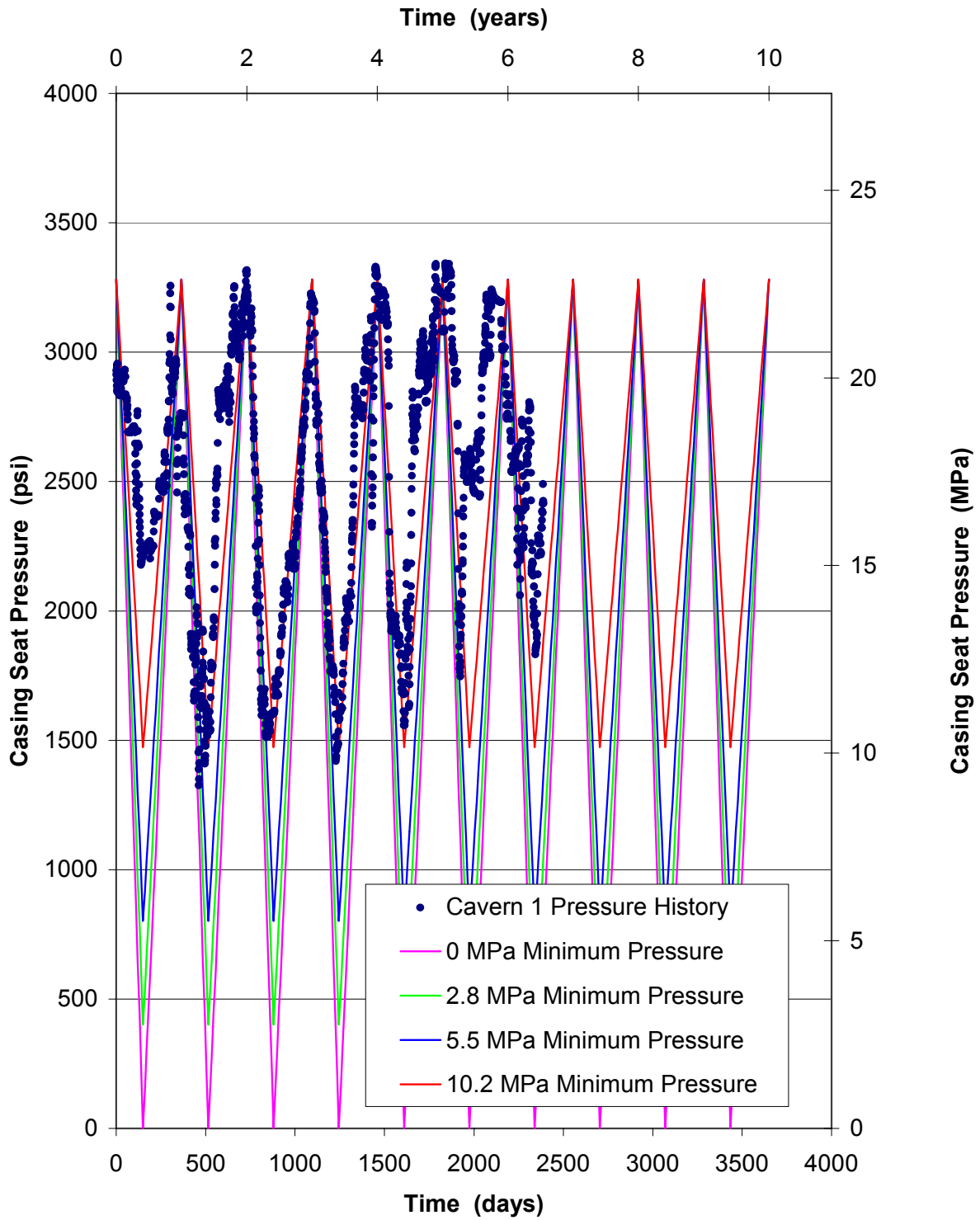
Figure 6-1. Bay Gas Well No. 1 and Well No. 2 Simulated Gas Service Pressure Cycles.

Because of the uncertainty in measuring the healing of damaged salt, it was decided not to take into account the benefit of salt healing until a better understanding of damage healing is obtained. Conservative results are produced by neglecting the beneficial healing effects.

An alternative approach used to determine the minimum gas pressure for the caverns was to assess the rate of damage accumulation assuming different minimum gas pressures. Using this approach, the minimum life expectancy of the caverns could be approximated based on the conservative estimate of 0.0025 for the damage variable. The results are considered conservative because the mechanical strength of salt does not decrease significantly until the onset of tertiary creep. Chan et al. [1996c; 1997] have proposed using 0.015 as the critical value for the damage variable as an indicator for the onset of tertiary creep. This value is significantly greater than the design criterion of 0.0025 used in this study and significantly lower than the value of 0.15 proposed by Chan et al. [1996c; 1997] for creep rupture.

In addition to using the MDCF model to determine the minimum allowable gas pressure for the Bay Gas caverns, a stress-based criterion referred to as the Damage Potential method was utilized for comparative purposes. Thus changes or improvements in cavern working gas capacity can be assessed for the new damage-based stability criterion. Damage Potential is defined as the ratio of $\sqrt{J_2}$ to I_1. A Damage Potential of 0.27 has been found to be the limiting stress state for dilation to occur in other Gulf Coast salts [Van Sambeek et al., 1993]. Dilation is expected to increase with increasing damage potential values. On the other hand, dilation is not expected when the damage potential is less than 0.27. A damage potential of 0.27 was used in this study as the limiting stress state for determining minimum gas pressure.

6.2 MINIMUM GAS PRESSURE BASED ON THE DAMAGE POTENTIAL METHOD

When the stress-based criterion is used to determine the minimum acceptable gas pressure for cavern stability, the common practice is to ensure that none of the salt surrounding the cavern experiences dilation. Salt dilation can be eliminated by maintaining an appropriate cavern pressure. To determine the appropriate cavern pressure using the stress-based criterion, the potential for salt dilation was evaluated as the cavern pressure decreases from maximum pressure to zero. The minimum allowable gas pressure was determined based on the pressure in the cavern when dilation of the salt was first observed. Figure 6-2 shows the volume of salt surrounding the caverns that exceeds the damage potential value of 0.27 as gas is withdrawn. *The minimum gas pressures necessary to satisfy the stress-based stability criterion for Bay Gas Well No. 1 and Bay Gas Well No. 2 are 8.3 and 6.9 MPa (1,200 and 1,000 psi), respectively.* These pressures correspond to pressures of 0.30 and 0.25 psi/foot depth at the casing shoe of the caverns.
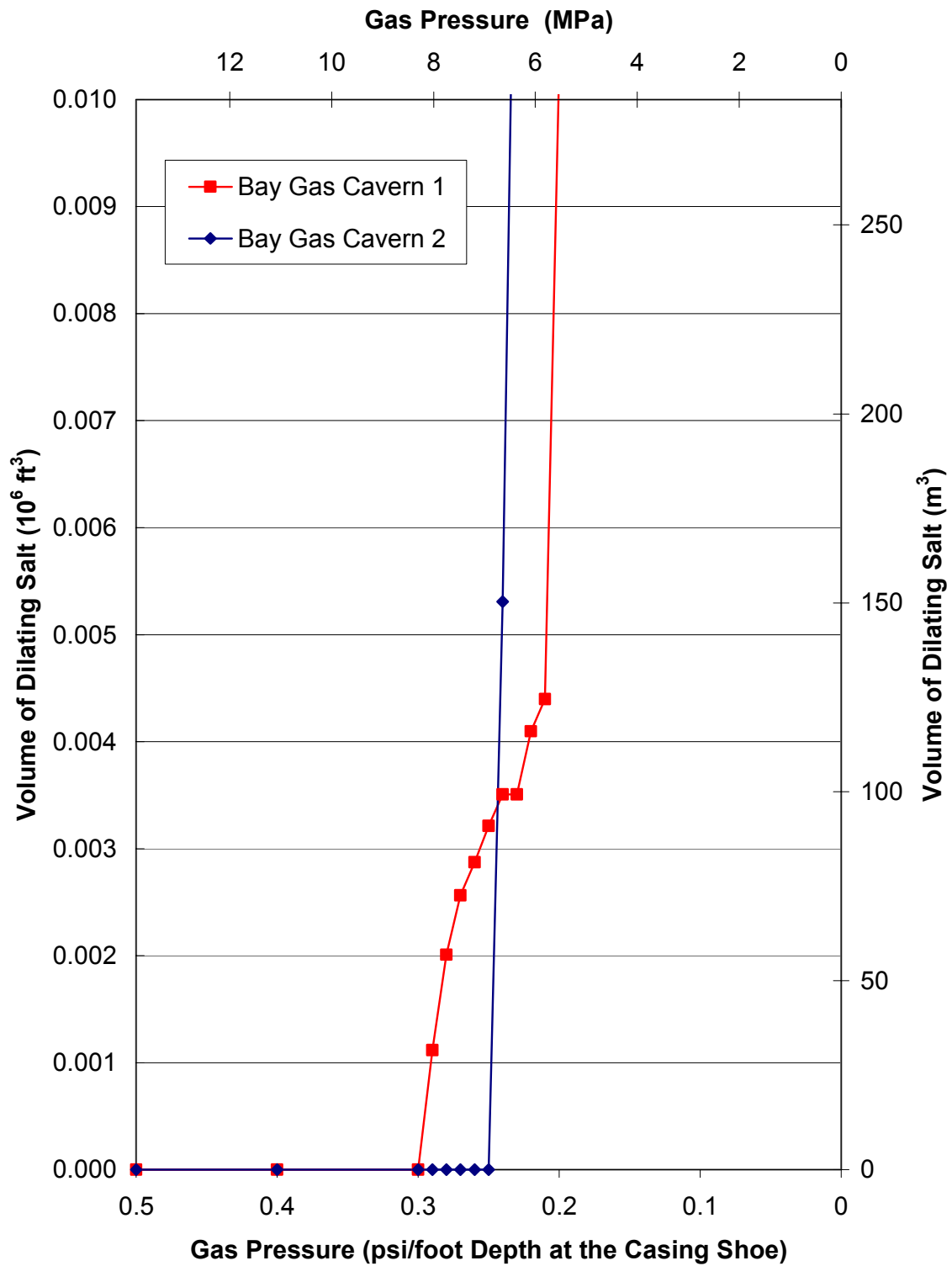
Figure 6-2. Volume of Dilating Salt Versus Gas Pressure Based on the Stress-Based Criterion.

6.3 MINIMUM GAS PRESSURE BASED ON THE CONTINUUM DAMAGE CRITERION

The minimum gas pressures for the Bay Gas caverns were assessed using both the original and alternative formulations for the power-conjugate equivalent stress measures for shear-induced damage (see Section 4.2). Results of these analyses are discussed in separate sections below.

6.3.1 Minimum Gas Pressure Based on Original MDCF Model Formulation

The results presented in this section were obtained using the original formulation of the MDCF model for the power-conjugate equivalent stress measures for shear-induced damage. This formulation of the model is not believed to be conservative for determining minimum gas pressure because it predicts salt to be stronger in triaxial extension than triaxial compression states of stress. Figure 6-3 shows the history of the damage variable at a point on the surface of Bay Gas Well No. 1 for the different minimum gas pressures investigated. The values provided in Figure 6-3 are given at the point where the maximum damage occurs in the salt around Bay Gas Well No. 1. As shown in Figure 6-3, the damage variable remains essentially unchanged throughout the 10 years simulated for the calculation that used minimum gas pressures of 5.5 and 2.8 MPa (800 and 400 psi) but exceeds the design limit during the first annual cycle for the calculation that simulated complete depressurization of the cavern. Results of the calculation performed based on the gas service cycle similar to that currently used by Bay Gas for Well No. 1 (minimum pressure of 10.2 MPa) is not shown in Figure 6-3 because no damage was predicted to occur in the salt during this simulation.

Figure 6-4 is similar to Figure 6-3 except results are provided for Bay Gas Well No. 2. The results for the two caverns are similar with only slightly lower damage values predicted for Well No. 2 during the first few gas service cycles of the calculation simulating a minimum gas pressure of 0 MPa. However, by the end of ten cycles, the maximum value for the damage variable is greater in the salt around Well No. 2 ($\omega = 0.030$) than Well No. 1 ($\omega = 0.028$). *Based on these results, a minimum gas pressure of 2.8 MPa (400 psi) is permissible in the Bay Gas caverns.*

6.3.2 Minimum Gas Pressure Based on Modified MDCF Model Formulation

Simulations of the Bay Gas Well No. 1 and Well No. 2 were performed with minimum gas pressures of 2.8 and 5.5 MPa (400 and 800 psi) using the alternative or modified formulation for the effective stress measures to shear-induced damage and flow. Figure 6-5 compares the history of the damage variable at a point on the surface of Bay Gas Well No. 2 using the pressure cycle with a minimum gas pressure of 2.8 MPa (400 psi). As previously shown, the damage variable is essentially unchanged throughout the simulation using the original formulation of the MDCF model; however, the design limit is exceeded within the first year assuming the modified stress measure formulation. *Based on these results, the behavior of salt*
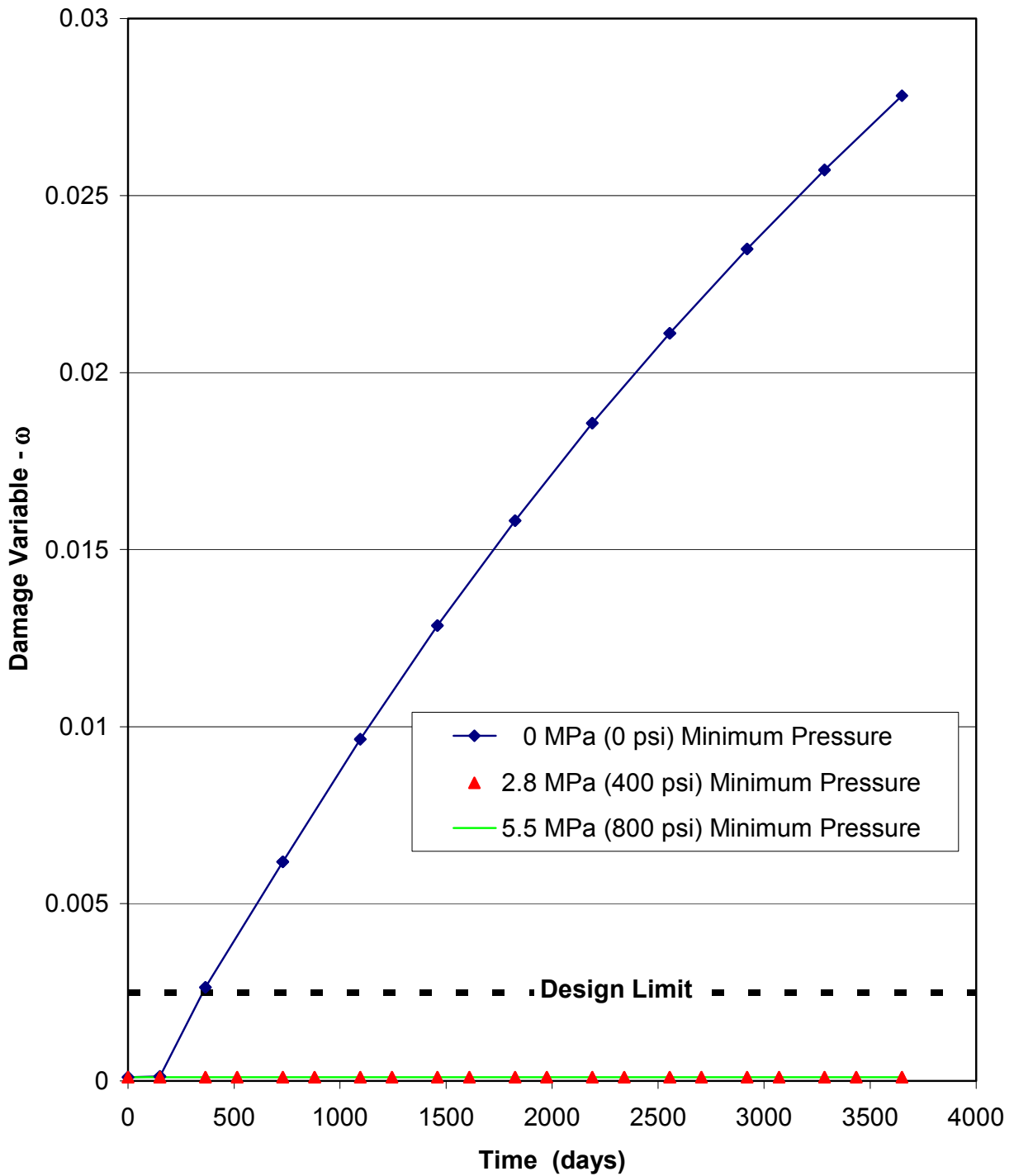
Figure 6-3. MDCF Damage State Variable Predicted During the Simulations of Bay Gas Well No. 1.
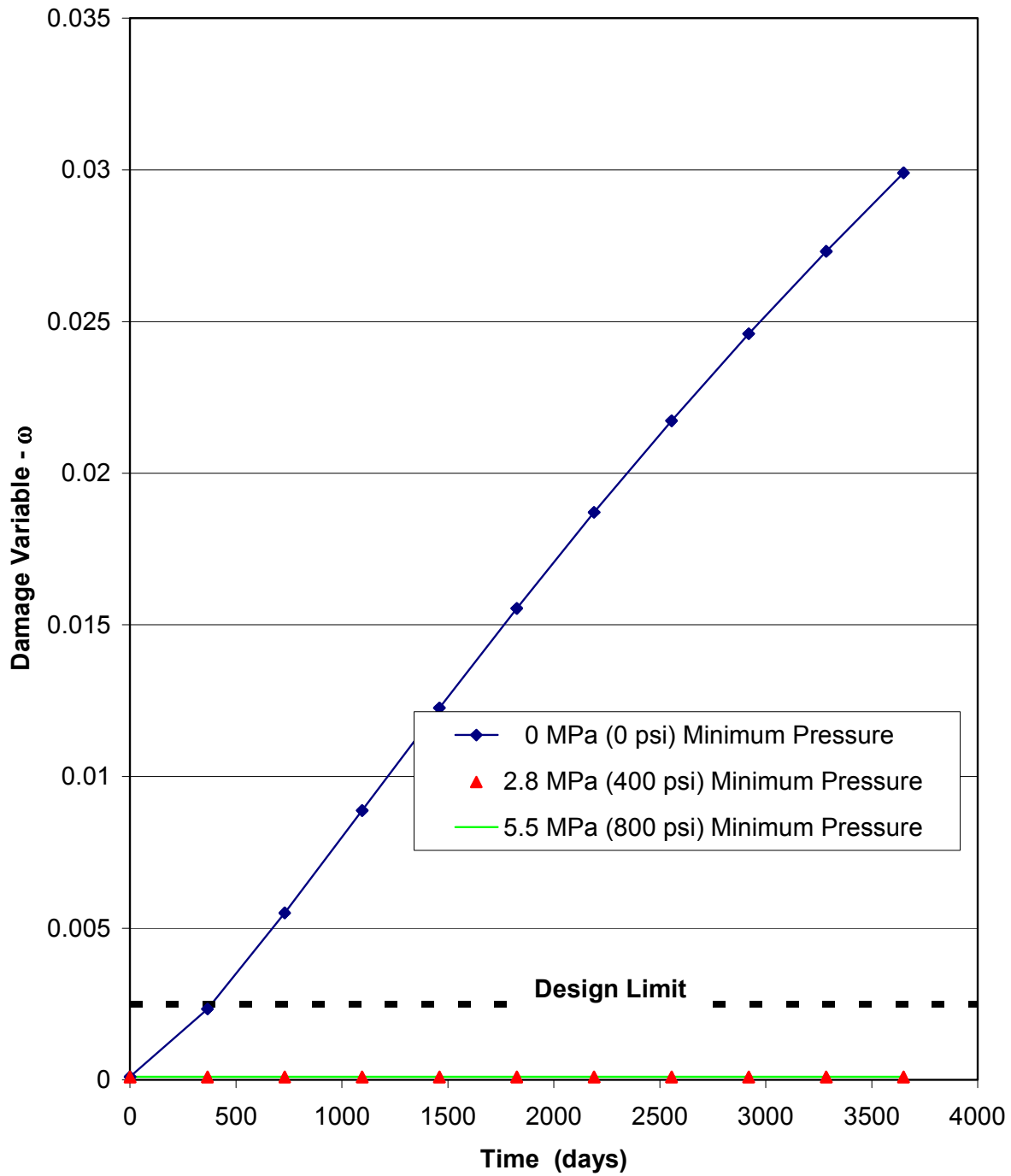
Figure 6-**4.** MDCF Damage State Variable Predicted During the Simulations of Bay Gas Well No. 2.
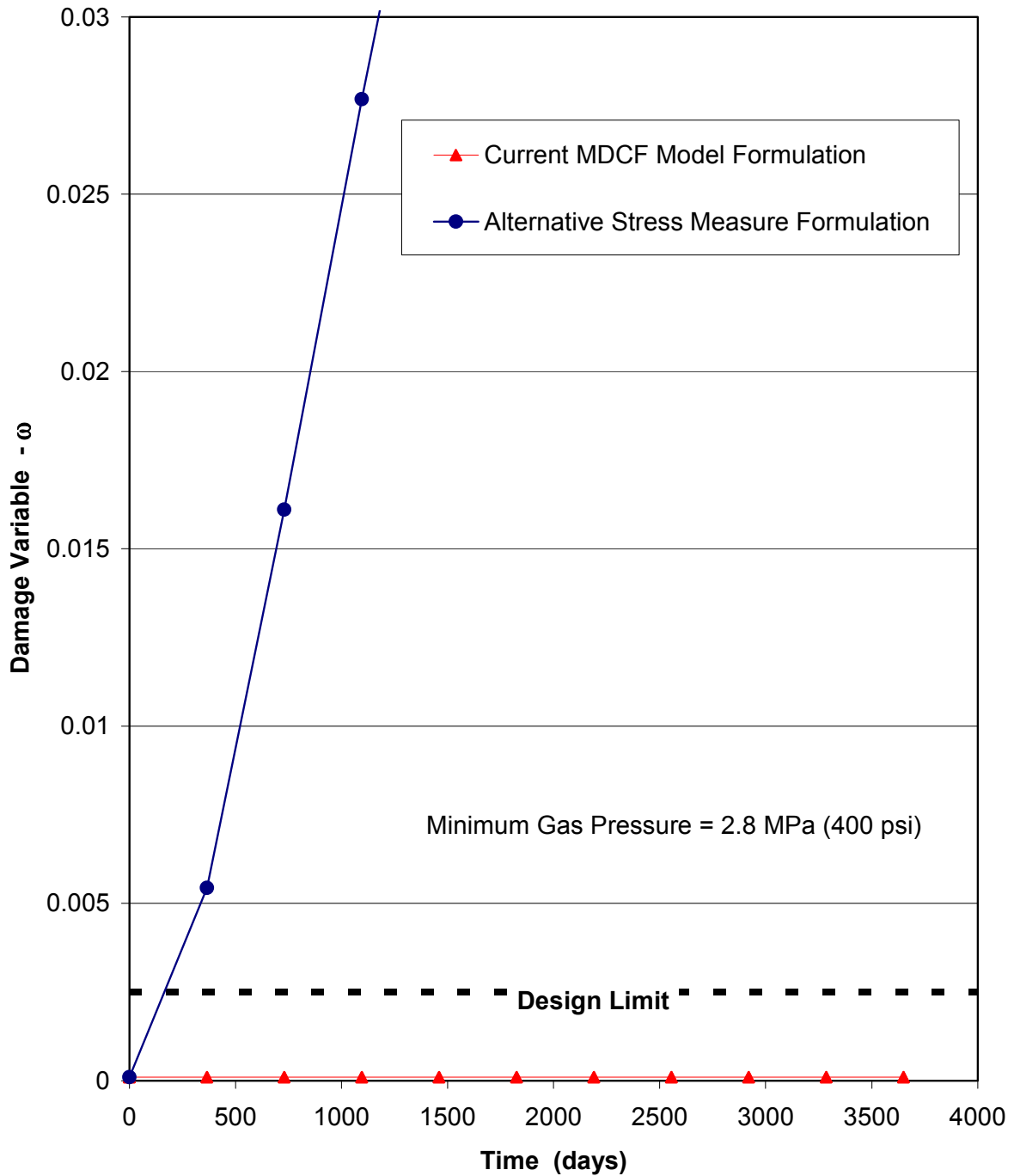
Figure 6-5. MDCF Damage State Variable Predicted in the Salt Surrounding Bay Gas Well No. 2 Using the Current and Alternative Formulations for the Power-Conjugate Effective Stress Measure for Shear-Induced Damage.

at stress conditions other than triaxial compression is extremely important in assessing cavern stability and warrants additional study.

Figure 6-6 shows the history of the damage variables at points on the surfaces of Bay Gas Well No. 1 and Well No. 2 for minimum gas pressures of 2.8 and 5.5 MPa (400 and 800 psi). Although damage does not accumulate as rapidly at a minimum pressure of 2.8 MPa (400 psi) for Well No. 1 compared to Well No. 2, the damage criterion is exceeded for both caverns during the 10-year simulation. A very small amount of damage was predicted to occur in both caverns during the 10-year simulation period assuming the 5.5 MPa (800 psi) minimum gas pressure cycle. However, the damage variable remains essentially unchanged throughout the simulation indicating the cavern will remain stable for the cycle with a minimum gas pressure of 5.5 MPa (800 psi). The 5.5 MPa (800 psi) pressure corresponds to pressures of 0.20 psi/foot depth at the casing shoe of the caverns.

6.4 RECOMMENDED MINIMUM GAS PRESSURE

Salt is weaker in triaxial extension than triaxial compression states of stress. The original formulation of the MDCF model does not capture this aspect of salt behavior. Therefore, the minimum gas pressure of 2.8 MPa (400 psi) determined for the Bay Gas caverns using the original MDCF model formulation may not provide a conservative estimate for the minimum allowable gas pressure that prevents excessive dilation of the salt. The alternative stress measures developed during this study predicts salt is weaker in extension than compression. This aspect of rock behavior was found to be extremely important for assessing cavern stability. Numerical calculations using the alternative stress measures developed during this study predicted that a minimum gas pressure of about 5.5 MPa (800 psi) is necessary to prevent excessive dilation within the salt surrounding the Bay Gas caverns. Parameter estimates that define the alternative effective stress measures for shear-induced damage and flow were determined from tests performed solely at triaxial compression states of stress; however, the assumed values are expected to yield conservative results. Without additional investigation into the behavior of salt at stress conditions other than triaxial compression, a more accurate prediction for the minimum allowable gas pressure cannot be made. Therefore, the more conservative results obtained using the alternative effective stress measures are recommended for the minimum gas pressures of the Bay Gas caverns. ***Based on these results for cavern stability, the minimum allowable pressure recommended for the two Bay Gas caverns is 5.5 MPa (800 psi).***

6.5 CAVERN CLOSURE

The closure rate of the Bay Gas caverns will depend not only on the minimum gas pressure, but also on how the pressure is cycled between the minimum and maximum gas pressures. The
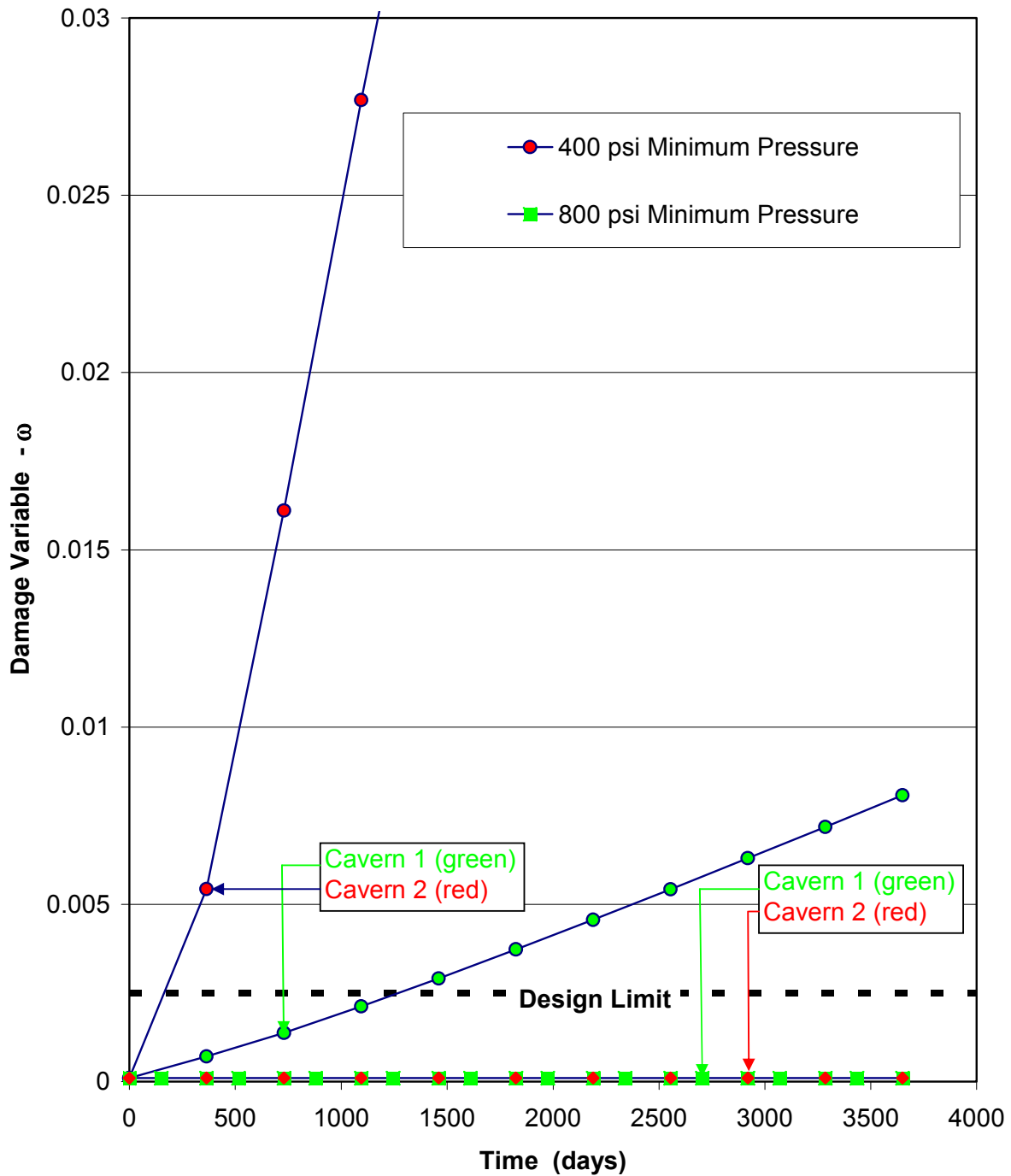
Figure 6-6. MDCF Damage State Variable Predicted in the Salt Surrounding Bay Gas Well No. 1 and No. 2 Using the Alternative Formulations for the Power-Conjugate Effective Stress Measure for Shear-Induced Damage.

75

cavern closure rate depends strongly on the difference between the salt stress and the internal cavern pressure. This difference is smaller during gas storage at maximum pressure than at low pressure conditions. In this study, the annual gas pressure cycles shown in Figure 6-1 were used to compute the volumetric closure rates of the two Bay Gas caverns. The 10-year closure history and annual closure rates were predicted for the four different minimum gas pressures identified in Figure 6-1: 10.2 MPa, 5.5 MPa, 2.8 MPa, and 0 MPa (1,470, 800, 400, and 0 psi).

Figures 6-7 and 6-8 present the cumulative closure history of Bay Gas Well No. 1 and Well No. 2, respectively, for the four gas service cycles using different minimum gas pressures. As illustrated in these figures, the influence of minimum gas pressure on the cumulative closure of the cavern is substantial. Assuming a minimum gas pressure of 10.2 MPa (1,470 psi), the closure after 10 years of service for Bay Gas Well No. 1 is approximately 11 percent. Reducing the minimum gas pressure to 5.5 MPa (800 psi) more than doubles the cumulative closure at 10 years with the predicted results being approximately 23 percent. Minimum gas pressures of 2.8 MPa (400 psi) and 0 MPa (0 psi) resulted in 10-year cumulative closures of about 33 and 45 percent, respectively, for Bay Gas Well No. 1.

The closure results of Bay Gas Well No. 2 are slightly less than Bay Gas Well No. 1. The 10-year cumulative closure of Bay Gas Well No. 2 is slightly more than 8 percent, assuming a minimum gas pressure of 10.2 MPa (1,470 psi), compared to 11 percent for Bay Gas Well No. 1. The faster closure rate of Bay Gas Well No. 1 is likely attributable to closure near the bottom of the cavern, which is at a lower elevation than the bottom of Bay Gas Well No. 2. The simulated bottom of Bay Gas Well No. 1 is approximately 1,615 meters (5,300 feet) compared to 1,524 meters (5,000 feet) for Bay Gas Well No. 2.

Predicted annual volumetric closure rates for Bay Gas Well No. 1 and Bay Gas Well No. 2 are provided in Tables 6-1 and 6-2, respectively. Closure rates were determined based on the incremental closure during each year of the 10-year simulation periods. Average closure rates are provided during the 1st, 2nd, 3rd, 5th, and 10th year of operation for both caverns for the four gas service cycles identified in Figure 6-1. Closure rate is based on the original cavern volume. The closure rates are greatest during the first year of the simulations and decrease every year thereafter. At the end of the 10-year simulation period, the annual closure rate appears to have reached a nearly constant value and would be expected to remain at this rate if the annual pressure cycle were repeated. This behavior is typical of caverns in salt and is indicative of the transient creep response of salt and stress redistribution within the formation resulting from cavern construction and operation.
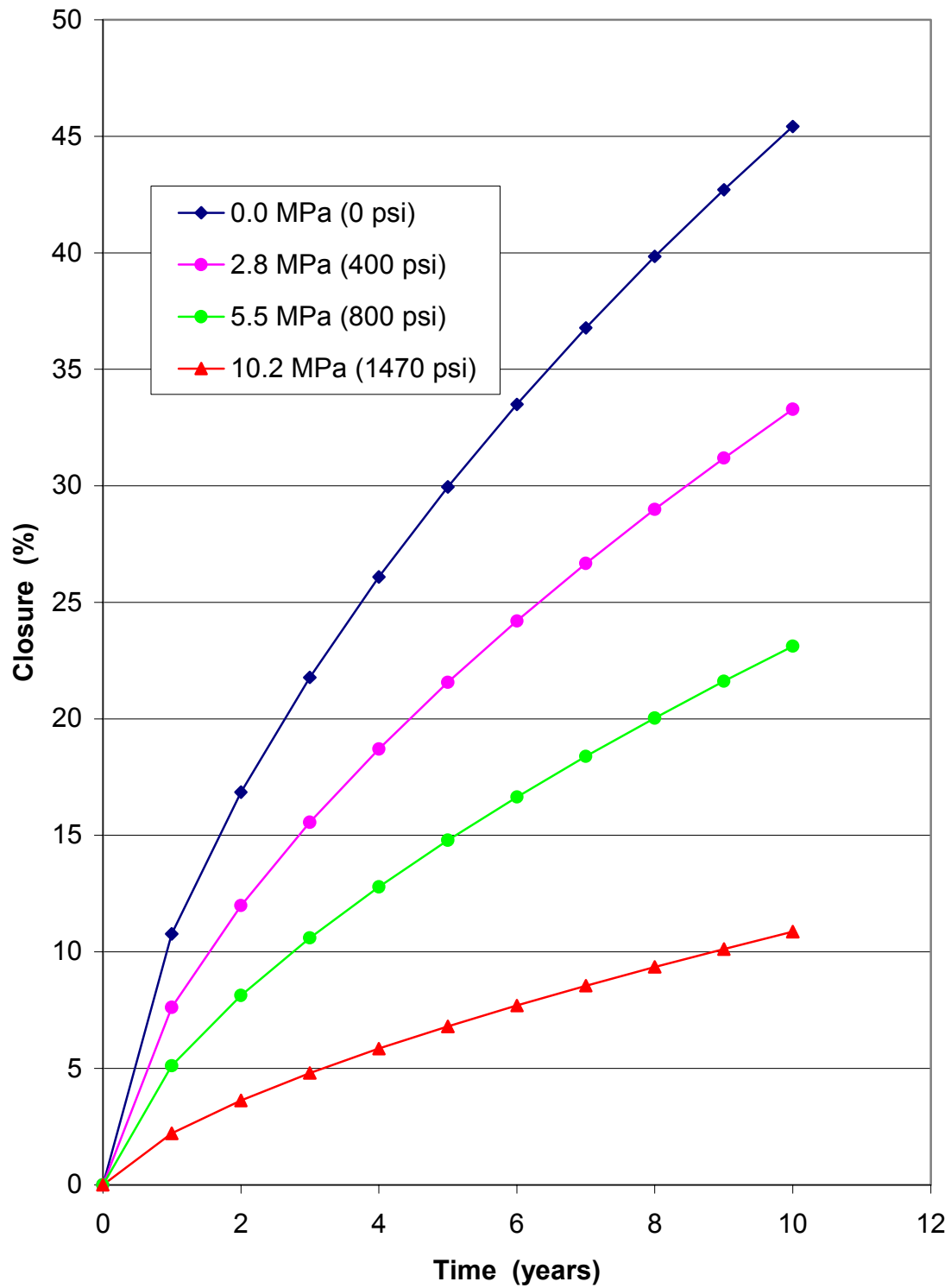
Figure 6-**7.** Predicted Closure History of Bay Gas Well No. 1 Assuming Different Minimum Gas Pressures.
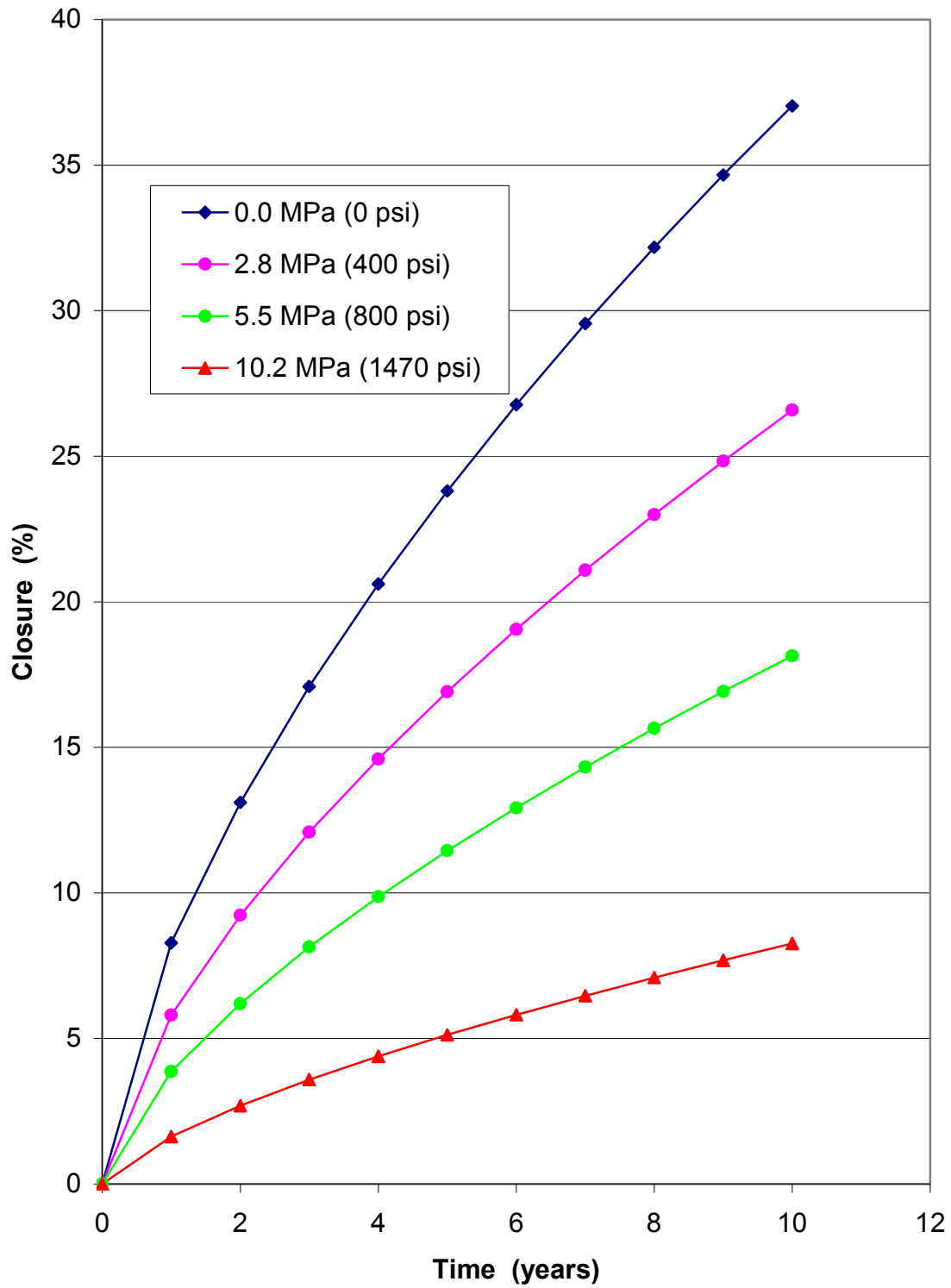
Figure 6-8. Predicted Closure History of Bay Gas Well No. 2 Assuming Different Minimum Gas Pressures.

Table 6-1. Volumetric Closure Rates of Bay Gas Well No. 1[a]

Closure Period	Minimum Pressure During Annual Cycle			
	0 MPa (0 psi)	2.8 MPa (400 psi)	5.5 MPa (800 psi)	10.2 MPa (1,470 psi)
1st Year	10.7	7.6	5.1	2.2
2nd Year	6.1	4.4	3.0	1.4
3rd Year	4.9	3.6	2.5	1.2
5th Year	3.9	2.9	2.0	1.0
10th Year	2.7	2.1	1.5	0.7

(a) Volumetric closure rates given as a percent of original cavern volume per year.

Table 6-2. Volumetric Closure Rates of Bay Gas Well No. 2[a]

Closure Period	Minimum Pressure During Annual Cycle			
	0 MPa (0 psi)	2.8 MPa (400 psi)	5.5 MPa (800 psi)	10.2 MPa (1,470 psi)
1st Year	8.3	5.8	3.9	1.6
2nd Year	4.8	3.4	2.3	1.1
3rd Year	4.0	2.8	1.9	0.9
5th Year	3.2	2.3	1.6	0.7
10th Year	2.4	1.8	1.2	0.6

(a) Volumetric closure rates given as a percent of original cavern volume per year.

6.6 WORKING GAS CAPACITY

The economics of CNG storage in salt caverns are largely dependent on maximizing the ratio between the working gas and the cushion gas volumes. This ratio depends directly on the values of the maximum and minimum gas pressures permitted in the storage cavern. An equation of state given by Coker [1993] relating a fluid's pressure to its density and temperature was assumed for natural gas to determine estimates for the working gas capacity of the Bay Gas caverns at different minimum gas pressures. The initial working gas capacities[2]

---

[2] Natural gas quantities are expressed in terms of normal cubic meters (Nm^3) with reference conditions of 0°C and 0.101325 MPa and in terms of standard cubic feet (cf) with reference conditions of 60°F and 14.73 psi. Gas-related computations were made assuming a gas composition of 100 percent methane.

of Bay Gas Well No. 1 and Bay Gas Well No. 2, based on the minimum gas pressures determined using the stress-based criterion of 8.3 and 6.9 MPa, are 0.58×10^8 Nm^3 and 1.01×10^8 Nm^3 (2.2 and 3.8 billion cubic feet (Bcf)), respectively.

Initial working gas capacities determined for Bay Gas Well No. 1 are 0.50×10^8, 0.69×10^8, and 0.80×10^8 Nm^3 (1.8, 2.6, and 3.0 Bcf), assuming minimum pressures of 10.2, 5.5, and 2.8 MPa (1,470, 800, and 400 psi), respectively. Similarly, the initial working gas capacity of Bay Gas Well No. 2, assuming minimum pressures of 10.2, 5.5, and 2.8 MPa (1,470, 800, and 400 psi), are 0.78×10^8, 1.10×10^8, and 1.27×10^8 Nm^3 (2.9, 4.1, and 4.7 Bcf), respectively. Thus the 5.5 MPa (800 psi) minimum gas pressure determined using the continuum damage method results in an increase of 0.11×10^8 Nm^3 (0.4 Bcf) for Bay Gas Well No. 1 and 0.09×10^8 Nm^3 (0.3 Bcf) for Bay Gas Well No. 2. *In terms of percentages, the initial working gas capacities determined using the continuum damage approach are about 18 and 8 percent greater than those predicted using the stress-based criterion for Well No. 1 and Well No. 2, respectively.*

The working gas capacity of the caverns is directly proportional to the volume of the caverns. Because creep of salt reduces the volume of the caverns with time, the rate of change of the working gas capacity of the caverns depends on the minimum gas pressure. Figure 6-9 provides estimates of the working gas capacity as a function of time for Bay Gas Well No. 1 for the four different minimum gas pressures investigated. Figure 6-9 shows that Bay Gas Well No. 1 can be operated for several years at gas pressures lower than that currently used and still maintain a greater working gas capacity.

Results similar to Bay Gas Well No. 1 were determined for Bay Gas Well No. 2, as shown in Figure 6-10. *In general, the benefit of lowering the minimum gas pressure will be negated when sufficient closure of the cavern has occurred to offset the increase realized using a lower minimum gas pressure. If closure of the cavern becomes excessive, the cavern will have to be leached again to regain lost storage capacity.*

6.7 ASSESSMENT OF RECOVERY FORMULATION

As shown above, lowering the minimum gas pressure increases the working gas capacity of a CNG storage cavern. However, a reduction in the minimum gas pressure is also accompanied by higher volumetric closure rates for the cavern. During injection of natural gas, pressure in the caverns increases, which reduces the deviatoric stress in the surrounding salt. The reduction in deviatoric stress or unloading puts much of the salt surrounding the cavern into a state of recovery. Accurate predictions of volumetric closure can only be obtained if the salt material model accurately predicts the creep rate of work-hardened salt in a state of recovery. A new recovery formulation for the MDCF model was developed during this project, as discussed in Chapter 4.0. In general, the new formulation predicts McIntosh salt will reach steady state sooner than predicted by the original recovery formulation.
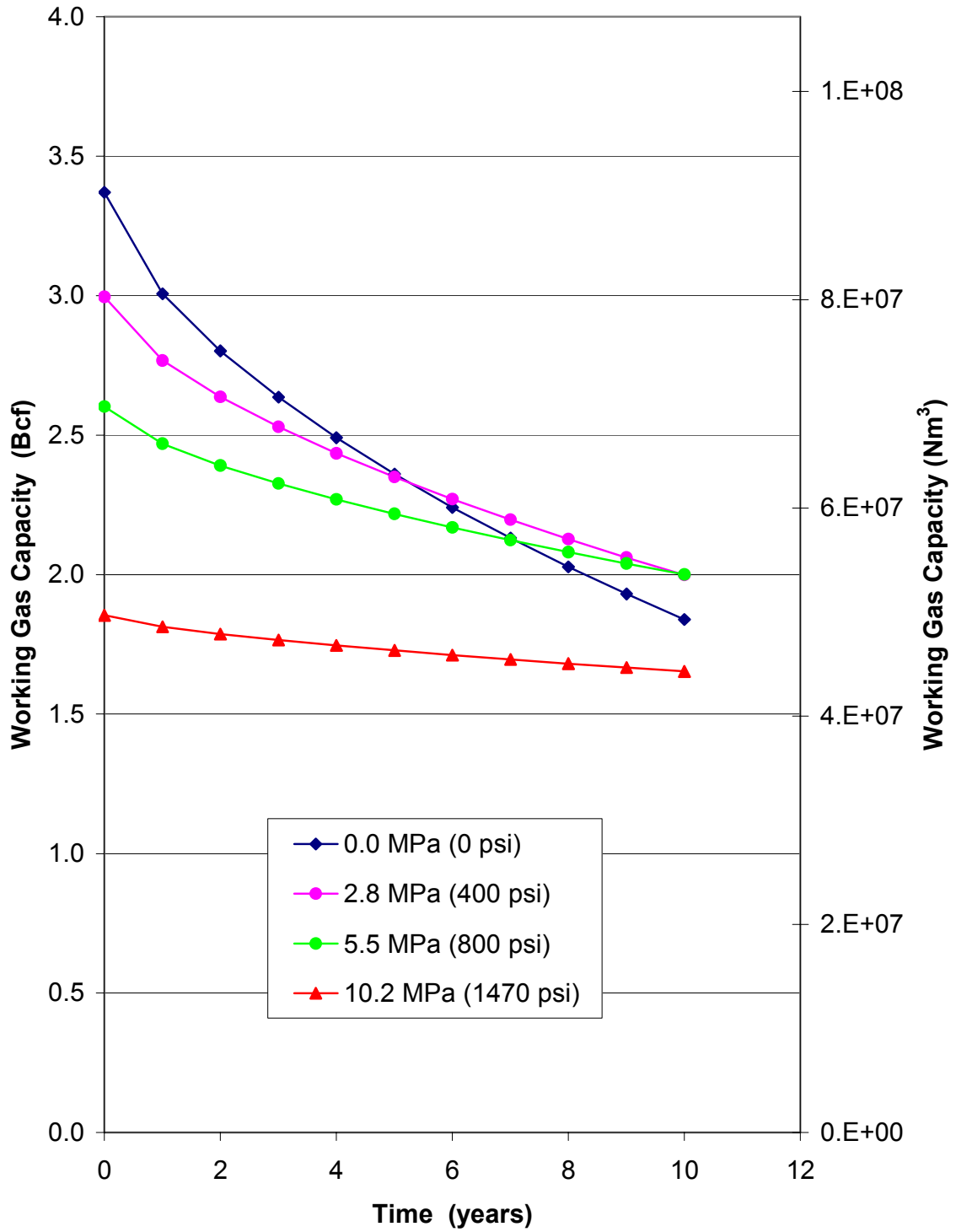
Figure 6-9. Predicted Working Gas Capacity for Bay Gas Well No. 1 Assuming Different Minimum Gas Pressures.
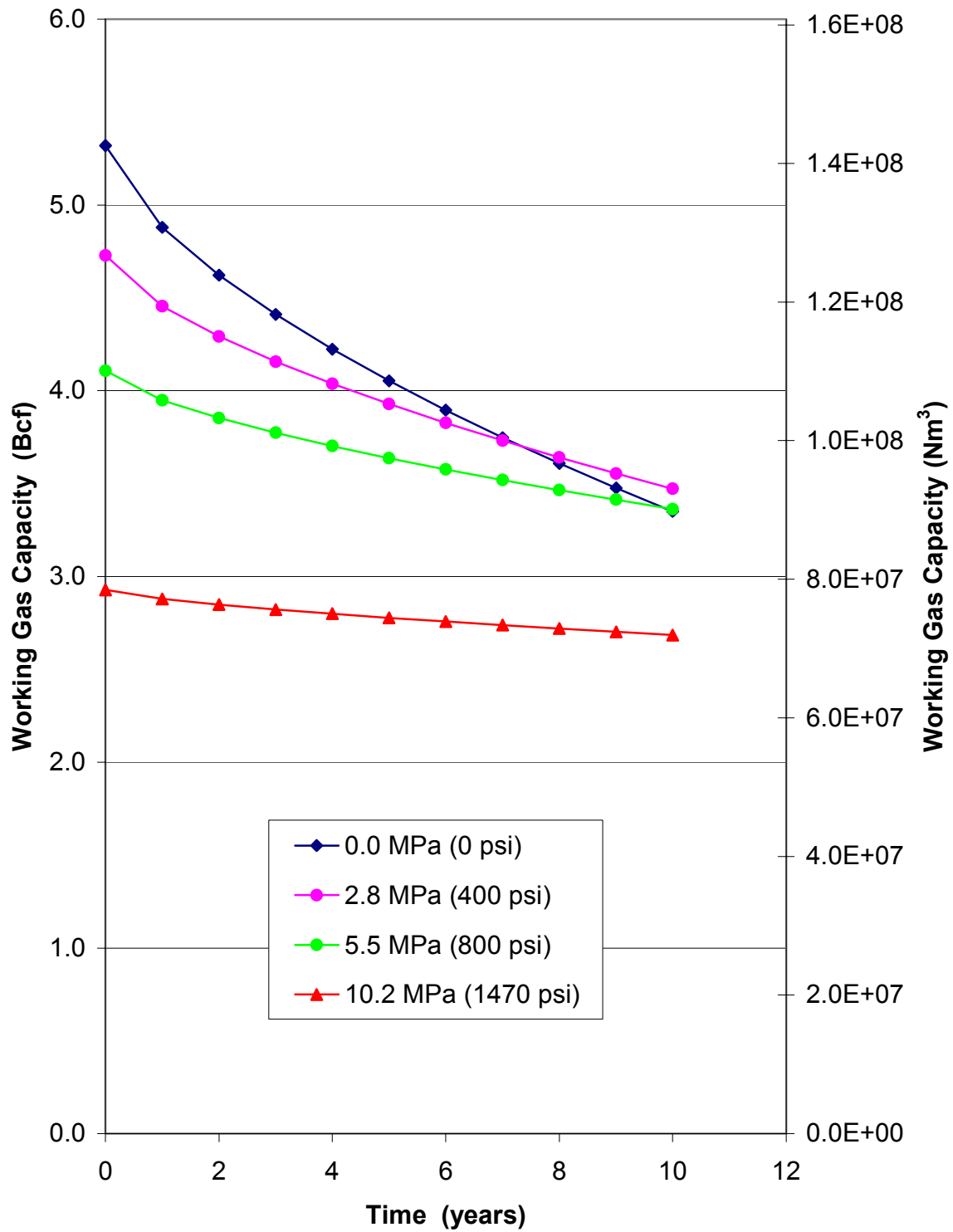
Figure 6-10. Predicted Working Gas Capacity of Bay Gas Well No. 2 Assuming Different Minimum Gas Pressures.

Figure 6-11 compares the 10-year closure history predicted for Bay Gas Well No. 2 using the original and new recovery formulations assuming the gas service cycle operates with a minimum gas pressure of 10.2 MPa (1,470 psi). Based on the original recovery formulation, closure of Bay Gas Well No. 2 is about 4.4 percent at 10 years. The predicted closure after 10 years, using the new recovery formulation developed as part of this project, is about 8.3 percent. Although additional research pertaining to the recovery of salt is recommended, the new recovery formulation is believed to provide a much improved prediction of CNG storage cavern response. This statement is supported by the loss in cavern volume obtained by comparing the 1994 and 2001 sonar data for Bay Gas Well No. 1. Closure of the cavern is estimated to be about 13 percent, based on the sonar measurements. The predicted closure using the new recovery formulation is about 10 percent during this period. Based on the results shown in Figure 6-11, substantially less closure would have been predicted than actually occurred if the old recovery formulation had been used to predict closure of Bay Gas Well No. 1.
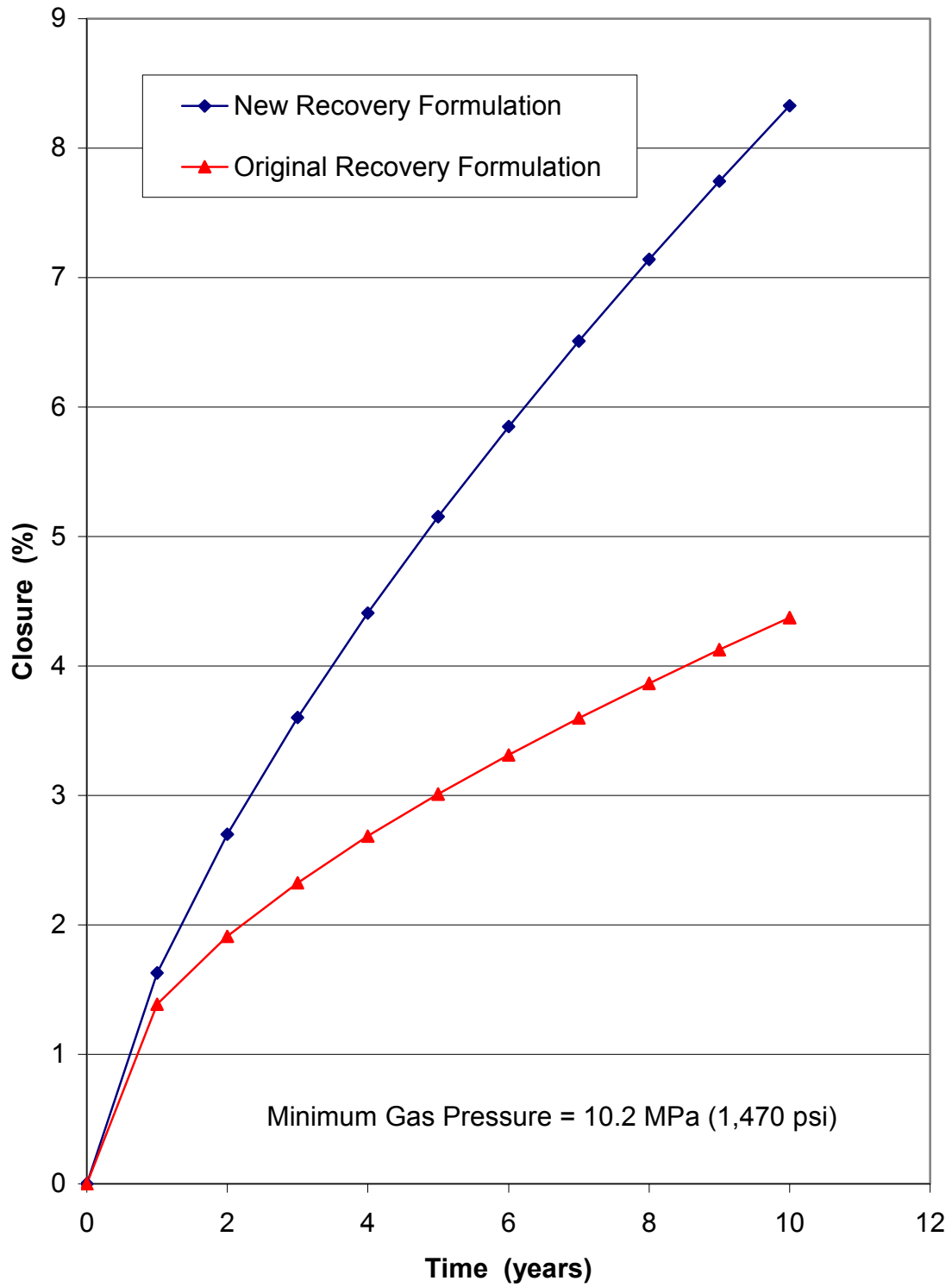
Figure 6-11. Comparison of Predicted Closure Histories of Bay Gas Well No. 2 Using the Original and New Recovery Formulations.

7.0 SUMMARY

The major goal of this research project was to answer the following two questions:

1. Is the laboratory test matrix proposed by Nieland et al. [1999] sufficient to determine all the parameter values of the MDCF model necessary to evaluate natural gas storage in salt formations?

2. Can a more advanced damage criterion for salt be demonstrated in a proof-of-concept project to produce an increase in the working gas capacity of an actual natural gas storage cavern using the salt damage criterion?

In response to the first question, two of the parameters that describe the damage strain rate stress dependency could not be determined from the proposed laboratory test matrix. The addition of one laboratory creep test and extending two creep tests to include multiple stages is necessary to evaluate these two parameters. A new test matrix was proposed as a result of this study. The proposed test matrix includes about the same number of tests as that proposed by Nieland et al. [1999]; however, more emphasis is placed on creep testing, with several of the creep tests containing multiple stages. Damage healing tests were deferred from the original test matrix because tests could not be identified that provided an appropriate quantitative measure of healing using conventional tests that most rock mechanics laboratories can perform.

The answer to the second question is yes, but requires clarification. Minimum allowable gas pressures were determined using a conventional stress-based criterion and the continuum damage mechanics approach with the MDCF model. The minimum gas pressures necessary to satisfy the stress-based stability criterion for Bay Gas Well No. 1 and Bay Gas Well No. 2 are 8.3 and 6.9 MPa (1,200 and 1,000 psi), respectively. The minimum gas pressure determined using the damage-based criterion was 5.5 MPa (800 psi) for both caverns. However, the continuum damage mechanics methodology was not completed as initially envisioned at the start of the project. Resolution of two issues was not fully realized by this project:

1. It was optimistically envisioned that the healing nature of salt could be adequately characterized such that the benefit of healing could be accounted for during the numerical calculations of the caverns. Pressure cycles could then be established that would result in complete healing of the damaged salt such that at the conclusion of the pressure cycle, the strength and behavior of the salt would be the same as that of previously undamaged salt. Conventional rock mechanics laboratory tests conducted during this study were not adequate to provide the desired level of confidence believed necessary to characterize the healing nature of salt. To overcome this problem, a more conservative approach was taken that neglects the beneficial healing effects. The criterion for determining the minimum gas pressure was to limit the level of damage throughout the expected life of the cavern.

85

2. Theoretical development of a modification to the MDCF model's damage effective stress and flow measures based on a Mohr-Coulomb type criterion was performed as part of this project. This modification was considered necessary because the original form of the MDCF model predicts salt to be stronger in triaxial extension than triaxial compression states of stress, which is contrary to the behavior of most rocks. Because much of the salt around the caverns is at or near a triaxial extension state of stress, it was determined that the original form of the model predicts less damage than would be expected. Hence, the original formulation of the MDCF model does not provide a conservative estimate for minimum gas pressure. Because of time and economic constraints, laboratory testing at stress states other than triaxial compression were limited to the completion of one successful creep test in triaxial extension. Because insufficient data are available to evaluate the parameters for the proposed effective stress measures, parameter values had to be determined based solely on triaxial compression tests. As a result, the assumptions regarding the material behavior of salt at stress states other than triaxial compression were not fully validated. Evaluation of salt behavior at different states of stress (Lode angles) was not an original objective of this study. Nonetheless, the importance and ramifications of this finding are very significant.

Major findings and accomplishments of this study are listed below:

- The original laboratory test matrix proposed by Nieland et al. [1999] comprised of 37 tests is sufficient for determining all free parameters of the MDCF model except for the two parameters that describe the damage strain rate stress dependency (n_3 and c_2). Additional multistage creep tests are necessary to determine these two parameters.

- Estimates for shear-induced damage strain rate parameters n_3 and c_2 determined for salt at the WIPP produce results that compared favorably with the laboratory measurements of McIntosh salt, suggesting that the damage strain rate dependency on stress might be similar for all salts. Additional studies are necessary to confirm this finding and substantiate the claim that estimates determined for the WIPP for these two parameters are applicable to other salt formations.

- Minimum allowable gas pressures for the two Bay Gas caverns were determined using the original stress measures for shear-induced damage and flow as well as alternative stress measures that predict salt is weaker in triaxial extension than triaxial compression states of stress. Results of these calculations suggest that the current formulation of the MDCF model may not be conservative in evaluating minimum gas pressures and cavern stability. The more conservative approach using the alternative stress measures was used here to recommend the minimum allowable gas pressures for the Bay Gas caverns. Additional research is recommended to more accurately describe the behavior of salt at stress conditions other than triaxial compression.

- At a minimum pressure of 5.5 MPa (800 psi), a small amount of damage is predicted to occur at the surface of the caverns around zones of high stress concentration. However, quantitative measures for damage do not indicate unstable growth that would lead to gross cavern instability.

- The minimum gas pressure determined for Bay Gas Well No. 1 using the continuum damage approach was determined to be 5.5 MPa (800 psi) compared with 8.3 MPa (1,200 psi) using a conventional stress-based criterion. The lower minimum gas pressure predicted using the continuum damage approach increases the initial working gas capacity of this cavern by 18 percent.

- The minimum gas pressure determined for Bay Gas Well No. 2 using the continuum damage approach was determined to be 5.5 MPa (800 psi) compared with 6.9 MPa (1,000 psi) using a conventional stress-based criterion. The lower minimum gas pressure predicted using the continuum damage approach increases the initial working gas capacity of this cavern by 8 percent.

- The healing term of the MDCF model was modified to better reflect the behavior of salt during the reversal of damage. However, laboratory tests were not able to quantify healing with desired precision, making assessment of the MDCF healing term questionable. Because of this uncertainty, it is recommended that the benefit associated with damage healing not be considered during evaluations of CNG storage caverns using continuum damage mechanics and the MDCF model. Conservative results are produced by neglecting the beneficial healing effects.

- Laboratory testing and constitutive model development efforts were performed to provide a better understanding of the behavior of salt following a decrease in the deviatoric stress similar to that experienced by salt during injection of natural gas into a cavern. As a result of these work efforts, a new formulation for the recovery of salt was developed that represents the behavior of salt better than the original formulation.

- A revised laboratory test matrix is recommended to determine parameter estimates of the MDCF model and material properties for salt necessary to characterize the behavior of salt during CNG storage. The revised test matrix eliminates the hydrostatic healing tests proposed in the original test matrix, adds an additional creep test, and identifies multiple stages for other creep tests.

8.0 RECOMMENDATIONS

Based on the results of this study, the continuum damage mechanics approach using the MDCF model is a viable option for determining the minimum gas pressure for CNG storage caverns. The caverns evaluated in this study show that the continuum damage mechanics analyses provide an increase in the working gas between 8 and 18 percent. However, it is recommended that further refinement and development of the MDCF model be performed before it is routinely applied to cavern analyses.

The formulation and parameter estimates for the effective stress measures for shear-induced damage and flow developed during this study should be validated with experimental data. Laboratory tests should be performed on salt specimens at stress conditions other than triaxial compression. Results of the laboratory testing may indicate that further refinements of the MDCF model may be necessary to better predict the behavior of salt over the entire range of stress states from triaxial compression to triaxial extension.

Significant expenditures would be necessary to quantify healing of damaged salt with the accuracy desired for evaluating CNG storage. A conservative approach of neglecting the beneficial healing effects is recommended.

A minimum gas pressure of 5.5 MPa (800 psi) at the casing shoe is recommended for the two Bay Gas caverns to satisfy the stability design constraint based on the potential for salt dilation. Because the closure rates of the caverns are significant at this pressure, extended periods with the caverns near minimum pressure are not recommended.

9.0 REFERENCES

Callahan, G. D., A. F. Fossum, and D. K. Svalstad, 1989. *Documentation of SPECTROM-32: A Finite Element Thermomechanical Stress Analysis Program*, DOE/CH/10378-2, prepared by RE/SPEC Inc., Rapid City, SD, for the U.S. Department of Energy, Chicago Operations Office, Argonne, IL, Vol. I and II.

Chan, K. S., 1993. *Further Development of Fracture Constitutive Model for Rock Salt,* Monthly Technical Report No. FY '93–8, prepared by Southwest Research Institute, San Antonio, TX, for Sandia National Laboratories, Albuquerque, NM, February.

Chan, K. S., 1996. *Final Development of the Multimechanism Deformation Coupled Fracture (MDCF) Constitutive Model*, Monthly Technical Report No. FY '96–2, Monthly Progress Report for Southwest Research Institute, Contract AQ-1458 with Sandia National Laboratories, February.

Chan, K. S., S. R. Bodner, A. F. Fossum, and D. E. Munson, 1992. "A Constitutive Model for Inelastic Flow and Damage Evolution in Solids Under Triaxial Compression," *Mechanics of Materials*, Vol. 14, pp. 1–14.

Chan, K. S., S. R. Bodner, A. F. Fossum, and D. E. Munson, 1995. "Constitutive Representation of Damage Healing in WIPP Salt," *Proceedings, 35th U.S. Symposium on Rock Mechanics*, University of Nevada, Reno, NV, June 5–7, J. J. K. Daemen and R. A. Schultz (eds.), A. A. Balkema, Rotterdam, pp. 485–490.

Chan, K. S., S. R. Bodner, D. E. Munson, and A. F. Fossum, 1996a. "Inelastic Flow Behavior of Argillaceous Salt," *International Journal of Damage Mechanics*, Vol. 5, No. 3, pp. 292–314, July.

Chan, K. S., D. E. Munson, A. F. Fossum, and S. R. Bodner, 1996b. "A Constitutive Model for Representing Coupled Creep Fracture, and Healing in Rock Salt." *Proceedings, Fourth Conference of the Mechanical Behavior of Salt,* École Polytechnique de Montréal, Mineral Engineering Department, Québec, Canada, June 17 and 18, M. Aubertin and H. R. Hardy Jr. (eds), Penn State University, Trans Tech Publications, Clausthal, Germany, 1998, pp. 221-234

Chan, K. S., D. E. Munson, S. R. Bodner, and A. F. Fossum, 1996c. "Cleavage and Creep Rupture of Rock Salt," *Acta Metallurgica et Materialia*, Vol. 44, No. 9, pp. 3553–3565.

Chan, K. S., S. R. Bodner, A. F. Fossum, and D. E. Munson, 1997. "A Damage Mechanics Treatment of Creep Failure in Rock Salt," *International Journal of Damage Mechanics*, Vol. 6, April, pp. 121–152.

Coker, A. K., 1993. "Program Calculates Z-Factor for Natural Gas," O*il and Gas Journal,* pp. 74–75, February 15.

DeVries, K. L., J. D. Nieland, and J. L. Ratigan, 1998. *Feasibility Study for Lowering the Minimum Gas Pressure in Solution-Mined Caverns Based on Geomechanical Analyses of Creep-Induced Damage and Healing,* RSI-0969, prepared by RESPEC, Rapid City, SD, for U.S. Department of Energy, Morgantown, WV.

Kachanov, L. M., 1958. "On the Creep Fracture Time," *Izv, Akad. Nauk, USSR, Otdgel. Tekh, Nauk.,* Vol. 8, p. 26.

Mellegard, K. D. and T. W. Pfeifle, 1998. "Laboratory Evaluation of Mechanical Properties of Rock Using an Automated Triaxial Compression Test With a Constant Mean Stress Criterion," *Nondestructive and Automated Testing for Soil and Rock Properties*, ASTM STP 1350, W. A. Marr and C. E. Fairhurst (eds.), American Society for Testing and Materials, West Conshohocken, PA.

Munson, D. E., A. F. Fossum, and P. E. Senseny, 1989. *Advances in Resolution of Discrepancies Between Predicted and Measured In Situ WIPP Room Closures,* SAND88-2948, Sandia National Laboratories, Albuquerque, NM.

Nieland, J. D., K. L. DeVries, and K. D. Mellegard, 1999. *Phase II Feasibility Study for Lowering the Minimum Gas Pressure in Solution-Mined Caverns Based on Geomechanical Analyses of Creep-Induced Damage and Healing*, RSI-1165, prepared by RESPEC, Rapid City, SD, for U.S. Department of Energy, Morgantown, WV.

Pfeifle, T. W., T. J. Vogt, and G. A. Brekken, 1995. *Correlation of Chemical, Mineralogic, and Physical Characteristics of Gulf Coast Dome Salt to Deformation and Strength Properties*, Research Project Report No. 94-004-S, prepared by RE/SPEC Inc., Rapid City, SD, for the Solution Mining Research Institute Inc., Woodstock, IL.

Ratigan, J. L., J. D. Nieland, and J. D. Osnes, 1993. "Rock Mechanics Aspects of Natural Gas Storage in Domal Salt," *Solution Mining Research Institute Fall Meeting*, Lafayette, LA, October 25–26.

Van Sambeek, L. L., J. L. Ratigan, and F. D. Hansen, 1993. "Dilatancy of Rock Salt in Laboratory Test," *Proceedings, 34th U.S. Symposium on Rock Mechanics*, University of Wisconsin-Madison, Madison, WI, June 27–30, B. C. Haimson (ed.), International Journal of Rock Mechanics and Mining Sciences & Geomechanics Abstracts, Pergamon Press, Vol. 30, No. 7, pp. 735–738.

APPENDIX A

**ORIGINAL FORMULATION
OF THE MDCF MODEL**

TABLE OF CONTENTS

APPENDIX A
ORIGINAL FORMULATION
OF THE MDCF MODEL

The Multimechanism Deformation Coupled Fracture (MDCF) model presented in this appendix is the form as developed for the Waste Isolation Pilot Plant (WIPP) and does not include modifications that were made as a part of this project for application to the natural gas storage industry. Modifications to the model made as a part of this study are discussed in Chapter 4.0 of this report and in separate appendices (Appendices C, D, and E). A detailed description of the original model is provided here for completeness.

The MDCF model is a constitutive model that provides a continuum description of the creep response and the associated damage evolution and healing of rock salt. Both dislocation motion and creep-induced damage are assumed to contribute directly to the macroscopic inelastic strain rate. In addition to a direct contribution to the inelastic strain rate, the MDCF model was formulated such that damage also produces a softening effect as proposed by Kachanov [1958]. The Kachanov damage variable reduces the load-bearing capacity through a reduction in the effective area using a continuum damage mechanics approach. The damage variable is determined from an evolutionary equation and provides a measure for the level of damage. For the MDCF model, the contribution of creep-induced damage and healing to the inelastic strain rate is incorporated through additional kinetic equations that are independent of the kinetic equation for dislocation mechanisms. The terms are combined using the approach given by Fossum et al. [1988] to derive a proper three-dimensional generalization using classical thermodynamic principles. The generalized form of the MDCF model is given by:

$$\dot{\varepsilon}_{ij}^{i} = \frac{\partial \sigma_{eq}^{c}}{\partial \sigma_{ij}} \dot{\varepsilon}_{eq}^{c} + \frac{\partial \sigma_{eq}^{\omega_s^*}}{\partial \sigma_{ij}} \dot{\varepsilon}_{eq}^{\omega_s} + \frac{\partial \sigma_{eq}^{\omega_t}}{\partial \sigma_{ij}} \dot{\varepsilon}_{eq}^{\omega_t} + \frac{\partial \sigma_{eq}^{h}}{\partial \sigma_{ij}} \dot{\varepsilon}_{eq}^{h} \qquad (A-1)$$

where $\dot{\varepsilon}_{ij}^{i}$ is the inelastic strain and $\sigma_{eq}^{c}, \sigma_{eq}^{\omega_s^*}, \sigma_{eq}^{\omega_t}, \sigma_{eq}^{h}, \dot{\varepsilon}_{eq}^{c}, \dot{\varepsilon}_{eq}^{\omega_s}, \dot{\varepsilon}_{eq}^{\omega_t},$ and $\dot{\varepsilon}_{eq}^{h}$ are power-conjugate equivalent stress measures and equivalent inelastic strain rates for the dislocation creep (c), shear damage (ω_s), tensile damage (ω_t), and damage healing (h) mechanisms, respectively. Details of the power-conjugate stress measures, kinetic equations, flow laws, and evolution equation for damage in the MDCF model are summarized below. Note that compression is taken to be negative.

A.1 KINETIC EQUATION FOR DISLOCATION FLOW

The kinetic equation representing the isochoric creep rate, $\dot{\varepsilon}_{eq}^{c}$; i.e., dislocation flow, is based on the modified M-D model [Munson et al., 1989]. The formulation remains unchanged with the exception that the six occurrences of the effective stress are divided by the term $(1-\omega)$,

which represents the reduction in the effective load-bearing area caused by the presence of damage. The kinetic equation for the dislocation mechanisms is:

$$\dot{\varepsilon}_{eq}^c = F\dot{\varepsilon}_s \tag{A-2}$$

where F is the transient function representing transient creep behavior, and $\dot{\varepsilon}_s$ is the steady-state strain rate. The steady-state creep of salt is the sum of three dominant mechanisms: (1) a high-temperature, low-stress regime controlled by dislocation climb; (2) a low-temperature, low-stress regime controlled by an undefined mechanism; and (3) a high-stress regime controlled by various possible dislocation glide mechanisms. The steady-state creep rates of the three relevant mechanisms, respectively, are given by:

$$\dot{\varepsilon}_{s_1} = A_1 e^{-Q_1/RT} \left(\frac{\sigma_{eq}^c}{\mu(1-\omega)} \right)^{n_1} \tag{A-3}$$

$$\dot{\varepsilon}_{s_2} = A_2 e^{-Q_2/RT} \left(\frac{\sigma_{eq}^c}{\mu(1-\omega)} \right)^{n_2} \tag{A-4}$$

$$\dot{\varepsilon}_{s_3} = \left| H\left(\frac{\sigma_{eq}^c}{1-\omega} - \sigma_0 \right) \right| \left(B_1 e^{-Q_1/RT} + B_2 e^{-Q_2/RT} \right) \sinh\left[\frac{q\left(\frac{\sigma_{eq}^c}{1-\omega} - \sigma_0 \right)}{\mu} \right] \tag{A-5}$$

where the A's and B's are constants, Q's are activation energies, T is the absolute temperature, R is the universal gas constant, μ is the shear modulus, n's are the stress exponents, q is the stress constant, and σ_0 is the stress limit of the dislocation slip mechanism. $|H|$ is a Heaviside step function. The transient creep function F is given by:

$$F = \begin{cases} \exp\left[\Delta\left(1 - \frac{\varsigma}{\varepsilon_t^*} \right)^2 \right] & \text{for } \varsigma < \varepsilon_t^* \\ 1 & \text{for } \varsigma = \varepsilon_t^* \\ \exp\left[-\delta\left(1 - \frac{\varsigma}{\varepsilon_t^*} \right)^2 \right] & \text{for } \varsigma > \varepsilon_t^* \end{cases} \tag{A-6}$$

which is composed of a work-hardening branch, an equilibrium branch, and a recovery branch, respectively. In Equation A-6, Δ and δ represent the work-hardening and recovery parameters, respectively, and ε_t^* is the transient strain limit. The transient strain limit is a function of temperature and stress and is represented by:

A-4

$$\varepsilon_t^* = K_0 e^{cT} \left(\frac{\sigma_{eq}^c}{\mu(1-\omega)} \right)^m \tag{A-7}$$

where K_0, c, and m are constants. The work-hardening and recovery parameters are functions of stress given by:

$$\varepsilon_t^* = K_0 e^{cT} \left(\frac{\sigma_{eq}^c}{\mu(1-\omega)} \right)^m \tag{A-8}$$

$$\Delta = \alpha_w + \beta_w \log \left(\frac{\sigma_{eq}^c}{\mu(1-\omega)} \right) \tag{A-9}$$

$$\delta = \alpha_r + \beta_r \log \left(\frac{\sigma_{eq}^c}{\mu(1-\omega)} \right) \tag{A-10}$$

where the α's and β's are constants with the subscripts denoting either work-hardening (w) or recovery (r). The evolution rate, $\dot{\varsigma}$, of the internal variable ς, given in Equation A-6 is governed by:

$$\dot{\varsigma} = (F-1)\dot{\varepsilon}_s \tag{A-11}$$

which diminishes to zero when the steady-state condition is achieved.

The maximum shear stress or Tresca criterion is used here for dislocation-induced flow. The power-conjugate equivalent stress measure, σ_{eq}^c, for the dislocation mechanisms, assuming the Tresca criterion, is given by:

$$\sigma_{eq}^c = 2\cos\psi\sqrt{J_2} = \sigma_1 - \sigma_3 \tag{A-12}$$

where ψ is the Lode angle, J_2 is the second invariant of the deviatoric stress tensor, and σ_1 and σ_3 are the maximum and minimum principal stresses, respectively.

A.2 FLOW LAW FOR DISLOCATION DEFORMATION

The shear-induced dislocation flow of rock salt is assumed to be associative. The flow potential is an important factor in extending data obtained from constant stress laboratory creep tests to generalized three-dimensional states of stress. Differentiation of the power-conjugate stress given by Equation A-12 with respect to stress leads to:

A-5

$$\frac{\partial \sigma^c_{eq}}{\partial \sigma_{ij}} = \left[\frac{\cos 2\psi}{\cos 3\psi}\right]\frac{s_{ij}}{\sqrt{J_2}} + \left[\frac{\sqrt{3}\sin\psi}{J_2\cos 3\psi}\right]t_{ij}$$ (A-13)

where s_{ij} is the deviatoric stress tensor and $t_{ij} = s_{ip}s_{pj} - 2/3\,J_2\delta_{ij}$. Equation A-13 is indeterminate when $\psi \to \pm\pi/6$. To eliminate this problem computationally, the flow potential is taken as the average of the flow potentials on either side of the indeterminacy and evaluated in the limit as $\psi \to \pm\pi/6$ whenever the lode angle is within 0.25 degree of the indeterminacy. For both conditions, the result is:

$$\frac{\partial \sigma^c_{eq}}{\partial \sigma_{ij}} = \frac{s_{ij}}{2\sqrt{3J_2}}$$ (A-14)

Thus at the corners of the Tresca potential, the indeterminacies are removed by assuming a von Mises flow which makes the direction of straining unique.

A.3 KINETIC EQUATIONS FOR DAMAGE-INDUCED FLOW

The kinetic equations for damage-induced flow are similar in nature to dislocation flow in that damage-induced transient creep is accommodated in the model through a multiplier on the kinetic equations for damage-induced flow during steady-state creep. The model was developed assuming damage can occur in compression as a result of sliding of microcracks by shear and the opening of wing-tip cleavage cracks that develop on some of the shear cracks. Tensile creep damage is also accounted for in the model and is based on the formation of cleavage microcracks aligned normal to the tensile stress. The kinetics of tensile damage in salt are substantially faster than shear damage and is, therefore, treated as a separate term. The equations describing the shear-induced (s) and tension-induced (t) damage are similar in form. Thus the subscript i is used to represent s and t in the equations to follow. The equivalent inelastic strain rate is given by:

$$\dot{\varepsilon}^{\omega_i}_{eq} = F^{\omega_i}\dot{\varepsilon}^{\omega_i}_s$$ (A-15)

where:

$$F^{\omega_s} = F\,\exp\left[\frac{c_4\left(\sigma^c_{eq} - c_5\right)}{\sigma_0\left(1 - \rho\right)}\right]$$ (A-16)

$$F^{\omega_t} = F\,\exp\left[\frac{c_4\left(\sigma^{\omega_t}_{eq} - c_5\right)}{\sigma_0\left(1 - \rho\right)}\right]$$ (A-17)

are the functions that account for the damage-induced inelastic strain rate in the transient region and ρ is the volume fraction of clay particles. The kinetic equation for damage-induced flow during steady-state creep is given by:

$$\dot{\varepsilon}_s^{\omega_i} = c_1 \omega_0 \exp(c_3 \omega) \left[\sinh\left(\frac{c_2 \sigma_{eq}^{\omega_i} H(\sigma_{eq}^{\omega_i})}{(1-\omega)(1-\rho)\mu} \right) \right]^{n_3} \tag{A-18}$$

with:

$$c_1 = c_0 \left(B_1 e^{(-Q_1/RT)} + B_2 e^{(-Q_2/RT)} \right) \tag{A-19}$$

where the c's and n_3 are material constants, ω_0 is the initial value of the damage variable (ω) and the B's and Q's are constants of the dislocation glide mechanisms. As shown in Equation A-18, the Heaviside step function prevents accumulation of damage whenever the power-conjugate equivalent stress measure is negative.

The power-conjugate equivalent stress measures are given by:

$$\sigma_{eq}^{\omega_s} = |\sigma_1 - \sigma_3| + f_p x_2 x_7 \operatorname{sgn}(I_1 - \sigma_3) \left(\frac{I_1 - \sigma_3}{3 x_7 \operatorname{sgn}(I_1 - \sigma_3)} \right)^{x_6} \tag{A-20}$$

$$\sigma_{eq}^{\omega_t} = x_1 \sigma_1 H(\sigma_1) \tag{A-21}$$

where x_1, x_2, x_6, and x_7 are material constants of the damage model; I_1 is the first stress invariant; and σ_1 and σ_3 are the maximum and minimum principal stresses, respectively, with compression assumed to be negative. The first term in Equation A-20 represents the driving force for shear-induced damage, which leads to the opening of "wing-tip" microcracks or grain boundary cracks. The second term in Equation A-20 represents the suppression of microcrack growth by a confining pressure. This term was recently extended to account for the increase in damage accumulation associated with increasing impurity of clay content [Chan et al., 1996a]. The material parameter, f_p, is related to the impurity content by:

$$f_p = 1 - p_1 \rho \tag{A-22}$$

where ρ is the impurity content parameter and p_1 is a material parameter, which is analogous to a local stress intensity factor.

The preceding equations include the damage variable (ω), which is described in terms of an evolutionary equation. The damage evolution equation is taken as:

$$\dot{\omega} = \dot{\omega}_s + \dot{\omega}_t - \dot{h} \tag{A-23}$$

A-7

where the damage rate components for the shear-induced and tension-induced damage are given by:

$$\dot{\omega}_s = \frac{X_4}{t_0}\omega\left[\ln\left(\frac{1}{\omega}\right)\right]^{\frac{X_4+1}{X_4}}\left[\frac{\sigma_{eq}^{\omega_s}H\left(\sigma_{eq}^{\omega_s}\right)}{(1-\rho)\xi_s}\right]^{X_{3s}} \tag{A-24}$$

$$\dot{\omega}_t = \frac{X_4}{t_0}\omega\left[\ln\left(\frac{1}{\omega}\right)\right]^{\frac{X_4+1}{X_4}}\left[\frac{\sigma_{eq}^{\omega_t}H\left(\sigma_{eq}^{\omega_t}\right)}{(1-\rho)\xi_t}\right]^{X_{3t}} \tag{A-25}$$

where x_4, x_{3s}, x_{3t}, ξ_s, ξ_t, and t_0 are material constants. The parameter, ξ_s, may have different values according to the magnitude of the effective shear-induced damage stress; i.e.,

$$\begin{aligned}\xi_s = \xi_s^1 \text{ for } \sigma_{eq}^c/(1-\omega) > \sigma_0 \\ \xi_s = \xi_s^2 \text{ for } \sigma_{eq}^c/(1-\omega) \le \sigma_0\end{aligned} \tag{A-26}$$

The healing term or damage recovery rate is discussed later under the discussion of the kinetic equation for healing.

A.4 FLOW LAW FOR DAMAGE-INDUCED INELASTIC DEFORMATION

The shear-induced inelastic damage flow is assumed to be nonassociative. The flow potential power-conjugate stress measure for shear-induced damage is given by (cf. Equation A-20):

$$\sigma_{eq}^{\omega_s^*} = |\sigma_1 - \sigma_3| + \frac{X_2 X_8}{3}\left(I_1 - \sigma_3\right) \tag{A-27}$$

where x_8 is a material constant. The flow potential power-conjugate stress measure for tension-induced damage is given by:

$$\sigma_{eq}^{\omega_t} = x_1\sigma_1 H\left(\sigma_1\right) \tag{A-28}$$

where x_1 is a material constant.

A.5 KINETIC EQUATION FOR DAMAGE RECOVERY FLOW (HEALING)

Reduction of damage in rock salt can occur by the closure of open microcracks and the sintering of microcracks. The kinetic equation representing the healing or damage recovery process gives the total inelastic healing rate as follows:

$$\dot{\varepsilon}_{ij}^{h} = \dot{\varepsilon}_{eq}^{h} \frac{\partial \sigma_{eq}^{h^{*}}}{\partial \sigma_{ij}} \tag{A-29}$$

where $\sigma_{eq}^{h^{*}}$ and $\dot{\varepsilon}_{eq}^{h}$ are the power-conjugate equivalent stress measure and the equivalent inelastic strain rate for the healing mechanisms, respectively.

The equivalent inelastic healing strain rate in Equation A-29 is given as [Chan et al., 1996b]:

$$\dot{\varepsilon}_{eq}^{h} = \frac{\varepsilon_{kk}^{i} \left(\sigma_{eq}^{h} - \sigma_{b} \right) H \left(\sigma_{b} - \sigma_{eq}^{h} \right)}{\tau \mu} \tag{A-30}$$

where $\dot{\varepsilon}_{kk}^{i}$ is the inelastic volumetric strain, τ is a characteristic time constant, and μ is the shear modulus. $H()$ is the Heaviside function; thus, the healing rate is zero if the equivalent stress measure σ_{eq}^{h} is less than σ_{b}. The equivalent stress measure used to describe the magnitude of the healing strain rate is different than the power-conjugate equivalent stress measure used to describe the flow potential (nonassociative formulation) and is given by:

$$\sigma_{eq}^{h} = \frac{1}{3} \left(I_{1} - \sigma_{3} \right) \tag{A-31}$$

The value for σ_{b} is determined from Equation A-20 by solving for the value of σ_{eq}^{h} when $\sigma_{eq}^{\omega} = 0$, which is given by:

$$\sigma_{b} = -X_{7} \left[\frac{\sigma_{1} - \sigma_{3}}{f_{p} X_{2} X_{7}} \right]^{\frac{1}{x_{6}}} \tag{A-32}$$

Then the quantity $\sigma_{eq}^{h} - \sigma_{b}$ coincides with the damage equivalent stress measure when $\sigma_{eq}^{w_{s}} = 0$ so that a distinct boundary exists between damage accumulation and damage healing. The characteristic time constant (τ) is taken to be a function of the inelastic volumetric strain and is written as:

$$\tau = \tau_{0} \exp \left(-k_{1} \varepsilon_{kk}^{i} \right) + \tau_{1} \tag{A-33}$$

where k_1 is a material constant and τ_0 and τ_1 are characteristic time constants. When the volumetric strain is large, the exponential term becomes insignificant and the limiting value for τ is τ_1. τ_1 is then the characteristic time associated with microcrack closure when the level of damage is high. When the inelastic volumetric strain becomes small, the limiting value of τ is $\tau_0 + \tau_1$, which is the characteristic time constant associated with crack sintering.

The damage variable (ω) is described in terms of the evolutionary equation given in Equation A-23. The healing portion of the equation (modified with the initial damage Heaviside) is taken from [Chan et al., 1996b]:

$$\dot{h} = \frac{\omega\, H(\omega - \omega_0)\left(\sigma_{eq}^h - \sigma_b\right) H\left(\sigma_b - \sigma_{eq}^h\right)}{\tau\,\mu} \tag{A-34}$$

A.6 FLOW LAW FOR HEALING-INDUCED INELASTIC DEFORMATION

The healing (damage recovery) inelastic damage flow is anisotropic because damage will typically accumulate normal to the major principal stress (compression negative). To implement the anisotropic nature of the healing, Chan et al. [1996b] have developed the flow potential based on stress-induced anisotropy. However, the state of stress does not provide information regarding the direction of damage. In addition, Chan's development includes indeterminant conditions under hydrostatic states of stress. Also, under triaxial extension test conditions, Chan's flow potential predicts axial shortening; whereas, under triaxial compression test conditions, axial lengthening is predicted. This condition creates deformation in the opposite direction of loading regardless of the magnitude of the load. For these reasons, a simple isotropic flow based only on mean stress was adopted. The power-conjugate effective stress measure developed for describing the flow potential is:

$$\sigma_{eq}^{h^*} = \sigma_m \tag{A-35}$$

and the flow potential is given by:

$$\frac{\partial \sigma_{eq}^{h^*}}{\partial \sigma_{ij}} = \frac{\delta_{ij}}{3} \tag{A-36}$$

A.7 REFERENCES

Chan, K. S., S. R. Bodner, D. E. Munson, and A. F. Fossum, 1996a. "Inelastic Flow Behavior of Argillaceous Salt," *International Journal of Damage Mechanics,* Vol. 5, No. 3, July, pp. 292–314.

Chan, K. S., D. E. Munson, A. F. Fossum, and S. R. Bodner, 1996b. "A Constitutive Model for Representing Coupled Creep Fracture, and Healing in Rock Salt," *Proceedings, Fourth Conference of the Mechanical Behavior of Salt,* École Polytechnique de Montréal, Mineral Engineering Department, Québec, Canada, June 17 and 18, M. Aubertin and H. R. Hardy Jr. (eds.), Penn State University, Trans Tech Publications, Clausthal, Germany, 1998, pp. 221–234.

Fossum, A. F., G. D. Callahan, L. L. Van Sambeek, and P.E. Senseny, 1988. "How Should One-Dimensional Laboratory Equations be Cast Into Three-Dimensional Form?," *Proceedings, 29th U.S. Symposium on Rock Mechanics,* University of Minnesota, Minneapolis, MN, June 13–15, P.A. Cundall, R. L. Starling, and A.M. Starfield (eds.), A. A. Balkema, Rotterdam, pp. 35–41.

Kachanov, L. M., 1958. "On the Creep Fracture Time," *Izv, Akad. Nauk, USSR, Otdgel. Tekh, Nauk.,* Vol. 8, p. 26.

Munson, D. E., A. F. Fossum, and P. E. Senseny, 1989. *Advances in Resolution of Discrepancies Between Predicted and Measured In Situ WIPP Room Closures,* SAND88-2948, Sandia National Laboratories, Albuquerque, NM.

APPENDIX B

**LABORATORY RESULTS OF
MECHANICAL PROPERTY TESTS
FOR MCINTOSH DOME SALT**

LIST OF FIGURES

LIST OF FIGURES
(Continued)

Figure B-1. Axial Stress Versus Axial and Radial Strain for an Unconfined Compressive Strength Test on McIntosh Salt Specimen MD/BG2/4149.8.
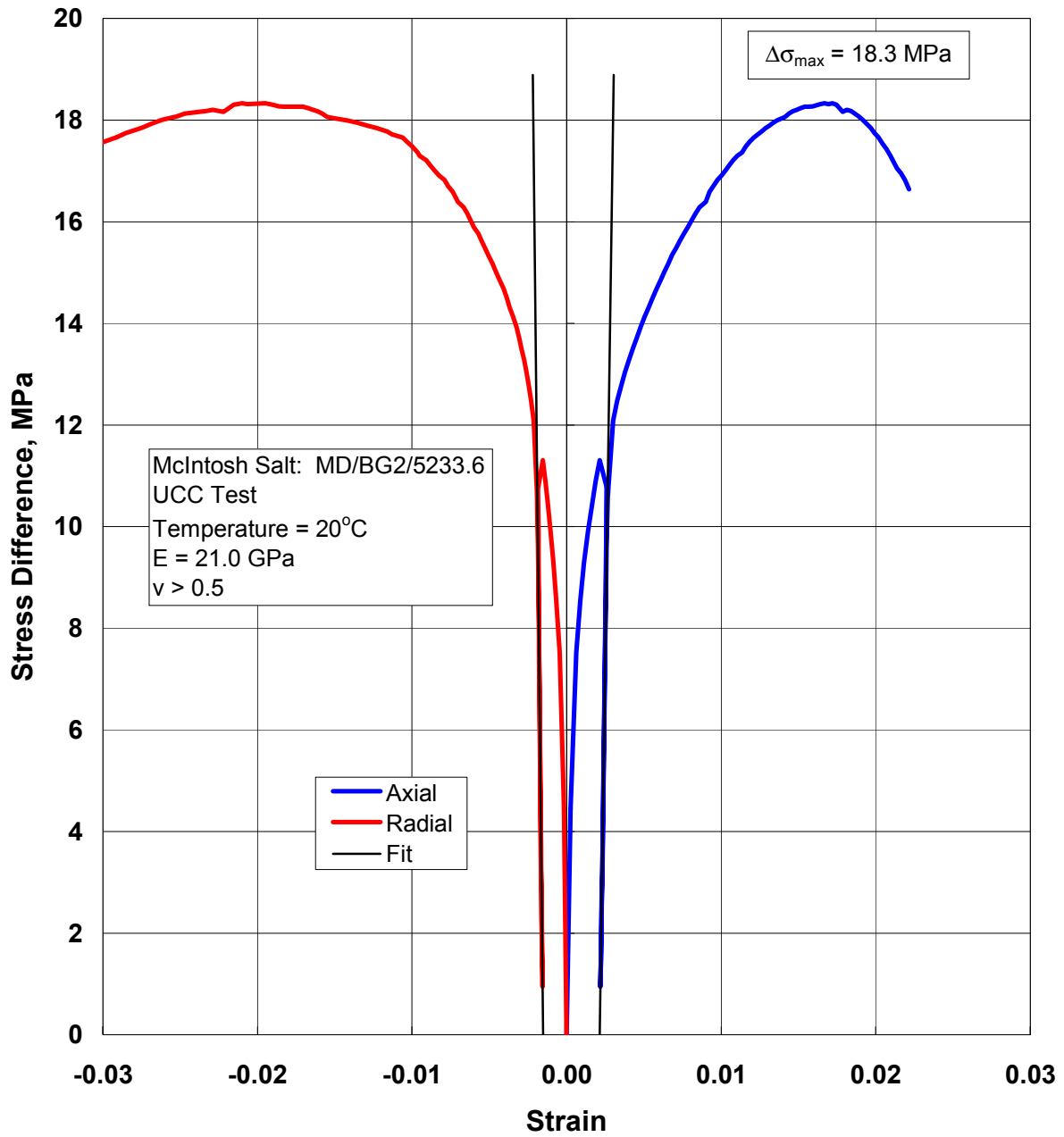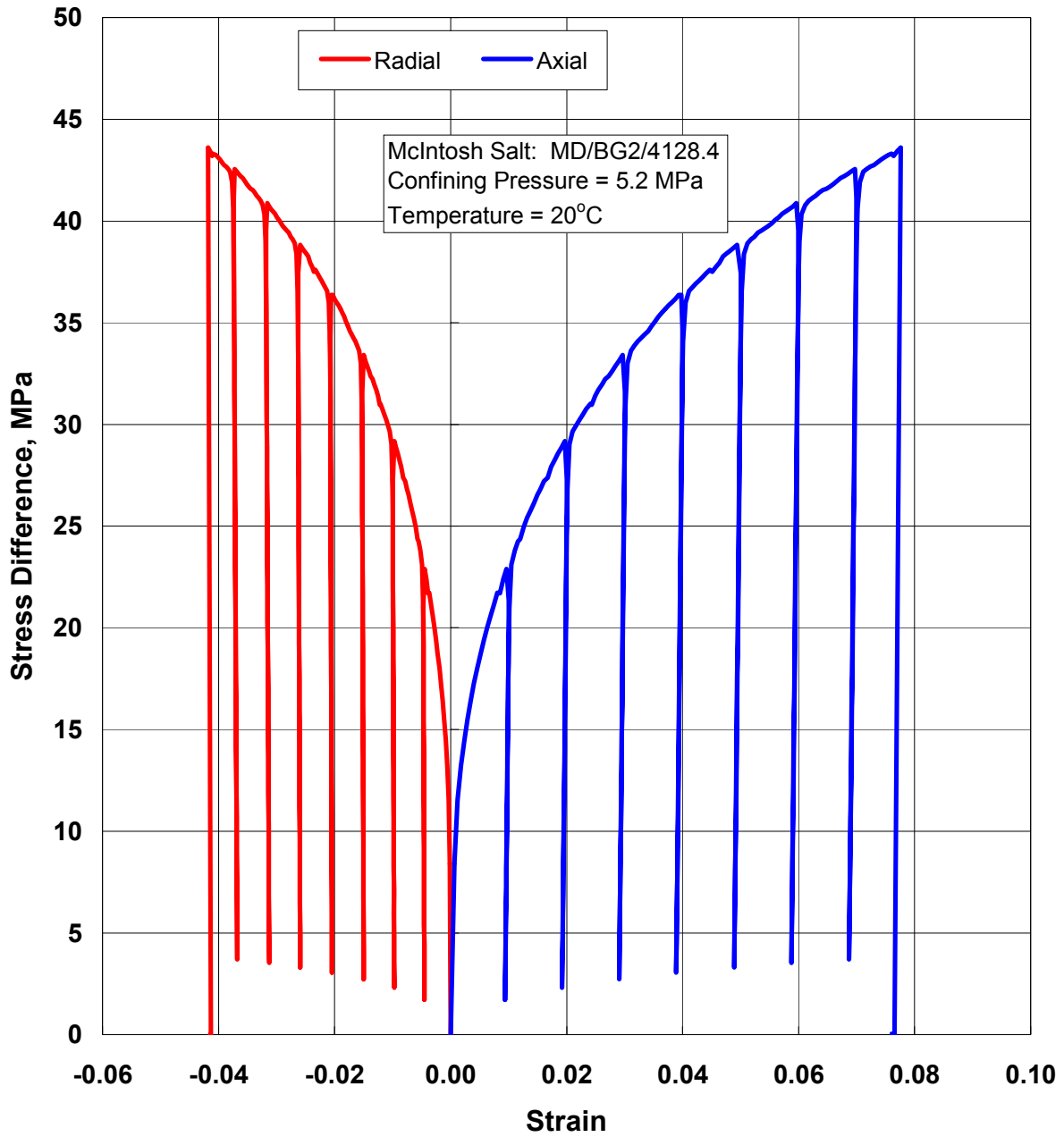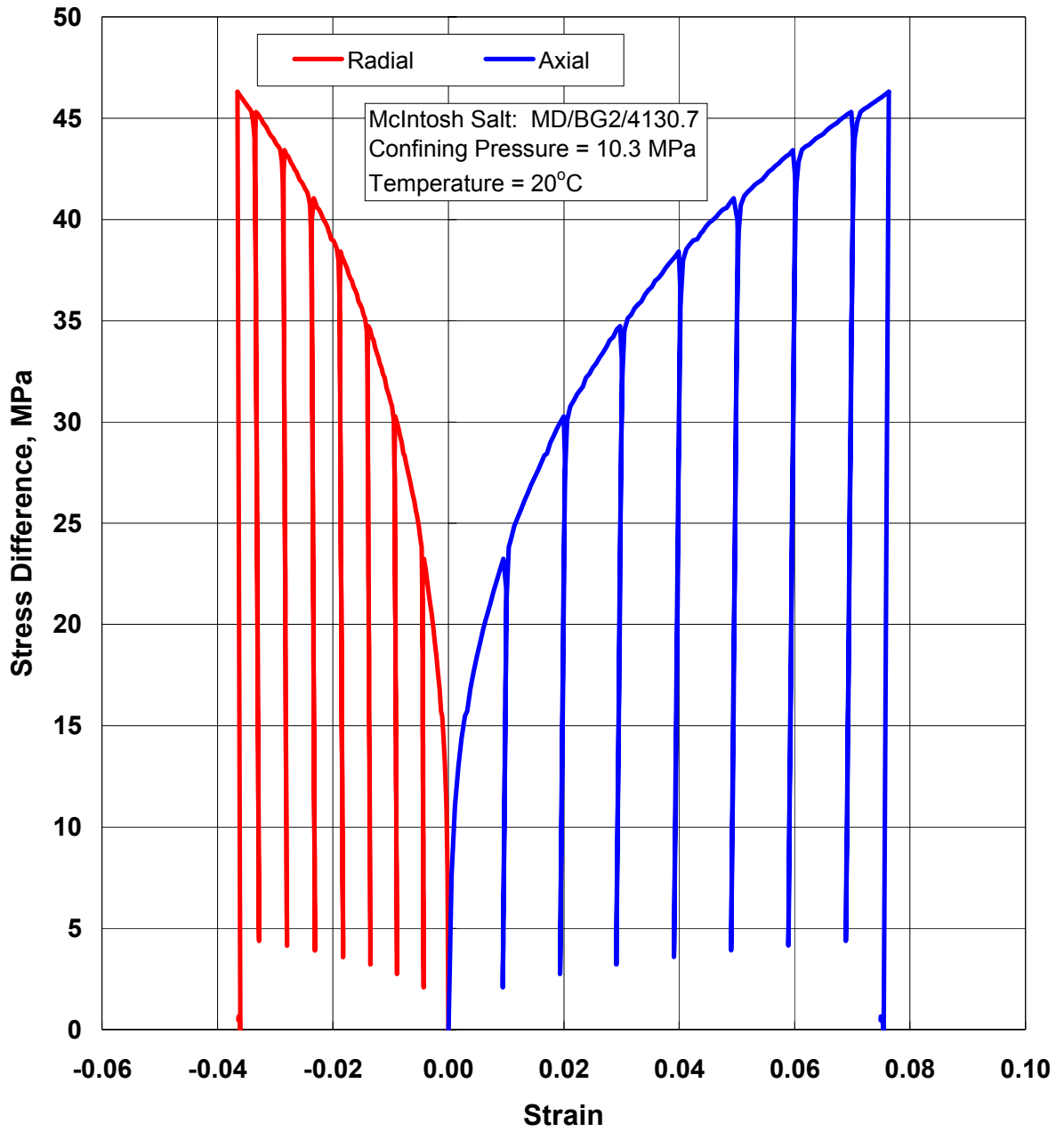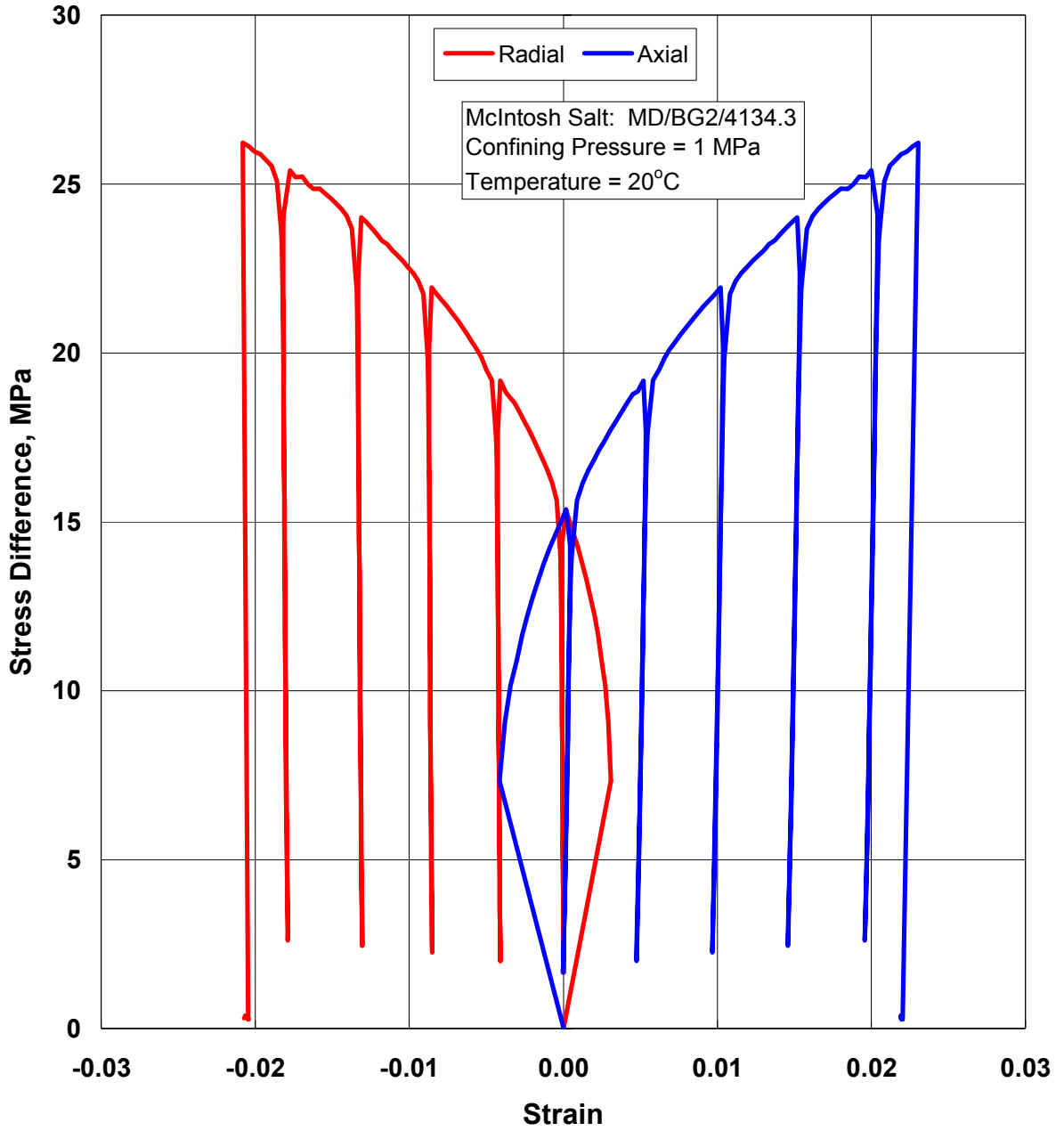
Figure B-2. Axial Stress Versus Axial and Radial Strain for an Unconfined Compressive Strength Test on McIntosh Salt Specimen MD/BG2/4153.0.
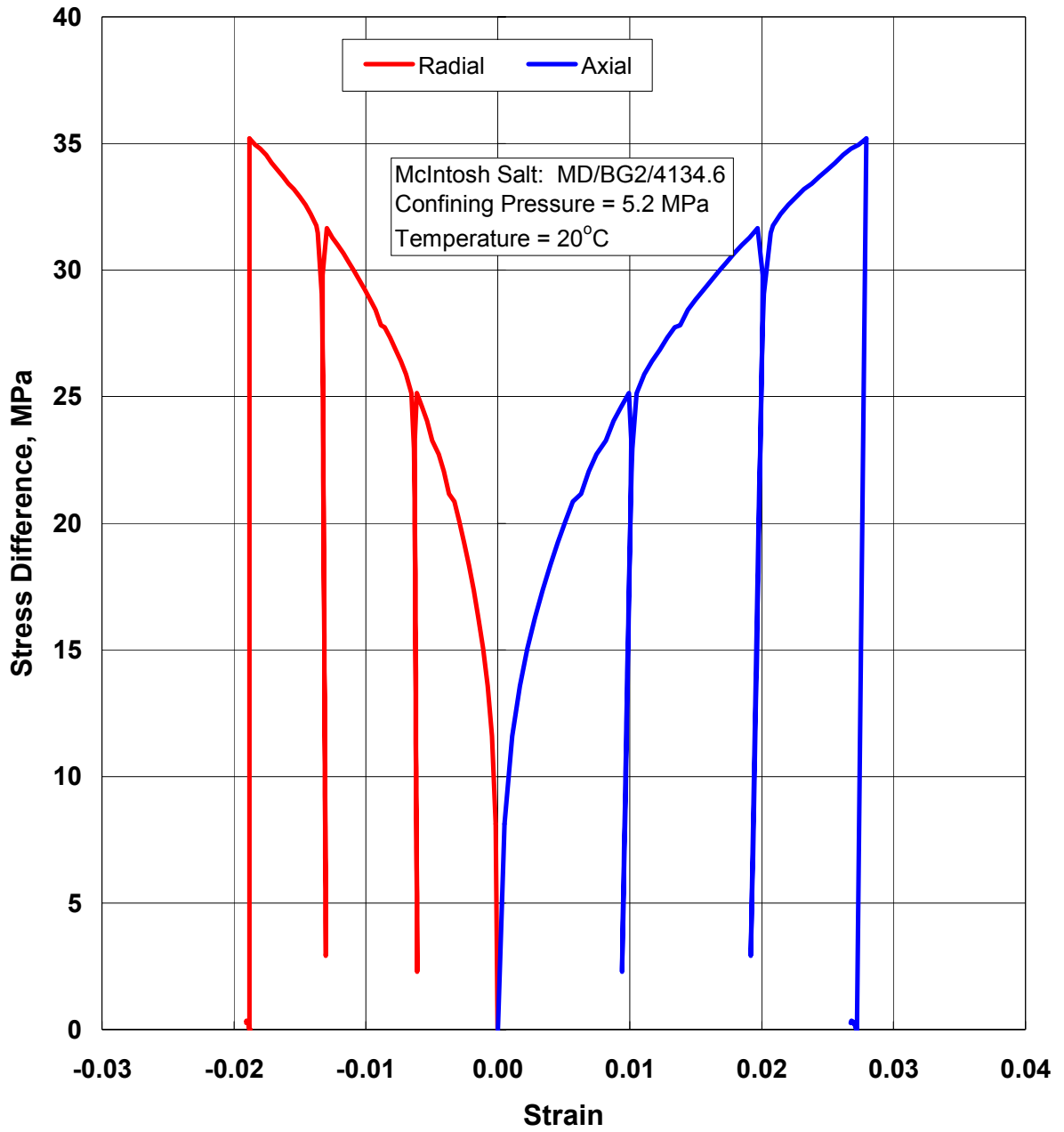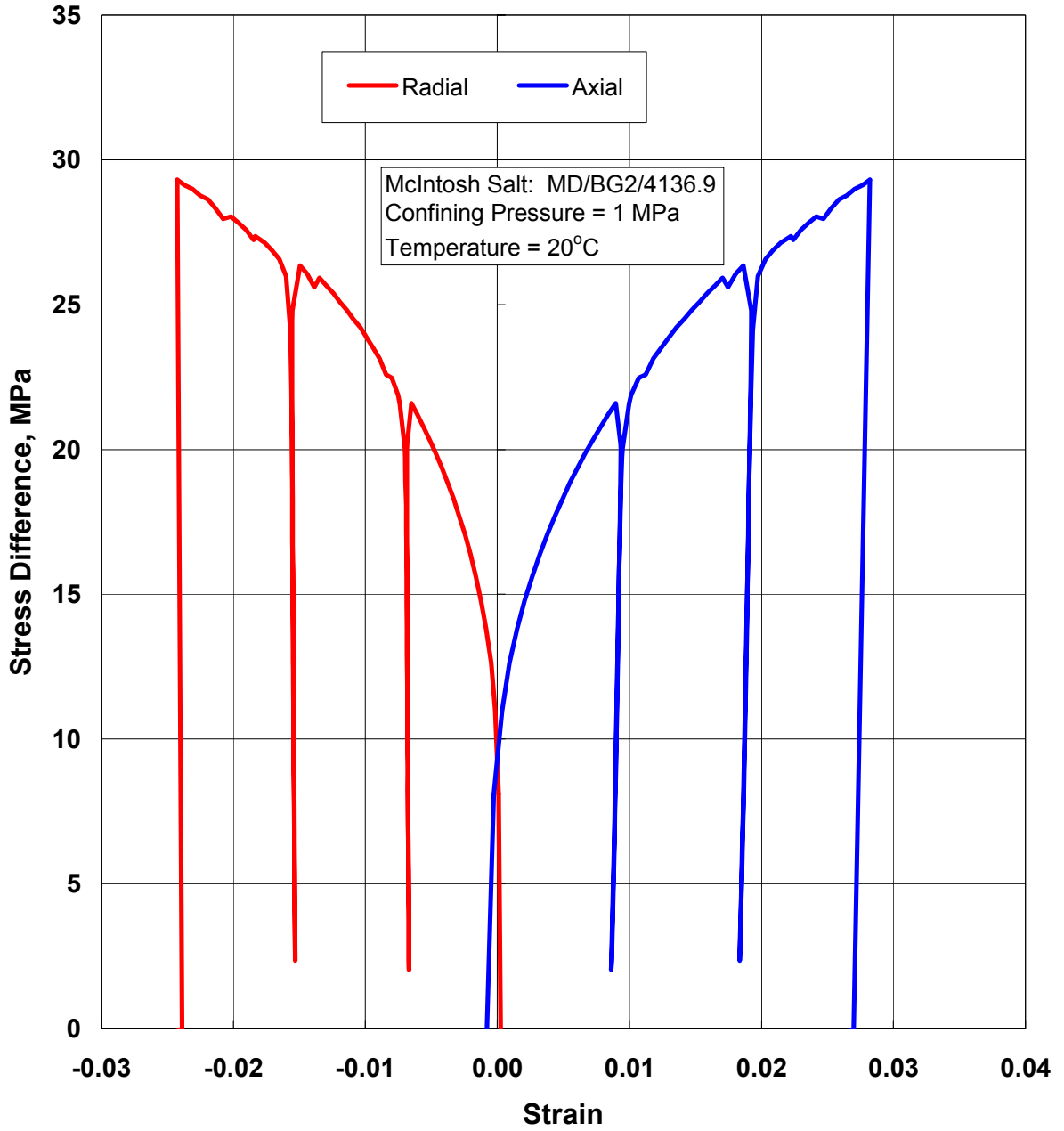
Figure B-3. Axial Stress Versus Axial and Radial Strain for an Unconfined Compressive Strength Test on McIntosh Salt Specimen MD/BG2/4637.1.
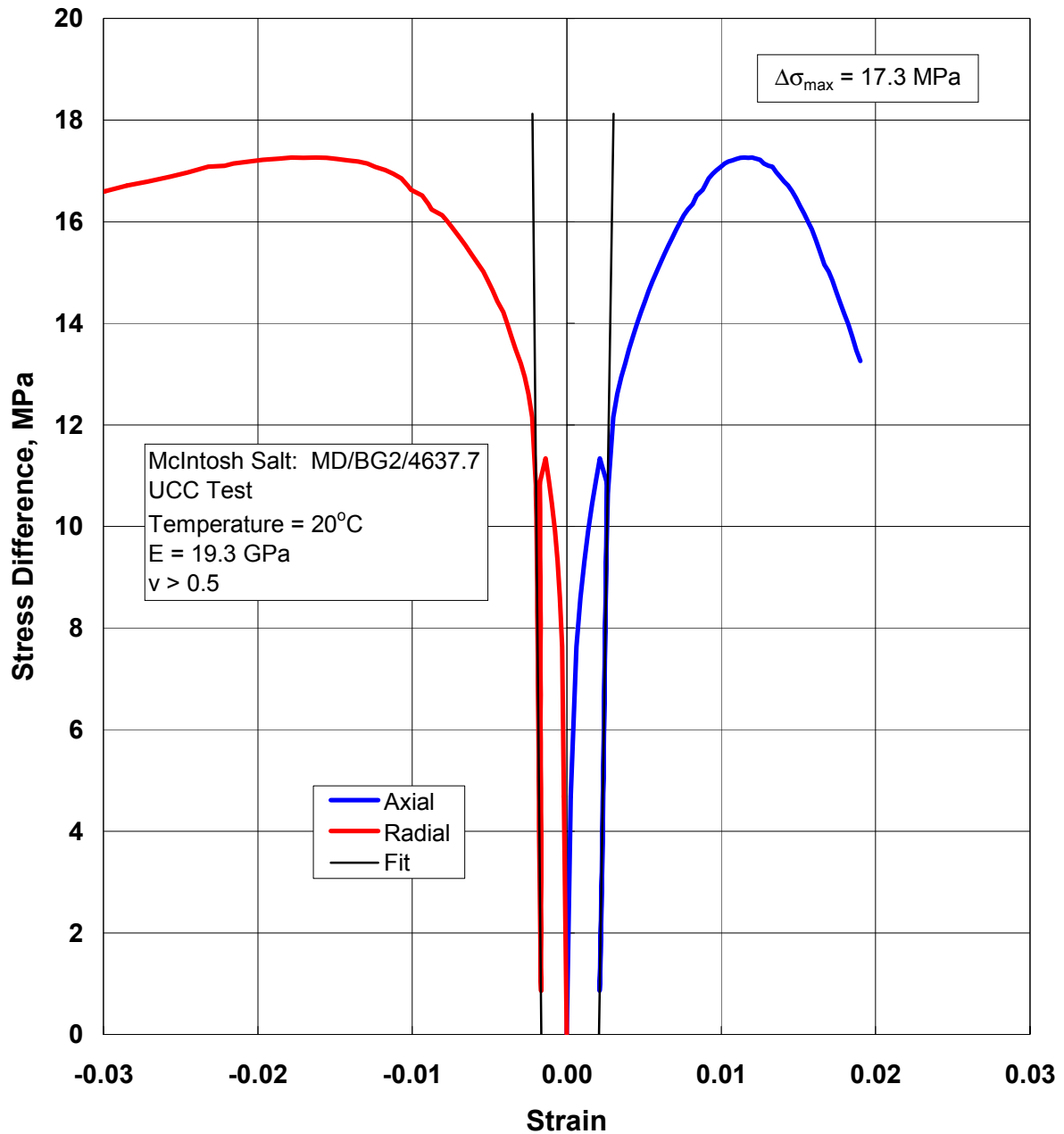
Figure B-4. Axial Stress Versus Axial and Radial Strain for an Unconfined Compressive Strength Test on McIntosh Salt Specimen MD/BG2/4637.7.
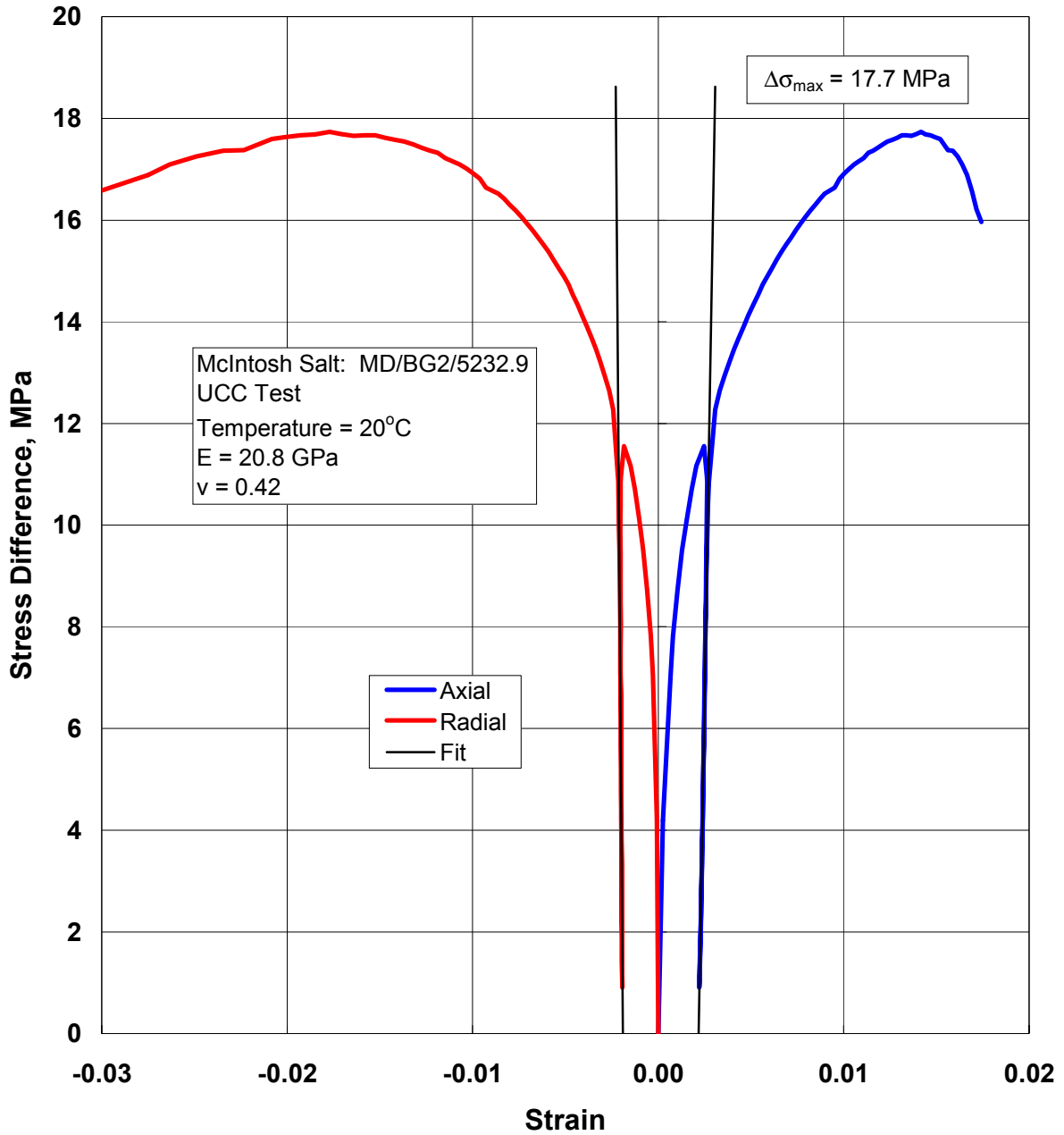
Figure B-5. Axial Stress Versus Axial and Radial Strain for an Unconfined Compressive Strength Test on McIntosh Salt Specimen MD/BG2/5232.9.

Figure B-6. Axial Stress Versus Axial and Radial Strain for an Unconfined Compressive Strength Test on McIntosh Salt Specimen MD/BG2/5233.6.
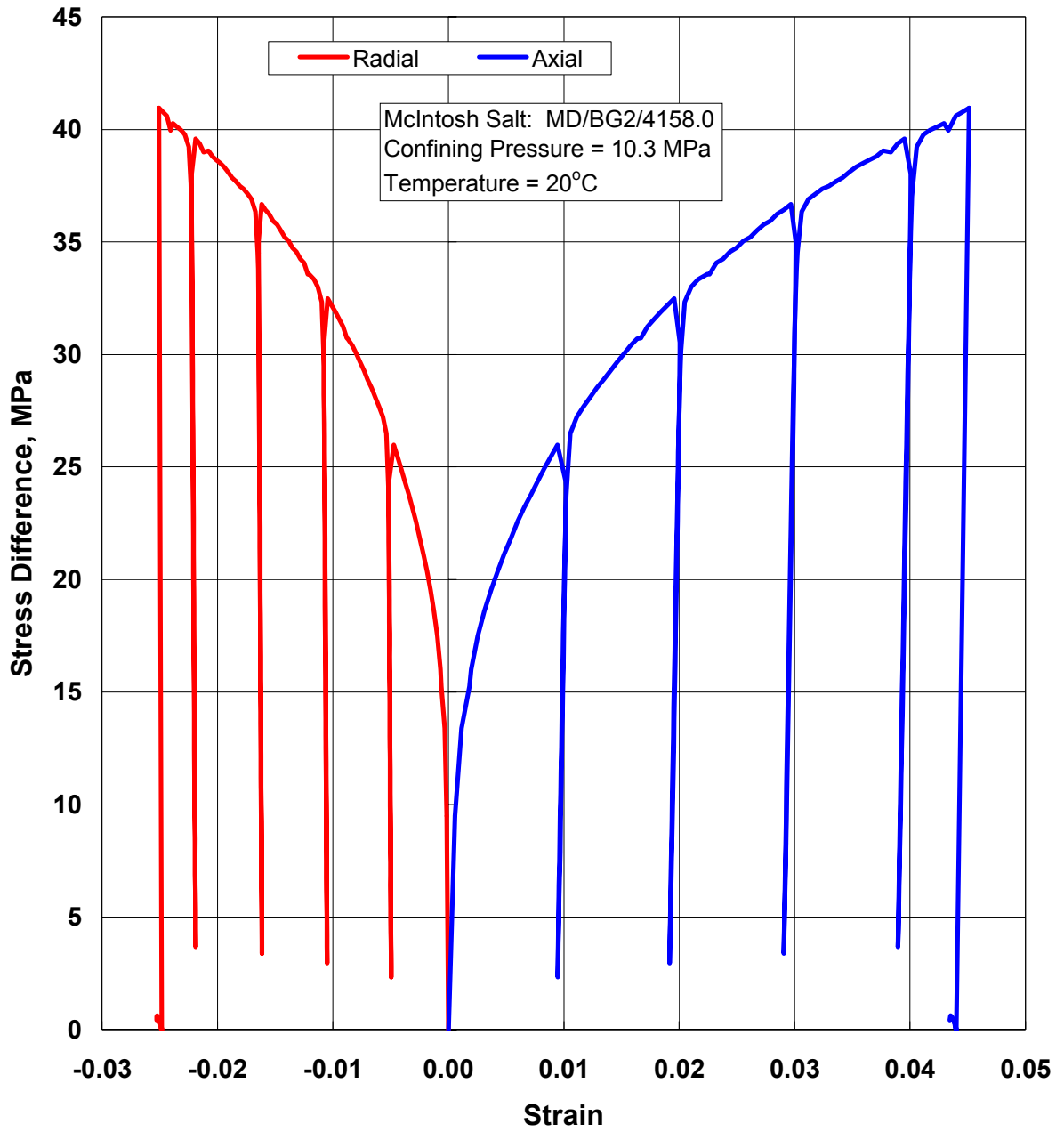
Figure B-7. Axial Stress Difference Versus Axial and Radial Strain for a Confined Constant Strain Rate Test on McIntosh Salt Specimen MD/BG2/4128.4.
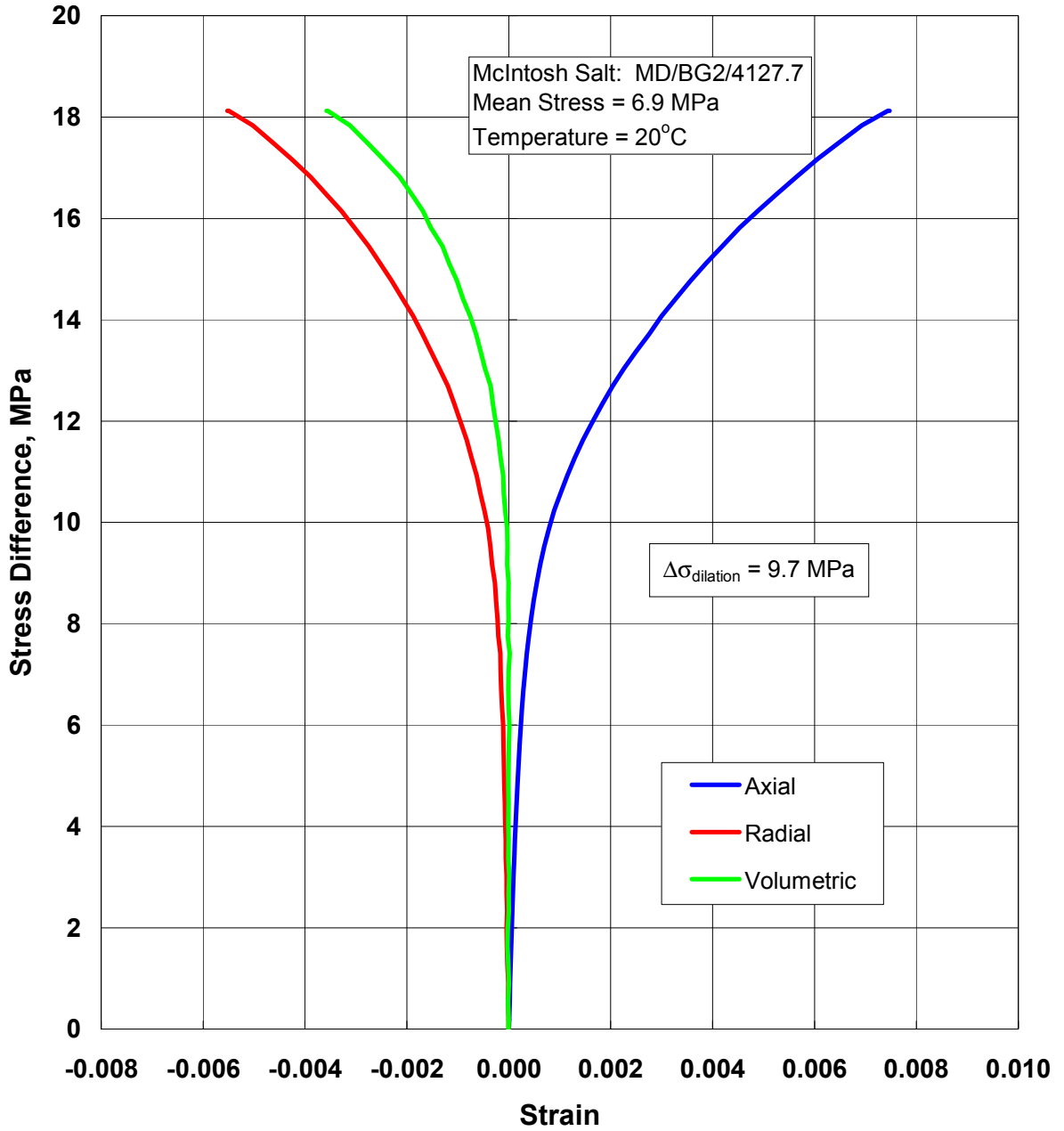
Figure B-8. Axial Stress Difference Versus Axial and Radial Strain for a Confined Constant Strain Rate Test on McIntosh Salt Specimen MD/BG2/4130.7.

Figure B-9. Stress Difference Versus Axial and Radial Strain for a Confined Constant Strain Rate Test on McIntosh Salt Specimen MD/BG2/4134.3.

Figure B-10. Axial Stress Difference Versus Axial and Radial Strain for a Confined Constant Strain Rate Test on McIntosh Salt Specimen MD/BG2/4134.6.

Figure B-11. Axial Stress Difference Versus Axial and Radial Strain for a Confined Constant Strain Rate Test on McIntosh Salt Specimen MD/BG2/4136.9.
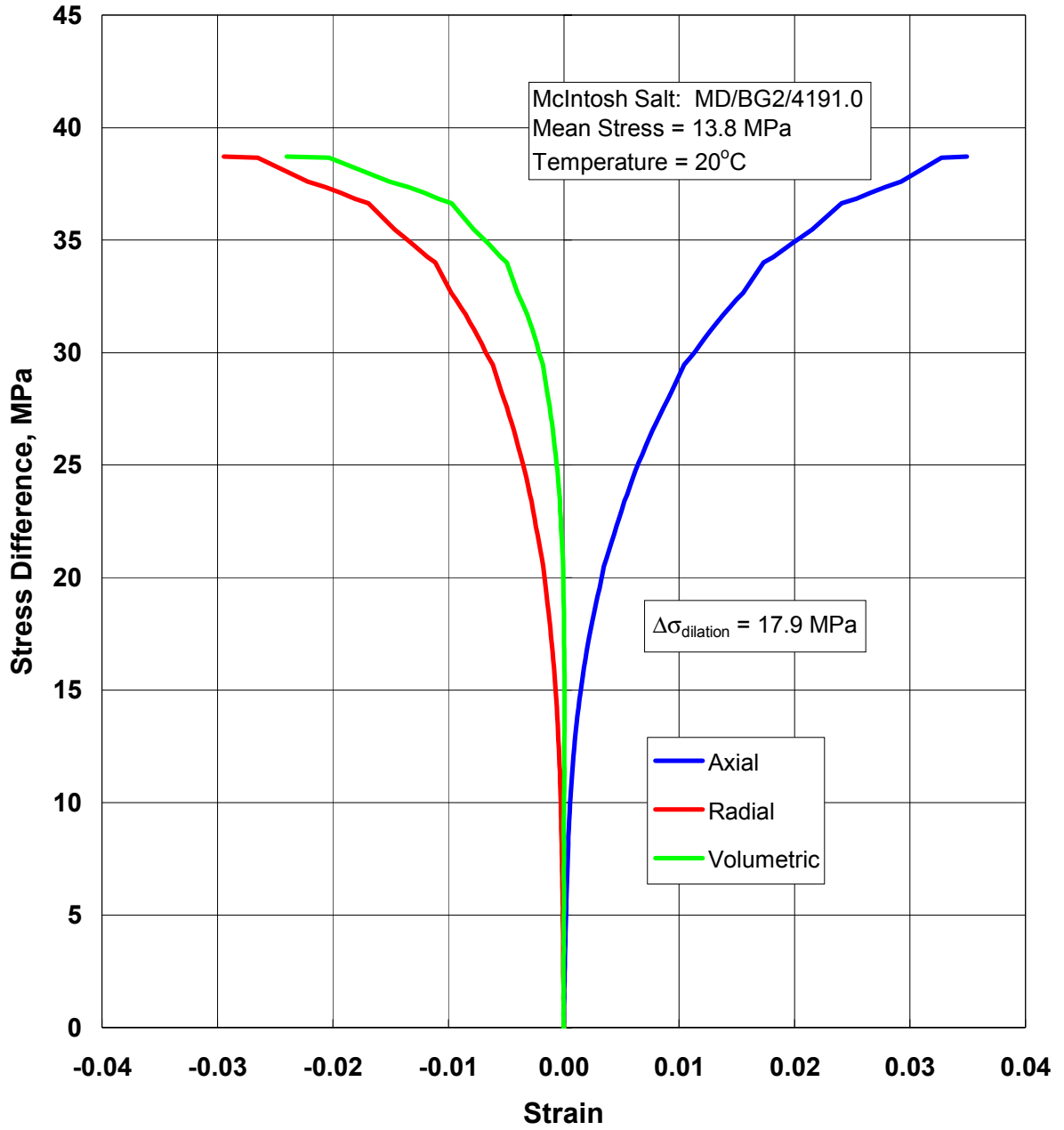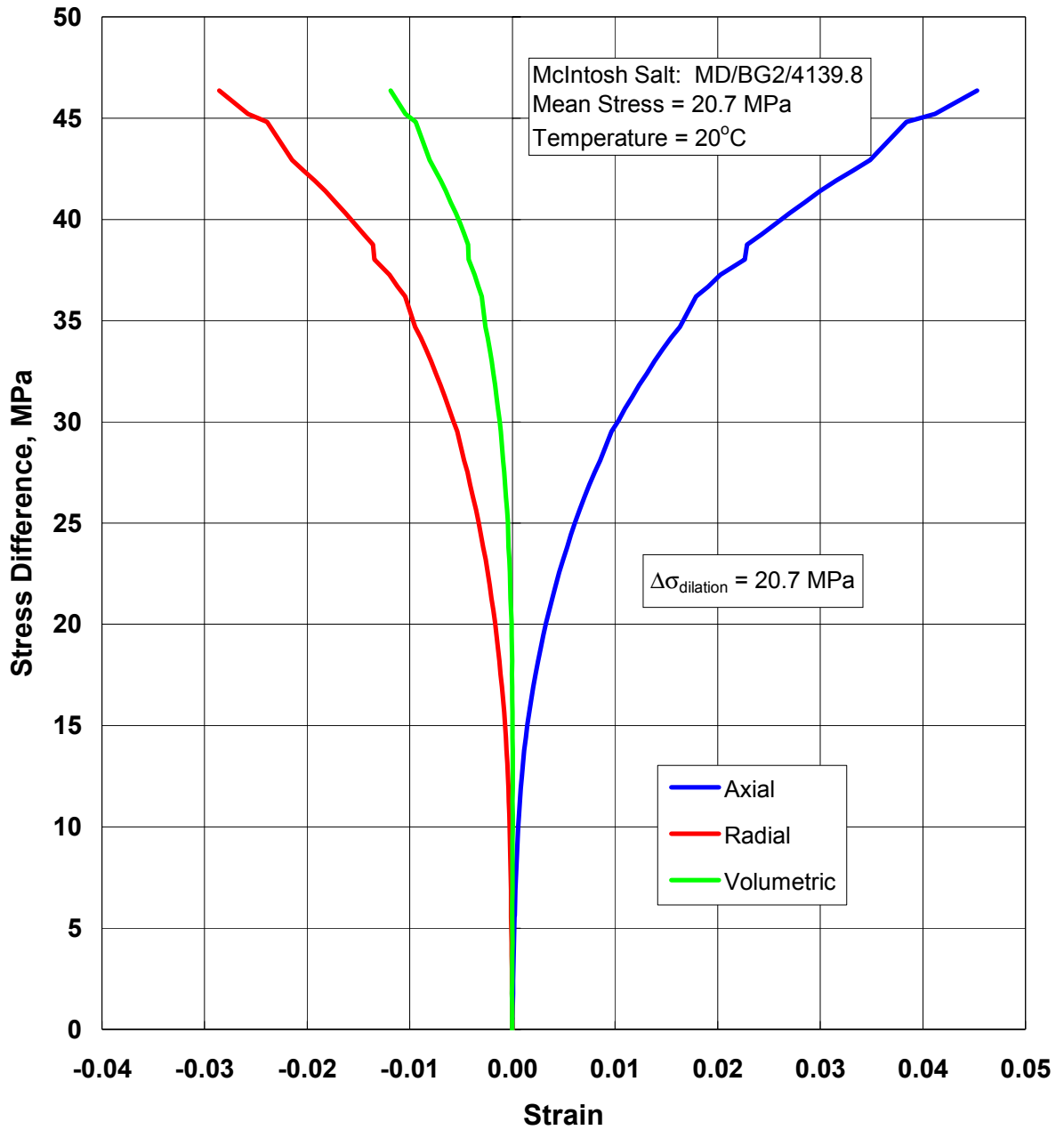
Figure B-12. Axial Stress Difference Versus Axial and Radial Strain for a Confined Constant Strain Rate Test on McIntosh Salt Specimen MD/BG2/4158.0.
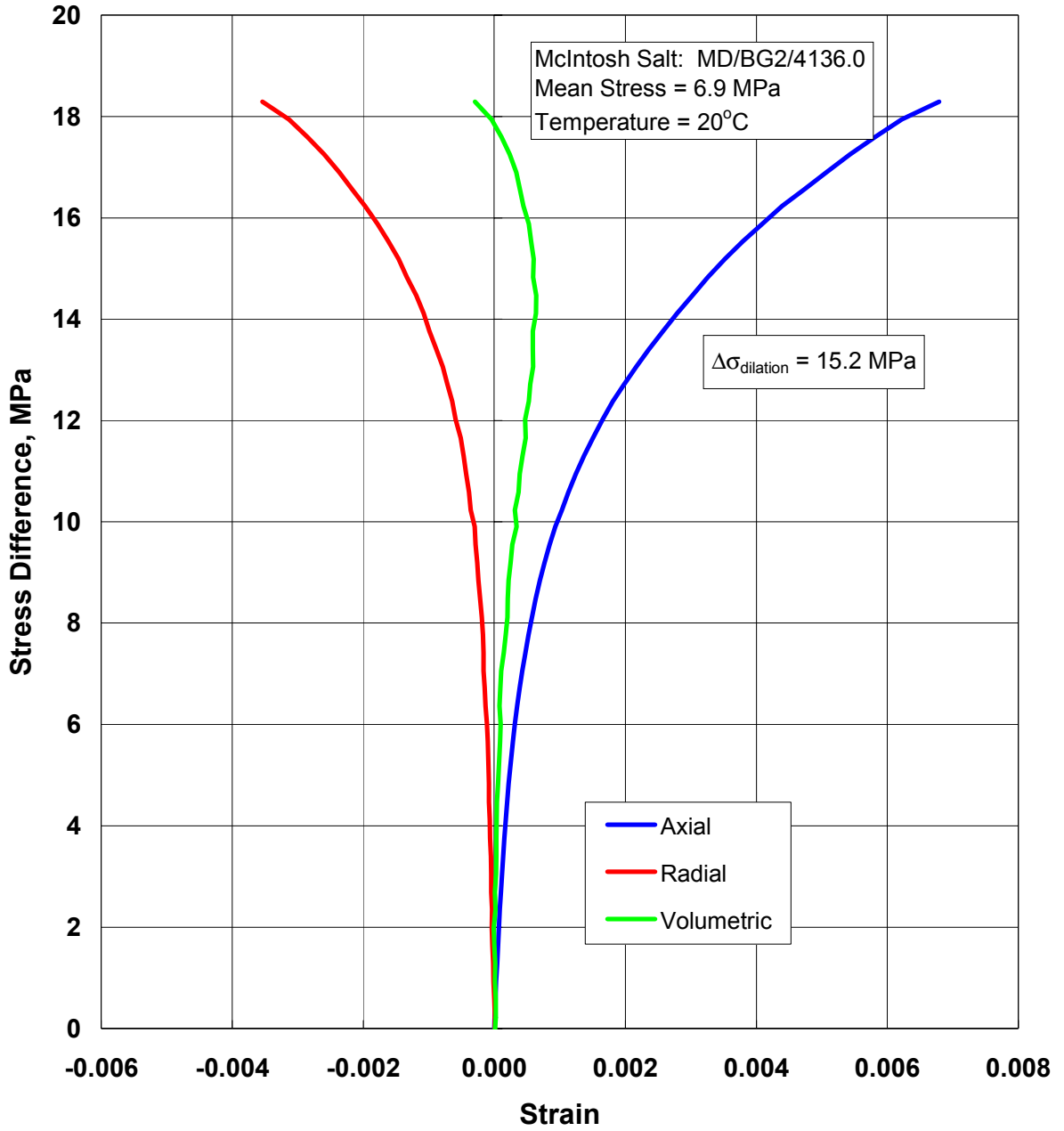
Figure B-13. Axial Stress Difference Versus Axial, Radial, and Volumetric Strain for a Constant Mean Stress Test on McIntosh Salt Specimen MD/BG2/4127.7.
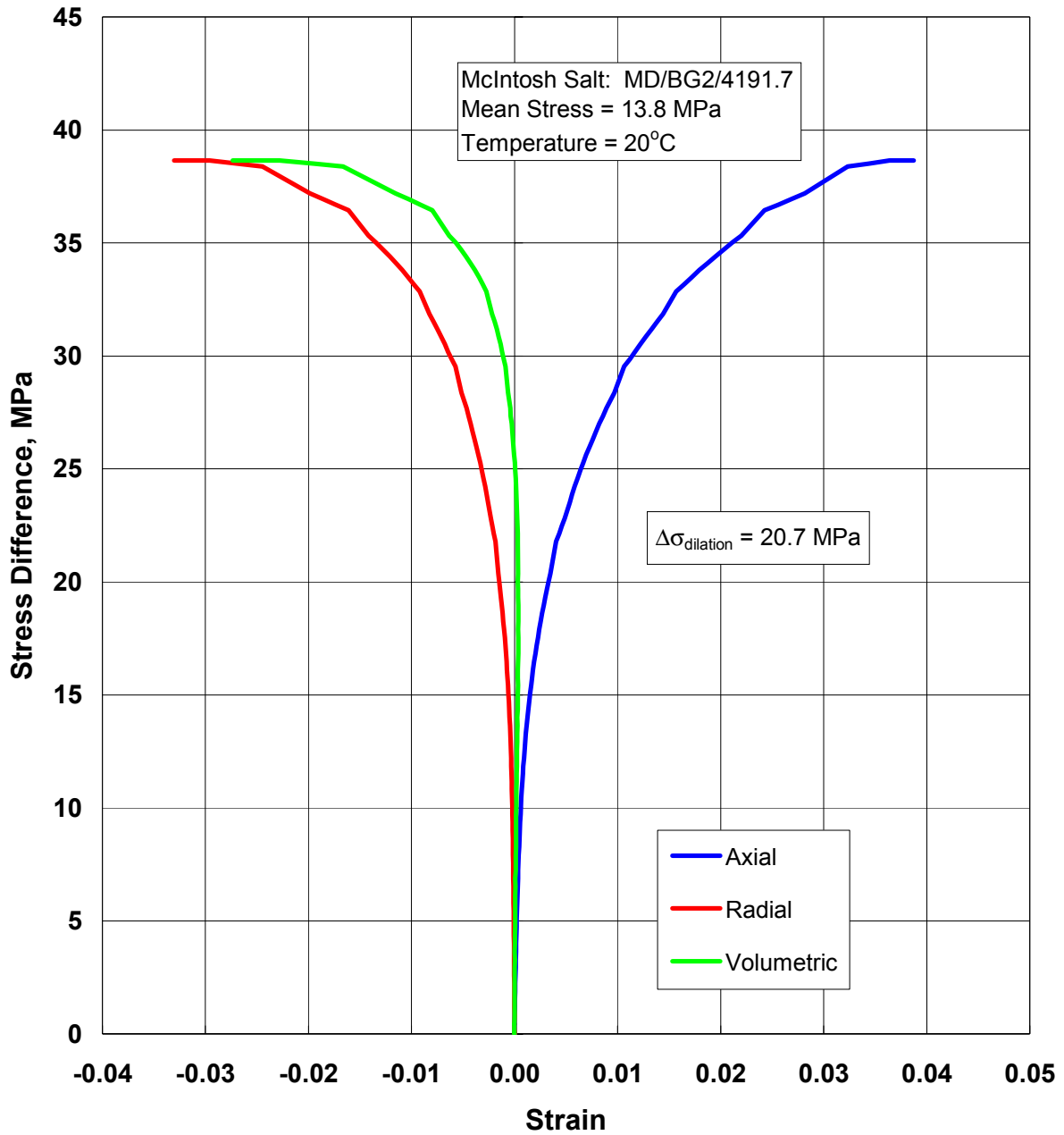
Figure B-14. Axial Stress Difference Versus Axial, Radial, and Volumetric Strain for a Constant Mean Stress Test on McIntosh Salt Specimen MD/BG2/4191.0.

Figure B-15. Axial Stress Difference Versus Axial, Radial, and Volumetric Strain for a Constant Mean Stress Test on McIntosh Salt Specimen MD/BG2/4139.8.

Figure B-16. Axial Stress Difference Versus Axial, Radial, and Volumetric Strain for a Constant Mean Stress Test on McIntosh Salt Specimen MD/BG2/4136.0.
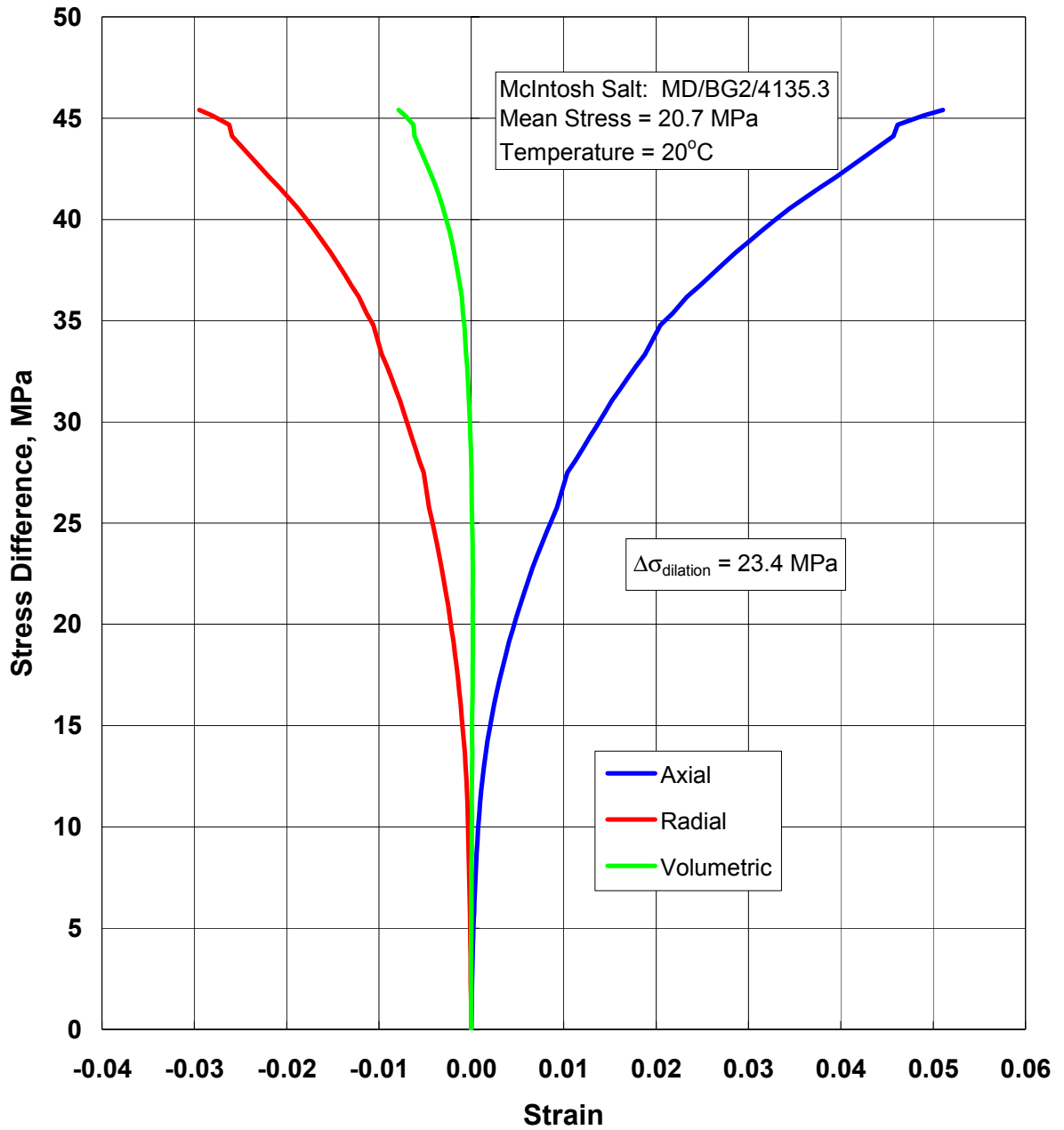
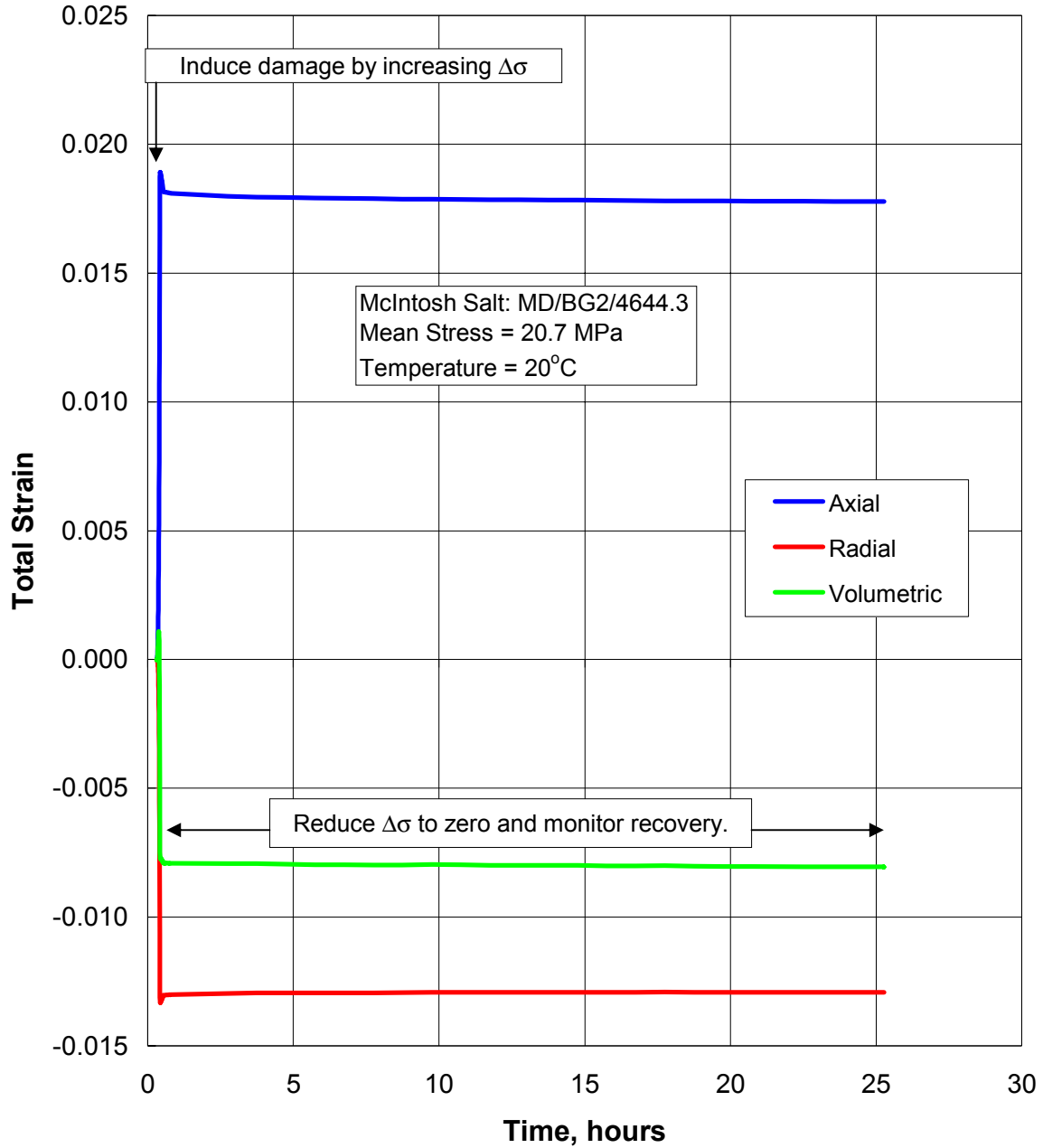**Figure B-17.** Axial Stress Difference Versus Axial, Radial, and Volumetric Strain for a Constant Mean Stress Test on McIntosh Salt Specimen MD/BG2/4191.7.

Figure B-18. Axial Stress Difference Versus Axial, Radial, and Volumetric Strain for a Constant Mean Stress Test on McIntosh Salt Specimen MD/BG2/4135.3.

Figure B-19. Axial, Radial, and Volumetric Strain as a Function of Time for a Constant Mean Stress Test on McIntosh Salt Specimen MD/BG2/4644.3.
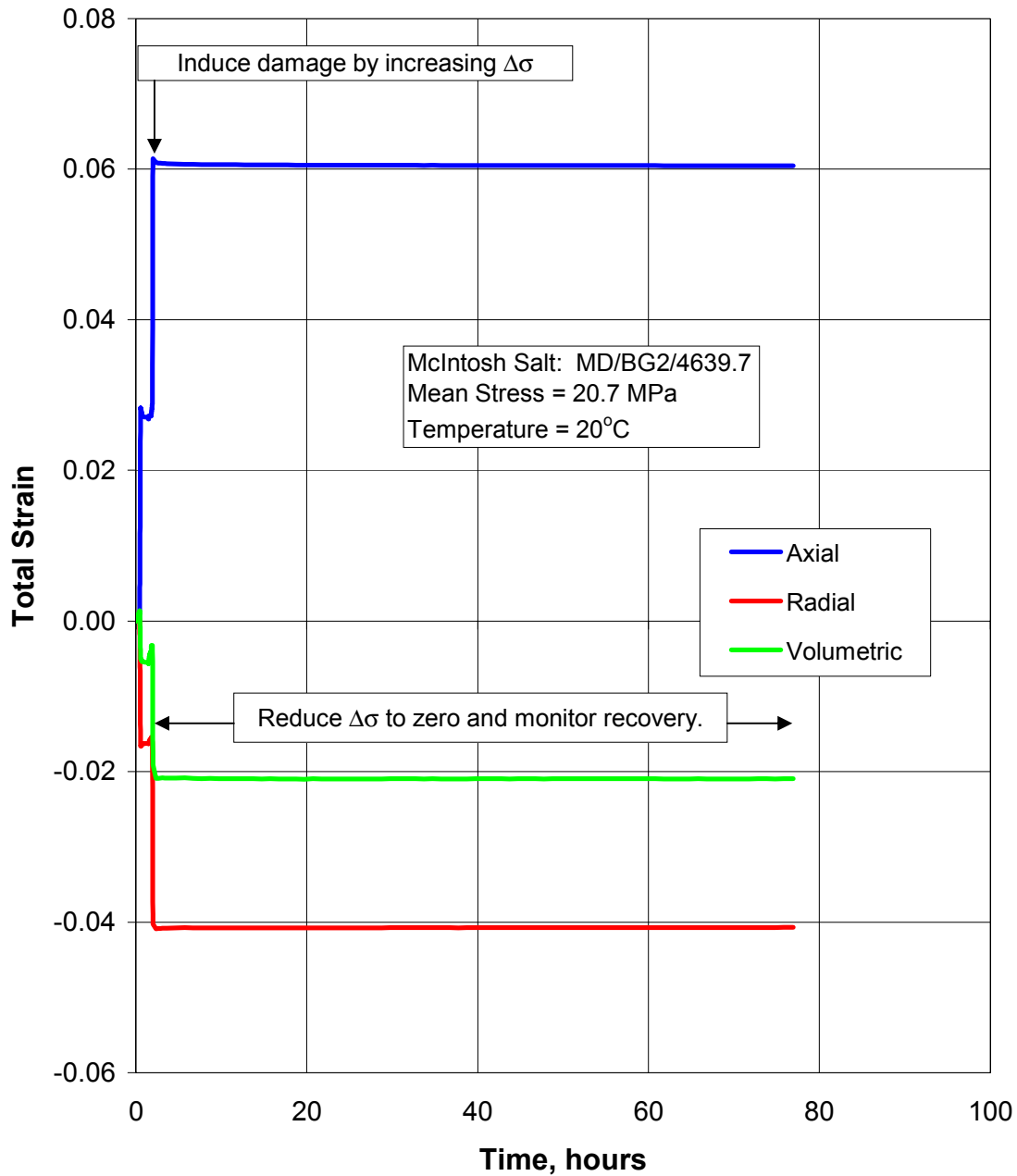
Figure B-20. Axial, Radial, and Volumetric Strain as a Function of Time for a Constant Mean Stress Test on McIntosh Salt Specimen MD/BG2/4639.7.

Figure B-21. Constant Stress Creep Test for McIntosh Salt Specimen MD/BG2/4133.4 (Stages 1 and 2 of 5).

Figure B-22. Constant Stress Creep Test for McIntosh Salt Specimen MD/BG2/4133.4 (Stages 3, 4, and 5 of 5).

Figure B-23. Constant Stress Creep Test for McIntosh Salt Specimen MD/BG2/4143.2 (Stage 1 of 1).

Figure B-24. Constant Stress Creep Test for McIntosh Salt Specimen MD/BG2/4145.8 (Stages 1, 2, and 3 of 3).
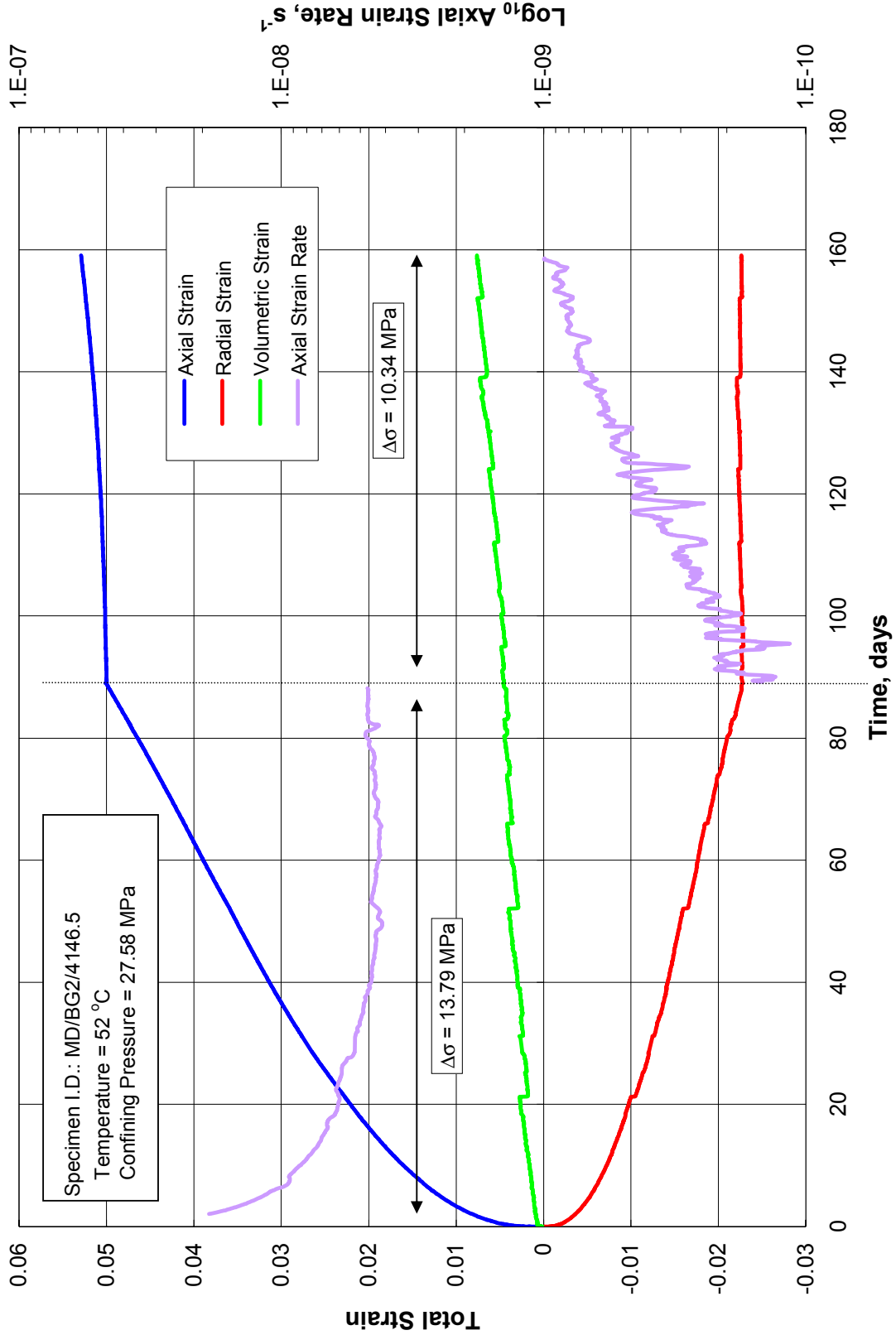
Figure B-25. Constant Stress Creep Test for McIntosh Salt Specimen MD/BG2/4146.5 (Stages 1 and 2 of 2).
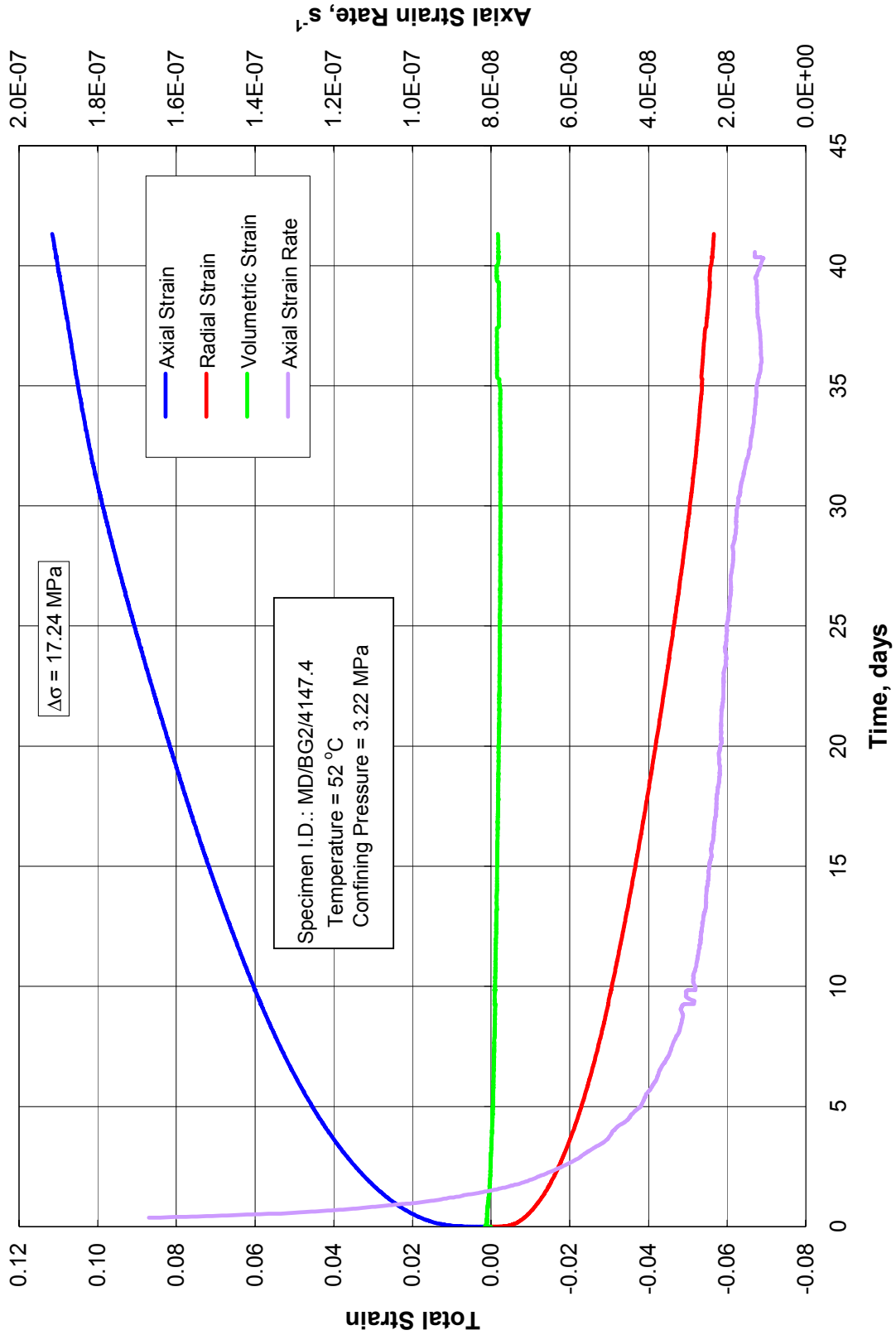
Figure B-26. Constant Stress Creep Test for McIntosh Salt Specimen MD/BG2/4147.4 (Stage 1 of 1).
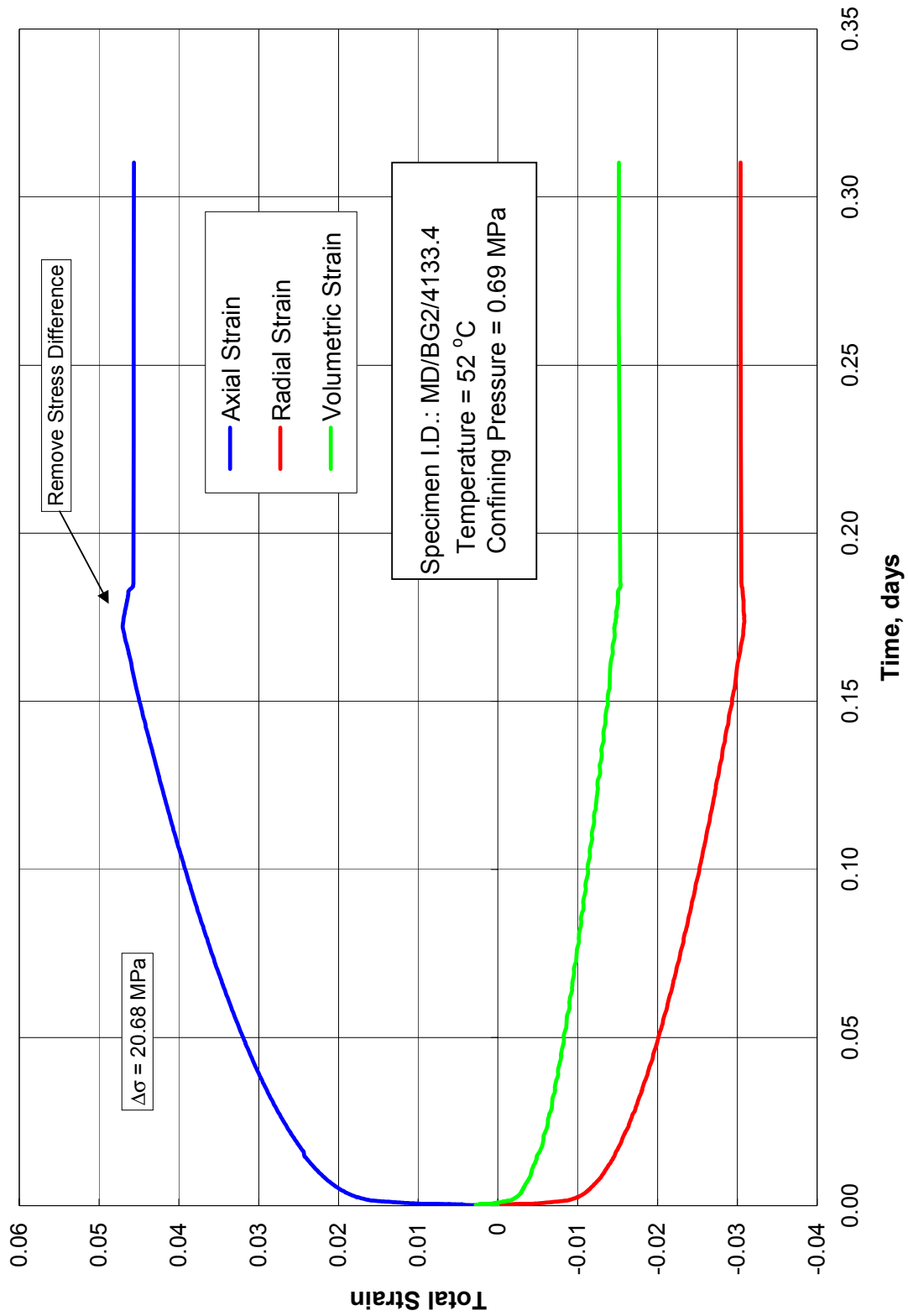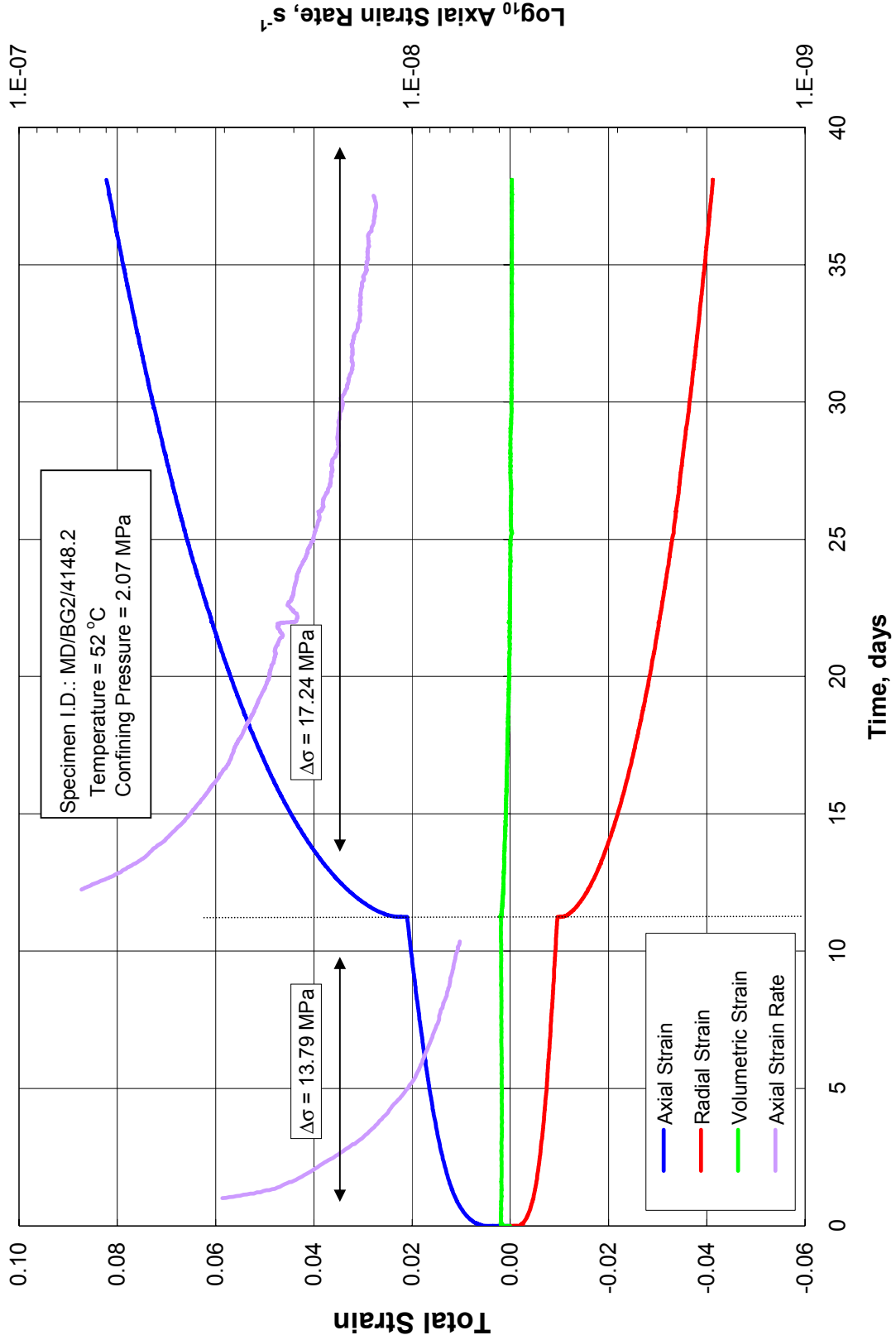
Figure B-27. Constant Stress Creep Test for McIntosh Salt Specimen MD/BG2/4148.2 (Stages 1 and 2 of 2).
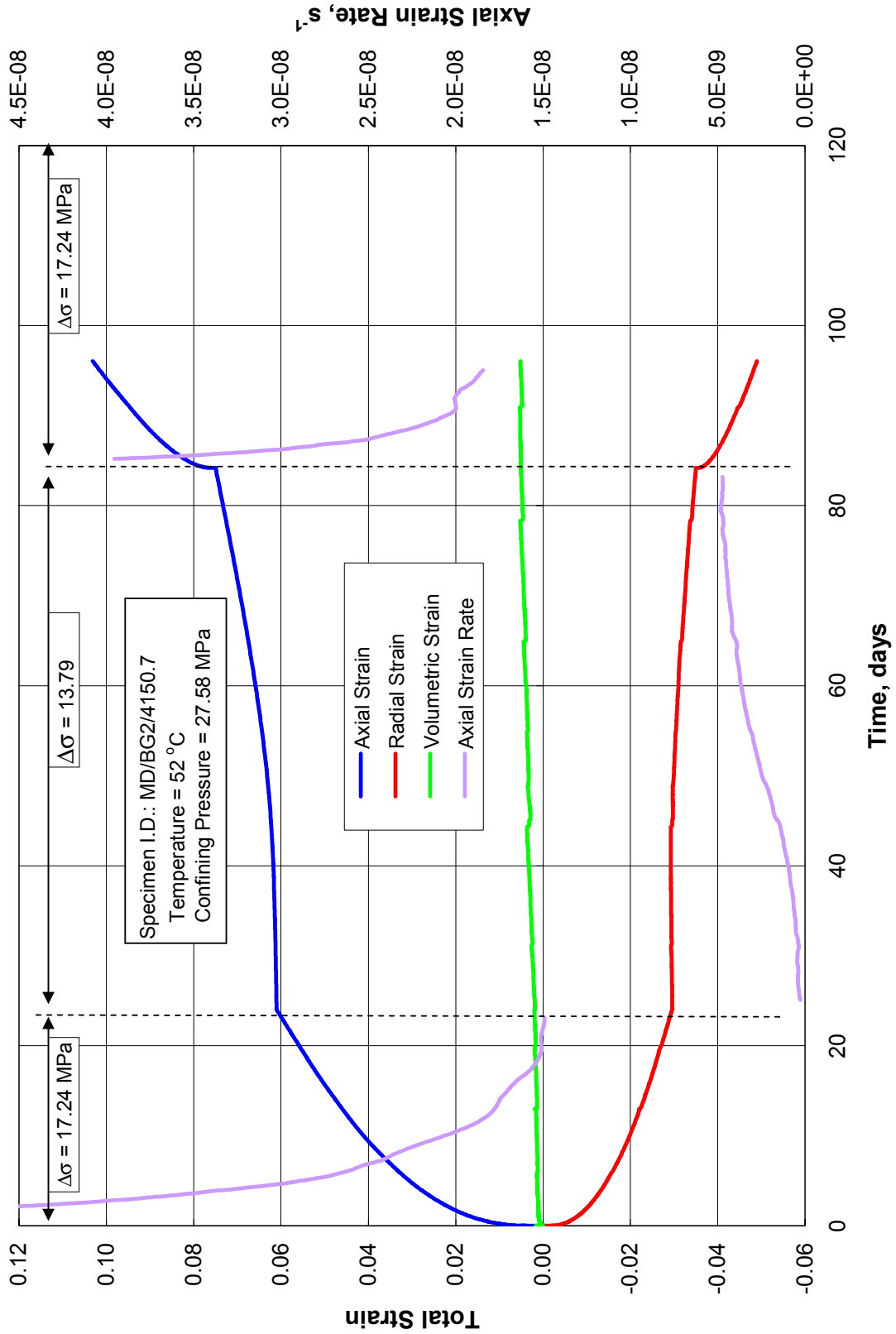
Figure B-28. Constant Stress Creep Test for McIntosh Salt Specimen MD/BG2/4150.7 (Stages 1, 2, and 3 of 3).
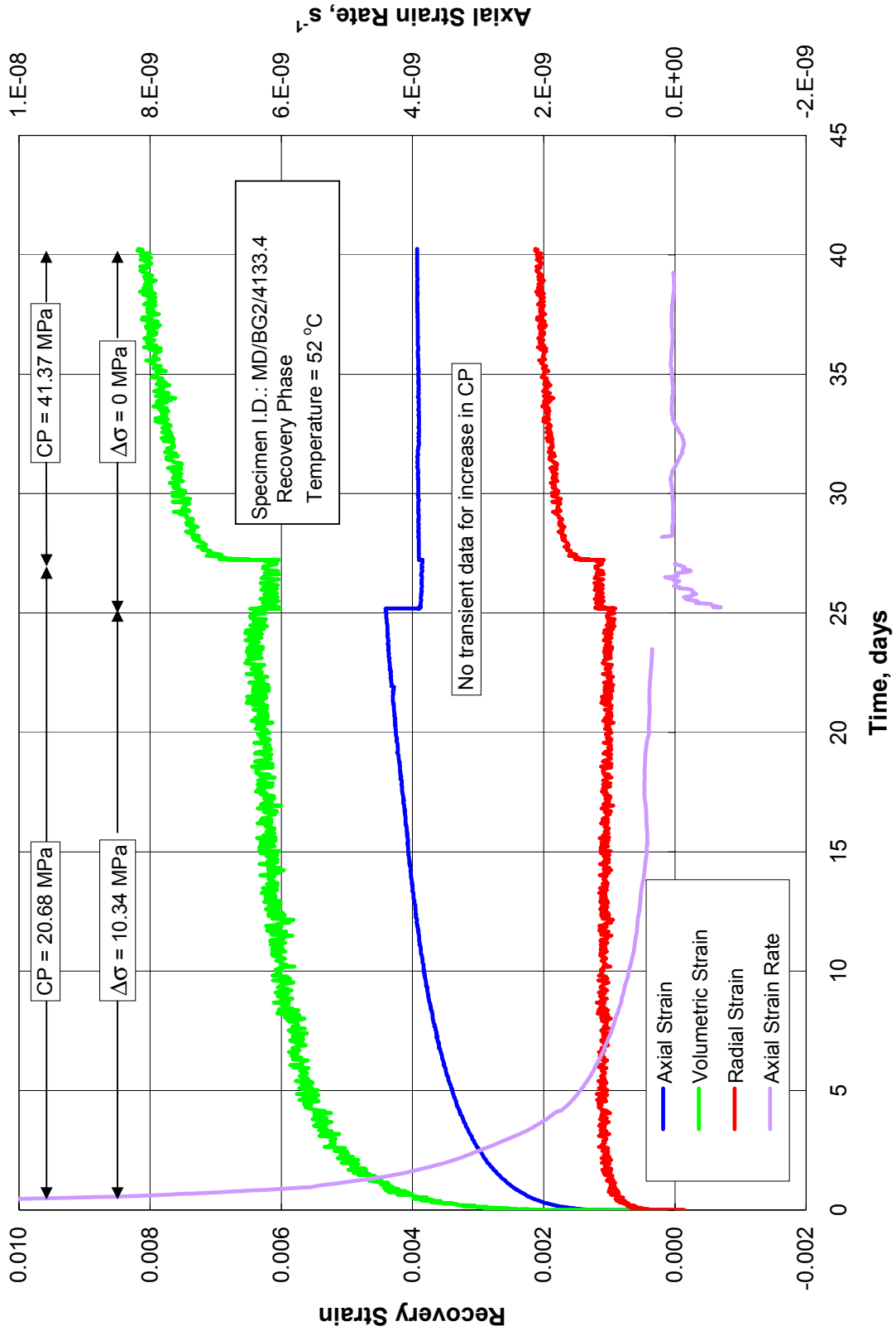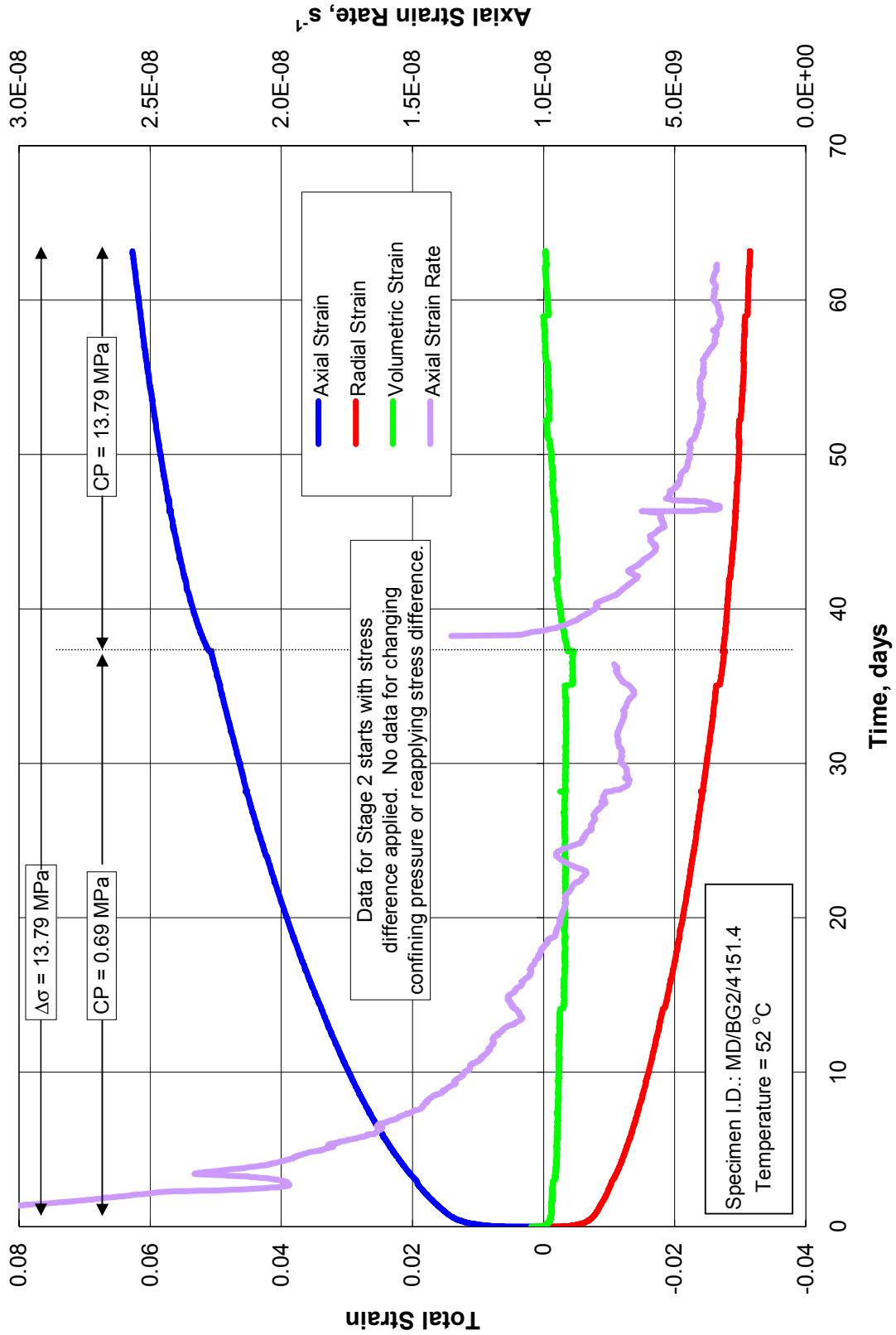
Figure B-29. Constant Stress Creep Test for McIntosh Salt Specimen MD/BG2/4151.4 (Stages 1 and 2 of 2).
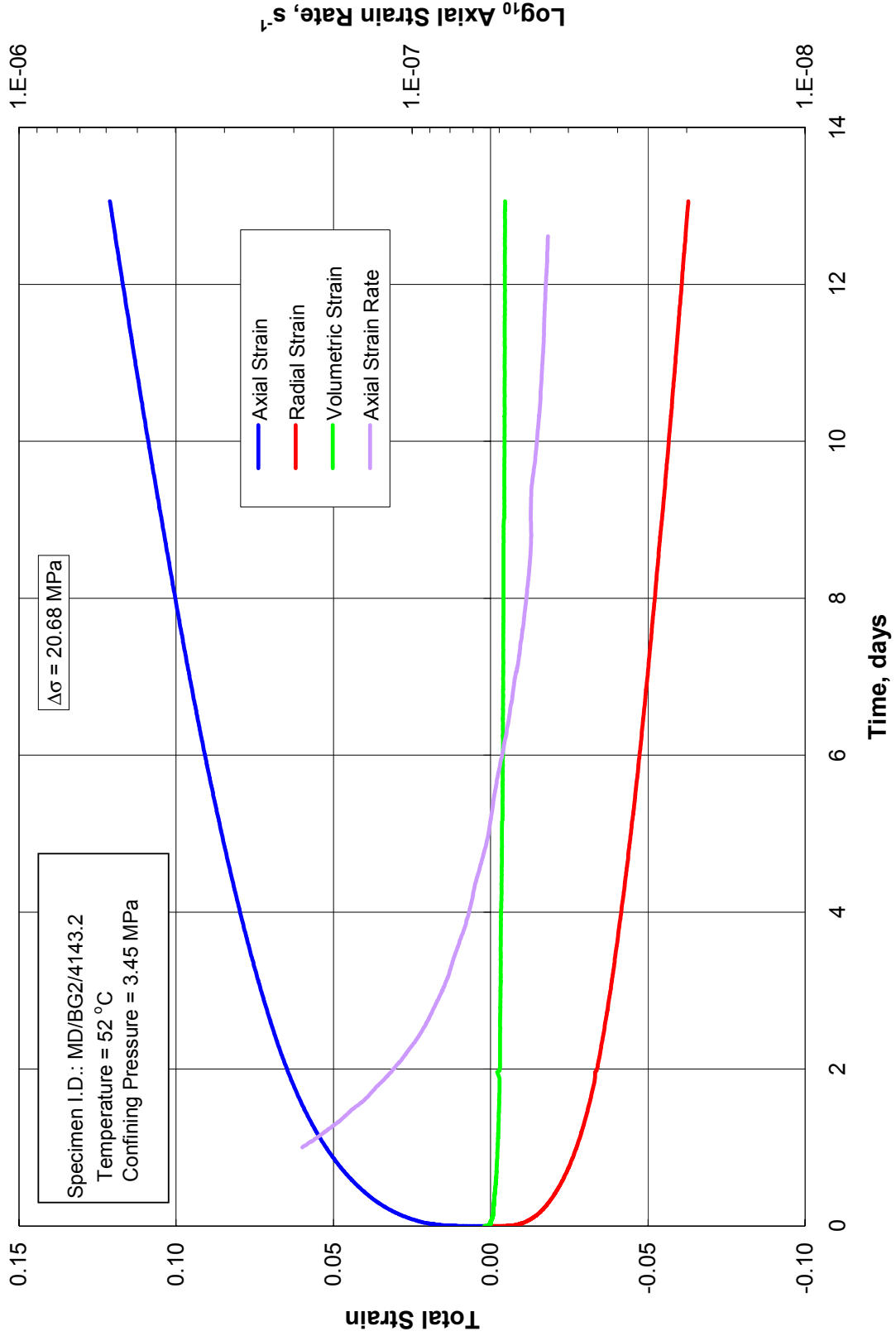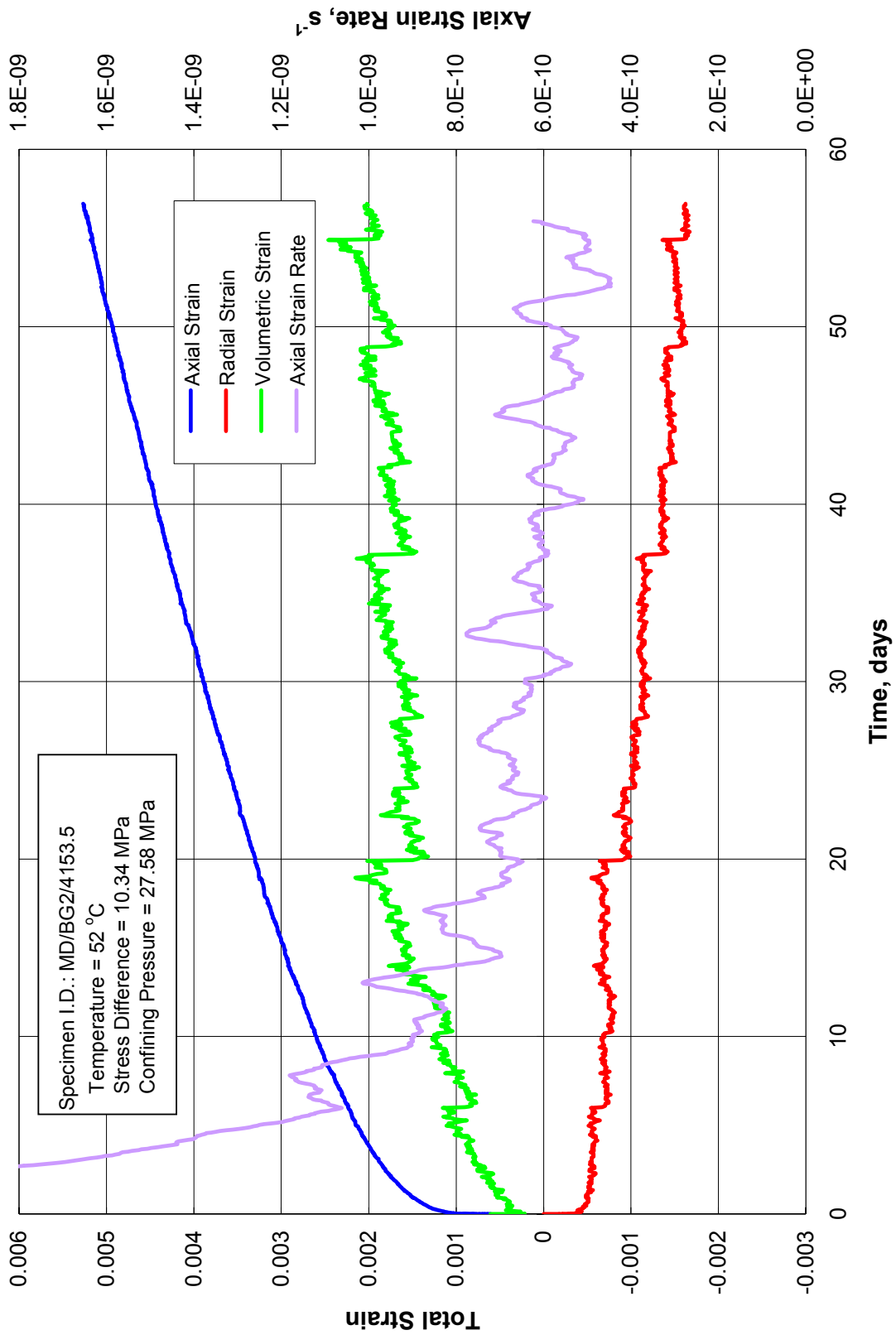
Figure B-30. Constant Stress Creep Test for McIntosh Salt Specimen MD/BG2/4153.5 (Stage 1 of 1).

Figure B-31. Constant Stress Creep Test for McIntosh Salt Specimen MD/BG2/4155.0 (Stage 1 of 1).

Figure B-32. Constant Stress Creep Test for McIntosh Salt Specimen MD/BG2/4156.3 (Stage 1 of 2).

Figure B-33. Constant Stress Creep Test for McIntosh Salt Specimen MD/BG2/4156.3 (Stage 2 of 2).

Figure B-34. Constant Stress Creep Test for McIntosh Salt Specimen MD/BG2/4641.5 (Stage 1 of 1).
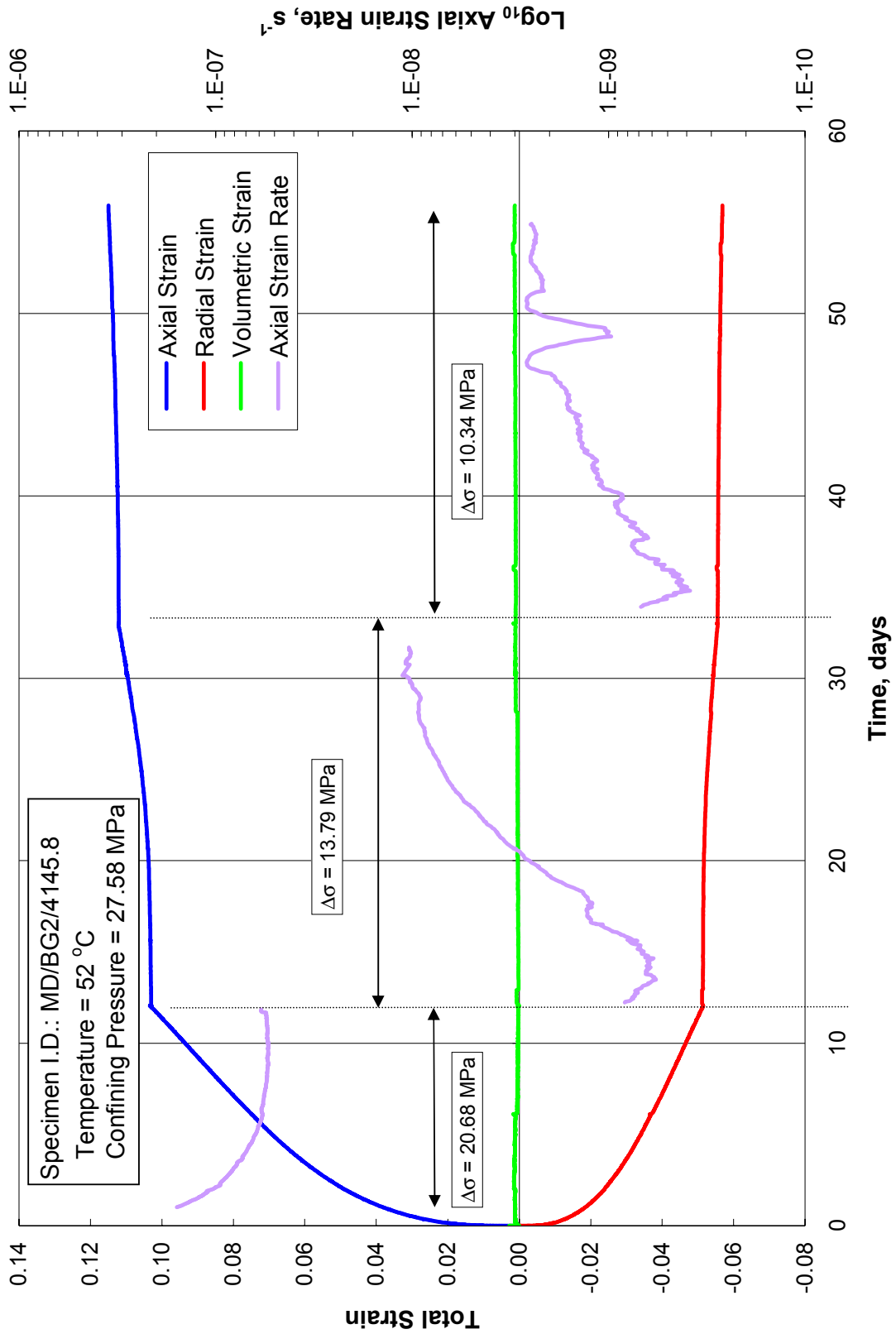
Figure B-35. Constant Stress Creep Test for McIntosh Salt Specimen MD/BG2/4642.2 (Stage 1 of 1).
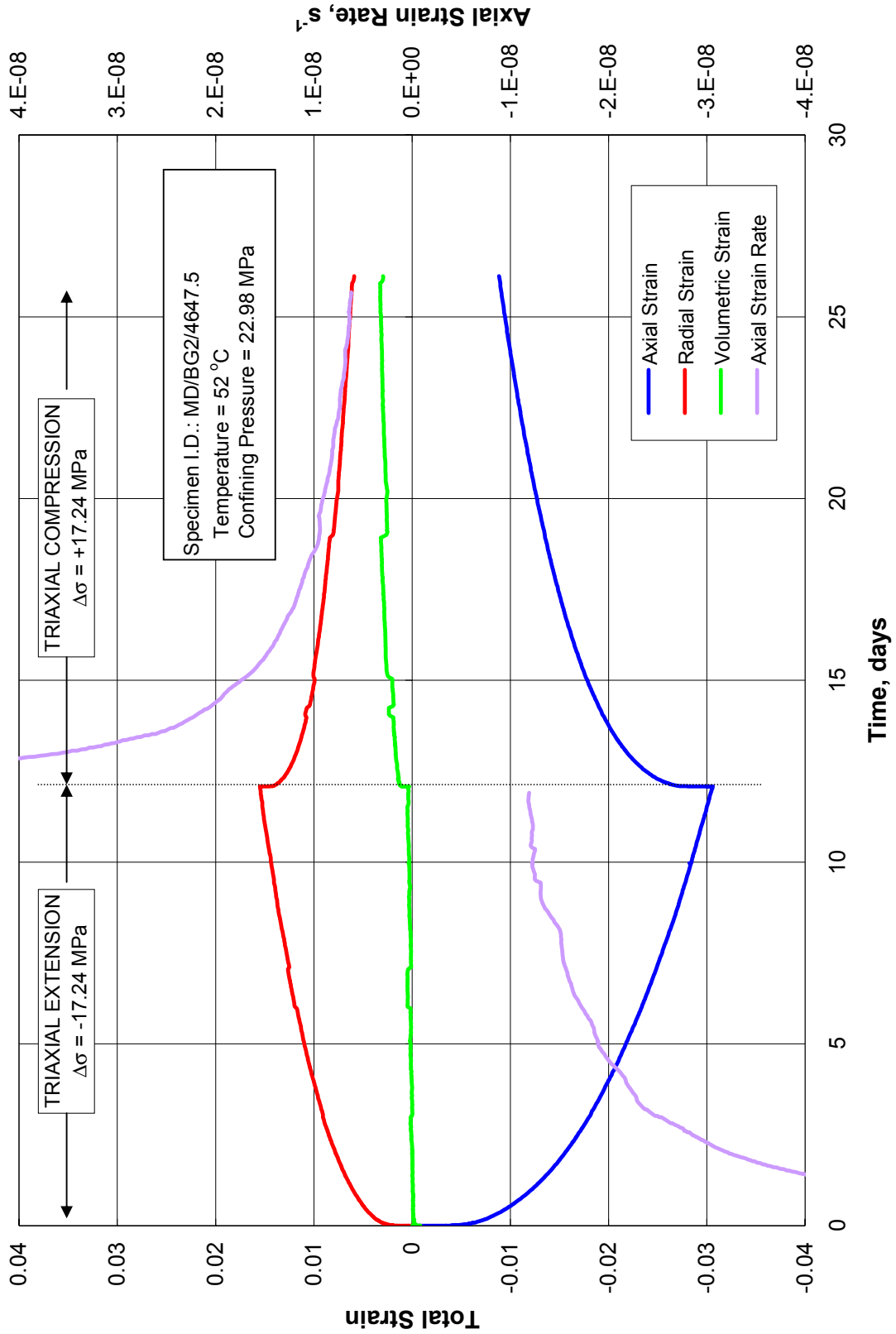
Figure B-36. Constant Stress Creep Test for McIntosh Salt Specimen MD/BG2/4647.5 (Stages 1 and 2 of 2).

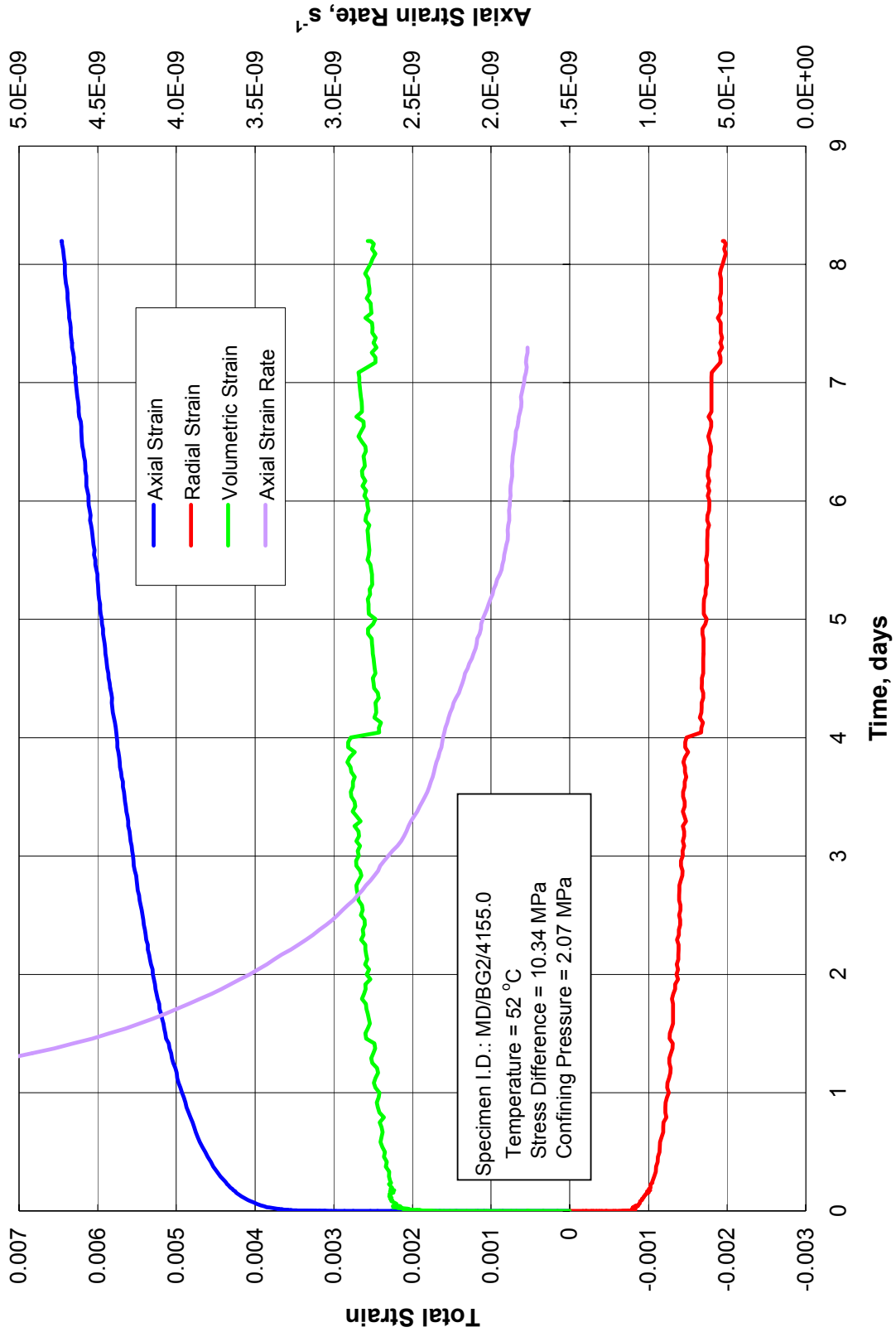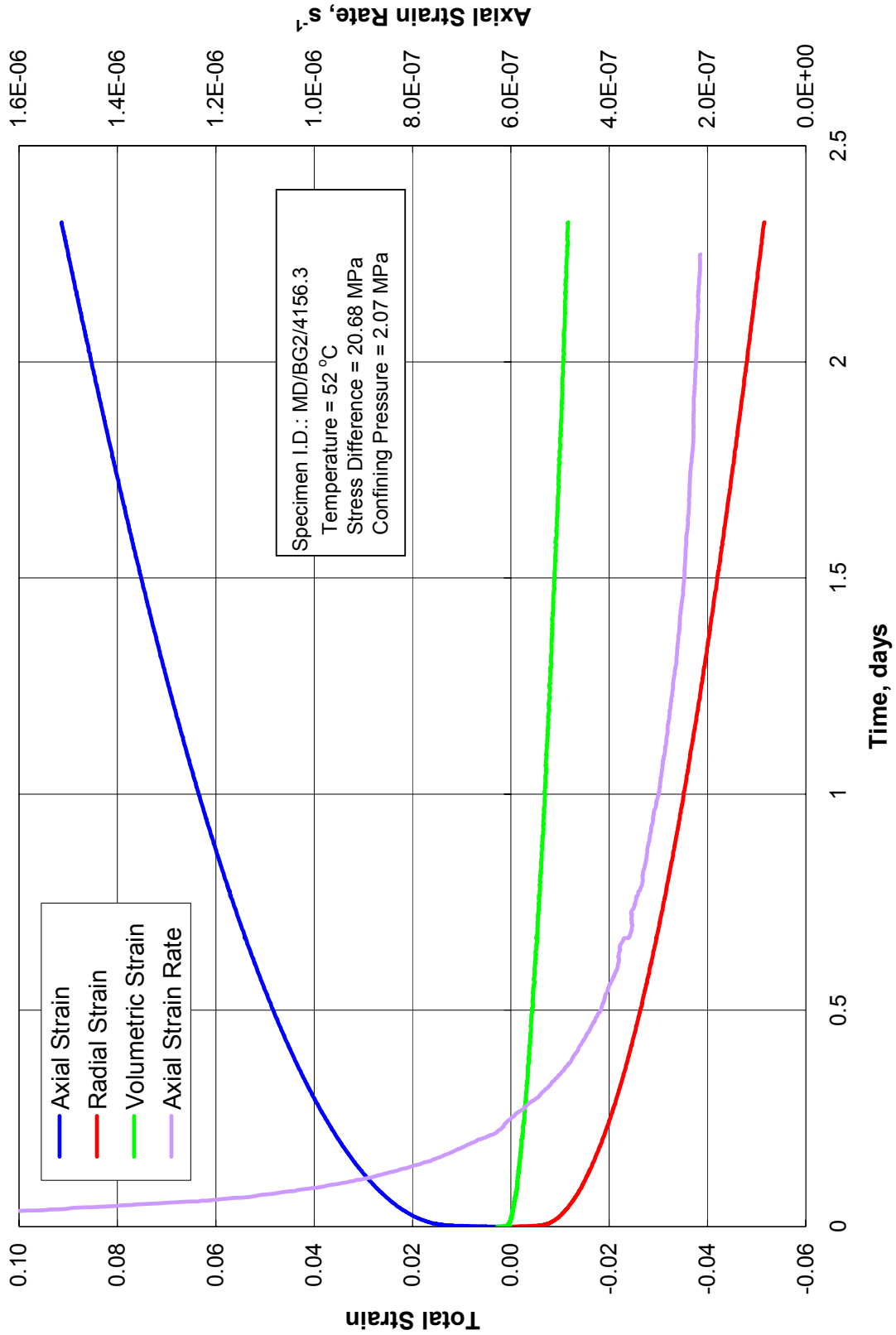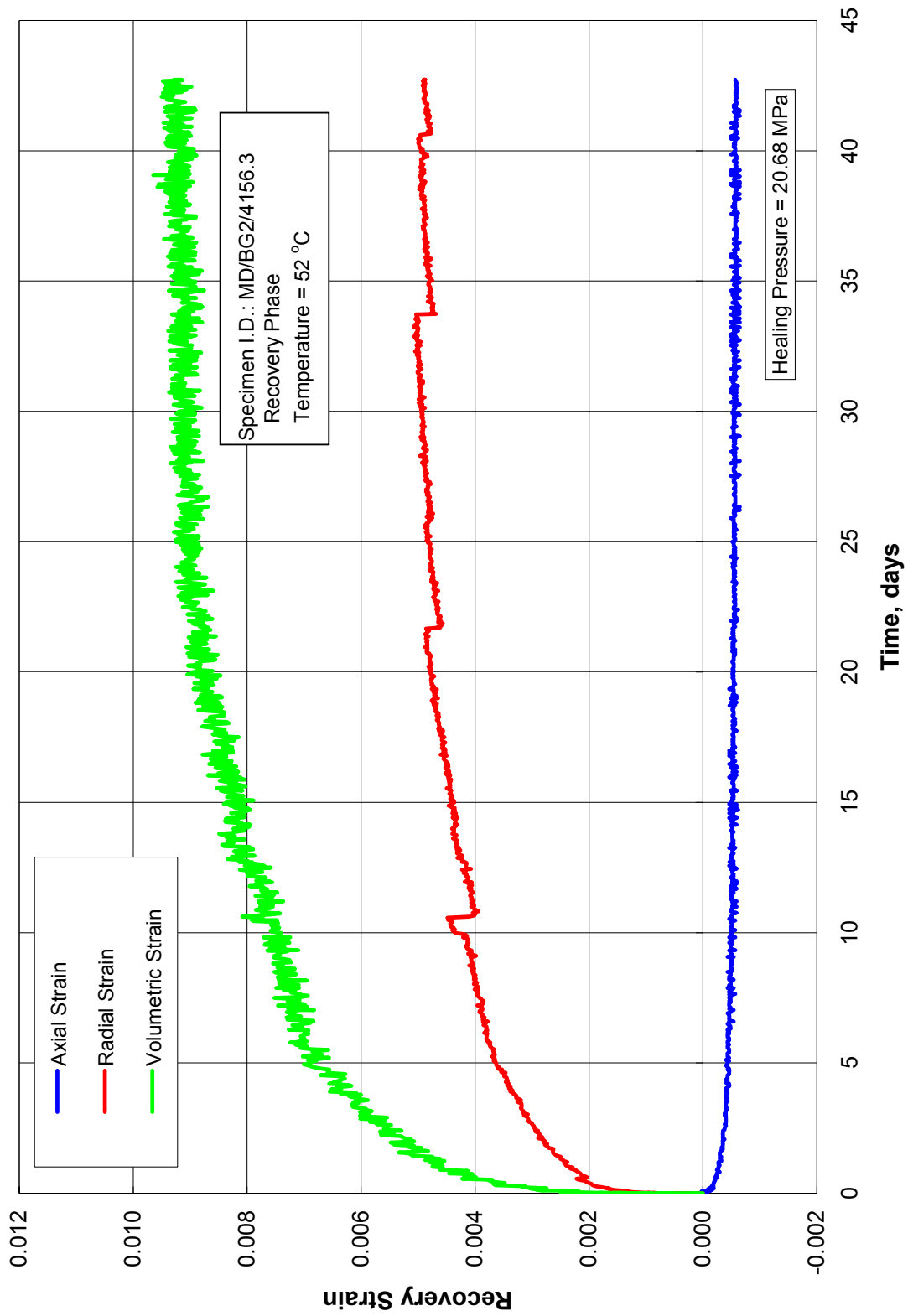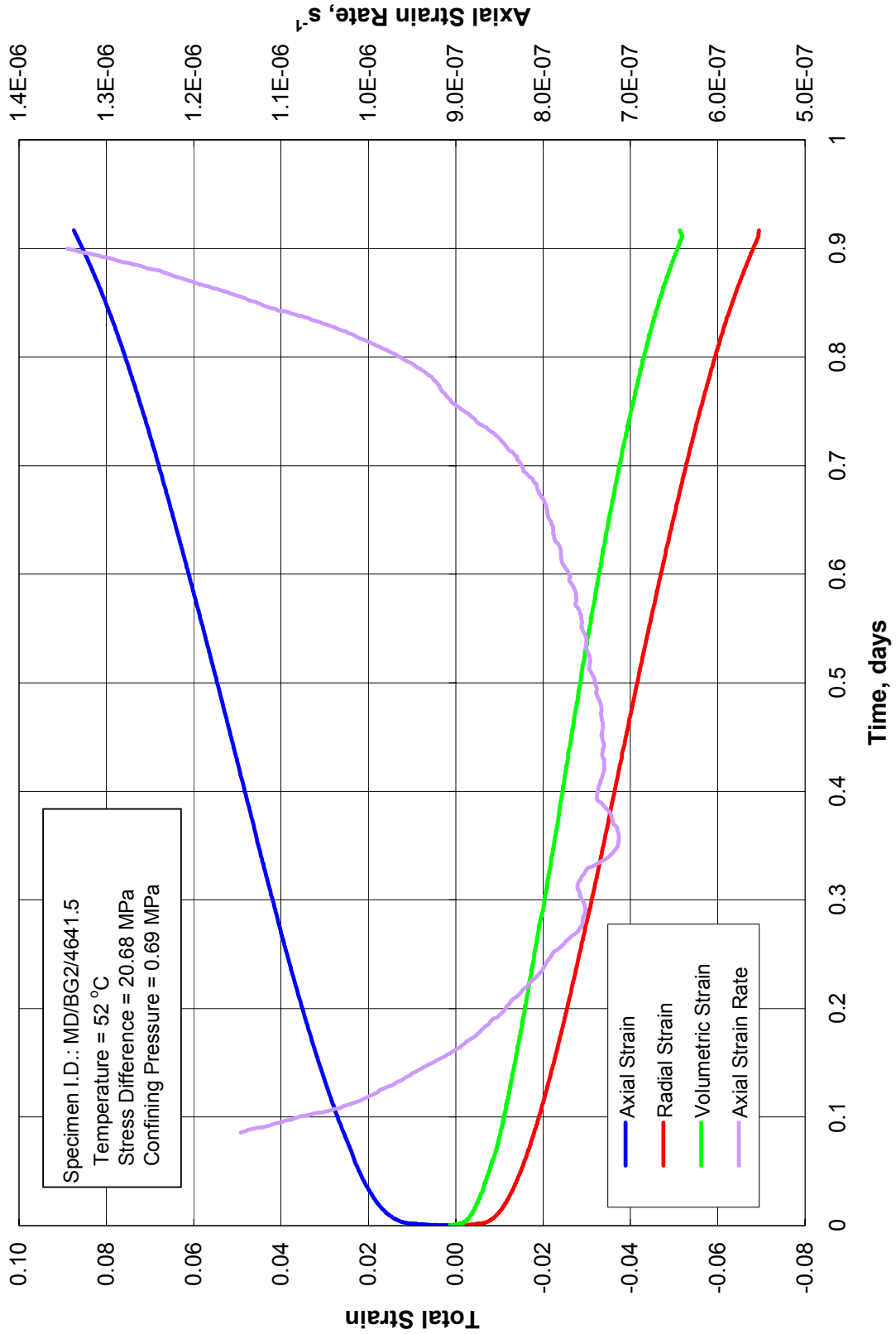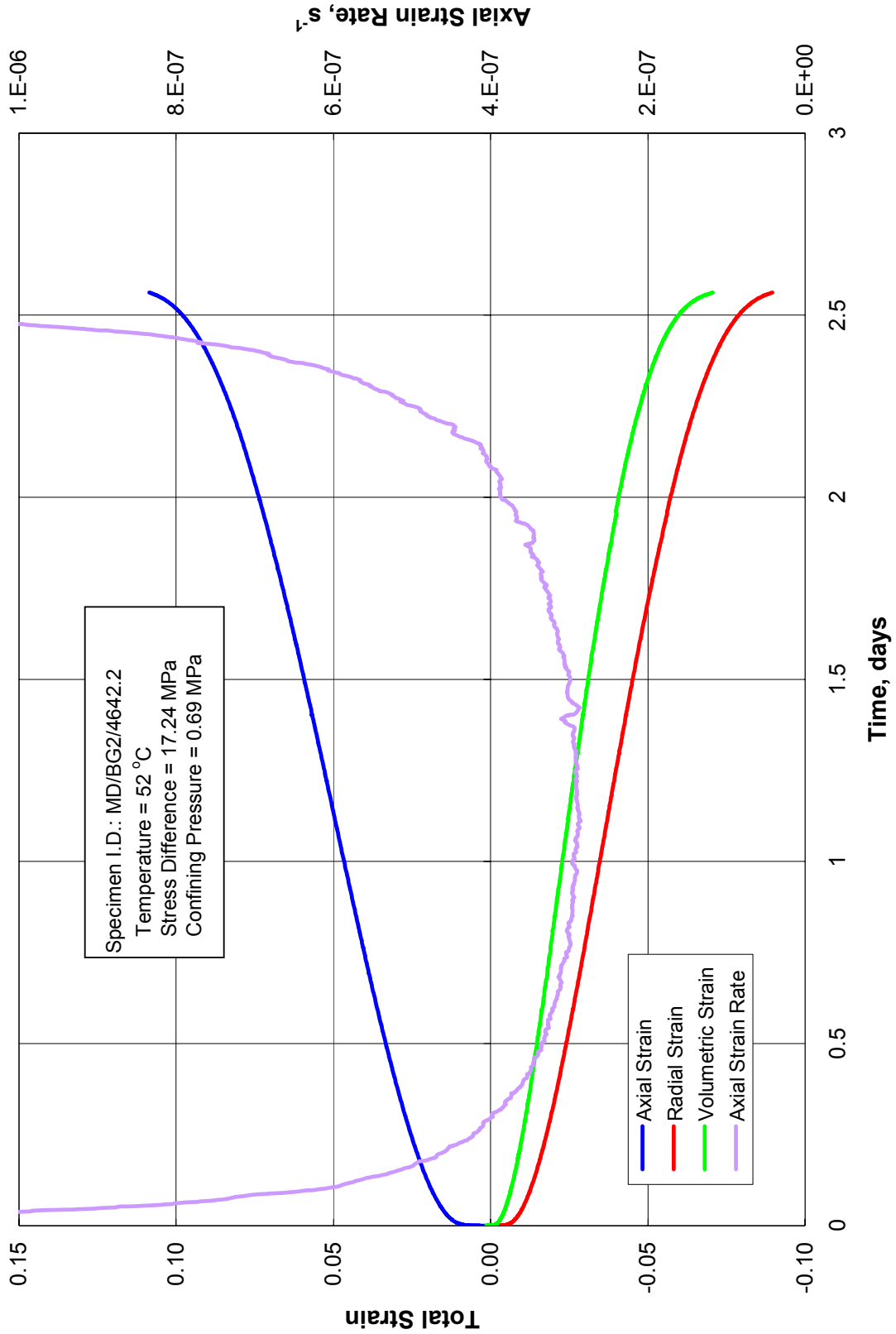**APPENDIX C**

**REVISED MATHEMATICAL FORMULATION
OF THE MDCF MODEL HEALING TERM**

TABLE OF CONTENTS

APPENDIX C
REVISED MATHEMATICAL FORMULATION
OF THE MDCF MODEL HEALING TERM

C.1 DEVELOPMENT OF THE REVISED MDCF MODEL HEALING FORMULATION

The total inelastic strain rate in the MDCF model is represented by three components:

$$\dot{\varepsilon}_{ij}^{i} = \dot{\varepsilon}_{ij}^{c} + \dot{\varepsilon}_{ij}^{d} + \dot{\varepsilon}_{ij}^{h} \tag{C-1}$$

The first inelastic strain rate represents dislocation-controlled creep; the second inelastic strain rate represents damage accumulation in the model; and the third inelastic strain rate represents healing in the model, which is our main interest. The kinetic equation representing the healing or damage recovery is written as:

$$\dot{\varepsilon}_{ij}^{h} = \dot{\varepsilon}_{eq}^{h} \frac{\partial \sigma_{eq}^{h}}{\partial \sigma_{ij}} \tag{C-2}$$

where σ_{eq}^{h} and $\dot{\varepsilon}_{eq}^{h}$ are the power-conjugate equivalent stress measure and the equivalent inelastic strain rate for the healing mechanism, respectively. The healing strain rate is written as:

$$\dot{\varepsilon}_{eq}^{h} = \frac{\varepsilon_{kk}^{i} \left(\sigma_{eq}^{h^{*}} - \sigma_{b} \right) H \left(\sigma_{b} - \sigma_{eq}^{h^{*}} \right)}{\tau \, \mu} \tag{C-3}$$

where ε_{kk}^{i} is the inelastic volumetric strain, τ is a characteristic time constant, and μ is the shear modulus. $H(\bullet)$ is the Heaviside function; thus, the healing rate is zero if the equivalent stress measure is less than σ_{b}. The addition of the Heaviside function is a modification of the form originally given by Chan et al. [1995]. The equivalent stress measure ($\sigma_{eq}^{h^{*}}$) used to describe the magnitude of the healing strain rate is different than the power-conjugate equivalent stress measure used to describe the flow potential (nonassociative formulation) and is given by:

$$\sigma_{eq}^{h^{*}} = \frac{1}{3} \left(I_{1} - \sigma_{3} \right) \tag{C-4}$$

where I_{1} is the first invariant of the stress tensor and σ_{3} is the minor (minimum) principal stress. The value for σ_{b} is determined from the shear-induced, power-conjugate equivalent stress measure for damage accumulation ($\sigma_{eq}^{\omega_{s}}$), which is written as:

$$\sigma_{eq}^{\omega_{s}} = \left| \sigma_{1} - \sigma_{3} \right| + f_{p} \, x_{2} \, x_{7} \, \text{sgn} \left(I_{1} - \sigma_{3} \right) \left[\frac{I_{1} - \sigma_{3}}{3 x_{7} \, \text{sgn} \left(I_{1} - \sigma_{3} \right)} \right]^{x_{6}} \tag{C-5}$$

where σ_1 is the major (maximum) principal stress; x_2, x_6, and x_7 are material parameters; sgn($\bullet$) represents the sign of its argument; and f_p is a material parameter related to the impurity content by:

$$f_p = 1 - p_1 \rho \tag{C-6}$$

where ρ is the impurity content and p_1 is a material parameter. Solving for $\sigma_{eq}^{h^*}$ when $\sigma_{eq}^{\omega_s} = 0$ yields the value for σ_b; viz,

$$\sigma_b = -x_7 \left[\frac{\sigma_1 - \sigma_3}{f_p \, x_2 \, x_7} \right]^{\frac{1}{x_6}} \tag{C-7}$$

The quantity $\sigma_{eq}^{h^*} - \sigma_b$ coincides with the damage equivalent stress measure when $\sigma_{eq}^{\omega_s} = 0$ so that a distinct boundary exists between damage accumulation and damage recovery (healing), and the processes are noncompeting. The characteristic time constant is taken to be a function of the inelastic volumetric strain and is written as:

$$\tau = \tau_0 \exp\left(-k_1 \varepsilon_{kk}^i\right) + \tau_1 \tag{C-8}$$

where k_1, τ_0, and τ_1 are material constants. When the volumetric strain is large, the exponential term becomes insignificant and the limiting value for τ is τ_1. τ_1 is then the characteristic time associated with microcrack crack closure when the level of damage is high. When the inelastic volumetric strain becomes small, the limiting value of τ is $\tau_0 + \tau_1$, which is the characteristic time constant associated with crack sintering.

Damage (ω) is described in terms of an evolutionary equation as:

$$\dot{\omega} = \dot{\omega}_s + \dot{\omega}_t - h\left(\omega, \sigma_{eq}^{h^*}\right) \tag{C-9}$$

where subscripts s and t represent the shear- and tension-induced damage accumulation rates, respectively, and h represents the damage recovery (healing) function. The healing portion of the equation is taken from Chan [1996] with a modification to halt healing when the material returns to its initial damage state:

$$h = \frac{\omega \; H(\omega - \omega_0) \; \left(\sigma_{eq}^{h^*} - \sigma_b\right) \; H\left(\sigma_b - \sigma_{eq}^{h^*}\right)}{\tau \, \mu} \tag{C-10}$$

The stress normal to the initial damage accumulation is adopted as the effective stress measure governing the flow potential. The assumption used is that microfractures will be generated parallel to the minor principal stress and that further damage accumulation will not alter the orientation of the microfractures. Thus the principal stress angle (at the initiation of damage accumulation) defines the orientation of the damage. Subsequently, when and if

C-4

conditions for damage recovery occur, the recovery (crack closure and sintering) will occur normal to the microfractures as dictated by the principal angle. Thus the power-conjugate equivalent stress measure (cf. Equation C-2) is written as:

$$\sigma_{eq}^h = \sigma_n \tag{C-11}$$

where σ_n is the stress normal to the damage defined by:

$$\sigma_n = \frac{\sigma_1 + \sigma_3}{2} + \frac{\sigma_1 - \sigma_3}{2} \cos(2\theta) \tag{C-12}$$

where:

σ_i = principal stresses ($i = 1, 3$)

$$\theta = \frac{\pi}{2} - \alpha + d \tag{C-13}$$

α = principal stress angle ($+$ccw from $+$x-axis)

d = damage angle ($+$ccw from $+$x-axis).

The principal stress angle can be defined in terms of the stress components in the plane and is written as:

$$\theta = \frac{1}{2}\tan^{-1}\left[\frac{2\sigma_{xy}}{\sigma_{xx} - \sigma_{yy}}\right] = \frac{1}{2}\tan^{-1}\left[\frac{2\sigma_{rz}}{\sigma_{rr} - \sigma_{zz}}\right] \tag{C-14}$$

For two-dimensional planar and axisymmetric problems, the out-of-plane and tangential stresses are always principal stresses. Thus the above definition of the normal stress only holds true when the out-of-plane or tangential stress is the intermediate principal. Cases where the out-of-plane or tangential principal stresses are the maximum or minimum principal stresses will be formulated following their consideration as the intermediate principal stress. From the above definition of normal stress, the flow potential for healing is written as:

$$\frac{\partial \sigma_{eq}^h}{\partial \sigma_{ij}} = \frac{\partial \sigma_n}{\partial \sigma_{ij}} = \frac{1}{2}\left\{\frac{\partial(\sigma_1 + \sigma_3)}{\partial \sigma_{ij}} + \frac{\partial(\sigma_1 - \sigma_3)}{\partial \sigma_{ij}}\cos(2\theta) + (\sigma_1 - \sigma_3)\frac{\partial \cos(2\theta)}{\partial \sigma_{ij}}\right\} \tag{C-15}$$

Performing the indicated tensor differentiation produces:

$$\frac{\partial \sigma_{eq}^h}{\partial \sigma_{ij}} = \frac{1}{2}\left\{\begin{array}{l} \dfrac{2\delta_{ij}}{3} + \dfrac{\sin(2\psi)}{\cos(3\psi)}\dfrac{s_{ij}}{\sqrt{3J_2}} + \dfrac{\cos(\psi)}{\cos(3\psi)}\dfrac{t_{ij}}{J_2} + \\[2ex] \left[\dfrac{\cos(2\psi)}{\cos(3\psi)}\dfrac{s_{ij}}{\sqrt{J_2}} + \dfrac{\sqrt{3}\sin(\psi)}{\cos(3\psi)}\dfrac{t_{ij}}{J_2}\right]\cos(2\theta) + \tau_{ij} \end{array}\right\} \tag{C-16}$$

C-5

where:

$$\delta_{ij} = \begin{cases} 1 & \text{if} \quad i = j \\ 0 & \text{if} \quad i \neq j \end{cases} \quad \text{(Kronecker delta)}$$

$$s_{ij} = \sigma_{ij} - \sigma_m \delta_{ij} \quad \text{(deviatoric stress)}$$

$$\sigma_m = \frac{\sigma_{kk}}{3} \quad \text{(mean stress)}$$

$$t_{ij} = s_{ik} \; s_{kj} - \frac{2}{3} J_2 \; \delta_{ij} \quad \text{(deviator of the square of the reduced stress)}$$

$$\psi = \frac{1}{3} \sin^{-1} \left[\frac{-3\sqrt{3}}{2} \frac{J_3}{J_2^{3/2}} \right] \quad \text{(Lode angle)}$$

$$J_2 = \frac{1}{2} \; s_{ij} \; s_{ji} \quad \text{(2^{nd} invariant of stress deviator)}$$

$$J_3 = \frac{1}{3} \; s_{ij} \; s_{jk} \; s_{ki} \quad \text{(3^{rd} invariant of stress deviator).}$$

τ_{ij} represents the last term in the differential in Equation C-15 given by:

$$\tau_{ij} = \left(\sigma_1 - \sigma_3 \right) \frac{\partial \cos(2\theta)}{\partial \sigma_{ij}} \tag{C-17}$$

with components defined by:

$$\tau_{11} = - \frac{\sin(2\theta)}{R} \sigma_{12}$$

$$\tau_{22} = \frac{\sin(2\theta)}{R} \sigma_{12}$$

$$\tau_{12} = \frac{\sin(2\theta)}{2R} \left(\sigma_{11} - \sigma_{22} \right) \tag{C-18}$$

$$\tau_{33} = 0$$

where:

$$R = \left[\left(\frac{\sigma_{11} + \sigma_{22}}{2} \right)^2 + \sigma_{12}^2 \right]^{\frac{1}{2}} \tag{C-19}$$

The flow potential is seen to be undefined when the Lode angle is ±30°. In other words, the flow potential forms corners for these values of the Lode angle. This occurs when two principal stress components are equal. If the two equal stress components are the major principal stress, a state of stress termed triaxial compression exists and the Lode angle is +30°. If the two equal

C-6

stress components are the minor principal stress, a state of stress termed triaxial extension exists and the Lode angle is −30°. At these corners, the direction of straining is not unique. To eliminate this problem computationally, the flow potentials on either side of the corner are averaged, which produces an indeterminate form that is examined in the limit as the Lode angle approaches ±30°.

At the triaxial compression corner ($\psi = 30°$), the average flow potential is written as:

$$\frac{\partial \sigma^h_{eq}}{\partial \sigma_{ij}} = \frac{1}{2} \left\{ \begin{array}{l} \left| \begin{array}{l} \dfrac{2\delta_{ij}}{3} + \dfrac{\sin\left(2\,\psi - \dfrac{\pi}{3}\right)}{2\cos(3\psi)} \dfrac{s_{ij}}{\sqrt{3J_2}} + \dfrac{\cos\left(\psi + \dfrac{\pi}{3}\right)}{2\cos(3\psi)} \dfrac{t_{ij}}{J_2} - \\[4mm] \left[\dfrac{\sqrt{3}\sin\left(2\,\psi - \dfrac{\pi}{3}\right)}{2\,\cos(3\psi)} \dfrac{s_{ij}}{\sqrt{J_2}} + \dfrac{3\cos\left(\psi + \dfrac{\pi}{3}\right)}{2\,\cos(3\psi)} \dfrac{t_{ij}}{J_2} \right] \cos(2\theta) + \tau_{ij} \end{array} \right. \end{array} \right\} \tag{C-20}$$

Examining the limit as $\psi \to 30°$, yields the flow potential at the triaxial compression corner:

$$\frac{\partial \sigma^h_{eq}}{\partial \sigma_{ij}}\Bigg|_{\substack{\lim \\ \psi \to \frac{\pi}{6}}} = \frac{1}{2}\left\{ \frac{2\delta_{ij}}{3} + \left[\cos(2\theta) - \frac{1}{3}\right]\left(\frac{s_{ij}}{\sqrt{3J_2}} - \frac{t_{ij}}{2J_2}\right) + \tau_{ij} \right\} \tag{C-21}$$

At the triaxial extension corner ($\psi = -30°$), the average flow potential is written as:

$$\frac{\partial \sigma^h_{eq}}{\partial \sigma_{ij}} = \frac{1}{2} \left\{ \begin{array}{l} \left| \begin{array}{l} \dfrac{2\delta_{ij}}{3} + \dfrac{\cos\left(2\,\psi - \dfrac{\pi}{6}\right)}{2\cos(3\psi)} \dfrac{s_{ij}}{\sqrt{3J_2}} + \dfrac{\sin\left(\psi + \dfrac{\pi}{6}\right)}{2\cos(3\psi)} \dfrac{t_{ij}}{J_2} + \\[4mm] \left[\dfrac{\sqrt{3}\,s\cos\left(2\,\psi - \dfrac{\pi}{6}\right)}{2\cos(3\psi)} \dfrac{s_{ij}}{\sqrt{J_2}} + \dfrac{3\sin\left(\psi + \dfrac{\pi}{6}\right)}{2\cos(3\psi)} \dfrac{t_{ij}}{J_2} \right] \cos(2\theta) + \tau_{ij} \end{array} \right. \end{array} \right\} \tag{C-22}$$

Examining the limit as $\psi \to -30°$, yields the flow potential at the triaxial extension corner:

$$\frac{\partial \sigma^h_{eq}}{\partial \sigma_{ij}}\Bigg|_{\substack{\lim \\ \psi \to -\frac{\pi}{6}}} = \frac{1}{2}\left\{ \frac{2\delta_{ij}}{3} + \left[\cos(2\theta) + \frac{1}{3}\right]\left(\frac{s_{ij}}{\sqrt{3J_2}} + \frac{t_{ij}}{2J_2}\right) + \tau_{ij} \right\} \tag{C-23}$$

C-7

If the out-of-plane or tangential stress in two-dimensional planar or axisymmetric problems is the maximum principal stress (i.e., σ_1), the flow potential is written in terms of the in-plane principal stresses as:

$$\frac{\partial \sigma_{eq}^h}{\partial \sigma_{ij}} = \frac{\partial \sigma_n}{\partial \sigma_{ij}} = \frac{1}{2}\left\{\frac{\partial(\sigma_2+\sigma_3)}{\partial \sigma_{ij}} + \frac{\partial(\sigma_2-\sigma_3)}{\partial \sigma_{ij}}\cos(2\theta) + (\sigma_2-\sigma_3)\frac{\partial \cos(2\theta)}{\partial \sigma_{ij}}\right\} \qquad \text{(C-24)}$$

Performing the indicated tensor differentiation produces:

$$\frac{\partial \sigma_{eq}^h}{\partial \sigma_{ij}} = \frac{1}{2}\left\{\begin{array}{c}\dfrac{2\delta_{ij}}{3} + \dfrac{\sin\left(2\psi-\dfrac{2\pi}{3}\right)}{\cos(3\psi)}\dfrac{s_{ij}}{\sqrt{3J_2}} + \dfrac{\cos\left(\psi+\dfrac{2\pi}{3}\right)}{\cos(3\psi)}\dfrac{t_{ij}}{J_2} - \\[2em] \left[\dfrac{\cos\left(2\psi-\dfrac{2\pi}{3}\right)}{\cos(3\psi)}\dfrac{s_{ij}}{\sqrt{J_2}} + \dfrac{\sqrt{3}\sin\left(\psi+\dfrac{2\pi}{3}\right)}{\cos(3\psi)}\dfrac{t_{ij}}{J_2}\right]\cos(2\theta) + \tau_{ij}\end{array}\right\} \qquad \text{(C-25)}$$

Again, the corners in the flow potential need to be evaluated. At the triaxial compression corner ($\psi = 30°$), the average flow potential is written as:

$$\frac{\partial \sigma_{eq}^h}{\partial \sigma_{ij}} = \frac{1}{2}\left\{\begin{array}{c}\dfrac{2\delta_{ij}}{3} + \dfrac{\sin\left(2\psi-\dfrac{\pi}{3}\right)}{2\cos(3\psi)}\dfrac{s_{ij}}{\sqrt{3J_2}} + \dfrac{\cos\left(\psi+\dfrac{\pi}{3}\right)}{2\cos(3\psi)}\dfrac{t_{ij}}{J_2} - \\[2em] \left[\dfrac{\sqrt{3}\sin\left(2\psi-\dfrac{\pi}{3}\right)}{2\cos(3\psi)}\dfrac{s_{ij}}{\sqrt{J_2}} + \dfrac{3\cos\left(\psi+\dfrac{\pi}{3}\right)}{2\cos(3\psi)}\dfrac{t_{ij}}{J_2}\right]\cos(2\theta) + \tau_{ij}\end{array}\right\} \qquad \text{(C-26)}$$

Examining the limit as $\psi\to30°$, yields the flow potential at the triaxial compression corner:

$$\frac{\partial \sigma_{eq}^h}{\partial \sigma_{ij}}\Bigg|_{\substack{\text{lim} \\ \psi\to\frac{\pi}{6}}} = \frac{1}{2}\left\{\frac{2\delta_{ij}}{3} + \left[\cos(2\theta)-\frac{1}{3}\right]\left(\frac{s_{ij}}{\sqrt{3J_2}} - \frac{t_{ij}}{2J_2}\right) + \tau_{ij}\right\} \qquad \text{(C-27)}$$

At the triaxial extension corner ($\psi = -30°$), the average flow potential is written as:

$$\frac{\partial \sigma_{eq}^h}{\partial \sigma_{ij}} = \frac{1}{2}\left\{\frac{2\delta_{ij}}{3} + \frac{\sin\left(2\psi-\dfrac{2\pi}{3}\right)}{\cos(3\psi)}\frac{s_{ij}}{\sqrt{3J_2}} + \frac{\cos\left(\psi+\dfrac{2\pi}{3}\right)}{\cos(3\psi)}\frac{t_{ij}}{J_2} + \tau_{ij}\right\} \qquad \text{(C-28)}$$

C-8

Examining the limit as $\psi \to -30°$, yields the flow potential at the triaxial extension corner:

$$\frac{\partial \sigma_{eq}^h}{\partial \sigma_{ij}}\bigg|_{\substack{\lim \\ \psi \to -\frac{\pi}{6}}} = \frac{1}{3}\left\{\delta_{ij} - \frac{s_{ij}}{\sqrt{3 J_2}} - \frac{t_{ij}}{2 J_2}\right\} + \frac{\tau_{ij}}{2} \qquad (C\text{-}29)$$

If the out-of-plane or tangential stress in two-dimensional planar or axisymmetric problems is the minimum principal stress (i.e., σ_3), the flow potential is written in terms of the in-plane principal stresses as:

$$\frac{\partial \sigma_{eq}^h}{\partial \sigma_{ij}} = \frac{\partial \sigma_n}{\partial \sigma_{ij}} = \frac{1}{2}\left\{\frac{\partial(\sigma_1+\sigma_2)}{\partial \sigma_{ij}} + \frac{\partial(\sigma_1-\sigma_2)}{\partial \sigma_{ij}}\cos(2\theta) + (\sigma_1-\sigma_2)\frac{\partial \cos(2\theta)}{\partial \sigma_{ij}}\right\} \qquad (C\text{-}30)$$

Performing the indicated tensor differentiation produces:

$$\frac{\partial \sigma_{eq}^h}{\partial \sigma_{ij}} = \frac{1}{2}\left\{ \begin{array}{l} \dfrac{2\delta_{ij}}{3} - \dfrac{\sin\left(2\psi-\dfrac{\pi}{3}\right)}{\cos(3\psi)}\dfrac{s_{ij}}{\sqrt{3 J_2}} - \dfrac{\cos\left(\psi+\dfrac{\pi}{3}\right)}{\cos(3\psi)}\dfrac{t_{ij}}{J_2} + \\[4ex] \left[\dfrac{\cos\left(2\psi-\dfrac{\pi}{3}\right)}{\cos(3\psi)}\dfrac{s_{ij}}{\sqrt{J_2}} + \dfrac{\sqrt{3}\sin\left(\psi+\dfrac{\pi}{3}\right)}{\cos(3\psi)}\dfrac{t_{ij}}{J_2}\right]\cos(2\theta) + \tau_{ij} \end{array} \right\} \qquad (C\text{-}31)$$

Again, the corners in the flow potential need to be evaluated. At the triaxial compression corner ($\psi = 30°$), the average flow potential is written as:

$$\frac{\partial \sigma_{eq}^h}{\partial \sigma_{ij}} = \frac{1}{2}\left\{\frac{2\delta_{ij}}{3} - \frac{\sin\left(2\psi-\dfrac{\pi}{3}\right)}{\cos(3\psi)}\frac{s_{ij}}{\sqrt{3 J_2}} - \frac{\cos\left(\psi+\dfrac{\pi}{3}\right)}{\cos(3\psi)}\frac{t_{ij}}{J_2} + \tau_{ij}\right\} \qquad (C\text{-}32)$$

Examining the limit as $\psi \to 30°$, yields the flow potential at the triaxial compression corner:

$$\frac{\partial \sigma_{eq}^h}{\partial \sigma_{ij}}\bigg|_{\substack{\lim \\ \psi \to \frac{\pi}{6}}} = \frac{1}{3}\left\{\delta_{ij} + \frac{s_{ij}}{\sqrt{3 J_2}} - \frac{t_{ij}}{2 J_2}\right\} + \frac{\tau_{ij}}{2} \qquad (C\text{-}33)$$

At the triaxial extension corner ($\psi = -30°$), the average flow potential is written as:

$$\frac{\partial \sigma_{eq}^{h}}{\partial \sigma_{ij}} = \frac{1}{2} \left\{ \begin{array}{l} \dfrac{2\delta_{ij}}{3} + \dfrac{\cos\left(2\,\psi - \dfrac{\pi}{6}\right)}{2\cos(3\,\psi)} \dfrac{s_{ij}}{\sqrt{3\,J_2}} + \dfrac{\sin\left(\psi + \dfrac{\pi}{6}\right)}{2\cos(3\,\psi)} \dfrac{t_{ij}}{J_2} + \\[4mm] \left[\dfrac{\sqrt{3}s\cos\left(2\,\psi - \dfrac{\pi}{6}\right)}{2\cos(3\,\psi)} \dfrac{s_{ij}}{\sqrt{J_2}} + \dfrac{3\sin\left(\psi + \dfrac{\pi}{6}\right)}{2\cos(3\,\psi)} \dfrac{t_{ij}}{J_2} \right]\cos(2\theta) + \tau_{ij} \end{array} \right\} \tag{C-34}$$

Examining the limit as $\psi \to -30°$, yields the flow potential at the triaxial extension corner:

$$\left.\frac{\partial \sigma_{eq}^{h}}{\partial \sigma_{ij}}\right|_{\substack{\lim \\ \psi \to -\frac{\pi}{6}}} = \frac{1}{2}\left\{ \frac{2\delta_{ij}}{3} + \left[\cos(2\theta) + \frac{1}{3}\right]\left(\frac{s_{ij}}{\sqrt{3\,J_2}} + \frac{t_{ij}}{2J_2}\right) + \tau_{ij} \right\} \tag{C-35}$$

C.2 REDUCTION TO TRIAXIAL COMPRESSION AND TRIAXIAL EXTENSION TESTS

For testing and observational purposes, it is useful to reduce the equations for healing to their simplest form under triaxial compression and triaxial extension test conditions. This work is partially accomplished in the previous section because of the indeterminacy encountered when two principal stresses are equal. Recall that the indeterminancies were evaluated in the limit as the Lode angle approaches ±30°. The equations presented in the previous section may be further simplified by substituting the numerical value of the stress invariants encountered for triaxial compression and triaxial extension. These values are:

Triaxial Compression Test

$$\sqrt{3\,J_2} = \Delta\sigma = \sigma_1 - \sigma_3$$

$$J_2 = \frac{\Delta\sigma^2}{3}$$

$$s_{11} = s_{22} = \sigma_{11} - \sigma_m = \frac{\Delta\sigma}{3} \tag{C-36}$$

$$s_{33} = \sigma_{33} - \sigma_m = -\frac{2\Delta\sigma}{3}$$

$$t_{11} = t_{22} = s_{11}^2 + s_{12}^2 - \frac{2}{3}J_2 = -\frac{\Delta\sigma^2}{9}$$

C-10

$$t_{33} = s_{33}^2 - \frac{2}{3} J_2 = \frac{2\,\Delta\sigma^2}{9}$$

$$\left(\frac{s_{11}}{\sqrt{3\,J_2}} - \frac{t_{11}}{2\,J_2} \right) = \left(\frac{s_{22}}{\sqrt{3\,J_2}} - \frac{t_{22}}{2\,J_2} \right) = \frac{1}{2}$$

$$\left(\frac{s_{33}}{\sqrt{3\,J_2}} - \frac{t_{33}}{2\,J_2} \right) = -1$$

Triaxial Extension Test

$$\sqrt{3\,J_2} = \Delta\sigma = \sigma_1 - \sigma_3$$

$$J_2 = \frac{\Delta\sigma^2}{3}$$

$$s_{11} = s_{22} = \sigma_{11} - \sigma_m = -\frac{\Delta\sigma}{3} \tag{C-37}$$

$$s_{33} = \sigma_{33} - \sigma_m = \frac{2\,\Delta\sigma}{3}$$

$$t_{11} = t_{22} = s_{11}^2 + s_{12}^2 - \frac{2}{3} J_2 = -\frac{\Delta\sigma^2}{9}$$

$$t_{33} = s_{33}^2 - \frac{2}{3} J_2 = \frac{2\,\Delta\sigma^2}{9}$$

$$\left(\frac{s_{11}}{\sqrt{3\,J_2}} + \frac{t_{11}}{2\,J_2} \right) = \left(\frac{s_{22}}{\sqrt{3\,J_2}} + \frac{t_{22}}{2\,J_2} \right) = -\frac{1}{2}$$

$$\left(\frac{s_{33}}{\sqrt{3\,J_2}} + \frac{t_{33}}{2\,J_2} \right) = 1$$

Substituting Equations C-36 and C-37 into Equations C-21 and C-23 (out-of-plane or tangential stress is the intermediate principal stress), Equations C-27 and C-29 (out-of-plane or tangential stress is major principal stress), and Equations C-33 and C-35 (out-of-plane or tangential stress is the minor principal stress) with the result substituted into Equation C-2, produces the strain rate for triaxial compression and extension tests. Performing the indicated operation and using subscripts *a, l,* and *v* for the axial, lateral, and volumetric components, respectively, produces:

Out-of-Plane or Tangential Stress is the Intermediate Principal Stress

In a triaxial compression test, $\theta = \pi$ so that the strain rates would be:

$$\dot{\varepsilon}_a^h = \dot{\varepsilon}_{eq}^h \frac{1}{2}(1 - \cos 2\theta) = 0$$

$$\dot{\varepsilon}_l^h = \dot{\varepsilon}_{eq}^h \frac{1}{4}(1 + \cos 2\theta) = \frac{\dot{\varepsilon}_{eq}^h}{2} \tag{C-38}$$

$$\dot{\varepsilon}_v^h = \dot{\varepsilon}_{eq}^h$$

In a triaxial extension test, $\theta = 0$ so that the strain rates would be:

$$\dot{\varepsilon}_a^h = \dot{\varepsilon}_{eq}^h \frac{1}{2}(1 + \cos 2\theta) = \dot{\varepsilon}_{eq}^h$$

$$\dot{\varepsilon}_l^h = \dot{\varepsilon}_{eq}^h \frac{1}{4}(1 - \cos 2\theta) = 0 \tag{C-39}$$

$$\dot{\varepsilon}_v^h = \dot{\varepsilon}_{eq}^h$$

Note that under both triaxial compression and triaxial extension conditions, $\tau_{ij} = 0$.

Out-of-Plane or Tangential Stress is the Maximum Principal Stress

In a triaxial compression test, $\theta = \pi$ so that the strain rates would be:

$$\dot{\varepsilon}_a^h = \dot{\varepsilon}_{eq}^h \frac{1}{2}(1 - \cos 2\theta) = 0$$

$$\dot{\varepsilon}_l^h = \dot{\varepsilon}_{eq}^h \frac{1}{4}(1 + \cos 2\theta) = \frac{\dot{\varepsilon}_{eq}^h}{2} \tag{C-40}$$

$$\dot{\varepsilon}_v^h = \dot{\varepsilon}_{eq}^h$$

In a triaxial extension test, $\theta = 0$ so that the strain rates would be:

$$\dot{\varepsilon}_a^h = \dot{\varepsilon}_{eq}^h \frac{1}{3}(1 - 1) = 0$$

$$\dot{\varepsilon}_l^h = \dot{\varepsilon}_{eq}^h \frac{1}{3}\left(1 - \left(-\frac{1}{2}\right)\right) = \frac{\dot{\varepsilon}_{eq}^h}{2} \tag{C-41}$$

$$\dot{\varepsilon}_v^h = \dot{\varepsilon}_{eq}^h$$

Out-of-Plane or Tangential Stress is the Minimum Principal Stress

In a triaxial compression test, $\theta = \pi$ so that the strain rates would be:

$$\dot{\varepsilon}_a^h = \dot{\varepsilon}_{eq}^h \frac{1}{3}(1-1) = 0$$

$$\dot{\varepsilon}_l^h = \dot{\varepsilon}_{eq}^h \frac{1}{3}\left(1 + \frac{1}{2}\right) = \frac{\dot{\varepsilon}_{eq}^h}{2} \tag{C-42}$$

$$\dot{\varepsilon}_v^h = \dot{\varepsilon}_{eq}^h$$

Note that the case given in Equation C-42 is impossible for axisymmetric geometry. This is true because the tangential stress is equal to the radial stress. In triaxial compression, the axial stress is the minimum principal stress. Thus if the tangential stress were the minimum principal stress, then a state of hydrostatic compression would have to exist. In a triaxial extension test, $\theta = 0$ so that the strain rates would be:

$$\dot{\varepsilon}_a^h = \dot{\varepsilon}_{eq}^h \frac{1}{2}(1 + \cos 2\theta) = \dot{\varepsilon}_{eq}^h$$

$$\dot{\varepsilon}_l^h = \dot{\varepsilon}_{eq}^h \frac{1}{4}(1 - \cos 2\theta) = 0 \tag{C-43}$$

$$\dot{\varepsilon}_v^h = \dot{\varepsilon}_{eq}^h$$

C.3 REFERENCES

Chan, K. S., 1996. *Final Development of the Multimechanism Deformation Coupled Fracture (MDCF) Constitutive Model*, Monthly Technical Report No. FY '96–2, Monthly Progress Report for Southwest Research Institute, Contract AQ-1458 with Sandia National Laboratories, February.

Chan, K. S., S. R. Bodner, A. F. Fossum, and D. E. Munson, 1995. "Constitutive Representation of Damage Healing in WIPP Salt," *Proceedings, 35th U.S. Symposium on Rock Mechanics*, University of Nevada, Reno, NV, June 5–7, J. J. K. Daemen and R. A. Schultz (eds.), A. A. Balkema, Rotterdam, pp. 485–490.

APPENDIX D

POTENTIAL MODIFICATION TO THE POWER-CONJUGATE EQUIVALENT STRESS MEASURES FOR SHEAR-INDUCED DAMAGE

TABLE OF CONTENTS

LIST OF FIGURES

APPENDIX D
POTENTIAL MODIFICATION TO THE POWER-CONJUGATE EQUIVALENT STRESS MEASURES FOR SHEAR-INDUCED DAMAGE

The MDCF model uses two different power-conjugate equivalent stress measures for shear-induced damage. One is the power-conjugate equivalent stress measure used to describe the inelastic shear-induced damage equivalent strain rate. The other is the associated power-conjugate stress measure used to describe the flow potential (hereafter called simply the equivalent stress measure and flow potential). Before discussing modifications to the power-conjugate equivalent stress measures for shear-induced damage, it is important to examine general states of stress and show the inability of the equivalent stress measure and flow potential, as they are currently defined, to represent the expected behavior at general states of stress. The equivalent stress measure $(\sigma_{eq}^{\omega_s})$ and flow potential stress $(\sigma_{eq}^{\omega_s^*})$ for shear-induced damage are currently defined as:

$$\sigma_{eq}^{\omega_s} = |\sigma_1 - \sigma_3| + f_p \, x_2 \, x_7 \, \text{sgn}(I_1 - \sigma_3) \left(\frac{I_1 - \sigma_3}{3 \, x_7 \, \text{sgn}(I_1 - \sigma_3)} \right)^{x_6}$$

$$\sigma_{eq}^{\omega_s^*} = |\sigma_1 - \sigma_3| + \frac{x_2 \, x_8}{3}(I_1 - \sigma_3)$$

(D-1)

where:

$$\sigma_i = \text{principal stresses } (i = 1, 2, 3)$$

$$I_1 = \text{first stress invariant} = \sigma_1 + \sigma_2 + \sigma_3$$

$$f_p = \text{material parameter related to impurity content} = 1 - p_1 \rho$$

$$x_2, \, x_6, \, x_7, \, x_8, \, p_1 = \text{material constants}$$

$$\rho = \text{impurity content}$$

$$\text{sgn}(\bullet) = \text{sign of the argument.}$$

Development of Equation D-1 was guided by laboratory test data collected predominately from triaxial compression tests $(\sigma_1 = \sigma_2 > \sigma_3)$ as illustrated in Figure D-1 (tension is assumed to be positive). The different equivalent stress measure and flow potential stress provide for a nonassociative type of formulation that provides greater flexibility in the ability to predict the volumetric behavior. In a triaxial compression test, the magnitude of the compressive confining pressure is less than the magnitude of the compressive axial stress. Figure D-1 also illustrates the triaxial extension test $(\sigma_1 > \sigma_2 = \sigma_3)$ where the magnitude of the compressive confining pressure is greater than the magnitude of the compressive axial stress. While these two types

of tests do not look substantially different, the results from these two types of tests can be dramatically different if the behavior of the material being tested depends on the intermediate principal stress. Most rocks behave differently in triaxial compression and extension with the material being weaker in extension. Fortunately, the generalized Mohr-Coulomb criterion captures this difference in material behavior.

RSI-1153-01-017

Triaxial Compression   **Triaxial Extension**

$$\sigma_1 = \sigma_2 > \sigma_3 \qquad\qquad \sigma_1 > \sigma_2 = \sigma_3$$
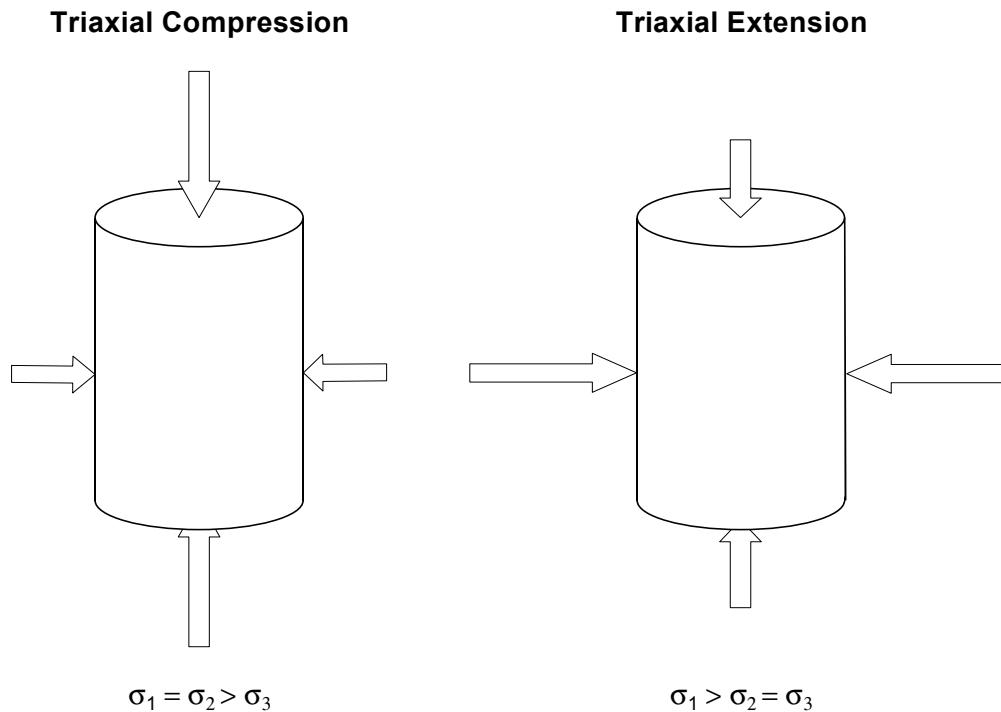
Figure D-1. Illustration of Triaxial Compression and Triaxial Extension Tests Performed on Circular Cylindrical Specimens.

The next section discusses the representation of states of stress in principal stress space, which will aid our examination of the existing equivalent stress measure and flow potential stress and help guide the development of alternative functional forms.

D.1 REPRESENTATION OF STATES OF STRESS IN PRINCIPAL STRESS SPACE

The representation of states of stress in principal-stress space is considered to help facilitate the discussion of states of stress around underground caverns and as a means to visualize those states of stress. Consider the state of stress at a point (Q) in a body represented by the principal stresses σ_i (i = 1, 2, 3) at that point as shown in Figure D-2. If the principal stresses are taken as the Cartesian coordinates in a three-dimensional space, an isotropic potential (or yield) surface may be mapped in the coordinate system. A vivid two-dimensional illustration of

D-5

the bounding states of stress is achieved by projecting these stresses into the π-plane or Haigh-Westergaard stress space (e.g., Chen and Han [1988]). The π-plane is a plane perpendicular to the hydrostatic axis $(\sigma_1 = \sigma_2 = \sigma_3)$ where the mean stress $(\sigma_m = (\sigma_1 + \sigma_2 + \sigma_3)/3)$ is zero, and Haigh-Westergaard stress space is similar to the π-plane but includes those planes where the mean stress is a nonzero constant. For simplicity, these representations will be referred to as the π-plane recognizing the shortcomings in nomenclature as stated above. Local two-dimensional Cartesian and polar coordinate systems embedded in the π-plane are convenient for representing yield or potential surfaces. This fact exists because a unique state of stress can also be uniquely defined by three stress invariants, and yield and potential functions are typically written in terms of stress invariants. Of particular interest are the invariants of the deviatoric stress tensor, S_{ij} $(S_{ij} = \sigma_{ij} - \sigma_m \delta_{ij})$, which are:

$$J_1 = 0$$

$$J_2 = \frac{1}{2} S_{ij} S_{ji}$$

(D-2)

$$J_3 = \frac{1}{3} S_{ij} S_{jk} S_{ki}$$

RSI-996-00-013
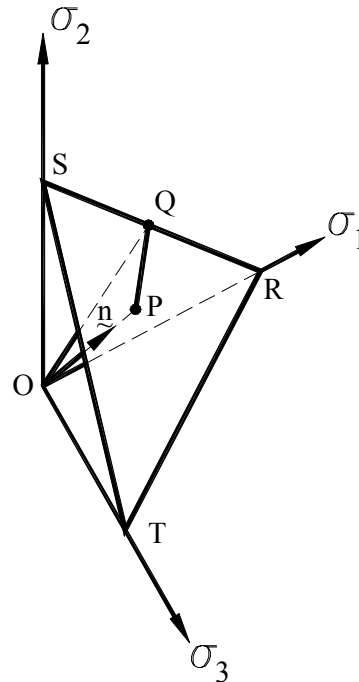
Figure D-2. Stress Points in Principal Stress Space.

Now consider the principal stress space of Figure D-3. Figure D-3 is a view looking directly down the hydrostatic axis. In this orientation, the principal stress coordinate axes appear to be 120° apart. Cartesian coordinates x and y are defined as shown in Figure D-3 (the choice is arbitrary). The x and y axes selected originate at point O on the hydrostatic axis. The x-axis is located 30° counter-clockwise from the $\sigma_1 - axis$, and the $y - axis$ lies along (but not parallel to) the $\sigma_2 - axis$. In terms of the principal stresses, the coordinates are:

$$X = \frac{\sigma_1 - \sigma_3}{\sqrt{2}} \tag{D-3}$$

$$y = \frac{2\sigma_2 - \sigma_1 - \sigma_3}{\sqrt{6}} \tag{D-4}$$

Equations D-3 and D-4 may be used to obtain a polar coordinate (r, ψ) system; viz,

$$r = \sqrt{x^2 + y^2} = \frac{1}{\sqrt{3}}\sqrt{\left(\sigma_1 - \sigma_2\right)^2 + \left(\sigma_2 - \sigma_3\right)^2 + \left(\sigma_3 - \sigma_1\right)^2} \tag{D-5}$$

$$\psi = \tan^{-1}\left(\frac{y}{x}\right) = \tan^{-1}\frac{1}{\sqrt{3}}\left[\frac{2\sigma_2 - \sigma_1 - \sigma_3}{\sigma_1 - \sigma_3}\right] \tag{D-6}$$

RSI-996-00-014
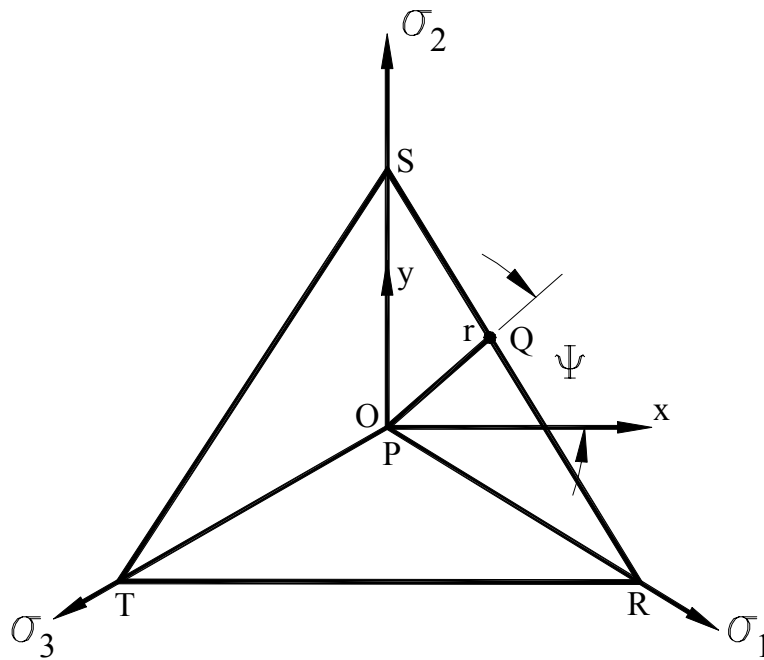
Figure D-3. Stress Points in Principal Stress Space Viewed Down the Hydrostatic Axis.

D-7

The angle ψ is referred to as the Lode angle. The Lode angle may be expressed in terms of the invariants J_2 and J_3 as [Nayak and Zienkiewicz, 1972]:

$$\psi = \frac{1}{3}\sin^{-1}\left[\frac{-3\sqrt{3}\,J_3}{2\,J_2^{3/2}}\right]$$

(D-7)

However, when the Lode angle is defined in this manner, it is restricted to $-30° \le \psi \le 30°$. This restriction requires symmetry of the yield condition in all 60° sextants in the π-plane. When J_2 is expressed in terms of the principal stresses, it becomes:

$$J_2 = \frac{1}{6}\left\{\left(\sigma_1 - \sigma_2\right)^2 + \left(\sigma_2 - \sigma_3\right)^2 + \left(\sigma_1 - \sigma_3\right)^2\right\}$$

(D-8)

From Equations D-5 and D-8, one readily sees that the distance from the hydrostatic axes to a stress point is equivalent to $\sqrt{2J_2}$ when lying in the π-plane. Potential or yield functions expressed in terms of these coordinate systems may be plotted in the π-plane easily. Figure D-4 illustrates the Mohr-Coulomb criterion plotted in the π-plane using these coordinate systems. Stress lines of interest (triaxial compression ($\psi = \pi/6$) and extension ($\psi = -\pi/6$)) are labeled along with the ordering of the principal stresses in the sextants.

Using this information, the flow potential equivalent stress presently defined for the MDCF model (Equation D-1) can be plotted in principal stress space as shown in Figure D-5. Figure D-5 reveals that the present flow potential equivalent stress actually describes a material that is stronger in triaxial extension than in triaxial compression, which is contrary to available information on the behavior of rock. This could be surmised by observing the role that the $I_1 - \sigma_3$ term plays in the definition of the stress measure in Equation D-1. Damage occurs when the effective stress measure is positive. Thus the $I_1 - \sigma_3$ term represents the stresses or confinement that suppresses damage. In a triaxial compression test (Figure D-1), $I_1 - \sigma_3$ represents the confining pressure in the test, which suppresses the microfracturing generated parallel to the axial direction in the test specimen. However, in a triaxial extension test where the microfractures would be generated perpendicular to the axial direction, the $I_1 - \sigma_3$ term is not indicative of the axial stress (the major principal stress (σ_1) in a triaxial extension test). The $I_1 - \sigma_3 = \sigma_1 + \sigma_2$ term obviously overestimates the magnitude of the stresses suppressing damage for a triaxial extension state of stress, making the material seem stronger than it actually is. Unfortunately, the functional form also makes the material appear to be stronger at all states of stress between triaxial compression and extension. To remedy this problem, new Mohr-Coulomb type functional forms are developed in the next section that makes the material weaker in extension.
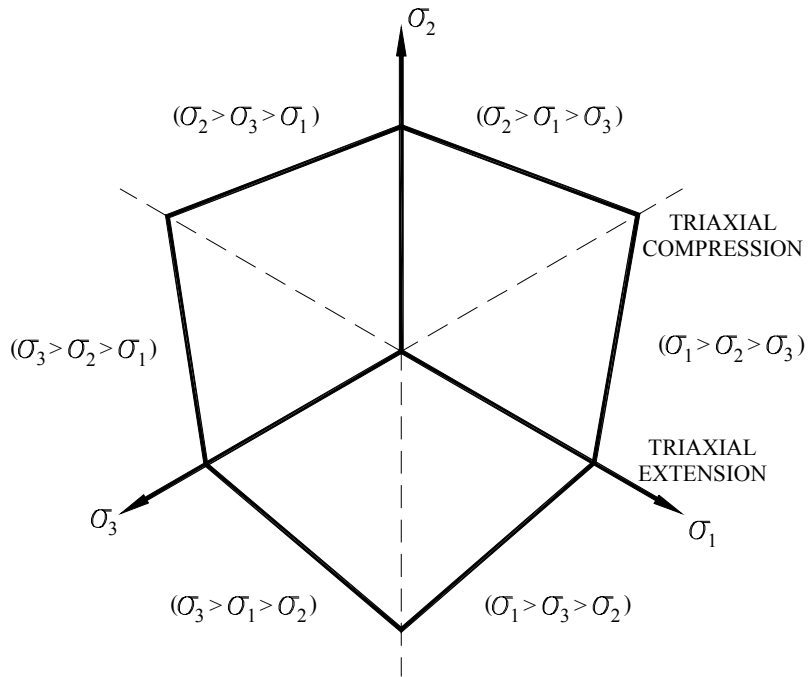
Figure D-4. Mohr-Coulomb Yield Surface in Principal Stress Space.
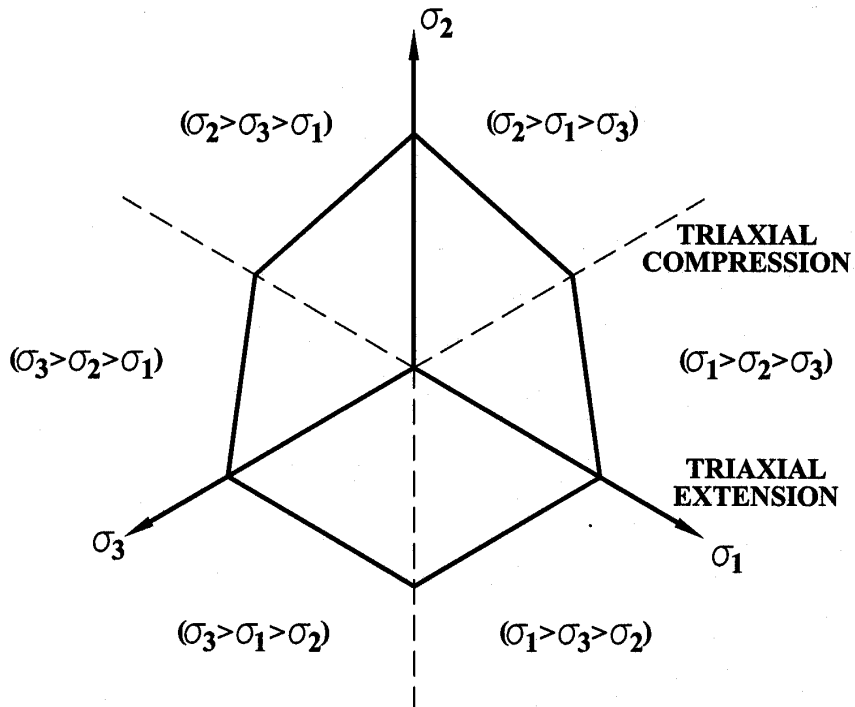
Figure D-5. Multimechanism Deformation Coupled Fracture (MDCF) Flow Potential Function Plotted in Principal Stress Space.

D.2 ALTERNATE DAMAGE EFFECTIVE STRESS AND FLOW POTENTIAL

The damage effective stress and flow potential presently defined in the MDCF model are given in Equation D-1. The objective of this section is to describe new functional forms that remove the deficiencies inherent in the current forms used in the MDCF model. To accomplish this task, alternative damage effective stress and flow potentials are developed based on the Mohr-Coulomb criterion. The Mohr-Coulomb criterion is typically written in its familiar linear form as:

$$|\tau| = S_0 - \sigma_n \tan\phi \tag{D-9}$$

where τ is the shear stress along the failure plane, σ_n is the normal stress on the plane, ϕ is the angle of internal friction, and S_0 is the material cohesion. The shear and normal stresses are written as:

$$\sigma_n = \frac{\sigma_1 + \sigma_3}{2} + \frac{\sigma_1 - \sigma_3}{2}\cos(2\gamma)$$

$$|\tau| = \left|\frac{\sigma_1 - \sigma_3}{2}\sin(2\gamma)\right| \tag{D-10}$$

$$\gamma = \frac{\pi}{4} + \frac{\phi}{2}$$

After substitution of Equations D-10 into Equation D-9 and rearrangement, Equation D-9 may be written as:

$$\frac{\sigma_1 - \sigma_3}{2} = S_0 \cos(\phi) - \frac{\sigma_1 + \sigma_3}{2}\sin(\phi) \tag{D-11}$$

and restated as:

$$\sigma_1 - \sigma_3 = 2S_0 \cos(\phi) - (\sigma_1 + \sigma_3)\sin(\phi) \tag{D-12}$$

When the Mohr-Coulomb criterion is written in invariant form using the invariants σ_m, J_2, and ψ, it becomes (e.g., Callahan [1982]):

$$2\sqrt{J_2}\left(\cos\psi - \frac{1}{\sqrt{3}}\sin\psi\,\sin\phi\right) + 2\sigma_m \sin\phi - 2S_0\cos\phi = 0 \tag{D-13}$$

When plotted in principal stress space, Equation D-13 reproduces Figure D-4. Thus adoption of functional forms similar to Equation D-13 will produce the desired weaker material in triaxial extension and remove the deficiencies inherent in the current functional forms of the effective stress measure and flow potential. Therefore, suggested functional forms for the damage effective stress and flow potential are:

$$\sigma_{eq}^{\omega_s} = 2\sqrt{J_2}\left(\cos\psi - \eta\,\sin\psi\right) + 2\sqrt{3}\,\eta\,\sigma_m - C$$

$$\sigma_{eq}^{\omega_s^*} = 2\sqrt{J_2}\left(\cos\psi - \kappa\,\sin\psi\right) + 2\sqrt{3}\,\kappa\,\sigma_m \tag{D-14}$$

where η, c, and κ are material constants to be determined through laboratory testing. Once test data are available, especially triaxial extension test data, the functional forms and material constants may require modification. For example, the influence of impurities and the nonlinear dependence on mean stress could be included much like the present functional forms given in Equation D-1.

The shear-induced damage strain rate $(\dot{\varepsilon}_{ij}^{\omega_s})$ is written in terms of the power-conjugate equivalent stress measures as:

$$\dot{\varepsilon}_{ij}^{\omega_s} = \dot{\varepsilon}_{eq}^{\omega_s}\frac{\partial\sigma_{eq}^{\omega_s^*}}{\partial\sigma_{ij}} \tag{D-15}$$

where the equivalent inelastic shear-induced damage strain rate $(\dot{\varepsilon}_{eq}^{\omega_s})$ definition has not changed, but the shear-induced damage effective stress $(\sigma_{eq}^{\omega}$ given in Equation D-14) that it depends upon has changed. The shear-induced flow potential is:

$$\frac{\partial\sigma_{eq}^{\omega_s^*}}{\partial\sigma_{ij}} = 2\kappa\frac{\delta_{ij}}{\sqrt{3}} + \left(\cos(2\psi) + \kappa\sin(2\psi)\right)\frac{S_{ij}}{2\sqrt{J_2}\cos(3\psi)}$$

$$-\sqrt{J_2}\left(\sin(\psi) + \kappa\cos(\psi)\right)\frac{\tan(3\psi)}{3J_3}t_{ij} \tag{D-16}$$

where:

$$t_{ij} = S_{ip}S_{pj} - \frac{2}{3}J_2\delta_{ij}$$

Reviewing the flow potential given in Equation D-16, one observes an indeterminacy when the intermediate principal stress is equal to either the maximum or minimum principal stress (i.e., triaxial compression and extension states of stress). In other words, a unique strain rate direction cannot be determined. Under these conditions, the Lode angle (ψ) is equal to $\pm\,\pi/6$. To eliminate this problem computationally, the flow potential is taken as the average of the flow potentials on either side of the corner and evaluated in the limit as $\psi \to \pm\,\pi/6$. Performing this limiting operation as $\psi \to \pm\,\pi/6$ (the triaxial compression corner), Equation D-16 becomes:

$$\frac{\partial\sigma_{eq}^{\omega_s^*}}{\partial\sigma_{ij}} = 2\kappa\frac{\delta_{ij}}{\sqrt{3}} + \frac{\sqrt{3}-\kappa}{6}\left[\frac{S_{ij}}{\sqrt{3J_2}} + \frac{\sqrt{J_2}}{3\sqrt{3}J_3}t_{ij}\right] \tag{D-17}$$

Equation D-17 may be further reduced for the triaxial compression conditions (i.e., $\sigma_1 = \sigma_2 > \sigma_3$) and substituted into Equation D-15 to yield the individual strain rate components; viz,

$$\dot{\varepsilon}_{11}^{\omega_s} = \dot{\varepsilon}_{22}^{\omega_s} = \dot{\varepsilon}_{eq}^{\omega_s}\left(\frac{2\kappa}{\sqrt{3}} + \frac{3+\kappa}{12} \right)$$

$$\dot{\varepsilon}_{33}^{\omega_s} = \dot{\varepsilon}_{eq}^{\omega_s}\left(\frac{2\kappa}{\sqrt{3}} - \frac{3+\kappa}{6} \right) \tag{D-18}$$

$$\dot{\varepsilon}_{V}^{\omega_s} = 2\sqrt{3}\ \ \kappa\ \ \dot{\varepsilon}_{eq}^{\omega_s}$$

Similarly, performing this limiting operation as $\psi \to -\pi/6$ (the triaxial extension corner), Equation D-16 becomes:

$$\frac{\partial \sigma_{eq}^{\omega_s^*}}{\partial \sigma_{ij}} = 2\kappa \frac{\delta_{ij}}{\sqrt{3}} + \frac{\sqrt{3}+\kappa}{6}\left[\frac{S_{ij}}{\sqrt{3J_2}} + \frac{\sqrt{J_2}\ t_{ij}}{3\sqrt{3}J_3} \right] \tag{D-19}$$

Equation D-19 may be further reduced for the triaxial extension conditions (i.e., $\sigma_1 > \sigma_2 = \sigma_3$) and substituted into Equation D-15 to yield the individual strain rate components; viz,

$$\dot{\varepsilon}_{11}^{\omega_s} = \dot{\varepsilon}_{22}^{\omega_s} = \dot{\varepsilon}_{eq}^{\omega_s}\left(\frac{2\kappa}{\sqrt{3}} - \frac{3+\kappa}{12} \right)$$

$$\dot{\varepsilon}_{33}^{\omega_s} = \dot{\varepsilon}_{eq}^{\omega_s}\left(\frac{2\kappa}{\sqrt{3}} + \frac{3+\kappa}{6} \right) \tag{D-20}$$

$$\dot{\varepsilon}_{V}^{\omega_s} = 2\sqrt{3}\ \ \kappa\ \ \dot{\varepsilon}_{eq}^{\omega_s}$$

Thus material parameter κ is seen to govern the magnitude of the volumetric strain generated during the microfracturing process associated with damage.

D.3 REFERENCES

Callahan, G. D., 1982. *A Plasticity Approach for Rock Containing Planes of Weakness,* Ph.D. Thesis, University of Minnesota, Minneapolis, MN.

Chen, W. F. and D. J. Han, 1988. *Plasticity for Structural Engineers,* Springer-Verlag, New York, NY.

Nayak, G. C. and O. C. Zienkiewicz, 1972. "A Convenient Form of Invariants and its Application in Plasticity," *Journal of the Structural Division,* ASCE, Vol. 98, pp. 949–954.

APPENDIX E

MODIFIED MDCF MODEL

TABLE OF CONTENTS

APPENDIX E
MODIFIED MDCF MODEL

The generalized form of the modified MDCF model developed for CNG storage is given by:

$$\dot{\varepsilon}_{ij}^i = \frac{\partial \sigma_{eq}^c}{\partial \sigma_{ij}}\dot{\varepsilon}_{eq}^c + \frac{\partial \sigma_{eq}^{\omega_s^*}}{\partial \sigma_{ij}}\dot{\varepsilon}_{eq}^{\omega_s} + \frac{\partial \sigma_{eq}^{\omega_t}}{\partial \sigma_{ij}}\dot{\varepsilon}_{eq}^{\omega_t} + \frac{\partial \sigma_{eq}^h}{\partial \sigma_{ij}}\dot{\varepsilon}_{eq}^h \tag{E-1}$$

where $\dot{\varepsilon}_{ij}^i$ is the inelastic strain and $\sigma_{eq}^c, \sigma_{eq}^{\omega_s^*}, \sigma_{eq}^{\omega_t}, \sigma_{eq}^h, \dot{\varepsilon}_{eq}^c, \dot{\varepsilon}_{eq}^{\omega_s}, \dot{\varepsilon}_{eq}^{\omega_t},$ and $\dot{\varepsilon}_{eq}^h$ are power-conjugate equivalent stress measures and equivalent inelastic strain rates for the dislocation creep (c), shear damage (ω_s) tensile damage (ω_t), and damage healing (h) mechanisms, respectively. The equations are simply presented in this appendix with compression taken to be negative. Details of the power-conjugate stress measures, kinetic equations, flow laws, and evolution equation for damage in the MDCF model are summarized in Appendices A, C, and D.

E.1 KINETIC EQUATION FOR DISLOCATION FLOW

$$\dot{\varepsilon}_{eq}^c = F\dot{\varepsilon}_s \tag{E-2}$$

$$\dot{\varepsilon}_{s_1} = A_1 e^{-Q_1/RT}\left(\frac{\sigma_{eq}^c}{\mu(1-\omega)}\right)^{n_1} \tag{E-3}$$

$$\dot{\varepsilon}_{s_2} = A_2 e^{-Q_2/RT}\left(\frac{\sigma_{eq}^c}{\mu(1-\omega)}\right)^{n_2} \tag{E-4}$$

$$\dot{\varepsilon}_{s_3} = \left|H\left(\frac{\sigma_{eq}^c}{1-\omega}-\sigma_0\right)\right|\left(B_1 e^{-Q_1/RT} + B_2 e^{-Q_2/RT}\right)\sinh\left[\frac{q\left(\frac{\sigma_{eq}^c}{1-\omega}-\sigma_0\right)}{\mu}\right] \tag{E-5}$$

$$F = \begin{cases} \exp\left[\Delta\left(1-\dfrac{\varsigma}{\varepsilon_t^*}\right)^2\right] & \text{for } \varsigma < \varepsilon_t^* \\[2mm] 1 & \text{for } \varsigma = \varepsilon_t^* \\[2mm] \exp\left[-\delta\left(1-\dfrac{\varsigma}{\varepsilon_t^*}\right)^2\right] & \text{for } \varsigma > \varepsilon_t^* \end{cases} \tag{E-6}$$

$$\dot{\zeta} = \text{sign}(\varepsilon_t^* - \zeta)(F_r - 1)\dot{\varepsilon}_s \tag{E-7}$$

$$F_r = \begin{cases} \exp\left[\Delta\left(1 - \dfrac{\varsigma}{\varepsilon_t^*}\right)^2\right] & \text{for } \varsigma < \varepsilon_t^* \\[3mm] 1 & \text{for } \varsigma = \varepsilon_t^* \\[3mm] \exp\left[\Delta\left(1 - \dfrac{\varepsilon_t^*}{\varsigma}\right)\right] & \text{for } \varsigma > \varepsilon_t^* \end{cases} \tag{E-8}$$

$$\varepsilon_t^* = K_0 e^{cT}\left(\frac{\sigma_{eq}^c}{\mu(1-\omega)}\right)^m \tag{E-9}$$

$$\Delta = \alpha_w + \beta_w \log\left(\frac{\sigma_{eq}^c}{\mu(1-\omega)}\right) \tag{E-10}$$

$$\delta = \alpha_r + \beta_r \log\left(\frac{\sigma_{eq}^c}{\mu(1-\omega)}\right) \tag{E-11}$$

$$\sigma_{eq}^c = 2\cos\psi\sqrt{J_2} = \sigma_1 - \sigma_3 \tag{E-12}$$

E.2 FLOW LAW FOR DISLOCATION DEFORMATION

$$\sigma_{eq}^c = 2\cos\psi\sqrt{J_2} = \sigma_1 - \sigma_3 \tag{E-13}$$

E.3 KINETIC EQUATIONS FOR DAMAGE-INDUCED FLOW

$$\dot{\varepsilon}_{eq}^{\omega_i} = F^{\omega_i}\dot{\varepsilon}_s^{\omega_i} \tag{E-14}$$

$$F^{\omega_s} = F\exp\left[\frac{c_4\left(\sigma_{eq}^c - c_5\right)}{\sigma_0(1-\rho)}\right] \tag{E-15}$$

$$F^{\omega_t} = F\exp\left[\frac{c_4\left(\sigma_{eq}^{\omega_t} - c_5\right)}{\sigma_0(1-\rho)}\right] \tag{E-16}$$

$$\dot{\varepsilon}_s^{\omega_i} = c_1 \omega_0 \exp(c_3 \omega) \left[\sinh\left(\frac{c_2 \sigma_{eq}^{\omega_i} H(\sigma_{eq}^{\omega_i})}{(1-\omega)(1-\rho)\mu} \right) \right]^{n_3} \tag{E-17}$$

$$c_1 = c_0 \left(B_1 e^{(-Q_1/RT)} + B_2 e^{(-Q_2/RT)} \right) \tag{E-18}$$

$$\sigma_{eq}^{\omega_s} = |\sigma_1 - \sigma_3| + f_p x_2 x_7 \, \mathrm{sgn}(I_1 - \sigma_3) \left(\frac{I_1 - \sigma_3}{3x_7 \, \mathrm{sgn}(I_1 - \sigma_3)} \right)^{x_6} \tag{E-19}$$

$$\sigma_{eq}^{\omega_t} = x_1 \sigma_1 H(\sigma_1) \tag{E-20}$$

$$f_p = 1 - p_1 \rho \tag{E-21}$$

$$\dot{\omega} = \dot{\omega}_s + \dot{\omega}_t - \dot{h} \tag{E-22}$$

$$\dot{\omega}_s = \frac{x_4}{t_0} \omega \left[\ln\left(\frac{1}{\omega} \right) \right]^{-\frac{x_4+1}{x_4}} \left[\frac{\sigma_{eq}^{\omega_s} H(\sigma_{eq}^{\omega_s})}{(1-\rho)\xi_s} \right]^{x_{3s}} \tag{E-23}$$

$$\dot{\omega}_t = \frac{x_4}{t_0} \omega \left[\ln\left(\frac{1}{\omega} \right) \right]^{-\frac{x_4+1}{x_4}} \left[\frac{\sigma_{eq}^{\omega_t} H(\sigma_{eq}^{\omega_t})}{(1-\rho)\xi_t} \right]^{x_{3t}} \tag{E-24}$$

$$\xi_s = \xi_s^1 \text{ for } \sigma_{eq}^c / (1-\omega) > \sigma_0 \tag{E-25}$$

$$\xi_s = \xi_s^2 \text{ for } \sigma_{eq}^c / (1-\omega) \le \sigma_0 \tag{E-26}$$

E.4 FLOW LAW FOR DAMAGE-INDUCED INELASTIC DEFORMATION

$$\sigma_{eq}^{\omega_s^*} = |\sigma_1 - \sigma_3| + \frac{x_2 x_8}{3}(I_1 - \sigma_3) \tag{E-27}$$

$$\sigma_{eq}^{\omega_t} = x_1 \sigma_1 H(\sigma_1) \tag{E-28}$$

E.5 KINETIC EQUATION FOR DAMAGE RECOVERY FLOW (HEALING)

$$\dot{\varepsilon}_{eq}^h = \frac{\varepsilon_{kk}^i \left(\sigma_{eq}^h - \sigma_b \right) H\left(\sigma_b - \sigma_{eq}^h \right)}{\tau \mu} \tag{E-29}$$

$$\sigma_{eq}^{h} = \frac{1}{3}\left(I_1 - \sigma_3\right) \tag{E-30}$$

$$\sigma_b = -X_7 \left[\frac{\sigma_1 - \sigma_3}{f_p X_2 X_7}\right]^{\frac{1}{x_6}} \tag{E-31}$$

$$\tau = \tau_0 \exp\left(-k_1 \varepsilon_{kk}^{i}\right) + \tau_1 \tag{E-32}$$

$$\dot{h} = \frac{\omega\, H\left(\omega - \omega_0\right)\left(\sigma_{eq}^{h} - \sigma_b\right) H\left(\sigma_b - \sigma_{eq}^{h}\right)}{\tau\, \mu} \tag{E-33}$$

E.6 FLOW LAW FOR HEALING-INDUCED INELASTIC DEFORMATION

$$\sigma_{eq}^{h} = \sigma_n \tag{E-34}$$

$$\sigma_n = \frac{\sigma_1 + \sigma_3}{2} + \frac{\sigma_1 - \sigma_3}{2}\cos\left(2\theta\right) \tag{E-35}$$

APPENDIX F

**MDCF MODEL PARAMETERS
FOR MCINTOSH DOME SALT**

LIST OF TABLES

APPENDIX F
MDCF MODEL PARAMETERS
FOR MCINTOSH DOME SALT

**Table F-1. MDCF Model Parameter Values for McIntosh Dome Salt
(Page 1 of 2)**

Parameter	Units	McIntosh Salt Value	Remarks
Elastic Parameter Values			
E	MPa	27,100	—
v	—	0.32	—
Dislocation Creep Parameter Values			
A_1	s^{-1}	8.39×10^{27}	WIPP Value
A_2	s^{-1}	4.05×10^{16}	—
Q_1/R	K	12,570	WIPP Value
Q_2/R	K	5,028	WIPP Value
n_1	—	5.5	WIPP Value
n_2	—	6.2	—
B_1	s^{-1}	6.09×10^6	WIPP Value
B_2	s^{-1}	3.03×10^{-2}	WIPP Value
q	—	5,335	WIPP Value
σ_0	MPa	25	WIPP Theoretical Value
μ	MPa	12,400	Normalizing Constant
m	—	3	WIPP Theoretical Value
K_0	—	7.69×10^5	—
c	K^{-1}	9.20×10^{-3}	WIPP Value
α_h	—	−17.40	WIPP Value
β_h	—	−7.74	WIPP Value
α_r	—	12.15	—
β_r	—	0.0	—

Table F-1. MDCF Model Parameter Values for McIntosh Dome Salt
(Page 2 of 2)

Parameter	Units	McIntosh Salt Value	Remarks
Damage and Healing Parameter Values			
x_1	—	Not Used	Tensile Term
x_2	—	11.4	—
x_{3s}	—	5.5	WIPP Value
x_{3t}	—	Not Used	Tensile Term
x_4	—	3	WIPP Value
ξ_s^1	MPa	100	—
ξ_s^2	MPa	100	—
ξ_t	MPa	Not Used	Tensile Term
x_6	—	0.3	—
x_7	MPa	1	Normalizing Constant
x_8	—	0.12	—
t_0	s	1	Normalizing Constant
τ_0	s	5,410	—
τ_1	s	182	—
c_0	—	111,460	—
c_2	—	850	WIPP Value
c_3	—	10	WIPP Value
c_4	—	0.04	—
c_5	MPa	25	WIPP Value
n_3	—	3	WIPP Value
k_1	—	1,155	—
p_1	—	Not Used	Impurity Parameter
ω_0	—	0.0001	Constant
ρ	—	Not Used	Impurity Parameter